Process Parameter Optimisation and Thermal Characterisation of Coaxial Multi-Laser Metal Wire Additive Manufacturing with 316L Stainless Steel

Matthew Roberts

School of Engineering

Lancaster University

A thesis submitted for the degree of

Doctor of Philosophy

February, 2024

Dedicated to the memory of Dennis Roberts.

Process Parameter Optimisation and Thermal Characterisation of Coaxial Multi-Laser Metal Wire Additive Manufacturing with 316L Stainless Steel

Matthew Roberts

School of Engineering, Lancaster University

A thesis submitted for the degree of *Doctor of Philosophy*. February, 2024.

Abstract

Laser Metal Wire Additive Manufacturing systems (LWAM), with coaxially mounted lasers, are emerging onto the additive manufacturing market. They use relatively fine wire feedstock and have high efficiency in terms of energy and deposition speeds compared to other metal wire technologies, making a credible technology to fill the gap between slower, precise metal powder technologies and faster, lower-fidelity wire-arc technologies. Limited research is available for this technology. Commercial slicing software, based on more forgiving polymers, is also limited in its ability to accommodate more complex dynamics of metal wire additive manufacturing.

This thesis uses the Meltio M450 to investigate the relationship between laser power, extrusion rate and head speed and the resulting track geometry and layer quality. The research identifies the process parameters required to produce high-quality tracks repeatedly. New insights are developed into the use of machine learning to predict quality and geometry of beads, showing how these tools reduce the need for experimental trials. Using Machine Learning to address uncertainty in the prediction of track widths adds new insights to the application of machine learning in the field of metal additive manufacturing.

A single-layer model is developed to predict layer height, adding to the existing body of work by quantifying the effect of the number of tracks and track separation on the resulting layer height. Experiments to measure interlayer temperature and bulk heating during the deposition process are used with modelling to show a new

method for using the base substrate temperature to infer interlayer temperatures when interlayer pauses of sixty seconds or longer are used.

This thesis has developed novel methods for process optimisation, geometry prediction and interlayer temperature control, which address some of the key research gaps for coaxial LWAM and add to the body of knowledge in this area to support improved slicing tools.

Acknowledgements

First and foremost, I must thank my wonderful wife, Jenny Roberts, who encouraged me to take the leap, quit my job and do this in the first place. She has provided unswerving support and encouragement throughout. I would not have started this and definitely would not have finished it without her.

I must also express my thanks and gratitude to my PhD supervisor, Professor Andrew Kennedy, who met with me every week, supported my decisions, kept pushing me to do a little bit more. I always looked forward to our meetings and the many hours of discussion that we have had. I will miss them. I am not sure that I can ever cover the cost of all of the coffee that he paid for, so can only offer my thanks in writing here!

My thanks to the technicians within the School of Engineering, Mike Mead at CREATE Education and Fran Carrasco from Meltio for promptly responding to the many calls for repairs, support and advice.

It is not possible to complete something like this without the support of your friends and family. I am grateful to have such wonderful support and encouragement from my Mum, Janet Roberts, and from Jude and Paul Wise, who also provided invaluable childcare, giving me much needed time to complete this. Our great friends here in Lancaster: Duncan Webster and Hannah Chadburn, Nathan and Gabbi Burley, Ben and Kim Dempster, Dave and Ruth Howarth and Clare and Ali Higham, who have helped and supported my family throughout this journey. I am particularly grateful to them for their support to us at the beginning of my PhD when we lost my Dad, I will never be able to repay them for their kindness during this time.

Finally, I must thank my children, Toby, Ewan and Elsie. They have put up with a lot during the past three years. Sometimes you aren't the best parent with the stresses of a PhD but they were always the best children!

Declaration

I declare that the work presented in this thesis is, to the best of my knowledge and belief, original and my own work. The material has not been submitted, either in whole or in part, for a degree at this, or any other university. Many of the ideas in this thesis were the product of discussion with my supervisor Professor Andrew Kennedy.

This thesis does not exceed the maximum permitted word length of 80,000 words. The estimated word count is: 35855 .

Matthew Roberts

February, 2024

Excerpts of this thesis have been published in the following conference manuscript.

Matthew Roberts, Min Xia, and Andrew Kennedy (2022). "Data-driven Process Parameter Optimisation for Laser Wire Metal Additive Manufacturing". In: *2022 27th International Conference on Automation and Computing (ICAC)*. IEEE, pp. 1– 6

Contents

List of Tables

List of Figures

xix

Abbreviations

AM . . . . Additive Manufacturing

ANN . . . . Artificial Neural Network

CAD . . . . Computer Aided Design

CMOS . . . . Complementary Metal-Oxide-Semiconductor

CNC . . . . Computer Numerical Control

CSA . . . . Cross-Sectional Area

CSAM . . . . Cold Spray Additive Manufacturing

CSV . . . . Comma-Separated Values

DED . . . . Direct Energy Deposition

DOE . . . . Design of Experiment

FEA . . . . Finite Element Analysis

FSAM . . . . Friction Stir Additive Manufacturing

FOM . . . . Flat-Top Overlapping Model

G-Code . . . . Geometry Code

GED . . . . Global Energy Density

GPR . . . . Gaussian Process Regression

HAZ . . . . Heat-Affected Zone

HCl . . . . Hydrochloric acid

HIP . . . . Hot Isostatic Pressing

HWR . . . . Height to Width Ratio

ID . . . . Identification

ISO . . . . International Standards Organisation

KNN .... K-Nearest Neighbours

LENS .... Laser Engineered Net Shaping

LWAM .... Laser Wire Additive Manufacturing

ML .... Machine Learning

PBF .... Powder Bed Fusion

PC .... Personal Computer

RMS .... Root Mean Squared

RMSE .... Root Mean Squared Error

RSS .... Residual Sum of Squares

SLM .... Selective Laser Melting

SMA .... Shape Memory Alloy

SVM .... Support Vector Machine

TC .... Thermocouple

TOM .... Tangent Overlapping Model

UK .... United Kingdom

USB .... Universal Serial Bus

WAAM .... Wire Arc Additive Manufacturing

WSF .... Wire Speed Factor

Chapter 1

Introduction

There are many, commercially available, mature Direct Energy Deposition (DED) technologies to produce metal components, which are comprehensively covered in the literature. However, this is not the case for Laser Metal Wire Additive Manufacturing (LWAM) systems with coaxially mounted lasers. These systems are beginning to emerge commercially, but there is limited research available to support this technology. Coaxial LWAM systems can use relatively fine wire feedstocks and have a high efficiency in terms of energy absorption and deposition speeds compared to other laser metal deposition technologies. Thus coaxial LWAM systems have the potential to become established as a credible technology to fill the gap between the slow but precise metal powder based technologies such as Powder Bed Fusion (PBF) or the Laser Engineered Net Shaping (LENS) DED technology and the much faster, high energy, lower fidelity, Wire Arc Additive Manufacturing (WAAM).

Coaxial LWAM technologies can produce fully dense, near-net-shaped components, using a range of metal alloys, such as stainless steel, mild steel, tool steel, Invar, 625 and 718 nickel and titanium 64. However, the published literature to validate this is limited. As with all DED technologies, LWAM systems face the same challenges in terms of characterising new materials, process quality assurance and certification, repeatability and consistency of parts. Therefore, it is critical that a body of research is developed to support these challenges.

1.1   Research Aims

The main aims of this work are to firstly determine how fundamental process parameters such as laser power, deposition head speed and extrusion rate are used to produce repeatable tracks, layers and parts with low variability compared to the planned part size and shape and, secondly, to develop models which can translate these parameters into predicted bead geometries and layer thicknesses to support the current gaps in both the literature and slicing tools with respect to this information. Through this approach, it is intended that process parameters can be identified to produce parts of consistent and repeatable high quality.

A key challenge to achieving a high-quality process, identified in the literature for metal AM technologies, is understanding the accumulation of heat within the deposited material and the effects that this has on the final part. The final aim of this work is to measure the developing thermal field as a part is produced and attempt to model it using off-the-shelf additive manufacturing modelling tools and to investigate whether these models can be used as part of the planning activities when producing a part using LWAM.

1.2   Thesis Structure

The thesis is organised into seven chapters, including the introductory chapter.

Chapter 2 - Literature Review

> Provides a review of the relevant literature relating to this field and from this identifies its key challenges and identifies knowledge gaps.

Chapter 3 - Experimental Methods

> Describes the experimental techniques, methodologies and equipment configuration required to undertake the experimental programme.

Chapter 4 - Effect of Process Parameters on Single-Track Geometry

> Defines what characteristics a high-quality track should have, its cross-

sectional shape, height and width. It identifies the optimal process parameters and describes process windows for various fixed powers. The chapter investigates whether Machine Learning tools can be used to reduce the experimental work required to explore the process window across a wider range of powers and to predict the quality and geometry of single tracks with high accuracy.

Chapter 5 - Optimisation of Single and Multi-Layer Deposition

Develops the optimal single tracks characterised in Chapter 4 into a single-layer model, investigating the effects of track spacing and the number of tracks used on the resulting layer height. These layers are used to investigate the optimum step height for multi-layer parts and the effects of different height increments on the resulting part height in terms of overbuilding or underbuilding.

Chapter 6 - Measuring and Modelling the Thermal History

Investigates the interlayer temperatures of small cuboid samples. It describes the general heating and cooling cycles of the part and the effect of the substrate on this. The effect of a range of interlayer pauses on the reduction of bulk heating and maintenance of consistent target interlayer temperatures is investigated. This section models these experiments to establish whether an off-the-shelf AM modelling tool can support the identification of an optimum interlayer pause duration to achieve a target maximum interlayer temperature.

Chapter 7 - Conclusions and Further Work

Summarises the main conclusions from the work and provides suggestions for future work.

Chapter 2

Literature Review

2.1 Laser Metal Wire Additive Manufacturing

Direct Energy Deposition (DED) is a family of metal AM technologies where a melt pool is created by an energy source, typically an electrical arc or a laser, and metal powder or wire feedstock is fed into the melt pool. The pool is moved to create a weld bead or track, which is overlapped to create a layer in the shape of the part. Subsequent layers are bonded to the layer below through remelting with the melt pool. Figure 2.1 shows the range of technology types within DED.
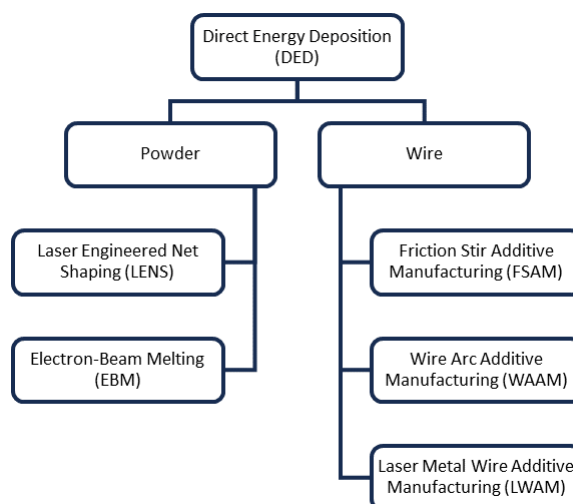
Figure 2.1: Hierarchy of DED Printing Technologies.

Wire DED technologies are becoming increasingly popular because of the wide availability of feedstocks, which are cheaper and easier to handle than powder. The resultant parts typically require post-processing, such as heat treatment and machining, but they have very low porosity, reduced waste material, and often have equal or better material properties than the cast or forged equivalents (Shamsaei et al., 2015).

The limitations of Laser Wire Additive Manufacturing (LWAM) compared to PBF and conventional subtractive technologies in terms of accuracy are compensated for by its speed, flexibility and versatile part geometries. The technology is increasingly being adopted by many different sectors such as aerospace, nuclear, automotive, rail and shipbuilding. The technology is suited to a wide range of alloys, such as stainless steels, tool steels, alloy steels, titanium-based alloys, cobalt-based alloys, nickel-based alloys, aluminium alloys, high-entropy alloys, inter-metallics, shape memory alloys (SMAs), ceramics, composites and functionally graded materials (Svetlizky et al., 2021).

Whilst both wire-based DED technologies, LWAM and Wire Arc Additive Manufacturing (WAAM) differ in their mechanisms and applications. LWAM's laser-based technology offers higher precision and control over the melting process, typically with shallower melting of the previous layer and less energy input, resulting in a finer resolution and better surface finish of parts. WAAM uses an electric arc as the energy source, which is more suited to large scale components, offering faster deposition rates. However, WAAM typically requires more post-processing due to its rougher surface finish and the potential for higher residual stress compared to LWAM.

LWAM also has advantages over conventional casting, forging and subtractive manufacturing methods. Without needing to meet the needs of the casting process, the amount of material in the component can be reduced and performance can be improved; it is therefore often possible to focus on optimising components functionally. The process also removes the need for tooling and moulds but often

requires further post-processing steps, such as heat treatments and machining to net shape. The material properties of the LWAM parts, such as yield strength and hardness, are often better than cast or wrought (Hatala et al., 2021). Through these benefits, the technology allows new alloys to be used and designs can be produced that would otherwise be too expensive using traditional manufacturing methods (Bandyopadhyay et al., 2022). The process does have its own inefficiencies, it is typical for many metal AM processes to use an iterative approach to achieve a final design and optimal print parameters for the resulting part; the production of components through LWAM is no exception to this and usually requires several print iterations to create successful and repeatable parts (Greer et al., 2019).

Historically, LWAM has been mostly used for component prototyping, due to the speed with which parts can be transferred from CAD models to the slicing software used to transform the 3D model into the appropriate machine commands and settings via G-code. However, now the technology is more focused on producing production components, which range from relatively small parts such as brackets up to very large-scale items weighing multiple tonnes. Svetlizky et al. (2021) suggests that the DED market is expected to reach around $755 million by 2025. This has been enhanced by the ability to integrate LWAM deposition heads into robotic arms and inside Computerised Numerical Control (CNC) machining systems, known as Hybrid Additive Manufacturing (Sefene, Hailu, and Tsegaw, 2022). This increases speed and flexibility in terms of part geometry and machine usage, whilst taking advantage of the benefits of better finishes from more conventional subtractive CNC machining.

Whilst the technology is seeing substantial growth, it requires significant operator knowledge and experience to deliver high-quality parts, most notably because AM CAD software and slicing tools were developed for polymer printing processes (Michel et al., 2019) and are yet to fully reflect the dynamic behaviours seen in DED processes.

2.2   Fundamentals of the LWAM Process

The LWAM deposition process requires a planned and coordinated control of multiple hardware elements. Central to this process is the laser, which provides the energy source to generate a melt pool. Figure 2.2 shows a simplified schematic of the equipment configuration for an LWAM system with coaxial lasers and Figure 2.3 a single laser system. At the same time, metal wire is extruded from a reel into this pool via a nozzle, closely positioned next to a metal plate, which acts as the print substrate. The lasers are arranged either radially or coaxially around the nozzle. The substrate is mounted to a deposition bed within an environment in which oxygen is displaced by an inert gas, which supports the stability of the process and minimises oxidisation. The relative motion between the deposition bed and the deposition head enables the formation of a weld track, known as a track.
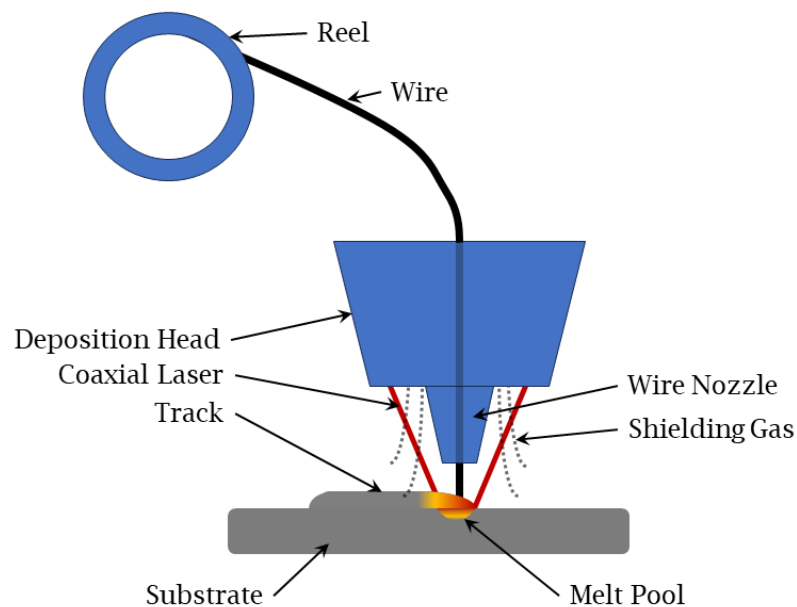
Figure 2.2: Schematic of the LWAM coaxial laser deposition head and track being deposited.
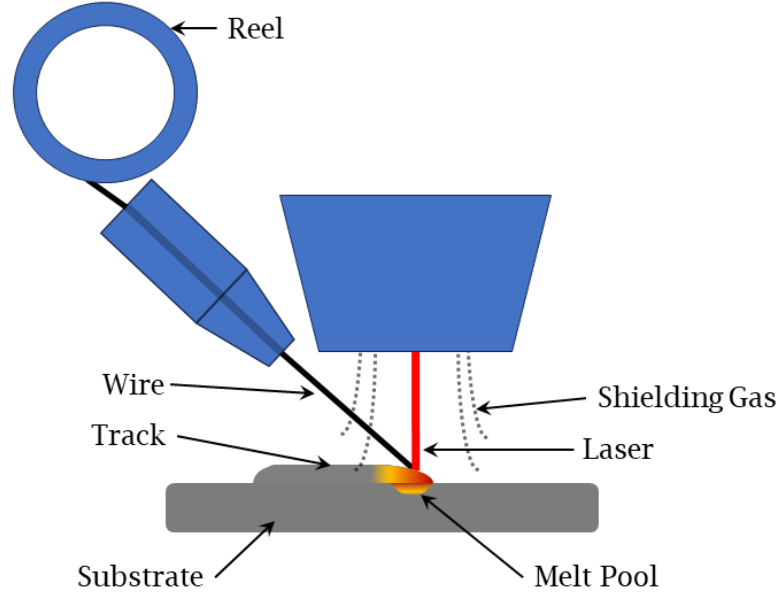
Figure 2.3: Schematic of the LWAM single laser deposition head with side-fed wire and track being deposited.

2.2.1   Benefits of Coaxial Laser Systems in LWAM

Developments of the practical applications of brighter lasers, which can use flexible optics to precisely position them at the deposition head, have made it possible for coaxial laser arrangements to be commercially practical (Motta, Demir, and Previtali, 2018). F. Liu et al. (2022) show that coaxial lasers are advantageous over the conventional radially arranged single beams for which most LWAM literature has been focused.

Coaxial lasers support vertical wire feeding, eliminating the interference from the wire in radial systems, which causes poorer substrate adhesion and material properties found when depositing tracks in the direction of the wire feed. This arrangement also creates a more uniform energy distribution, contrasting with the

Gaussian profile of a single laser, producing much more uniform multi-directional tracks. Figure 2.4 contrasts the energy distribution of a single laser with that of a 3-laser coaxial system. It shows that the coaxial laser energy distribution results in more consistent energy across a wider melt pool but with a shallower penetration into the substrate. This results in tracks which are well bonded to the substrate at their edges and have a more uniform root (F. Liu et al., 2022). Conversely, the Gaussian energy profile of a single laser source leads to a deeper melt pool at the centre, creating a deeper root and therefore increased remelting between layers. Figure 2.5 compares an etched track and root from (a) a three-laser system and (b) from a single-laser system of equivalent energy. This profile is consistent with the melt pool described in Figure 2.4, cross-sections of the track from a three-laser system have a shallower melted depth and the bonding at the edges is enhanced (F. Liu et al., 2022). The single-laser track shows a deeper melted depth caused by the high energy concentration in the centre of the melt pool.
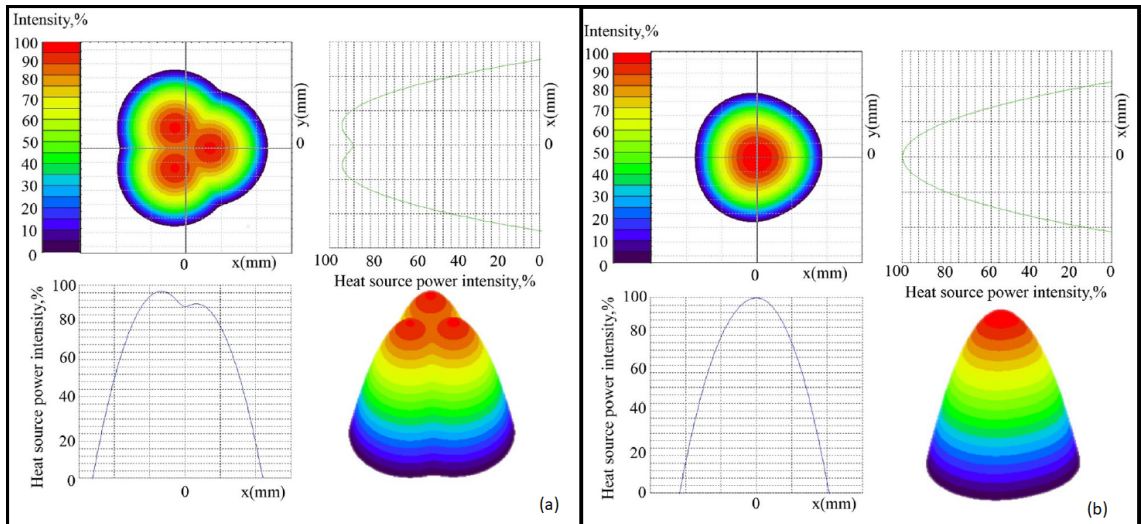
Figure 2.4: Comparison of energy distributions of (a) three-laser coaxial and (b) single-laser systems. (F. Liu et al., 2022).
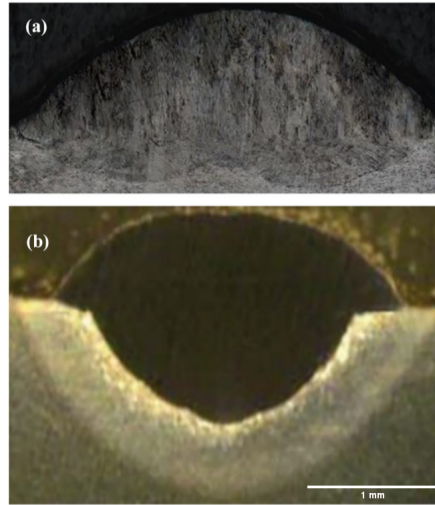
Figure 2.5: Comparison of track cross section for (a) a three laser coaxial system and (b) a single laser system (scale bars approximate) (F. Liu et al., 2022).

A more consistent distribution of energy across the melt pool produced by coaxial lasers reduces the Marangoni effect, the fluid flow generated by gradients in surface tension. Greater thermal gradients created by uneven heating exacerbate this effect and can result in uneven spreading of the track, reducing the symmetry of the track profile.

2.2.2 Process Dynamics During Track Deposition

The physical mechanisms that occur during the deposition process are complex; however, the fundamental success of the manufacturing process is based on the control of five main elements. These are laser power, extrusion rate, deposition head speed, laser offset or working distance (the distance between the deposition head and the substrate) and laser spot size (Roch, Tournier, and Lavernhe, 2023; Amine, Newkirk, and Liou, 2014). These parameters must be carefully selected and are typically tested experimentally to ensure that they are optimised for the materials used. They are fundamental to creating a high-quality track.

Laser power and the focus of the beams, set through the offset height, must be configured to ensure that there is sufficient energy to melt both the wire and the

substrate, leaving them well bonded together, forming the track as the deposition head moves. Insufficient energy results in 'stubbing', where poorly bonded tracks and wire can be seen, conversely, where there is too much energy or the focus of the beams is poor, the wire melts before it reaches the substrate in an effect called 'balling' or 'dripping' (Abuabiah et al., 2023). Examples of dripping and stubbing compared to good tracks can be seen in Figure 2.6.

The parameters for head speed and extrusion rate have a close interdependency and must be set together to ensure that wire is extruded at a rate that is as fast or faster than the head speed. This relationship, the Wire Speed Factor (WSF) (Caiazzo, 2018) or the Speed Ratio (Zapata et al., 2022), is the ratio of the extrusion rate to the head speed and should always be greater than 1 to ensure that the material is extruded at a speed higher than the deposition head moves across the substrate. This relationship between extrusion rate and head speed is therefore equivalent to the ratio between the cross-sectional area of the track and the cross-section of the wire, because of the principle of conservation of volume. This is expressed in Equation 2.1, where v_f is the extrusion rate, v_h is the head speed, A_t the cross-sectional area of a track and A_w the cross-sectional area of a wire.

$$WSF = \frac{V_f}{V_h} = \frac{A_t}{A_w} \qquad (2.1)$$
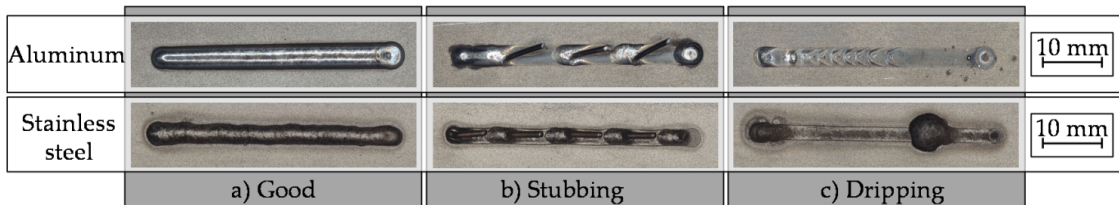
Figure 2.6: Examples of good tracks, stubbing and dripping with stainless steel and aluminimum (Zapata et al., 2022).

This can be rearranged as shown in Equation 2.2. As the area of the wire is fixed, it shows that if the extrusion rate is increased, it will increase the cross-section of the track. Conversely an increase in head speed will reduce the cross-section of the track.

$$A_w \times V_f = A_t \times V_h \tag{2.2}$$

The geometry of a single track plays a significant role in determining the smoothness of a deposited surface, the thickness of the layers, their consistency, and the precision of the final part geometry (Xiong et al., 2014; Roch, Tournier, and Lavernhe, 2023). Figure 2.7 shows the cross-section of a theoretical high-quality track, taken normal to the length of the track. Figure 2.8 shows etched cross sections of track profiles with different properties, the track with 'unacceptable wettability' has a contact angle greater than 90°, resulting in poor bonding at the edges of the track. The track with 'acceptable wettability' has a contact angle lower than 90°. Wettability refers to the ability of the liquid metal to maintain contact with the substrate. It is commonly quantified using the contact angle, the angle where the track edge meets the solid surface, shown in Figure 2.7. High wettability is indicated by a low contact angle, meaning that the liquid spreads more across the surface, while low wettability is indicated by a high contact angle (Oliari, D'Oliveira, and Schulz, 2017).
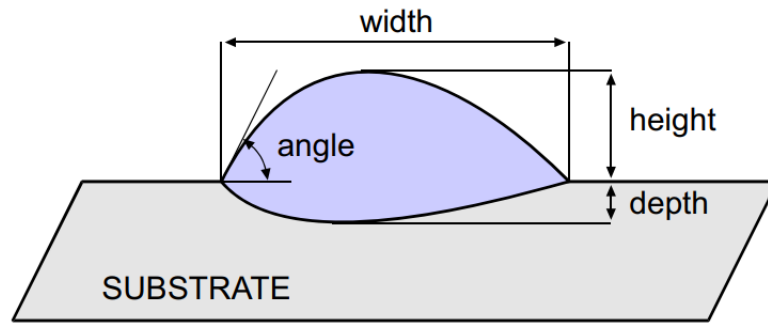
Figure 2.7: Cross-section of theoretical high-quality track (Caiazzo, 2018).
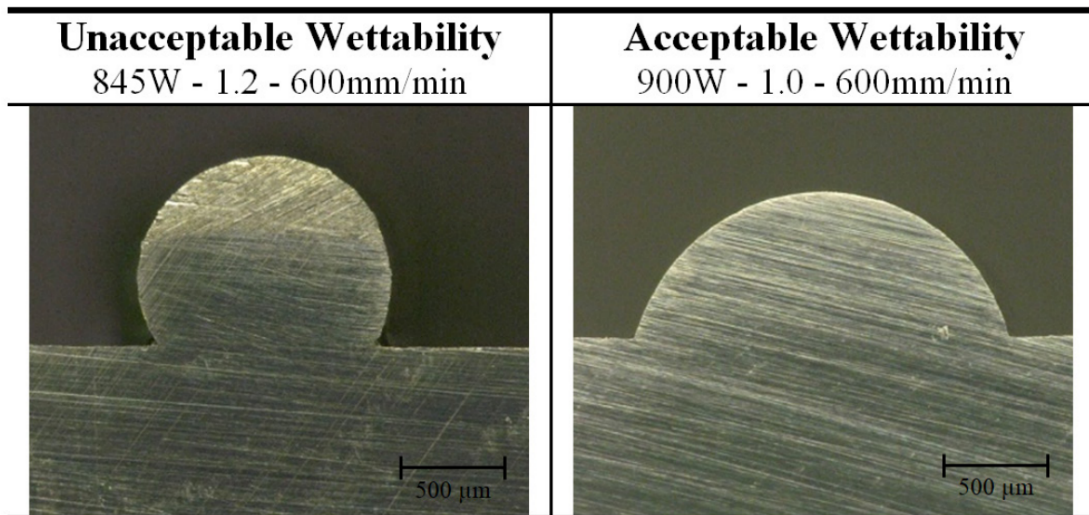
Figure 2.8: Example track cross-sections showing contact angle greater than 90° (Unacceptable Wettability) and less than 90° (Acceptable Wettability) for WSF of 1.2 and 1.0 (Oliari, D'Oliveira, and Schulz, 2017).

Although WSF and laser power have the most significant effect on the macro-level quality of the deposited track, there are several other system parameters that affect track quality. Careful substrate preparation is required, a clean, flat surface with low reflectivity, to ensure a high-quality melt pool and good surface adhesion. Substrate temperature control is also important; higher substrate temperatures promote homogeneity throughout the build, support more effective remelting of the substrate surface through Marangoni convection and increase the wettability of the track, reducing the surface roughness (Froend et al., 2018). Higher temperature

gradients between the melt pool and the substrate reduce the stability of the melt pool and therefore reduce the range of optimal head speeds, extrusion rates and laser powers available (Abadi et al., 2023).

It is imperative that an inert shielding gas is used to reduce oxidisation during the deposition process, this is typically argon or nitrogen. Most technologies use a flow of argon locally to the melt pool, however as the substrate is moved relative to the deposition head to create a track, the deposited material can move outside the local shielding and oxidise, a fully inert printing environment is often used to address this (Leach et al., 2019). Oxidisation can lead to several defects, summarised in Section 2.2.4 - Defects Occurring in the LWAM Process.

In single laser systems, the effectiveness of the track's bonding to the substrate and the subsequent quality of the deposited track are also affected by the laser angle and wire feed angle (Syed, Pinkerton, and L. Li, 2005). This effect is negated by a coaxial architecture. Despite a range of fundamental research for coaxial laser systems, no research was found discussing the effects of the laser angle with this arrangement.

Roch, Tournier, and Lavernhe (2023) investigated the effects of head rotation, which is the angle of offset from normal to the substrate; they found variations in the power density profile. Head rotation had a clear effect on the symmetry of energy distribution across the melt pool. Symmetrical tracks were created by symmetric power densities and asymmetrical tracks were created by asymmetric densities. They also identified the importance of accurately establishing the height of a deposited track, an inadequate estimate leads to an incorrect working distance, which influences power density and, therefore, the uniformity of the track. Figure 2.9 shows the impact on the power density distribution with a three-laser system. It shows the effect on the spread of the laser spot with varied z-axis offsets and the resulting energy density.
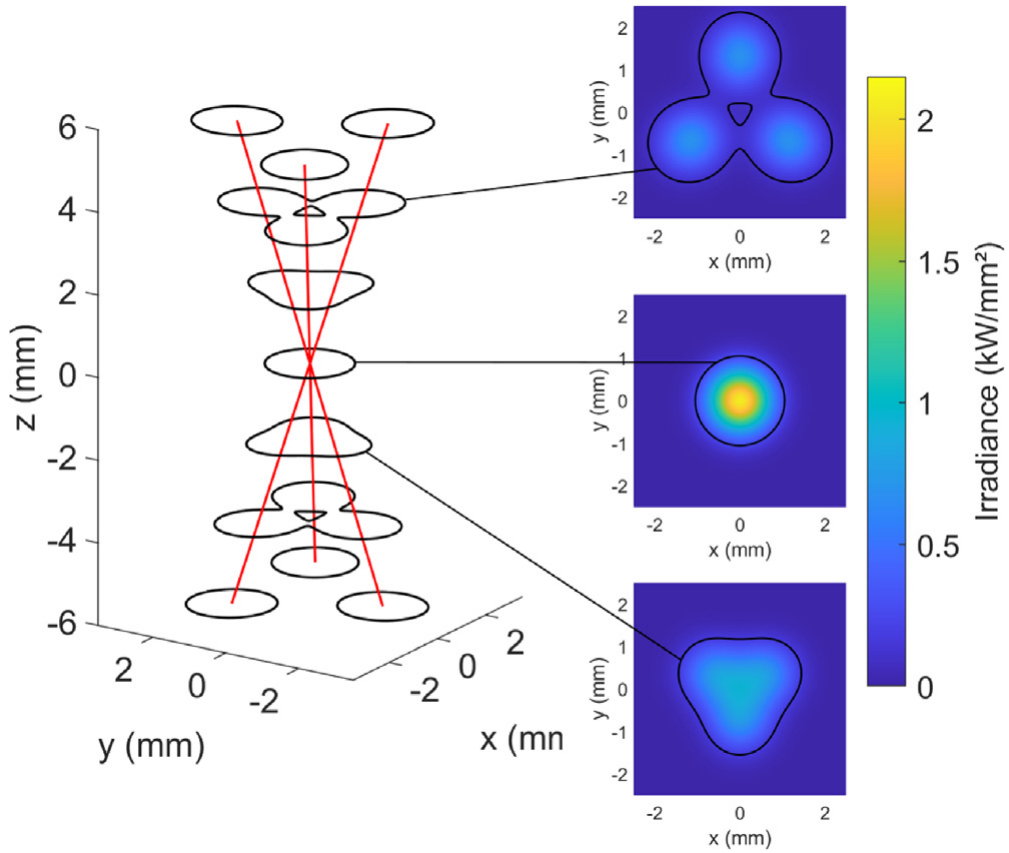
Figure 2.9: Effect of offset from the focal point for a three-laser coaxial LWAM system (Roch, Tournier, and Lavernhe, 2023).

2.2.2.1 Visual Assessment of Single Tracks

Visual assessment of deposited single tracks is a common methodology for the initial evaluation of track quality (Zapata et al., 2022; Oliari, D'Oliveira, and Schulz, 2017; Motta, Demir, and Previtali, 2018; Abioye et al., 2017). It allows tracks to be quickly classified and ruled out as candidates for further use due to obvious faults, without the need for more costly and time-consuming processes such as microscopy or sectioning, polishing and etching.

Visual assessment is typically performed by depositing short tracks of 40 mm - 50 mm and assessing the centre section of the track; Figure 2.10 shows a schematic of how this is arranged on the substrate and the measurement region within the track. Most assessments simplistically characterise tracks as either dripping, stubbing or

good (Abioye et al., 2017). Motta, Demir, and Previtali (2018) extends this by identifying a 'transition zone' between tracks characterised as dripping and those characterised as good, for tracks that do not exhibit dripping or stubbing, but begin to show discontinuity or waviness and therefore are not of sufficient quality to be considered a 'good deposition'

Oliari, D'Oliveira, and Schulz (2017) detail an important aspect of the evaluation, the criticality of the contact angle of a track. A 'Good' track has the profile of a semi-ellipse and has a smooth transition to the substrate, a contact angle lower than 90°, shown in Figure 2.8. This image shows a cross-section of a track that approximates a cylinder shape with a contact angle greater than 90°, leaving the sides of the track undercut. Oliari, D'Oliveira, and Schulz (2017) show that this can be conducive to porosity in multi-track depositions and should be avoided.
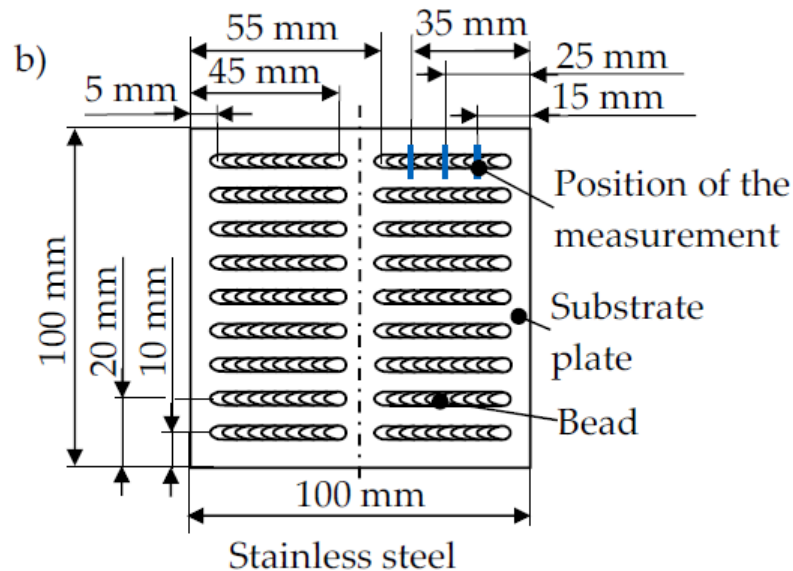
Figure 2.10: Schematic of single track deposition arrangement for identification of optimum print parameters (Zapata et al., 2022).

2.2.2.2 Track Geometry Model

To fully define the track formation process, the geometry of the track must be defined in terms of its height, width and contact angle, and how these relate to the fundamental process parameters. Understanding track geometry is particularly crucial for effective planning and modelling of track overlaps to form layers.

A track is described principally in terms of its cross-sectional profile, its overall volume and length (Zapata et al., 2022). Track profiles can be described as parabolic (Suryakumar et al., 2011; Roch, Tournier, and Lavernhe, 2023; Caiazzo and Alfieri, 2019), sinusoidal segments (Cao et al., 2011), Gaussian (Z. Li et al., 2023), or semi-ellipse (Oliari, D'Oliveira, and Schulz, 2017; P. Kumar, Jain, and Mayur Sudhakar Sawant, 2022). The literature describing these shapes are for a number of DED technologies, however only Oliari, D'Oliveira, and Schulz (2017) uses a radial laser LWAM system. Coaxial systems may well have a different cross-sectional profile because of the change in dynamics caused by the wire feed direction and uniformity of the melt pool. Other experimental conditions such as substrate temperature and material properties could also affect the wettability of the track, resulting in a different shape (M. Kumar, S. S. Kumar, and A. Sharma, 2021). Suryakumar et al. (2011), who propose a parabolic cross-section illustrate the properties of the cross-section well, Figure 2.11 shows this.
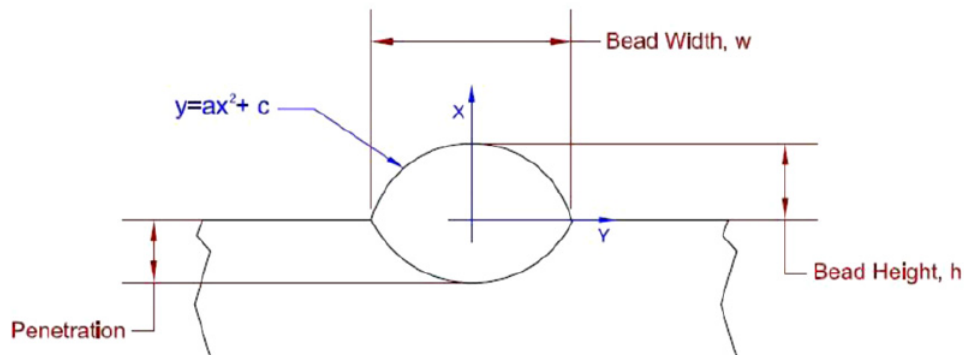
Figure 2.11: Suryakumar et al. (2011) description of a parabolic track cross-section.

They describe the track as a symmetric parabola of the form $y = a + cx^2$, describing the geometric form of the parabola in terms of height, h, and width, w, as shown in Equation 2.3.

$$y = h[1 - (\frac{2}{w}x)^2] \tag{2.3}$$

Further to this, Suryakumar et al. (2011) describe the cross-sectional area of the parabola in terms of head speed, V_h, extrusion rate, V_f, and wire diameter, d_w, which is shown in Equation 2.4. The equivalent for a semi-ellipse is shown in Equation 2.5.

$$A = \frac{2}{3}hw = \frac{2V_f d_w^2}{3V_h} \tag{2.4}$$

$$A = \frac{\pi hw}{4} = \frac{\pi V_f d_w^2}{4V_h} \tag{2.5}$$

Suryakumar et al. (2011) state that although height and width depend only on the process parameters described in the previous section, definitively proving their relationship to track height and width is too difficult to calculate, requiring modelling of the complex phenomena which occur during the deposition process. Phenomena which affect the final track geometry include surface tension (Marangoni effect), cooling rates, viscosity and gravitational effects, which determine the wetting and fluid flow of the track.   Equation 2.2 describes the relationship between extrusion rate and head speed on the track cross-sectional area. The relationship of process parameters specifically to height and width must therefore be determined experimentally (Zapata et al., 2022).

S. Liu, Brice, and X. Zhang (2021) showed experimentally that track width has a strong relationship with head speed and laser power, increasing laser power increases wetting and therefore the track width and increasing head speed reduces the width of the track as the rate of material deposited per unit length is effectively reduced. For track width however, laser power, laser spot size and extrusion rate were dominant; consistent with the effect on width, increases in laser power reduce the height and

increases in extrusion rate increased track height due to additional material being deposited.

2.2.2.3   Describing Optimum Parameters with Process Windows

The relationship between process parameters and resulting track profiles are commonly described using process windows. A process window defines the range of process parameter combinations within which high-quality manufacturing outcomes can be consistently achieved (Zapata et al., 2022). It outlines in graphical form how the settings for variables such as laser power, extrusion rate, head speed etc translate into track height and width and which combinations are considered to be optimal. These process windows are typically populated through carefully designed experiments, such as Design of Experiment (DOE) method, which isolate the effects of changing different process variables and the resulting outcomes. The resultant process windows provide invaluable guides to support engineers in selecting settings that lead to quality or geometric outcomes, minimising trial and error. An example of process windows for stainless steel and aluminium from a single laser LWAM process can be seen in Figure 2.12. Where the overall process window of available good parameter combinations grows with increases in laser power and typically there are successful parameter combinations for all traverse speeds (head speeds) in the range tested, but not for all wire speeds (extrusion rates).
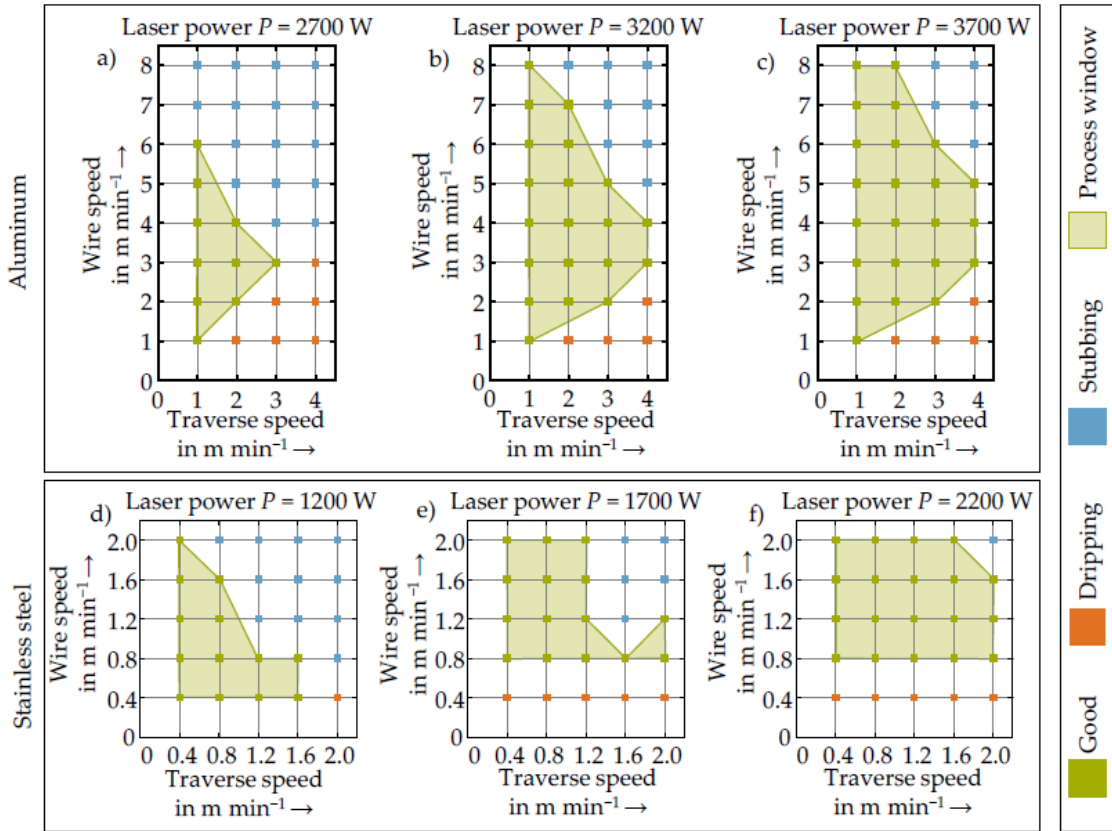
Figure 2.12: Example process windows describing wire speed (extrusion rate) and traverse speed (head speed) effects on track quality for aluminum (a–c) and stainless steel (d–f) (Zapata et al., 2022).

2.2.2.4 Optimisation of Process Parameters for High Quality Tracks

It is widely regarded that in metal DED there is a lack of repeatability and consistency between builds, machines and processes (DebRoy et al., 2019; Cunningham et al., 2018; Tapia and Elwany, 2014; C. Xia et al., 2020), which often manifests itself in defects or dimensional inconsistencies. Integrated process control and optimisation methodologies are considered key to overcoming this (DebRoy et al., 2019; C. Xia et al., 2020; K. Zhu, Fuh, and Lin, 2021). Although significant research on process optimisation and consistency has been published, the Vafadar et al. (2021) review of metal additive manufacturing states that much more progress is required to improve production efficiency. This is particularly the case for LWAM, which is

behind its powder-based equivalent and WAAM (Svetlizky et al., 2021). Vafadar et al. (2021) go on to state that the characterisation of the complex interactions of different control parameters is still not well understood, particularly as the optimum parameters change as a build progresses due to changes in geometry and bulk heating.

Effective process optimisation is important to fully exploit the potential of the technology, particularly with respect to the development of alloys that cannot be used in other manufacturing methods, functionally graded materials and adaptive control of microstructure. Process optimisation also increases the predictability of the process, supporting manufacturing quality requirements, particularly when using multiple machines, and is important for the overall efficiency of the wider end-to-end manufacturing process.

Significant research has been carried out to characterise individual properties of a built part (such as hardness, residual stress, porosity, etc.), usually for simple geometries, summarised by Cunningham et al. (2018), Tapia and Elwany (2014), O'Regan et al. (2016), and K. Zhu, Fuh, and Lin (2021). This limitation to simple geometries such as cubes and thin walls is identified as a limiting factor in further adoption of the technology within industry in the Thomas-Seale et al. (2018) review from UK Industry perspective.

Considering multiple properties of complex parts and trade-offs to optimise them is an important next stage to advancing the technology and improving its utility (Tapia and Elwany, 2014). Machine learning tools are increasingly overcoming the challenges of complexity and uncertainty, covered in the Machine Learning section below.

2.2.2.5   Key Equations Describing Process Dynamics

To fully describe the LWAM deposition process and support its optimisation, more variables than power, head speed and extrusion rate are required. Summarised from Mukherjee et al. (2017) and Dass and Moridi (2019), the equations which define the mechanisms of the DED process are summarised in Equations 2.6 to 2.10.

Dimensionless Heat Input Equation 2.6 - the energy per unit length of material used to deposit tracks, which directly affects cooling rates, solidification parameters, shape and size of the fusion zone. High values improve the strength of interlayer bonding, reducing overall defects. P is laser power, V_h is head speed, P_R and V_R are laser power and head speed that provide the lowest viable heat input per unit length. P/P_R must be 1 or greater.

$$Q* = \frac{P/V_h}{P_R/V_R} \tag{2.6}$$

Marangoni Number Equation 2.7 defines the magnitude of the surface tension force relative to the viscous force in the melt pool and is a measure of the strength of the convective transport of heat. High values improve interlayer bonding and overall material properties, but are more likely to result in asymmetrical track cross sections. μ is dynamic viscosity, α is thermal diffusivity of the alloy, w the width of the melt pool, ΔT the difference between the maximum temperature inside the pool and the solidus temperature of the alloy and $d\gamma/dT$ the sensitivity of the surface tension gradient with respect to temperature.

$$M_a = -\frac{d\gamma}{dT}\frac{w\Delta T}{\mu\alpha} \tag{2.7}$$

Fourier number Equation 2.8 is the ratio of the rate of diffusive heat transport to the rate of heat storage. Critical in understanding the damage heat can do to the component. A high number ensures rapid cooling, low thermal distortion and a high temperature gradient between the melt pool liquid and solidification outside it. Where α is the thermal diffusivity of the alloy, τ the melt pool length/melt pool speed and L the length of the melt pool.

$$F_o = \frac{\alpha \tau}{L^2} \tag{2.8}$$

Dilution Equation 2.9 defines the dilution of a track with the surface on which it is printed. Where x is the depth of the melt pool below the substrate level, h is the height of the material deposited above the substrate level. A minimum level is desirable to maximise bonding but minimise heat accumulation, optimal values are considered to be between 10% and 30%. Low h indicates low laser power or high extrusion rate; high x indicates high laser power or low extrusion rates.

$$D = \frac{x}{h + x} \tag{2.9}$$

Global Energy Density Equation 2.10, the Global Energy Density (GED), correlates with the dilution and has a 'goldilocks value' for most processes. Lower values of GED lead to less dilution, where lack of fusion defects are likely, higher values of GED lead to high dilution where keyhole porosity may form. Here P is the laser power, V_h the head speed and d_l the laser spot diameter.

$$D = \frac{P}{V_h d_l} \tag{2.10}$$

Wire Speed Factor Equation 2.1 is the ratio of the extrusion rate to the deposition head speed, which must be greater than or equal to 1. V_f is the extrusion rate and V_h the head speed.

These equations encapsulate the mathematical framework underpinning the dynamics of the LWAM process. It consolidates critical behaviours that translate from thermal dynamics of the process to physical properties of the component. However, they cannot provide a definitive model of the process without further experimental work and are dependent on the specific configuration of each deposition system.

2.2.3   Geometry Control

Geometry control in LWAM ensures part accuracy and involves the precise management of track and layer spacing, typically defined within the slicing software. The arrangement of individual tracks, the gap between them, and the consistent thickness of each layer directly affect the dimensional accuracy and mechanical properties of the final part. Careful geometry control mitigates some of the causes of porosity and reduces uneven surfaces and structural weaknesses, ensuring that the resulting part remains within tolerance.

The path followed by the deposition head, with appropriate track spacing and the subsequent z steps to form layers directly affect the achievement of flat layers and prevents overbuild or underbuild in the z axis. The literature covers well the optimisation of track deposition and layer formation (Suryakumar et al., 2011; M. Kumar, S. S. Kumar, and A. Sharma, 2021; Cao et al., 2011; Caiazzo and Alfieri, 2019; Ding et al., 2015), however there are few papers that cover this for LWAM technologies (Oliari, D'Oliveira, and Schulz, 2017; Huang et al., 2021; Ye et al., 2017) and no papers were found for coaxial systems.

In general terms, the objective of geometry control parameters is to determine track and layer separation that can be used by slicing tools to create machine

instructions. Geometry planning and optimisation is first based on a high-quality track, which is repeatedly overlapped to form a layer. The objective of the overlap is to achieve the flattest possible layer, which ensures geometric consistency of the final part. This minimises the probability of porosity through gaps between tracks and reduces material wastage due to subsequent machining of overbuilt layers (Sefene, Hailu, and Tsegaw, 2022; Suryakumar et al., 2011). The track, its optimal overlap and the resulting surface are the 'Layer Geometry Model'. This model is then repeated in the Z plane with an optimal layer overlap, resulting in the 'Multi-Layer Geometry Model'

The principles are common across the different models used in the literature, despite the different technologies, a general model for simple track to layer to part geometry can be described. The work of Oliari, D'Oliveira, and Schulz (2017), which uses an LWAM process, and M. Kumar, S. S. Kumar, and A. Sharma (2021), a WAAM process, form the basis of the following description of a single-layer geometry model.

2.2.3.1 Single-Layer Geometry Model

To determine a layer model and experimentally prove it, the simplest layer geometry is used, which is a small patch of tracks deposited in parallel straight lines. The critical parameter that determines the layer geometry is the distance between the centre points of each deposited track. As is the case with many aspects of this field, there are a number of names for this, such as hatch spacing, overlap ratio, overlapping coefficient and offset distance. They are referred to either as a physical distance or, more typically, as a ratio of the track width. A ratio provides the benefit of applying to any track dimensions that fit the same cross-section shape profile (e.g. parabolic, semi-ellipse etc).

The Flat-Top Overlapping Model (FOM), shown in Figure 2.13 and Figure 2.14, considers a single track with a height h and width w, and the centre-to-centre distance d between adjacent tracks. When d is greater than the width of the tracks,

there is no overlap between the tracks (image a, Figure 2.14). As d decreases, the overlap between tracks increases, creating a valley, which reduces in depth as d gets smaller (image b, Figure 2.14). This effect is caused by the accumulation of additional material where the tracks overlap. At a certain point, the overlap area equals the valley area above it, leading to an optimally flat surface (image c, Figure 2.14). Beyond this point, a further reduction in d results in excessive overlap, increased layer thickness, and a highly irregular surface (image d, Figure 2.14). The optimal value for d is achieved when the overlapping area equals the valley area; in practice, a perfectly flat surface is not achievable (Ding et al., 2015) due to a combination of the effects of the deposition process.
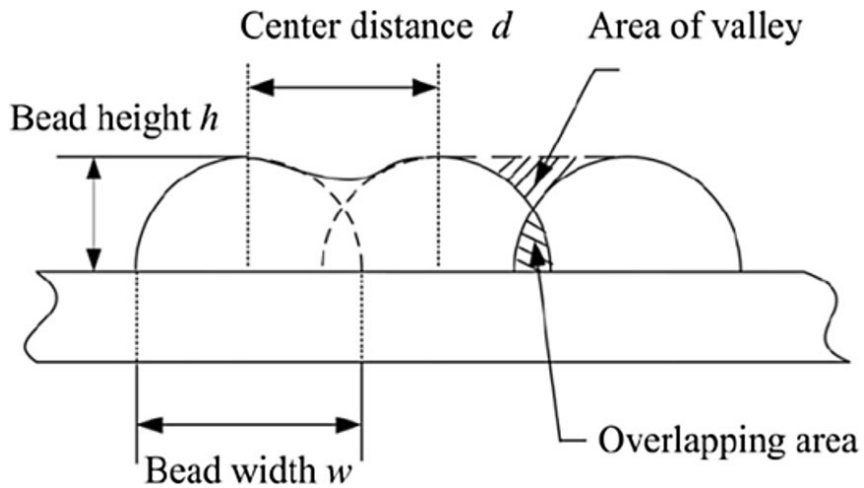
Figure 2.13: Sketch of the Flat-Top Overlapping Model (Ding et al., 2015).
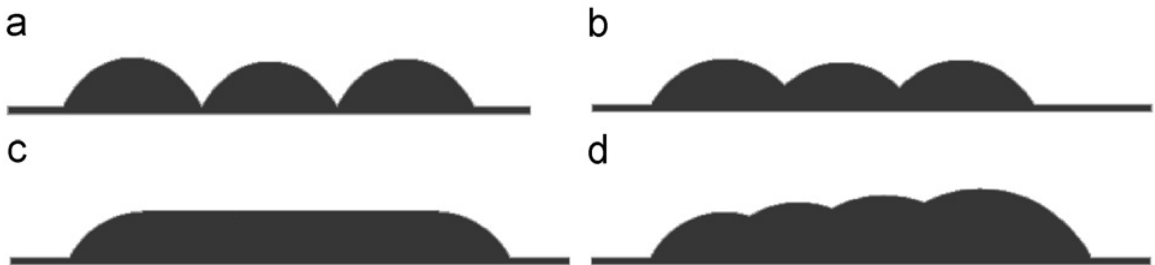
Figure 2.14: Cross-section sketch showing layer height and track pile up as centre to centre distance decreases (Cao et al., 2011).

In the FOM, the track profiles were represented as the sum of the two parabolas at the point of overlap. This model does not accurately reflect the profile changes that occur. An improved model, the Tangent Overlapping Model (TOM), suggests that the overlapping volume forms a fillet in the valley between the parabolas, shown in Figure 2.15.

TOM allows for a more nuanced description of the overlapping shape. Where d is large, the volume of overlapped material is smaller than the volume of the valley, leading to the formation of a concave fillet from the excess material (image c, Figure 2.15). Where d is optimal, these volumes equalise, transforming the fillet into a straight line, but not creating a 'flat top' (image b, Figure 2.15). Further reduction in d causes a convex fillet to form, extending beyond the peaks of the parabolas (image d, Figure 2.15).

The TOM model refines the Layer Geometry Model approach by introducing the concept of a "critical valley," which accounts for the asymmetric nature of track overlap and the varying track heights resulting from different centre distances. This model provides a more accurate representation of the layer profile, Ding et al. (2015) compared the optimum values for d for FOM (2/3) and TOM (0.738) and found that the latter has a more consistent finish and lends itself to more stable multi-layer builds. Different optimal values for d have been identified in the literature. Table 2.1 summarises these, expressed in terms of the proportion of the total width of the track (d/w).
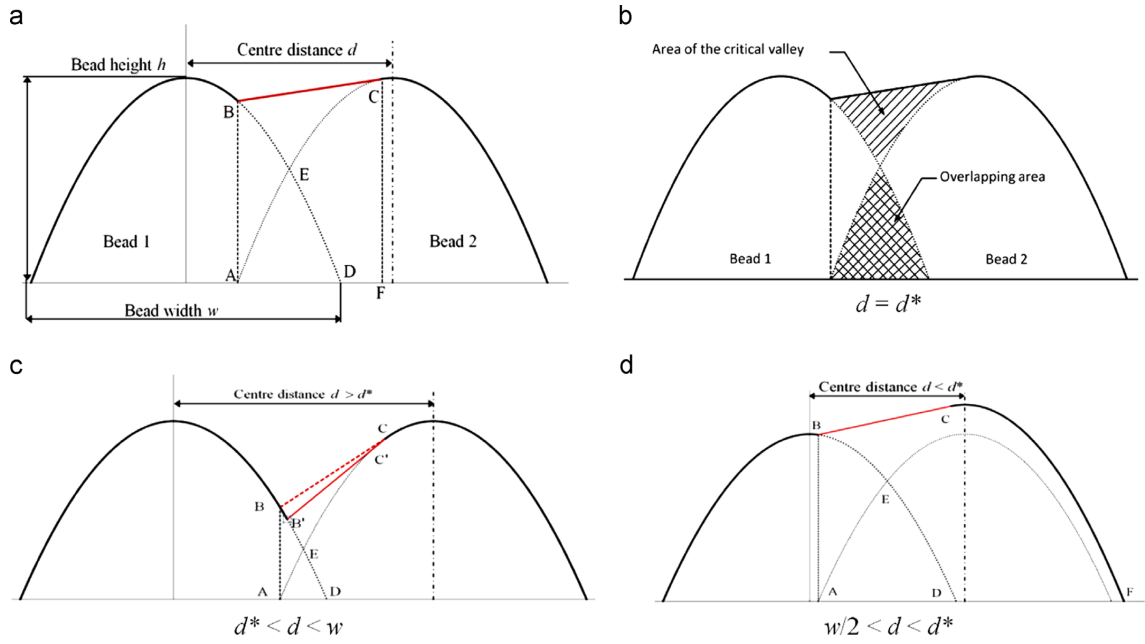
Figure 2.15: Sketch of the Tangent Overlapping Model (Ding et al., 2015).

Paper	Single Track Shape	Offset
Oliari, D'Oliveira, and Schulz (2017)	Semi-Ellipse	0.819
Suryakumar et al. (2011)	Parabola	2/3
M. Kumar, S. S. Kumar, and A. Sharma (2021)	Parabola	2/3
Cao et al. (2011)	Sine Function	$2/\pi$
Caiazzo and Alfieri (2019)	Parabola	2/3
Ding et al. (2015)	Parabola	0.738

Table 2.1: Summary of optimal values identified for d, the track centre-to-centre distance

Ding et al. (2015) also described in their model that as the number of tracks in a layer, n, increases, so does the overall layer height, shown in Figure 2.16, and it cannot be assumed that the layer height for $n = 2$ is the same for $n = 8$, the thickness of the layer increases as more tracks are added. They did not go on to quantify or mathematically describe this effect.

In practice, parts are much more complex than the simple square shapes used in this model. Little is published in the literature about the effects of layer shapes on layer height; Michel et al. (2019) suggests a modular path planning approach, but this is to address part accuracy in the x-y plane. Adaptive planning of layer height is covered, both in terms of adaptive layer thicknesses to meet the CAD model (Y. Zhang et al., 2003), introducing planned 'compensation layers' to correct the development of underbuild inaccuracies more effectively in process (Spranger et al., 2018) or in-process monitoring and adaption (Xu et al., 2022). Experimentation, similar to that which investigates the effects of the tool path on residual stress and interlayer temperatures by Aliyev, Lee, and Ahn (2022) and Kim et al. (2021) would add value to the layer models developed.
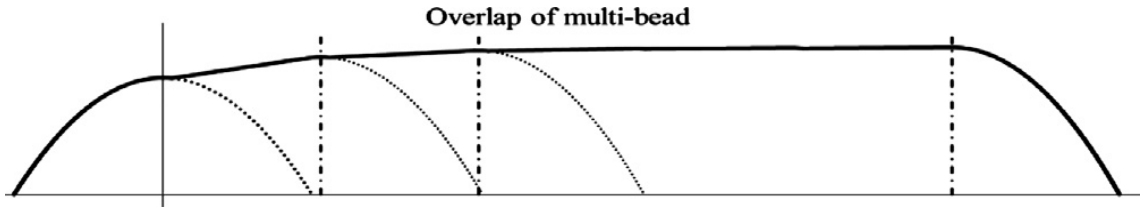
Figure 2.16: Sketch of layer height increasing with n - the number of tracks (Ding et al., 2015).

2.2.3.2 Multi-Layer Geometry Model

Layers with known height, width and surface conditions can be repeated at known intervals in the Z-plane to create three-dimensional parts. Once a layer is deposited, the next layer is created by adjusting the deposition head height to increase the distance between it and the previously deposited layer. The Z-step increment

assumes that the previously deposited layer is flat and that the top of the layer is the same distance from the deposition head as the laser offset for the first layer. P. Kumar, Jain, and Mayur S Sawant (2020) assume this distance to be the layer thickness, which is: $t_t = k - R$. Where k is the height from the substrate of the centre of the concave circular fillet formed between two adjacent tracks and R is the radius of the concave circular fillet, which approximates the Root Mean Squared (RMS) height of the layer; shown in Figure 2.17. Other studies such as M. Kumar, S. S. Kumar, and A. Sharma (2021), Caiazzo and Alfieri (2019) and Ding et al. (2015) used the height of the track. No comparative studies between the two values could be found to quantify the effect on overall accuracy in terms of part height.

Figure 2.17: Sketch multi-track deposition illustrating the layer thickness t_t (M. Kumar, S. S. Kumar, and A. Sharma, 2021).

In these studies, which do not include coaxial systems, the effects of the flatness of single layers on the overall layer height are well investigated. Caiazzo and Alfieri (2019) showed that an optimal centre distance for the flatness of the layer would result in an under-build against the predicted total height of the part and higher centre distances would increase this effect. Ding et al. (2015) showed similar effects, shown in Figure 2.18 below (image a – closer tracks with overbuild; image b – optimal value for a flat layer with slight underbuild). P. Kumar, Jain, and Mayur Sudhakar Sawant (2022) support this, suggesting that while the accuracy of the prediction for a single layer is strong, an accuracy of approximately 90% was possible due to the effects of the unavoidable variability in the layer surface and reheating.

These studies show first that minimising the variability of the layer is important for the consistency and flatness of the final part and that consistent use of the same layer height over a multi-layer part is likely to result in geometric inaccuracies in terms of the Z height of the part, which requires planning variable layer heights or 'compensation layers' or variable Z increments within the build process to correct
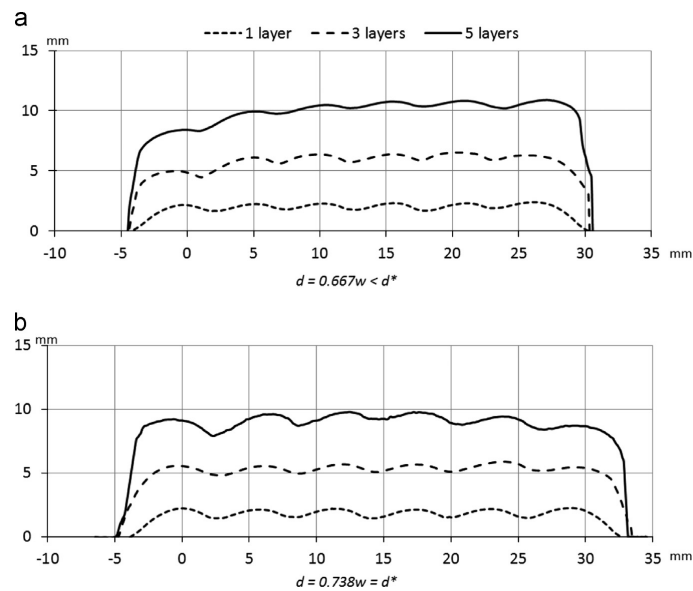
Figure 2.18: Data showing the effect of the flatness of a single layer on a multi-layer build, creating (a) underbuild when suboptimal and (b) a consistent layer height when optimal (Ding et al., 2015).

for this (Y. Zhang et al., 2003; Spranger et al., 2018).

2.2.4   Defects Occurring in the LWAM Process

A lengthy dynamic deposition process such as LWAM allows many opportunities for defects to occur. These can occur spontaneously during the deposition process or be caused by decisions made during the preparation of the build, for example choosing a part orientation that leads to an excessive overhang, poor track separation that results in porosity, or poor management of the thermal properties of the part.

Defects have a significant effect on the cost of the build process as they are often difficult to fix. Minimisation and identification of defects is particularly important for quality management processes and supports the drive for repeatability. Careful consideration is needed for each unique part and its end-to-end design and production.

Characteristics such as overbuilding or underbuilding can also occur, which are not strictly defects, but a poor build resulting in material waste and possible non-conformance with the required part geometry. The following sections summarise the main defects seen in LWAM processes.

2.2.4.1   Porosity in Multi-Layer Builds

Porosity is one of the most common defects in LWAM, characterised by the presence of unintended voids or holes within the solid material. Porosity affects the density and material properties and can lead to components with lower than desired mechanical strength. Holes caused by porosity can create micro-cracks, bringing lower tolerance to fatigue and reduced mechanical strength (B. Wu et al., 2018; X. Chen et al., 2021).

Porosity can develop through gases trapped within the melt pool; these can be created by contaminants on the wire feedstock such as grease or oxides, poorly chosen process parameters, particularly laser power, which causes vaporisation of the wire and keyholing, inclusions (particulate contaminants from the environment)

or through poor path planning resulting in gaps between tracks (B. Wu et al., 2018; Brennan, Keist, and Palmer, 2021). Figure 2.19 shows an example of porosity in an LWAM thin wall component.

Mitigations to this include the use of clean, high purity feedstock, careful control of the cleanliness of the substrate and the deposition environment, optimising the process parameters for the material and sufficient shield gas (Tomar, Shiva, and Nath, 2022). Post-process treatments such as Hot Isostatic Pressing (HIP) can heal pores and the resulting micro-cracks (Brennan, Keist, and Palmer, 2021).

Figure 2.19: Example of pores from a poorly built thin wall part printed using the Meltio M450 during intial experimental preparations.

2.2.4.2 Cracks in Multi-Layer Builds

Cracks are fractures or separations in the material, which can severely compromise the mechanical integrity and performance of the part. They are often caused by thermal stresses due to rapid heating and cooling cycles, poor bonding between layers, or porosity. In most cases, these are due to inappropriate process parameters or poor control of the thermal field within the part. Thermal-metallurgical interactions influencing the susceptibility to solidification cracking in LWAM include steep thermal gradients, rapid cooling rates, material composition, molten pool dynamics, gas evolution, strain and stress development and interlayer temperature variations (Brennan, Keist, and Palmer, 2021). Figure 2.20 shows images of etched parts containing cracks that have developed through stresses as the part cools. Substrate pre-heating, controlling the cooling rate of the part, optimising process parameters and thermal modelling of the process can help to reduce residual stresses and prevent cracking.
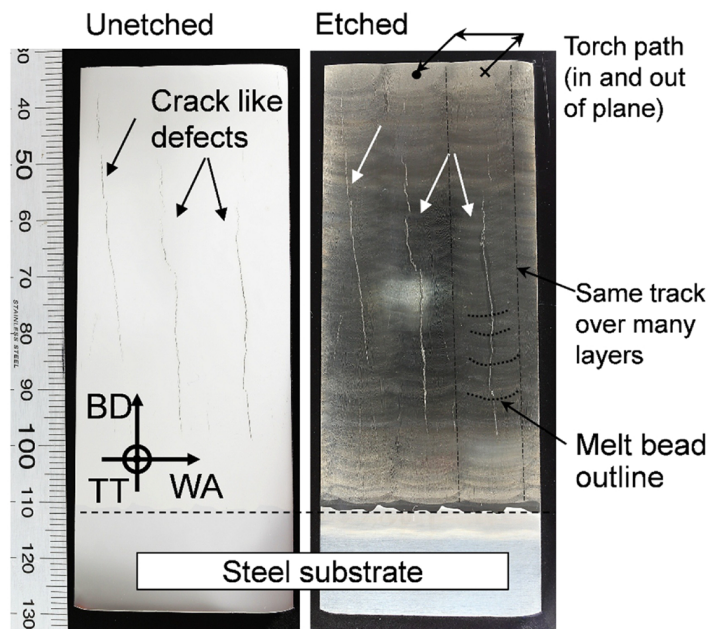
Figure 2.20: Example of crack development in a multilayer WAAM component (Tomar, Shiva, and Nath, 2022).

2.2.4.3 Delamination

Delamination refers to the separation of adjacent layers within a printed part, causing cracking and compromising the integrity of the part. It can result from insufficient heat input to remelt previously deposited layers, leading to poor interlayer bonding or from differences in thermal expansion between layers that result in residual stress (B. Wu et al., 2018).

Once delamination has occurred, it cannot be repaired by post processing (B. Wu et al., 2018). However, proper heat input, substrate preheating, maintaining consistent temperature across layers, use of compatible materials in multi-material deposition and appropriate layer thicknesses can help prevent delamination.

2.2.4.4 Distortion

Distortion is the warping or deformation of the part during or after the manufacturing process, resulting in the part being geometrically out of tolerance. It is caused by uneven heating and cooling, leading to thermal gradients and residual stresses.

Pauses for interlayer cooling, controlled cooling at the end of the deposition process, and the use of simulation software to predict and compensate for thermal-induced stresses are all effective mitigation (B. Wu et al., 2018). Post-process heat treatments are considered to be effective at reducing residual stress.

2.2.4.5 Anisotropy

Anisotropy refers to different mechanical properties such as tensile strength and ductility in different directions within the printed part. This phenomenon is due to the layer-wise building process, directional cooling and solidification patterns, resulting in columnar grains in the build direction (Tomar, Shiva, and Nath, 2022). Interlayer rolling (X. Chen et al., 2021; B. Wu et al., 2018), post-process heat treatments and controlled cooling can reduce anisotropy. Tomar, Shiva, and Nath (2022) suggest mitigating the effects by design as much as possible, suggesting that

part design could also consider adopting orthotropic models (Laghi et al., 2021) of the material.

2.2.4.6   Oxidisation

Oxidisation is the reaction of the deposited material with oxygen in the surrounding environment, typically either reacting with the melt pool or during the cooling of the deposited material. This leads to deposits of oxides forming between the layers and on the outer surface of the component, changing the properties of the material and surface quality. Figure 2.21 shows an example of oxide between deposited layers in an LWAM deposition process.

It is almost impossible to avoid oxidisation when producing components of any scale using DED technologies (L. Zhang et al., 2022). Oxidisation can reduce the performance of the material's ductility and the oxides can provide the starting point for cracks to form and propagate. Although some level of oxidisation is unavoidable, there are a number of mitigations, such as using shield gases like argon to inert locally around the melt pool, inerting the wider build environment and minimising the time that the component is exposed to high temperatures by using techniques such as passive or active interlayer cooling (B. Wu et al., 2018).
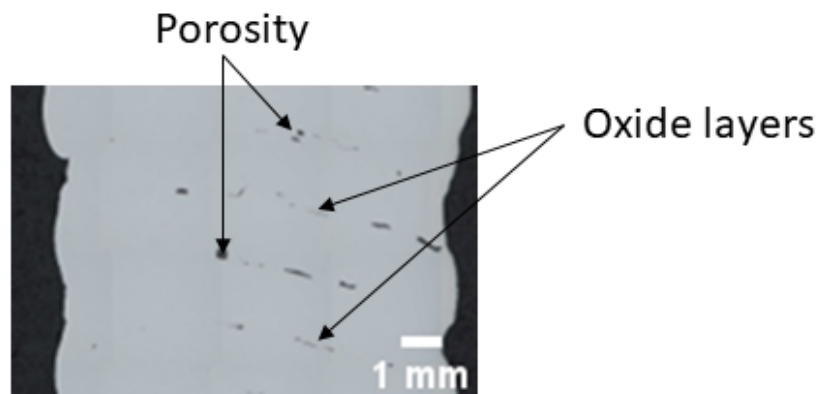
Figure 2.21: Example of oxide between the layers of a multilayer LWAM component, confirmed using scanning electron microscope.

2.3 Thermal Effects in LWAM

Understanding and managing the thermal conditions are vital for the success of the LWAM process. The Heat-Affected Zone (HAZ), heating and cooling cycles, thermal gradients, and melt pool dynamics are critical factors that influence mechanical properties, consistency, residual stress, structural integrity and geometric accuracy of the final component (Gurmesa and Lemu, 2023). There is significant research into modelling the thermal field and its effects (Yan et al., 2018; Fetni et al., 2021; Lu et al., 2019; Nalajam and Varadarajan, 2021; Srivastava et al., 2021; Z. Zhang, Z. Liu, and D. Wu, 2021; Q. Zhu, Liub, and Yana, 2020; Denlinger et al., 2015; Singh et al., 2021) for various wire-based DED technologies. These are summarised with respect to the high-level themes associated with LWAM.

2.3.1 Melt Pool Geometry

The Key Equations section above defined the mechanism for creating successful tracks and highlighted the importance of the thermal properties of the material and the interconnected nature of the relationship between the process parameters. A known cause of both anisotropy and deviation in the overall geometry of the part is the effects of bulk heating developed as multiple layers accumulate. This is compounded by the cyclical effects of reheating previously deposited layers (DebRoy and Bhadeshia, 2021; Svetlizky et al., 2021; Yan et al., 2018). Mukherjee et al. (2017) show that due to bulk heating, the melt pool width grows by 6mm over 6 layers of thin wall deposition if all print parameters remain fixed. This growth in the melt pool reduces its stability as well as reducing the concentration of energy around the wire and the overall consistency of the resulting tracks and layers.

Shamsaei et al. (2015) summarises LENS research on melt pool shape control to mitigate the effect of bulk heating. The research summarised in this paper found that a consistent melt pool shape could be maintained by reducing the laser power as the layers increase. The point to begin the power reduction and the rate depended on

the alloy used, using this method they showed that the shape could be maintained irrespective of extrusion rate and head speed. The appropriate head speed and extrusion rate can then be selected to achieve a desired track geometry, constraining the laser power to maintain the same Global Energy Density (GED) throughout the build.

Power reduction alone will not be sufficient to control bulk heating; over a long print, the reduction in power may result in requirements on head speed or feed rates that cannot be supported because of the limitations of the process window. At this point, other thermal management strategies can be employed, such as interlayer pauses (or dwell time) (Nalajam and Varadarajan, 2021; Z. Zhang, Z. Liu, and D. Wu, 2021; Denlinger et al., 2015; Singh et al., 2021). Refined through modelling and experimentation for the particular part and process, interlayer cooling through pauses or active cooling with forced air is used to achieve a consistent interlayer temperature. This has been shown to support the consistency of the melt pool throughout the deposition process, reducing the bulk heating of the part and residual stresses (Singh et al., 2021). Interlayer pauses have also been shown to improve grain refinement with some alloys, because of higher cooling rates and lower temperature gradients. This can improve microhardness and compression strength due to the finer grain structure (Singh et al., 2021). It is unclear, however, whether this also reduces the overall anisotropy across the part.

Further fine control of melt pool size and GED may be possible with coaxial LWAM systems. Roch, Tournier, and Lavernhe (2023) experimental and simulation work have shown that for a three-laser coaxial system, the overall GED can be affected by the focus of the laser spots, as the deposition surface moves further away from the focal point of the lasers, the laser energy is spread further across a larger spot. Deliberate defocussing could therefore reduce the GED.

An important driver for undertaking thermal modelling of the deposition process is to understand the temperature field as the material is deposited. Lower temperatures in previous layers increase the contact angle of the track deposited for

the subsequent layer, resulting in a narrower but taller track, as more of the laser energy is required to reheat the previous layer, reducing wetting (Oliari, D'Oliveira, and Schulz, 2017), see Figure 2.8.

The Marangoni effect describes fluid motion driven by gradients in surface tension, the scale of this effect is particularly dependent on temperature differences across the melt pool. As the temperature increases, the surface tension decreases. The centre of the melt pool, where it is hotter, will have a lower surface tension compared to the relatively cooler edges. If the underlying layer is hot, the temperature gradient within the molten pool is reduced, leading to a more uniform surface tension. This results in a flatter, wider track as the fluid spreads more evenly (Singh et al., 2021). A cooler layer has a steeper temperature gradient, causing more pronounced fluid movement through the Marangoni effect. This leads to an uneven distribution of the molten material, increasing the height of the track and the contact angle of the track and reduces its ability to spread.

Singh et al. (2021) refer to cooler layers as reducing the 'Deposition Efficiency' of the process. The paper does not provide a specific definition of 'Deposition Efficiency', but is likely similar to 'Manufacturing Efficiency' in Cheng et al. (2023), the efficiency of the process in terms of the speed of deposition, the rate of material use and the overall energy required. The objective of this efficiency in these studies appears to be speed. This efficiency is achieved by increasing the overall energy used, which has been shown to have a strong correlation with the accumulation of residual stress and anisotropy.

2.3.2   Residual Stress

Inconsistent heating and cooling cycles are a leading cause of residual stresses and anisotropic properties (Gurmesa and Lemu, 2023). Residual stress is the development of internal stresses in the component due to differential cooling rates and phase transformations during the deposition process that remain after the process completes. Very localised heating and rapid cooling generate thermal

gradients that lead to the expansion and contraction of the material in an uneven manner. This results in tensile and compressive stresses within different regions of the part.

Should high levels of residual stress develop, the part can warp and, in severe cases, crack propagation can occur. The result of these effects is poor geometric accuracy, reduced fatigue life, structural reliability and suboptimal microstructure. Y. Liu, J. Shi, and Y. Wang (2023) state in their review paper that residual stress generated in DED processes is still a significant barrier for industrial use of AM for high-performance, large metal parts.

Residual stress in LWAM can be comparatively less severe than in other DED processes; this is due to lower heat input that leads to a reduced, more localised heat affected zone (Bastola et al., 2023). This reduced heat input can result in smaller thermal gradients and consequently lower residual stress. However, the severity of residual stresses is highly dependent on the specific parameters of the process, including head speed and extrusion rate, the alloy used and the specific part geometry. Residual stress increases particularly with the number of layers, as this inevitably results in the heat in the part growing (Aliyev, Lee, and Ahn, 2022; Denlinger et al., 2015).

Residual stress is conventionally mitigated through in-process and post-processing techniques. The process parameters can be planned to minimise excessive heating and cooling cycles for instance during the deposition process (Bastola et al., 2023).

Post-process treatments are typically heat treatments, which are effective in homogenising stress gradients and material properties across a component. These homogenising effects also have the benefit of improving the consistency of microstructures and the properties of the resulting material (Bastola et al., 2023).
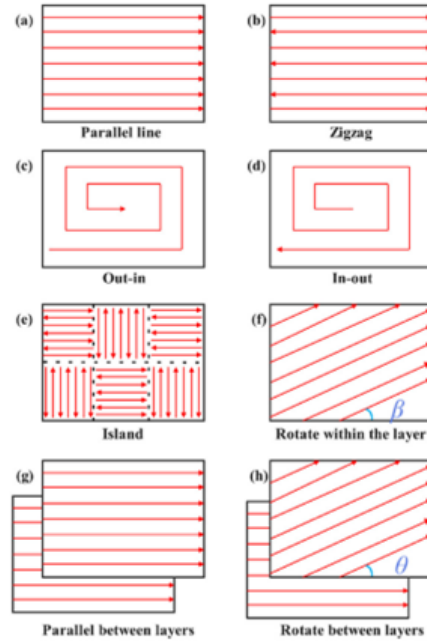
Figure 2.22: A range of tool path strategies used in LWAM (S.-G. Chen et al., 2022).

2.3.3 Temperature Management and Control

2.3.3.1 Thermal Control Using Toolpath Planning

The term "toolpath" refers to the predetermined route that the deposition head follows to create tracks in each layer as defined by the slicing software. There are various strategies available to guide the deposition head that directly determine where energy is applied during the deposition process. As a result, it directly impacts the development and distribution of temperature across the build, affecting the overall quality and properties of the final part. Figure 2.22 shows a range of infill patterns from S.-G. Chen et al. (2022), who investigated the effects of different infill patterns on the distortion of the overall part.

When successive layers are deposited, the toolpath creates overlapping heat zones, causing higher temperatures in certain areas. This is especially true in complex geometries, where the toolpath may require multiple passes over the same region. Quickly repeated passes over the same region leads to localised areas of

high temperature (Donghong Ding et al., 2014). By carefully designing the toolpath to avoid excessive overlap or by incorporating pauses, this effect can be mitigated, leading to more uniform layer temperatures and material properties.

Typical mitigations through toolpath design include choosing infill orientations that create the longest possible tracks along the part to reduce the amount of time that the melt pool spends in a particular area and evaluating the effects of different infills for the specific geometry being produced (Petrat et al., 2018).

Kim et al. (2021) trialled several rectilinear deposition strategies for simple cubes using a powder DED process. They showed that the heat distribution and residual stresses were most uniform in the deposition patterns where each layer is printed perpendicular to the previous one, with starting points at an opposite corner. They found that alternating the direction of the deposition layers reduced the overall residual stress in the part by 11% compared to repeating the same deposition strategy over each layer.

Ghasempour, Afonso, and Torcato (2021) compared four deposition strategies for a similar cube and showed that an 'outside in' contouring strategy significantly reduced the overall peak temperature compared to rectilinear toolpaths. This is because of the long travel time for the outer tracks, which have time to cool before the subsequent tracks are laid next to them. Their longer profile and additional time allow convection cooling to be maximised. This conclusion was reached in similar work by Aliyev, Lee, and Ahn (2022). Ghasempour, Afonso, and Torcato (2021) also supports the work of Kim et al. (2021) and Aliyev, Lee, and Ahn (2022), showing that this deposition strategy reduces the bulk heat in the component and the overall stress.

2.3.3.2 Thermal Control Using Interlayer Pauses

Interlayer pauses are a useful tool to control the temperature development within a part. This is especially significant for smaller parts or narrow sections where high temperatures can accumulate rapidly (Singh et al., 2021). Interlayer pauses enable

consistent interlayer temperatures throughout the part. This reduces geometric and microstructure variability and overall bulk heating. Yu et al. (2022) showed interlayer pauses could reduce the melt pool temperature by approximately 200°C by reducing bulk heating.

For larger parts, an effective pause in deposition can occur naturally during the deposition process, even without stopping. The size of the layers in the x-y plane are large enough that there is minimal heat input across much of the layer's surface for extended periods. This can create the opposite issue to smaller parts, where parts cool down too much and absorb too much of the melt pool heat during passes of the laser on subsequent layers. Preheated substrates are typically used to address this problem (Kim et al., 2021).

2.3.3.3 Thermal Control Using Process Parameters

In the Key Equations section, it was established that process parameters influence the dynamics of the deposition process, such as the Marangoni effect, Fourier and Peclet numbers. When material properties remain fixed, controlling process parameters becomes the main way to influence the dynamics of the process.

The dynamic nature of the process and the non-uniform shape of 'real life' parts means that the temperature of the part as it is built will be constantly changing. Therefore, parameter and path planning with a slicing tool, working with Finite Element Analysis (FEA) tools to determine the likely thermal behaviour of the component during the deposition process is necessary to understand these heating and cooling cycles and subsequently develop a dynamic set of process parameters to influence this.

There are many publications (Svetlizky et al., 2021; Cunningham et al., 2018; Yan et al., 2018) that investigate the need for adaptive process parameters to accommodate the changing properties of the part as the build progresses. To support this, a substantial amount of literature has been published covering process characterisation for various metal AM technologies. Very little of this can be used

directly for LWAM, and there is no clear approach that can be universally used to develop adaptive process parameters and plan them for a built part. Significant empirical testing for specific equipment is required to fully characterise a particular process and the material used before it can be fully effective in manufacturing parts (Feenstra, Molotnikov, and Birbilis, 2021).

Tapia and Elwany (2014) highlighted that most of the research on process optimisation focused on simple tracks and geometries. Research has since moved on to understanding the relationship between tracks and the macro-scale geometries of a build (Oliari, D'Oliveira, and Schulz, 2017; C. Wang et al., 2020; Graf et al., 2018), but there is still little published regarding how this can be translated to complex parts. Most research recommends a modular approach towards breaking a part down into sections which have similar characteristics, yet there is little that demonstrates this in practice. Several papers which use Machine Learning techniques (Fetni et al., 2021; Nalajam and Varadarajan, 2021; Z. Zhang, Z. Liu, and D. Wu, 2021) show promise for modelling more complex geometries, as ML models can be applied to conditions that they have not had direct training data for.

There is a general requirement to undertake a 'trial and error' approach (Yan et al., 2018; Ferro et al., 2020) to choose the most effective parameters and defect mitigations, tailoring for individual parts. Equipment configuration, the part geometry and the number of parts being produced at once all need to be considered. There is an overriding requirement to remove or reduce the need for this approach, both to improve the efficiency in terms of time and material costs but also to reduce the skill requirement to produce a new part.

2.4 Machine Learning

Machine Learning (ML) has been applied to many of the stages of the AM design and production lifecycle (Grierson, Rennie, and Quayle, 2021) and is therefore a large field. This review is limited in scope to how ML techniques have been used to improve DED technologies and, specifically, how they have been used to support the design and optimisation of the deposition process.

ML has many applications within AM and pervades AM research, with applications throughout design and production processes (C. Wang et al., 2020). ML is particularly valuable in metal AM because of its ability to cope with non-linearity and outliers in data, its fast computation once trained and the ability to interpret complex data without the need for accurate calibration of input parameters (C. Wang et al., 2020; Mozaffar et al., 2018).

ML is particularly useful when assisting with modelling activities to reduce the time required, current simulation methods take many hours and need to be iteratively rerun for optimisation. ML can act as a complementary tool to reduce the amount of simulation required.

Most ML applications within DED use Artificial Neural Networks (ANNs), which are relatively 'shallow' compared to those used in more complex activities such as image processing. ANNs are typically chosen because they can be trained and perform accurately with relatively small datasets of tens or hundreds of data points (Farias, Cruz Payão Filho, and Oliveira, 2021). ANNs are structured with multiple layers of neurons or nodes which are typically structured as a set of input nodes on the first layer, several hidden layers and an output layer. The connections between the nodes in these layers are defined by weights that are adjusted during a training activity to enhance the accuracy of the prediction. Figure 2.23 is an example of an ANN architecture with a single hidden layer, showing the many connections and variety of functions of each node.
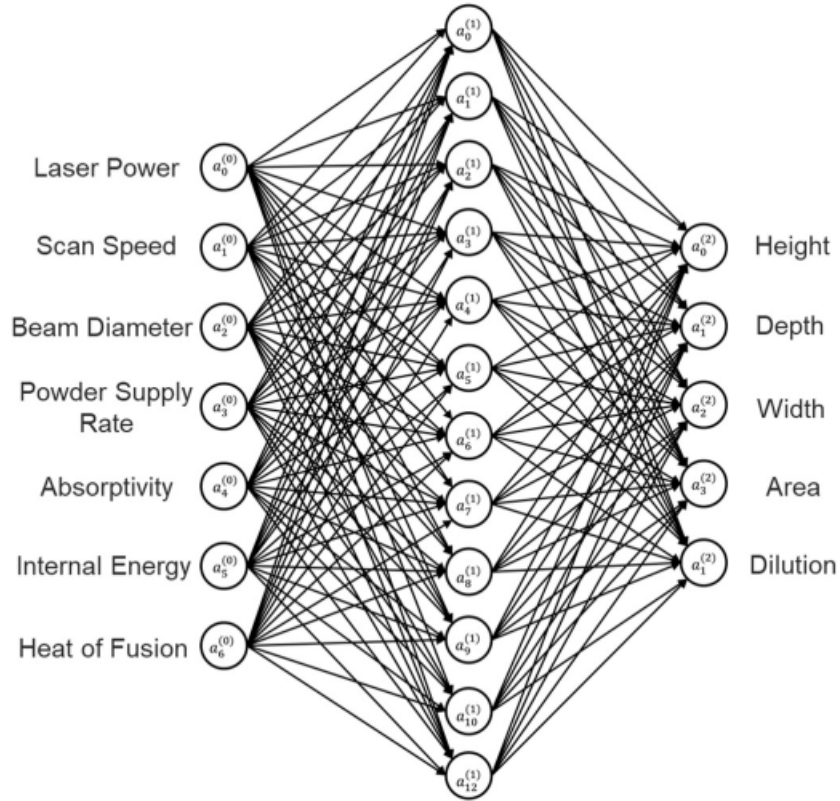
Figure 2.23: Example ANN with input, output and hidden layer nodes (Feenstra, Molotnikov, and Birbilis, 2021).

Training a neural network involves using a training algorithm to input data from a training dataset and modifying the weights between the nodes based on the difference between the predicted output of the network and the actual output, typically using backpropagation. This process allows the network to minimise prediction errors. The network's performance depends significantly on its architecture: the number of layers and nodes, its transfer functions and the data used to train it. The quality and quantity of training data are critical for neural network performance. Large, well-curated datasets enhance model accuracy.

2.4.1 Machine Learning for LWAM

A significant limitation for ML in this field is the comparatively small datasets available to train ML models. There are several mitigations to this, such as using modelled data to augment experimental data, transfer learning (X. Li et al., 2018), data augmentation (Cui et al., 2020) and combining multiple AM methods in an ensemble (Kshirsagar et al., 2019).

Svetlizky et al. (2021) highlight in their review of DED challenges that the link between simulation, monitoring and control is still immature for AM technologies. The ability to act during the build process, to preempt or rectify a defect is currently limited. They highlight the impact that ML techniques are starting to have upon this problem both in terms of process optimisation as well as monitoring and control.

ANNs can be used to model process windows, such as R. Sharma et al. (2023). The Feenstra, Molotnikov, and Birbilis (2021) model can accurately predict track geometries for a variety of DED powder alloys based on process parameters. Extending these models to predict track geometry based on the number of tracks, layers and temperature may support layer height prediction for more complex parts. Wacker et al. (2021) show that these trained models can be applied to geometries unused during the training process. Applying ML tools to more complex issues such as these would begin to capitalise on the strengths of ML tools beyond processes that can easily be modelled using conventional mathematical techniques.

2.4.2 Using Machine Learning for Geometry Prediction

Wacker et al. (2021) write that the current state of the art for ML in AM allows for the prediction of deviation from the planned geometry due to residual stress when using WAAM. Their approach achieved a 3% error rate in its predictions of distortion for each layer deposited of thin walls. Their work also evaluated the sensitivity of the training process to outliers in the training data by intentionally introducing outliers and noise. This is particularly important for applications in this field where repeatability and consistency in the process can be challenging.

The novelty of this paper is the use of only the ML model and feedback within the ANN architecture to predict distortion. Wacker et al. (2021) used a simple ANN model with two hidden layers. The trained network is used recursively to predict geometry distortion of subsequent layers of welding tracks printed on top of each other. The data input to the model includes the process parameters for the layer to be produced and feedback from the model's prediction for the previous layer's geometry and distortion.

This approach allows the distortion of the entire build of the wall to be modelled layer by layer. Once optimised, the feedback in the architecture can be replaced with measured data to use the model for in-process monitoring, control and prediction. An elegant use of the same model to address the gap between simulation, monitoring and control identified in Svetlizky et al. (2021).

This approach demonstrates that a simple ANN design can be reliably used to predict outcomes of distortions in tracks, considering previously deposited layers. Currently this approach has not been attempted with anything more complicated than thin walls and has yet to be used beyond simulation.

2.4.3   Machine Learning Conclusions

Machine Learning's strength in handling non-linearity, outliers, its fast computation once trained and ability to detect unforeseen relationships between variables lends itself well to process optimisation tasks in DED. ANNs are commonly used in DED research and offer accuracy with smaller datasets, which is a common challenge for this field due to the lack of portability of data between experiments and the difficulty in generating large volumes of experimental data. ML's potential for real-time defect rectification and process optimisation is emerging, with models predicting track geometries and part distortions with significant accuracy. This approach shows promise in bridging gaps in simulation, monitoring, and control in AM technologies.

2.5 Knowledge gaps

2.5.1 Precision, Geometry Variability and Toolpaths

A key challenge for research in LWAM lies in the difficulty of replicating experiments and directly comparing processes, primarily due to variations in system performance and the inconsistencies of how these are described in the literature. This issue becomes more complex for coaxial systems, as more variables are introduced and the precision of laser calibration becomes increasingly critical. Detailed documentation of system configurations, particularly laser calibration and actual energy measurements for the system, is crucial for reliable comparisons and advancements.

Furthermore, coaxial laser systems offer many benefits in this field due to their precision, efficiency and tolerance of variability in geometry. However there is limited research in this area. Studies mostly focus on single laser systems, leaving a gap in understanding the intricacies of coaxial systems, including their impact on track morphologies, melt pool dynamics, and overall thermal effects.

Research into toolpaths shows a departure from strategies traditionally employed in polymer technologies. While there exists a reasonable amount of literature in this area, it often leans towards simplistic approaches, again requiring combinations of techniques such as zoning and contouring with speed and layer height correction into a single process. A shift towards integrating multiple approaches is crucial for supporting the transition to using the technology to create complex geometries with high integrity.

2.5.2 Temperature Management Strategies

Research into temperature control strategies, such as forced air cooling and interlayer pauses and incremental laser power reduction, is typically limited to single techniques, however for complex components, combinations of approaches are required. The application of much of the research described uses simple geometries,

which are not representative of the shapes that these technologies will be applied to.

Techniques for interlayer pauses are described within the literature and their use to maintain consistent interlayer temperatures, which is now being integrated with process parameter control. There is limited work published that combines modelling techniques with experimental measurements of the effects of these results, or how interlayer pauses can be applied to structures that are not monolithic. This is further compounded by the little amount published covering the thermal modelling at a part level of coaxial laser systems, which no doubt in part is because it is much harder to model these systems given that there are currently no thermal modelling tools that have prebuilt configurations to model the lasers.

2.5.3   Machine Learning for LWAM

The rapidly growing applications of Machine Learning offer much to assist with optimisation, characterisation and control for LWAM, particularly for complex geometries and real-time defect detection. Its ability to cope with limited data is a strength, but it remains limited by data portability and calibration between different experimental configurations. It is likely that ML has the potential to address this issue, using information about the experimental equipment in its training alongside the usual physical training parameters.

Chapter 3

Experimental Methods

The experimental methods outlined in this chapter describe the characterisation of single-tracks, single-layers and multi-layer LWAM builds using the Meltio M450 with 316LSi stainless steel wire feedstock. The different deposition processes are described and how they are run in terms of G-code machine commands. Subsequent preparation and measurement using a range of geometric and thermal measurement techniques are described.

3.1   Experimental Equipment - Meltio M450

All experimental work has been undertaken using the Meltio M450, a coaxial multi-laser metal wire, LWAM commercial printer, intended for small to medium-sized multi-metal part fabrication. The Meltio M450 is designed to print with two separate metal wire feedstocks in one deposition process. Figure 3.1 shows an image of the machine, Figure 3.2 a schematic sketch of the machine and Figure 3.3 a schematic of the deposition head.

Figure 3.1: Meltio M450 Laser Metal Wire printer (*Meltio* 2021).
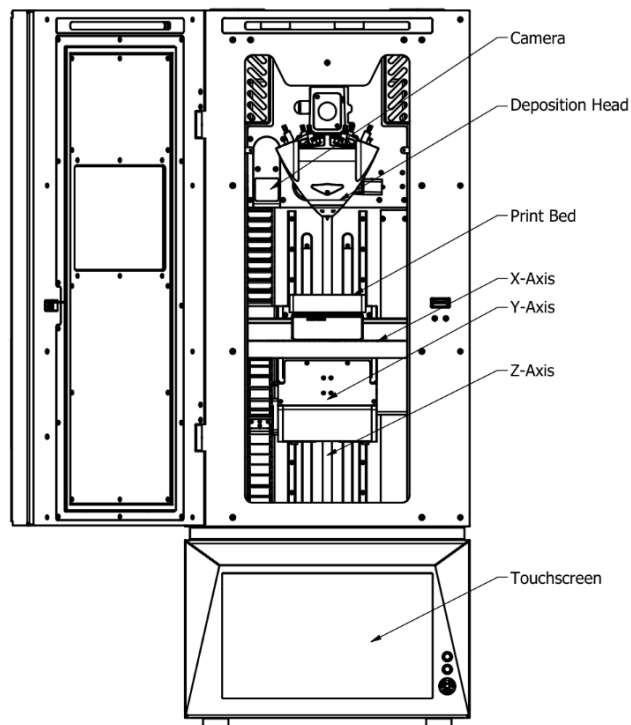
Figure 3.2: A schematic of the Meltio M450 (*Meltio* 2021).
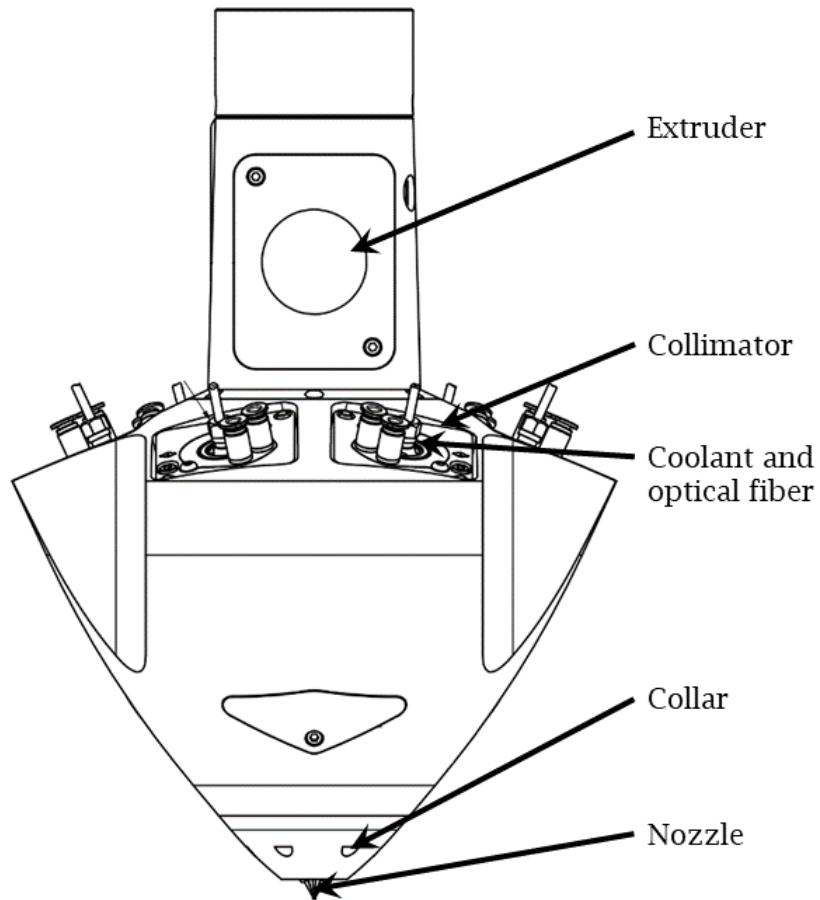
Figure 3.3: Schematic of Meltio M450 Deposition Head (*Meltio* 2021).

The deposition process is delivered through synchronised control of the print bed and the fixed deposition head, which contains the laser source, wire feed and inert gas supply to the melt pool. Six 200W, 976nm laser diodes provide the laser energy source, fed via optical fibres into collimators coaxially arranged within the deposition head around the feed nozzle. Wire reels are mounted in compartments on either side of the control screen. The 1mm diameter wire is routed internally to the extruder at the top of the deposition head and driven by the extruder through the centre of the head to the nozzle above the print bed. Argon shield gas flows through the deposition head into a collar around the nozzle to inert the melt pool. A hotwire function can be used from $0 - 125$A, which preheats the wire before it is melted by the laser.

The print bed can be moved in x, y and z planes beneath the deposition head, with the print substrate bolted to it. The print bed, collimators and laser diodes are water cooled. Table 3.1 provides a summary of the machine's specifications.

Specification	Value
Print Envelope (WxDxH)	145 x 168 x 390mm
Laser Type	6 x 200W direct diode lasers
Energy Distribution	Gaussian (single laser)
Laser Wavelength	976nm
Total Laser Power	1200W
Hotwire	0 - 125A
Process Control	Closed-loop, laser and wire modulation
Enclosure	Laser-safe, sealed, controlled atmosphere
Interface	USB, ethernet, wireless datalink
Cooling	Active water-cooled
Wire Feedstock Diameter	0.8 – 1.2mm
Wire Feedstock Spool	BS300
Oxygen sensor accuracy	±0.2%
Process control range	4.8V-5V
x and y axis tolerance (per 100mm of displacement)	0.2mm
z axis tolerance (per 100mm of displacement)	0.1mm
Material extrusion tolerance	±5%
Inert gas system tolerance	±0.5l/min

Table 3.1: Meltio M450 Machine Specification.

A 'process control' function is provided to ensure continuity is maintained between the wire and the substrate; this is achieved by monitoring the electrical connection in the hotwire system. Should there be a break in continuity, the controller increases the extrusion rate to attempt to regain a connection. Process control and hotwire functionality has not been used in any experiment, as it would not be possible to determine the extrusion rate used and whether it was consistent throughout the process.

3.1.1 Calibration of the Lasers

The six laser spots are calibrated to an overlapping circular arrangement, to ensure the energy distribution across the melt pool is as uniform as possible and to maintain a consistent shape of the melt pool whilst travelling in any direction. This shape was empirically determined by the manufacturer to be most effective for the deposition process.

A Meltio CMOS calibration camera is used to arrange the lasers at a predetermined offset distance, which is the distance between the nozzle and the surface of the substrate. Figure 3.4 shows an image taken with the calibration camera. It shows the location for each laser spot (red circles), the profile created by the lasers (white ring) and the wire fed into the centre of the spots (black circle). The arrangement of the circles is set based on the wire diameter. The calibrated laser spot shown is for a wire diameter of 1mm; each laser has a diameter of 1.13mm, creating a combined diameter of 2.25mm for the entire spot.
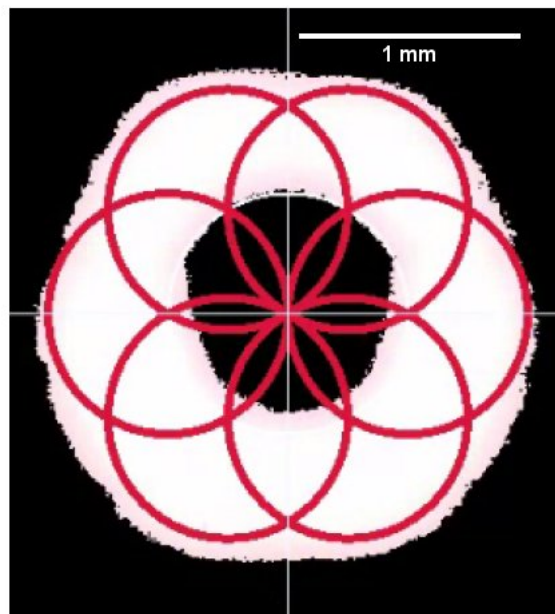
Figure 3.4: Calibration of Meltio M450 lasers into circular configuration with wire at the centre.

Calibrating the lasers in this arrangement effectively sets the focal length beneath the substrate's surface. The focal length is the distance from the collimator lenses to the point where the lasers converge into a single spot. For ease of measurement by the operator, the focal point's distance is measured from the deposition nozzle to the substrate surface, which is called the offset distance.

The lasers are calibrated to an offset distance (h) of 6mm. When using 1mm wire, the distance (d) between this offset distance and the focal point is 1.39mm, Figure 3.5 illustrates this. The calibration of both the offset distance and the spot alignment was verified before each experiment.

The conical shape formed by the lasers creates an extremely hot area for the wire to pass through, which risks melting the wire prior to it reaching the substrate. Ideally a melt pool is created at the substrate's surface where the wire and substrate are simultaneously melted. If the wire melts before reaching the substrate, because the extrusion rate is too slow, it results in an accumulation of molten material above the surface, leading to dripping. This effect constrains the minimum extrusion rate achievable.
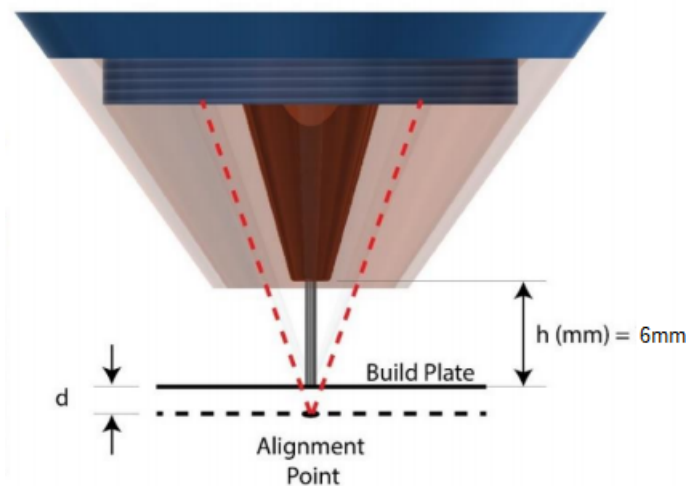
Figure 3.5: Focal length of the Meltio M450 lasers, showing the offset distance (h) and distance (d) to the focal point (*Meltio M450 Manual* 2022).

3.1.2 Print Environment – Inert Gas and Cooling

The system uses an external chiller to provide 14°C chilled water, which cools the build plate, collimators, laser diodes and bed motors. Void spaces between the build chamber and the external case of the machine are ventilated with cooling fans, as is the internal void within the door to cool the laser glass used in its window. The build chamber has an air blower which is intended for cleaning the air through a filter after builds are completed. The door fan and chamber blower inhibit the machine's ability to maintain a fully inert environment and increase the cooling rate of completed components. Except for large muti-layer components, neither were operated during experiments and were only used once the deposition process and part cooling had completed.

An inert build chamber is used to minimise oxidation of the deposited surface. Argon is fed locally to the melt pool via the deposition head collar with a flow rate of 10 litres per minute. The chamber atmosphere is made inert by flooding the chamber until the oxygen sensor has a reading of 0% (sensor accuracy $\pm0.2\%$).

3.1.3 Feedstock

The same wire feedstock was used throughout the experimental programme, ensuring uniformity in the material properties for all deposition processes. Stainless steel 316LSi wire was used with a diameter of 1mm, $\pm0.05mm$ with the chemical composition described in Table 3.2 and material specification in Table 3.3.

Element	Weight Percent (%)
Fe	Balance
C	0.02
Si	0.9
Mn	1.7
Cr	18.5
Ni	12
Mo	2.7

Table 3.2: Stainless Steel 316LSi Wire Feedstock Chemical Composition.

Wire Diameter	1.0mm
Spool Type	BS300
Wire Coating	Uncoated
Melting Point	1398ºC(1671K)

Table 3.3: Stainless Steel 316LSi Wire Feedstock specification.

3.2   Generation of Experimental G-code

G-code is a programming language, based on ISO 6983, that directs machine operations and tool movements to create 3D printed objects layer by layer. Standard G-code is modified by manufacturers to accommodate the specific functionality and requirements of their additive manufacturing machines. These modifications ensure that G-code effectively translates digital models into precise instructions suitable for the machine, but these modifications prevent the G-code from being transferable between machine types and manufacturers.

G-code is generated by a slicing tool, which is configured with the characteristics of the machine, including its unique commands, track and layer geometries, track and layer separation distance, head speeds, extrusion rates, etc. A CAD model is first translated into a format compatible with the slicer (for example OBJ or STL

file format), the slicer converts this model, using the predefined characteristics, into a G-code file. This file, tailored to both the material and the machine, contains step-by-step instructions for the machine, from its initiation, start and end locations of moves, process parameters for each move and extrusion rates, to its finishing and shut down instructions.

To ensure accurate control of the process parameters and to avoid any unknown modification to the deposition process provided by the slicing software, the G-code for all experiments was generated using bespoke code written using MatLab R2022a for these experiments. The process flow charts for the G-code generated are described in the following experimental sections and shown in Appendix A.

3.3 Single-Track Experiments

The focus of the single-track experiments is to investigate which process parameter combinations result in high-quality tracks and to define the process window for optimal parameters, laser powers between 550W and 800W were used, head speeds and extrusion rates were between 5mm/s and 25 mm/s in an all factor design. Single tracks are the fundamental building blocks of parts, identifying process parameters which produce a high-quality track is crucial. Flaws or inconsistencies due to poor track quality can propagate through an entire part, compromising the mechanical properties and overall reliability of the final part.

This experiment explores a range of combinations of extrusion rates and head speeds for different laser powers, to determine which configurations lead to consistently defect-free tracks. The tracks are initially visually assessed for obvious signs of defects and subsequently analysed using a 3D laser scanning confocal microscope to determine the height, width and consistency of tracks identified as high-quality.

Tracks measuring 50mm in length were systematically deposited in two parallel columns on a 316L stainless steel sheet, each track was spaced 6mm apart. To minimise thermal influences on the track deposition process and distortion of the sheet, each track deposition was separated by a three-minute pause. The sequence of the tracks' locations on the plate was randomised to further reduce the heat build-up in the plate and to mitigate any potential biases arising from the order of printing. Bespoke G-code was written to run the experiment ensuring that no modifications were made by slicing software or the machine's control systems which could result in different process parameters than those in the experimental plan.

Sheets of 3mm thick 316L stainless steel were used for the print substrate with dimensions of 200mm x 150mm, their chemical composition is described in Table 3.4. Holes of 8mm diameter were drilled in the corners to secure them to the print bed. Stainless steel sheets were chosen to ensure that that the substrate was compatible with the weight limits of the microscope stage (described below).

Element	Weight Percent (%)
C	≤0.08
S	≤1.00
Mn	≤2.00
P	≤0.045
S	≤0.030
Cr	16-18
Ni	16.0-18.5
Mo	2.0-3.0

Table 3.4: Stainless Steel 316L Plate Chemical Composition.

The print surface of the substrates used in each experiment was prepared using the following process:

1. Remove any residual material on plate's print surface from previous prints using a 40-grit zirconium dioxide flap disc on a hand grinder.

2. Inspect the plate's print surface, ensuring it is flat and level.

3. Surface roughening and cleaning of the print surface by abrasive blasting, using aluminium oxide media, between 60 and 80 grit, to achieve a uniform surface finish.

4. Thorough cleaning of the entire plate using a light detergent, applied with a hard plastic bristle brush to ensure removal of surface contaminants.

5. Rinse the entire plate with tap water.

6. Dry the plate using a lint-free cloth.

7. Wash the print surface with isopropyl alcohol, using a white, lint-free cloth. The cloth is inspected to confirm that the print surface is clean.

3.3.1 Single Track G-code Generation

The convention in the literature is to describe the process parameters in terms of millimetres per second for head speed (V_h) and extrusion rate (V_f) and Watts for the laser power (P). G-code instructions express head speed as millimetres per minute (F) and the extrusion rate is determined by the machine through defining the length of material in millimetres to extrude (E) over the distance defined for a particular track. The values for E and F are calculated as described in equations 3.1 and 3.2, where l is the track length:

$$E = \frac{V_f \times l}{V_h} \tag{3.1}$$

$$F = V_h \times 60 \tag{3.2}$$

The flow chart for the generation of the G-code is shown in Figure A.1 of Appendix A.

3.3.2 Measurement of Single Tracks

The 50mm tracks were measured in the centre section of the track to ensure the assessment of the track was representative of a steady state deposition process, Figure 3.6 shows the assessment region of the track.

In the Literature Review, visual assessment of deposited single tracks was established as a commonly used method for initial evaluation of track quality due to its efficiency. This step is necessary to filter out poor quality and failed tracks to ensure only those which are of a high quality are measured. A 'high quality' track is one which could be used for a multi-track deposition. These tracks are uninterrupted and consistent along their length, characterised by a smooth surface with a regular cross-section. Their edges are clean and straight along the length of the track, securely bonded to the substrate with a contact angle well below 90°.

Tracks which meet this description are defined as 'Printable' tracks and are likely good candidates for multi-track and multi-layer deposition.

3.3.2.1 Optical and Laser Microscopy of Single Tracks

An Olympus LEXT OLS5000 SAF confocal optical 3D laser microscope was used to measure the dimensions of the deposited tracks. The microscope provides high accuracy, non-contact laser and optical measurements and high-resolution images. Using confocal optics and a 405nm laser light source, it is capable of lateral x/y-axis measurements up to a resolution of 0.02µm and z-axis vertical measurement accuracy of up to 0.012µm, with a maximum field of view over the z-range of 5.1mm; it can detect slopes up to 87.5° from horizontal. The controllable stage has a maximum sample weight of 3 kilograms, which limits it to assessments of thin plates or samples cut from the substrate.

The microscope incorporates a laser confocal optical system, which helps to eliminate blur and enhance image contrast, this is particularly valuable for imaging the highly reflective surface of stainless steel tracks. The short wavelength laser
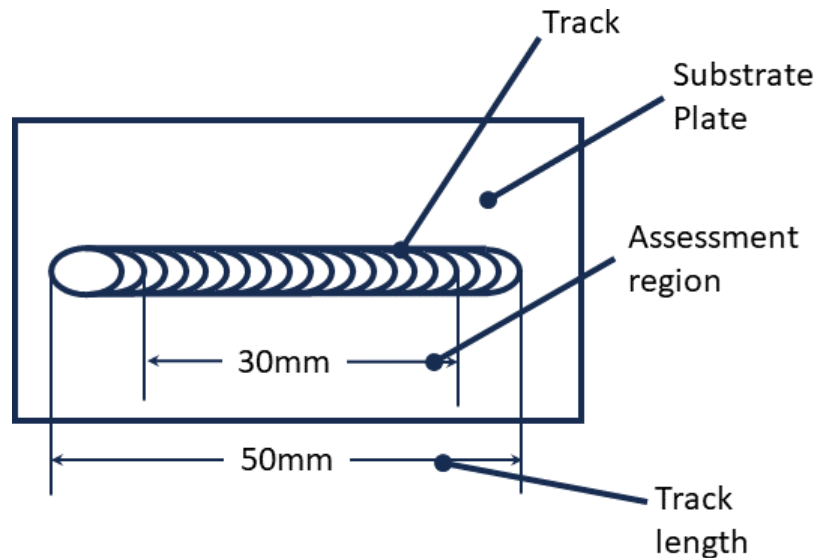
Figure 3.6: Schematic diagram of single track deposition showing the assessment region.

allows for the detection of finer patterns and defects that would be missed by conventional optical and red lasers, enabling high accuracy measurements even when using low magnification lenses. All measurements made used the laser sensor data, sampled with a resolution of one measurement every 2.5µm in the x and y axis.

Microscopy was used to assess single tracks printed on thin plates which had been categorised as 'Printable'. The experimental plan was designed to minimise bending in the plate due to thermal stress, however a small amount of bend in the plate was unavoidable. Each track was therefore imaged individually and then post processed using the microscope's analysis software to remove the bend from the data.

Tracks with contact angles close to 90° approached the limit of the microscope's 87.5° slope detection; this high contact angle combined with the highly reflective surface causes significant noise at the boundary between the substrate and the track. Consequently, it is difficult to determine the shape of the track consistently where this effect is seen. The track width was therefore measured at 5% of the track height to avoid errors due to these effects.

Each track was imaged using the 5x magnification lens, which produces images of 2.5mm square, these were stitched together to create an image of a whole track. Five measurements of the track were taken at random points in the assessment region described in Figure 3.7. The following method was used to take the measurements and analyse them.

1. Image tracks – the whole track was imaged both optically and using the microscope's laser, using a series of 2.5mm square images, stitched together by the microscope's analysis software.

2. Post Processing – The image was filtered to remove noise and skew, using the automated analysis tool, which applies a low pass filter to remove the high frequency noise generated by the reflective surface of the metal. The tool detects the skew created by the bend in the plate and subtracts it from the data.

3. Cross-Section Measurements – Using the microscope's analysis software, a guideline was drawn parallel to the track to ensure that cross-sections were taken perpendicular to the track's edge. Figure 3.7 below illustrates this. Five cross-sections were measured across the track and exported to a Comma Separated Value (CSV) file.

4. Measure tracks – Cross-section CSV files were processed using code written in MatLab R2022a. Each cross-section was measured for height by averaging the 20 highest height values, width was measured at 5% of this value, standard deviations of height and width were calculated for the five measured values and a mean contact angle calculated using a slope function, at the 5% height measurement point.

3.3.3 Machine Learning

Supervised Learning algorithms were trained to generate predicted process windows for printable tracks and to predict the track's height, width and consistency. The objective was to establish a reliable predictive model that could not only identify the conditions under which printable tracks could be formed but also adapt to predicting
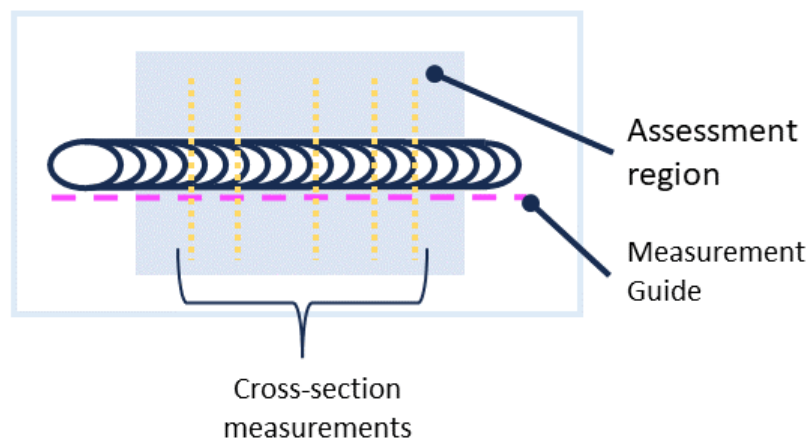
Figure 3.7: Schematic diagram of cross section measurements in the assessment region of a single track.

outcomes for extrusion rates and head speeds at other powers not validated through experimentation.

A training dataset was developed through the accumulation of the experimental data from the single-track experiments described above. Data describing the classification of tracks as printable or not printable had 255 measurements in total and 74 tracks were measured for height and width. The process parameters of laser power, extrusion rate and head speed were used as training inputs, augmented by power/extrusion rate, power/head speed, energy per unit length, Fourier number, the heat required to melt the wire and the energy density.

MatLab R2022a was used to methodically identify a suitable network architecture and its subsequent training and optimisation. This method aligns with the best practice guidelines recommended by MatLab (MatLab, 2022). The training data was split randomly to use 70% for training the network, 15% for validation of the training and 15% to test the trained network. All of the Supervised Learning and Artificial Neural Network (ANN) architectures available within MatLab (eg. Support Vector Machines, Decision Trees, K Nearest Neighbours etc) were evaluated to determine which could most accurately predict the responses to the inputs. Once the most suitable architecture was identified, the network's structure and hyperparameters were refined to optimise it for this application.

MATLAB's Classification Learner Interface was used for the initial identification of the most suitable network architecture. This allows multiple network architectures to be swiftly trained and compared using the same training data. A key development in this phase was adopting two separate networks to deliver the overall functionality of process windows and track geometry prediction. This was principally due to the nature of the training data; tracks which were determined to not be printable were not measured and therefore skewed the accuracy of the geometry prediction if combined with predicting classification in one network. Two networks were trained, the first to ascertain the classification of the track as printable and the second to predict track geometry for those printable tracks.

MatLab code was written to iteratively vary the hyperparameter settings and compare the accuracy of the resulting trained models. Accuracy of the network was further improved through using data augmentation, a technique where the existing training data is duplicated and added back to the original dataset. This repetition of the data doubles the training set, allowing the network to train on the same data twice, improving its performance.

3.4 Single-Layer Multi-Track Experiment

The single-layer experiments investigate the effects of overlap ratio on the quality of single layers. To investigate this, different overlap ratios were explored for predefined process parameters identified as high-quality tracks in the single-track experiments. A series of 25mm x 25mm single layers were deposited onto sheets of 3mm thick 316L stainless steel, as described in the single-track section above. Each layer was deposited in a single 'out and back' toolpath, shown in Figure 3.8. This approach would deposit the entire layer in one continuous deposition process, representative of a sliced layer from a part. The layers were subsequently analysed using a 3D laser scanning confocal microscope to characterise their height and overall consistency.

3.4.1 Single-Layer G-code Generation

Generation of G-code instructions follows a similar approach to the single-track experiments. The out and back toolpath required an additional value of E to be calculated for the head move between the longer tracks. The number of tracks (n) required to create a 25mm patch was dependent on the width of the track and the overlap ratio. Equation 3.3 was used to calculate n, where l represents the length and width of the square layer, w_t the track width and d the overlap ratio. The flow chart for the generation of the G-code is shown in Figure A.2 in Appendix A.

Figure 3.8: Toolpath for the 'out and back' deposition of a single layer.

$$n = \frac{l - w_t}{d \times w_t} + 1 \tag{3.3}$$

3.4.2 Optical and Laser Microscopy of Single-Layers

The assessment of the single-layer samples used the same methodology as the single tracks, using the LEXT OLS5000 microscope. The assessment region of the top of the surface being 10mm in from the edge of the layer, as illustrated in Figure 3.9. The following measurements were taken of the randomly chosen cross-sections, inside the measurement region:

Maximum Height mean height of the 20 highest peak values of each cross-section.

Average Height mean height of the entire cross-section.

Minimum Height mean height of the 20 lowest trough values of the entire cross-section.

Standard Deviation The standard deviation of the entire cross-section.
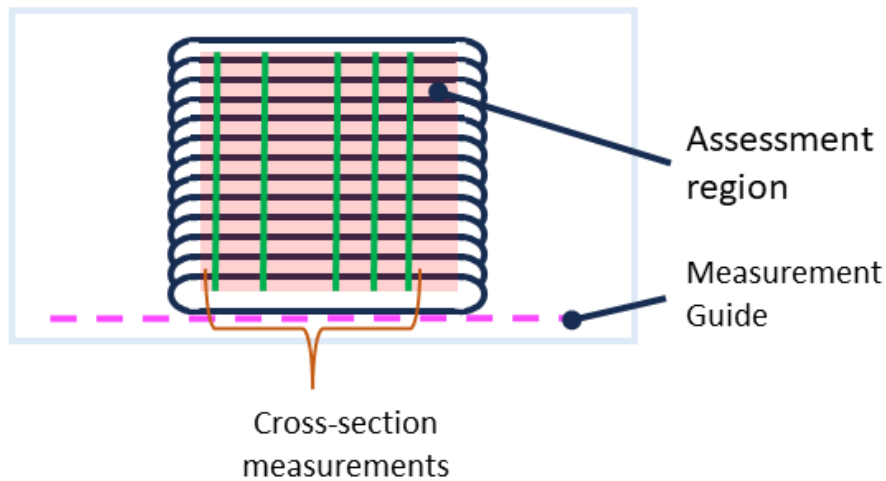
Figure 3.9: Schematic diagram of cross-section measurements in the assessment region of a single layer.

3.5   Multi-layer Experiment

High-quality multi-layer parameters are crucial for ensuring the structural integrity and geometric accuracy of the final part. This experiment extends the single layer experiments by evaluating the effects of different z-step increments on the overall part height, consistency and quality of the final part. The objective is to identify z-axis increments that result in flat layers, with minimal overbuild or underbuild and minimal porosity. The experiment uses the best quality layers identified in the single-layer experiments.

Multi-layer blocks were deposited onto plates of 25mm thick, cold rolled 316L stainless steel of dimension 200mm x 150mm, with chemical composition described in Table 3.4. The print surface was prepared as described in the single-track section above.

The blocks were formed with a series of 25mm x 25mm layers, using the same 'out-and-back' toolpath used in the single-layer experiments. The toolpath was rotated by 90° on alternate layers. The blocks were repeated with 5, 10, 15 and 20 layers all using the same parameters to create a set. This was to investigate the quality of the block as the build progressed. Each set investigated a particular Z-height increment, calculated based on the track height used. Where samples were removed from the plates, a bandsaw was used with a bimetal blade, with teeth made of M42 high speed steel (8% cobalt, hardened to 67-69 Hardness Rockwell C).

3.5.1   Multi-Layer G-code Generation

Generation of G-code instructions follows a similar approach to the single-layer experiments. With different toolpaths being created for the 90° rotations. The flow chart for the generation of the G-code is shown in Figure A.3 of Appendix A.

3.5.2 Laser Displacement Measurement of Multi-Layer Parts

The deposition of parts that are larger than a single layer generates too much heat to use on 3mm thin plates, causing them to buckle, requiring the thick plates for all multi-layer builds. Due to the weight limit of the microscope stage, thick plates cannot be analysed using this method. To address this, a Micro-Epsilon optoNCDT ILD1320-100 laser displacement sensor was installed within the deposition chamber to accurately measure these parts, using the print bed as the stage to move the parts under the sensor. An image of it mounted next to the deposition head can be seen in Figure 3.10.

The ILD1320-100 is designed for industrial and laboratory applications, used for process monitoring in glass and metal fabrication. It employs optical triangulation with a 670nm laser diode. The sensor has a z-axis measuring range of 100mm, linearity of less than ±100µm, and a measurement accuracy of 10µm. Test measurements of tracks were made with both the displacement sensor and microscope to confirm that measurements were within the 10µm range of accuracy.
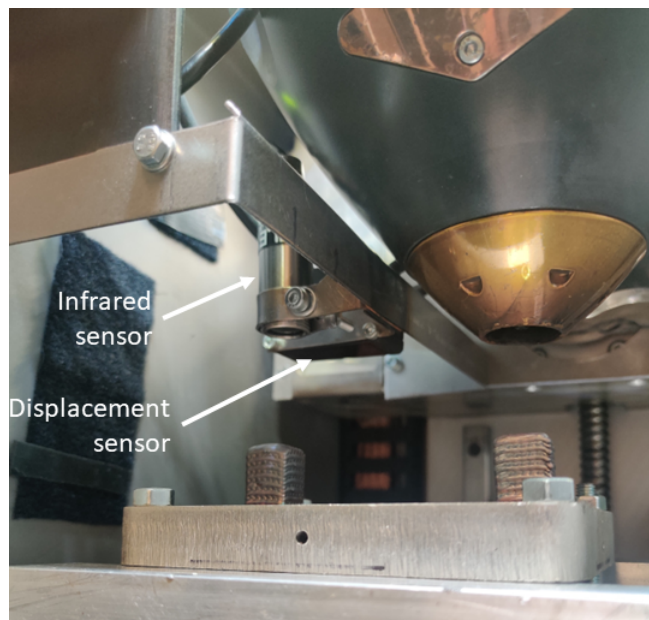
Figure 3.10: Mounting arrangements for laser displacement sensor and infrared thermal sensor in the build chamber.

The optoNCDT 1320 is effective at measuring highly reflective surfaces despite not operating in the blue range, due to its optical triangulation, narrow detector apertures and signal processing. The sensor has a standoff where this range begins of 50mm from the sensor's lower surface, it can therefore measure surfaces up to 150mm away. The technology uses a laser source and a separate detector which receives the reflected laser, see Figure 3.11. The arrangement makes it significantly more accurate when the surface being measured travels in the direction normal to the plane of the laser and its sensor.

G-code commands were used to position the part within the measurement range of the sensor and then move the part at a fixed speed of 2mm/s past the sensor to measure the cross-section, at a sample rate of 750Hz. The data was logged using Micro-Epsilon's SensorTOOL (v1.10.0.53) data logging software. Before measurements were taken sensor data was output in CSV format and post processed using bespoke code written in MatLab R2022a to perform the following steps:

Invert data - the sensor measures how far objects are away from it, making the component appear upside down. The entire dataset is inverted to address this.

Remove skew - A straight line is plotted between the two ends of the scanned cross-section, the slope of the line defining the skew on the plate. This line is subtracted from the measured data to remove the skew.

Remove noise - as with the microscope data, some high frequency noise is present in the measured data, which is removed with a moving mean filter, with a window of 30 samples.

After processing, maximum height, average height, minimum height and standard deviation were measured using the same assessment region criteria described above for the single-layers.
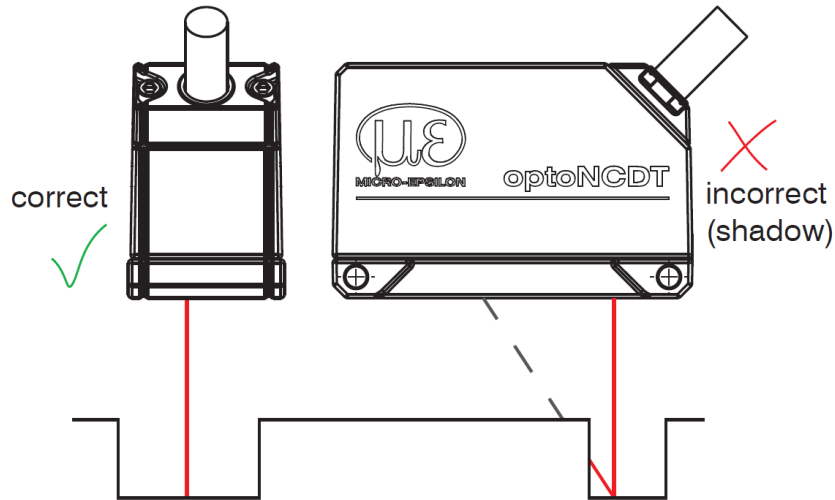
Figure 3.11: Effect of scanning direction on the optoNCDT 1320 laser displacement sensor.

3.5.3 Etching of Multi-Layer Parts for Defect Identification

To examine the internal structure of multi-layer parts, components were cut, milled, ground, polished and chemically etched. Tracks and small components were cut across their vertical cross-section into small samples. Larger multi-layer blocks were cut from the substrate and subsequently cut in half.

Samples were ground and polished using a multi-step procedure to successively reduce the roughness of the cut surface to a scale consistent with the polishing media used. Initially, the samples were ground with 800 and 1200 grit silicon carbide, followed by polishing using a 3µm diamond suspension. Between each polishing stage, the samples were cleaned with tap water to remove residual polishing media. The samples were etched immediately after polishing to minimise oxidation of the polished surface.

The etching was performed using Marble's Reagent (4g of CuSO4, 20ml of HCl, and 20ml of H2O), which is effective due to its ability to rapidly etch the surface while simultaneously staining defects. The hydrochloric acid component etches the surface, uncovering grain boundaries and microstructural details, while

copper sulphate provides selective staining, particularly highlighting defects such as porosities or inclusions. Samples were swabbed with reagent for a pre-defined time and examined using microscopy to determine the optimum duration. This was determined to be 30s. The samples were subsequently rinsed with distilled water and dried with a lint free cloth. Images of each etched sample were then taken with the LEXT OLS5000 SAF confocal microscope to identify defects and examine the consistency of the parts, dilution of tracks and layers was measured through using ImageJ with a calibration image to scale the measurements.

3.6   Multi-Layer Thermal Measurement

The importance of understanding and controlling heat accumulation during the deposition process was discussed in the Literature Review. It is particularly important for achieving consistency of the part in terms of its geometry, microstructure and geometric accuracy. In this experiment, the impact of interlayer pauses on the bulk heating and how these can be used to control the part temperature are investigated.

Blocks of 20mm x 20mm layers were deposited on plates of 15mm thick cold rolled 316L stainless steel of dimension 114mm x 96mm, with the chemical composition described in Table 3.4. The print surface was prepared as described in the single-track section above.

Blocks were produced using process parameters, track and layer overlap ratios and toolpaths established as optimal in previous chapters, with a range of interlayer pauses from 30 to 150 s. The temperature of the block and plate was monitored throughout the deposition process. A laser pyrometer is used to monitor the underside of the plate and a thermocouple monitors the temperature under the block. Each block is intermittently moved under an infrared temperature sensor adjacent to the deposition head during pauses.

The plates were painted on the underside (non-print surface) with heat-resistant matt black spray paint to increase the emissivity value of the surface. This also improves the consistency of the finish compared to rough stainless steel, maximising the reproducibility of the laser pyrometer readings.

3.6.1 Multi-Layer Thermal Experiment G-code Generation

G-code was generated using the same principles as in the multi-layer experiment. Additional code was added to move the block under the infrared sensor and wait for the appropriate pause time, then move back to the deposition head. The z-height of the print bed was adjusted to ensure that the top surface of the block was at a consistent height under the infrared sensor. The flow chart for the generation of the G-code is shown in Figure A.4 of Appendix A.

3.6.2 Temperature Monitoring of the Multi-Layer Process

The thermal modelling and experimentation required coordinated monitoring of the temperature of the bottom of the build plate, inside the plate and the deposited layer as it cools. To ensure that the data can be compared to the equivalent thermal models, the measurements must be carefully synchronised and accurately positioned.

The Meltio M450's print chamber is sealed to maintain an inert atmosphere and to contain smoke and dust generated during deposition. This sealed environment restricts cable access to sensors inside the chamber. Additionally, the limited space in the chamber, mounting points and movement of the print bed and z-axis sensor arm further constrain sensor installation. Three sensors were selected that could accommodate these constraints: a Micro-Epsilon CSL-CF2 Laser Pyrometer, a Calex PMU201 Infrared Temperature Sensor and a K-type thermocouple with a Lascar EL-USB-TC-LCD data logger. The cables for the infrared and laser sensors were routed through an existing cable penetration gland used for the chamber lighting and the battery powered thermocouple data logger could be securely placed at the bottom of the chamber.

The CSL-CF2 laser pyrometer was used to measure the underside of the substrate, mounted on the deposition bed directly underneath the substrate. It is designed for precise non-contact temperature measurements in a temperature range of -50°C to 975°C, with an accuracy of ± 1°C or $\pm 1\%$, with a response time of 150 ms. The sensor works well on a range of surfaces with a spectral range of 8 - 14μm

and can be configured for a range of emissivity settings between 0.2 and 0.95. The sensor uses two lasers which converge at the focal point of 150mm from the sensor, measuring a 3mm diameter spot. To aid positioning of the sensor it has two 1mW, 635nm aiming lasers. Data were recorded using Micro-Epsilon's Compact Connect (v1.10.9) data logging software.

The emissivity of 316L stainless steel varies significantly with temperature and oxidation (Valiorgue et al., 2011), to minimise this effect, heat resistant matt black spray was applied to the underside of the substrate to reduce reflection and increase the emissivity of the surface to the highest possible value. The maximum emissivity value of 0.95 was used and calibrated through heating a sample to 240°C which was representative of the plate. The sensor's measurements were validated with a thermocouple attached to the sample's surface.

The Calex PMU201 Infrared Temperature Sensor is a compact, non-contact sensor. It measures surface temperatures ranging from -20°C to 1000°C, with a response time of 125ms and an accuracy of $\pm 1\%$ or ± 1°C. The sensor has a spectral range of 8 to 14μm and the emissivity range can be set between 0.2 and 1.0. The sensor provides an average temperature across its spot, it has a spot diameter of 11.9mm at the sensor's lens, the diameter increases by 1mm for every 20mm from the lens. With an 8mm standoff the spot size was 12.3mm. This sensor was used for measuring the temperature of the deposited layer, mounted next to the deposition head (see Figure 3.10), the part was moved under the sensor by the print bed and held there for the duration of the pre-planned pause prior to moving back to the deposition head for the next layer. Data was logged using Calex Config (v1.17) data logging tool.

Due to the nature of the use of this sensor for measuring interlayer temperature and cooling, a paint treatment could not be used. An empirical value of the emissivity of 0.24 was determined through heating a sample which was representative of the surface immediately after deposition. The infrared sensor's measurements were validated with a K-type thermocouple attached to the sample's surface.

An inert chamber was used with a local flow of shielding gas to minimise oxidation of the surface, the machine's oxygen sensor had a reading of 0.0% (sensor accuracy ±0.2%). An inert chamber was not possible for builds larger than seven layers due to the machine requiring cooling fans to be used for its glass window. Chamber humidity was measured to be between 40% to 50% for all builds.

A K-type thermocouple with a Lascar EL-USB-TC-LCD datalogger was used for measuring the temperature inside the substrate. The 3mm diameter thermocouple with a stainless steel sheath was fitted into a drilled hole directly under the centre of the deposited layers. The thermocouple provided a measurement range of -200°C to +1350°C. The datalogger offered a resolution of 0.5°C and an accuracy of ±1°C, measured at 1Hz.

Figure 3.12 shows the schematic arrangement of the sensors about the centre line of the experiment, which was fixed at the centre of the plate. A mounting arrangement was used to secure the substrate to the print bed whilst allowing for sufficient room to mount the laser pyrometer underneath, accommodating its 150mm focal distance.

The clocks for the sensors' logging software were synchronised and logging was initiated prior to the print process commencing. All sensors logged data during the deposition process, however the infrared sensor's data was only relevant whilst the printed component was positioned underneath it during cooling pauses, travel time to the sensor was an estimated 8s after layer completion. The Z height of the bed was adjusted for each measurement to ensure that the top surface of the part as it grew was always at the same distance from the sensor. A flowchart for the deposition process for this experiment can be seen in Figure 3.13.
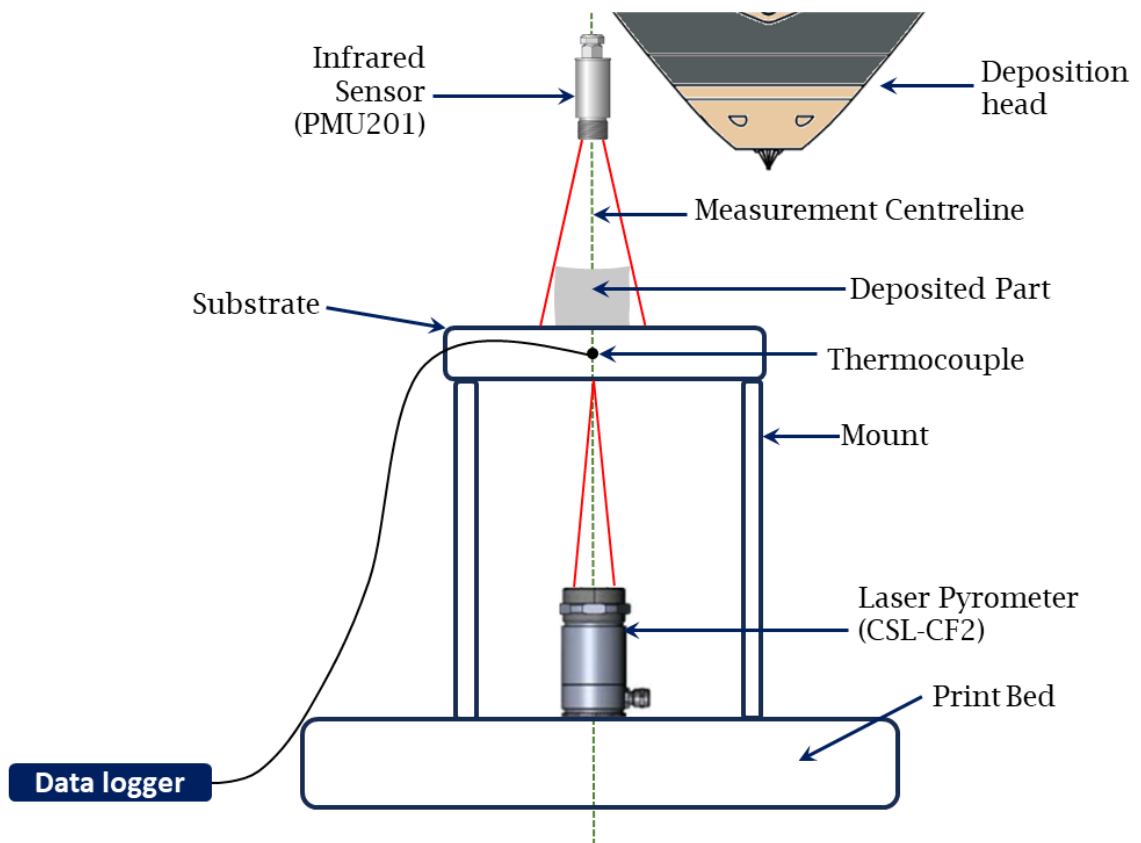
Figure 3.12: Sketch showing the mounting arrangement for the build plate and thermal sensors.
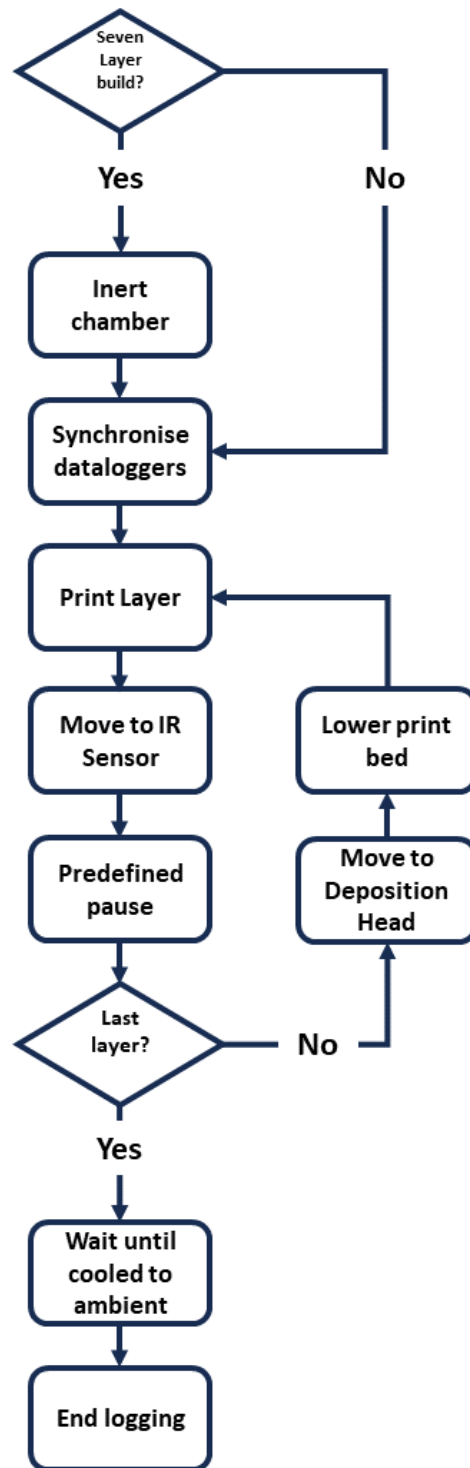
Figure 3.13: Flow chart for the deposition and measurement process for multi-layer thermal experiments.

3.6.3 Thermal Modelling of Multi-Layer Deposition

The multi-layer experiments described above were simulated using Autodesk's Netfabb Local Simulation (2023.0, Solver Version 23.0.0.81). This was to investigate whether the thermal fields observed through experimentation could be duplicated through modelling and explore whether an off the shelf engineering tool could support the identification of an optimum interlayer pause.

Netfabb Local Simulation is a finite element thermo-mechanical simulation tool, specifically tailored for PBF and wire DED applications. It is intended to function as a pre-build analysis and parameter optimisation tool specifically focused on the development of thermal fields and the consequent mechanical stresses caused and resulting deformation. Netfabb Local Simulation was chosen primarily for its specialist tailoring for the LWAM process, in contrast to the more broader capabilities of tools such as ANSYS. Netfabb has pre-constructed libraries of material models including stainless steel and has predefined the physics of the deposition process for a single laser LWAM process.

The software uses an 'lsr' file format, which is converted from a CAD model of the part to be simulated. The file describes the power and angle of the laser source, its direction, distance and speed for each track to be deposited; Table 3.5 summarises the file format. The tool uses a moving volumetric heat source with a uniform profile to represent the laser energy source. Although this is a simplistic model and not an accurate description of the laser energy distribution, it is sufficient to support thermal modelling at a macro scale (Bayat et al., 2021), allowing quick simulations to be run in a few hours with low processing requirements sufficient for a PC.

The intention for the thermal modelling is to evaluate whether, at a macro level, the thermal field created during the deposition process can be replicated and the impact of pauses investigated. Cuboid blocks were simulated using the same tool path, head speed and track dimensions as used in the multi-layer experiments described above. The material properties were specified from Netfabb's material

library, summarised in Table 3.6, Table 3.7 summarises the configurable parameters within the software and Figure 3.14 shows a screenshot of the tool with a 16 layer block. Boundary conditions, key thermal equations and meshing functions were fixed within the toolset fot all simulations (Autodesk, 2023).

Laser Power	Point source laser power specified in Watts.
Laser Vector	X, Y, Z description of the laser source position relative to the element being deposited.
Start Point	X, Y, Z position of the start of the track.
End Point	X, Y, Z position of the end of the track.
Laser Radius	Radius of the laser spot in millimetres.
Laser Velocity	Head speed of the track deposition in mm/s.
Start Time	Time stamp for track deposition to begin.

Table 3.5: Netfabb Local Simulation LSR file format.

Temperature probes were located to extract modelling data aligned with the same measurement points used with the thermal sensors during the multi-layer thermal experiment. Figure 3.15 shows the location of these probes on a cross section of a 16-layer block simulation.

Netfabb Local Simulation uses an adaptive meshing method to define elements for simulating a part. A finer mesh is used near the melt pool to accurately capture high temperature gradients. As the laser moves away, the mesh is coarsened to improve simulation efficiency. Autodesk recommends one or two elements per laser radius in the laser path and at least two elements through the substrate thickness. The tool also uses adaptive time steps to further improve simulation efficiency. The simulation uses a solver with a cutback limit per time increment, adjusting calculations as needed for convergence. In practice, this results in high numbers of data points during heating cycles as material is deposited and fewer data points during cooling cycles.
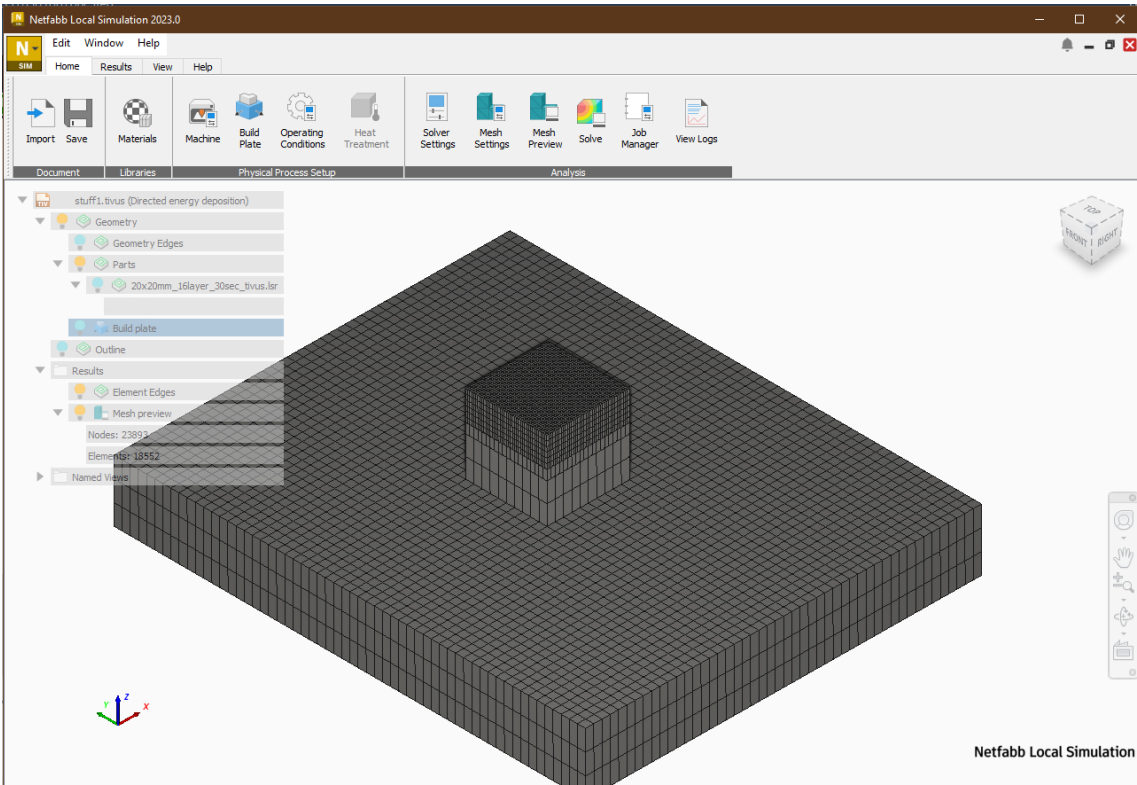
Figure 3.14: Screenshot of Netfabb Local Simulation Software.

Density	7.9 mg/m^3
Conductivty	14 W/m K (20°C)
	20 W/m K (500°C)
Emissivity	0.28 (24°C)
	0.66(949°C)
Melting Temperature	1420°C
Specific Heat	464 W/m K (20°C)
	592 W/m K (1200°C)

Table 3.6: Netfabb Stainless Steel 316L material specification.

Absorption efficiency	1% - 100%
Plate mounting	Simply Supported or Cantilevered
Thermal Conditions (plate and ambient starting temperature)	0°C - 1000°C
Coefficient of convection	5×10^{-4} $W/m^2 K$ - 200 $W/m^2 K$
Meshing elements	Elements per heat source 1 - 10
	Fine layers below 1 - 10000
	Adaptivity levels 1 - 6

Table 3.7: Netfabb configurable parameters.

Netfabb operates its simulation with a single coefficient of convection, h, which is used throughout the simulation and does not vary for material or over time. However, h varies quite significantly with temperature and as the size and surface of the part change during the deposition process.
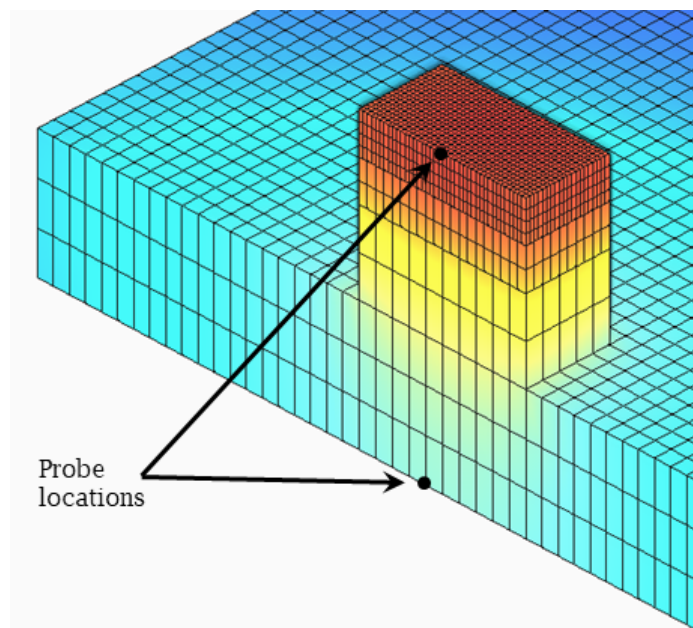
Figure 3.15: Cross section image of 16 layer cuboid simulation in Netfabb Local Simulation, showing location of temperature probes.

Chapter 4

Effect of Process Parameters on Single-Track Geometry

The characterisation of process parameters into process windows is an important first step towards understanding the macro-level dynamics of an LWAM deposition process. The subsequent characterisation of the shape of the track's cross-section and describing its geometry in terms of height and width are key pieces of information for developing a single-layer and multi-layer model. This approach is key to ensuring a range of viable parameters are available for process planning, supporting flexibility in terms of choosing different speeds for the overall deposition of a layer, energy density and layer height. This is particularly important when planning optimal process parameters for complex geometries with different thicknesses and overhangs.

4.1 Exploration of the 800W Process Window

Characterising the deposition process requires significant amounts of material and time for track measurement and analysis. Consequently, the experimental focus has been on the 800W process window, using Meltio default parameters as a baseline. The experiments in the subsequent chapters, which build on this initial work, adopt

a reductive approach, narrowing the parameter range taken forward for single-layer and multi-layer builds. Although tracks using different powers were produced during this experimental phase, they were used to understand how the process window varies with power and these tracks were not measured.

4.1.1 Initial Visual Assessment - Screening of Tracks

Tracks are first judged using a visual assessment before measuring their height and width, only tracks that meet the initial assessment of being 'Printable' are measured. A categorisation has been developed for the assessment of the single-track experiments; different terms have been deliberately chosen to those used in the literature to not confuse them with other definitions. The terms used are: Printable, Thin, Broken or No Track. Figure 4.1 shows example tracks for each of these categories. The definitions for these categories are:

Printable A high-quality track, which could be used for multi-track deposition. The track is uninterrupted and consistent along its length, characterised by a smooth surface. Its edges are clean and straight along the length of the track and is securely bonded to the substrate with a contact angle well below 90°. There are no visible ripples on the surface.

Thin A track which is not considered suitable for multi-track deposition but is still well bonded to the substrate and consistent along its length. A 'transition' classification between 'Printable' and 'Broken' tracks, where the tracks are beginning to show discontinuity or waviness due to dripping or stubbing. This classification includes tracks that are undercut (contact angle above 90°) and exhibit a cylinder-like shape.

Broken Tracks which have clear inconsistencies throughout their length, typically due to dripping or stubbing. Tracks may be partially bonded to the substrate due to more extreme dripping or stubbing and tracks could be discontinuous or could have sections of unmelted wire.

No Track This refers to track parameters where no material has fused to the substrate.
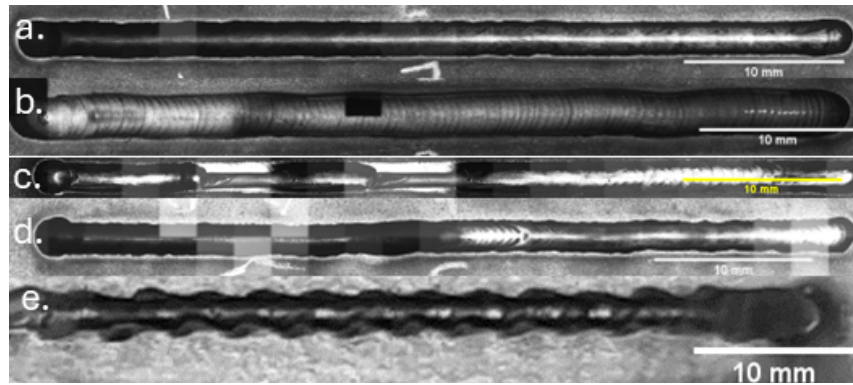
Figure 4.1: (a) Printable; (b) thin track with indications of stubbing; (c) broken track with unmelted wire; (d) broken track with stubbing; (e) broken track with dripping (all scale bars 10mm).

4.1.2 Identification of 800W Process Window

The first stage to fully characterise the process window explored combinations of extrusion rate and head speed across the machine's usable range. Tracks were created for parameter combinations between 5mm/s and 25mm/s in increments of 0.5mm/s, for combinations with a Wire Speed Factor (WSF) of one or higher. All combinations were repeated three times. The results of the track classification across the process window can be seen in Figure 4.2 and an example plate of tracks from this process can be seen in Figure 4.3. This image shows tracks across the range of classifications, with Printable tracks marked with a tick and tracks with other classifications marked with a cross.

Figure 4.4 expands on Figure 4.3, showing a successful track within the likely process window (image a), away from this region, different characteristics are seen. As the head speed increases (image b), the energy density decreases, resulting in lower wire and substrate melting causing unfused wire and inconsistent bonding with the substrate. As the head speed slows (image c) and the energy density increases, unstable wavy tracks are formed from the excessive material in the melt pool. When the extrusion rate is too slow (image d), the wire melts before it reaches the substrate, creating balling, and when the extrusion rate is too high (image e), above 15.5mm/s, there is insufficient energy to melt, resulting in stubbing.
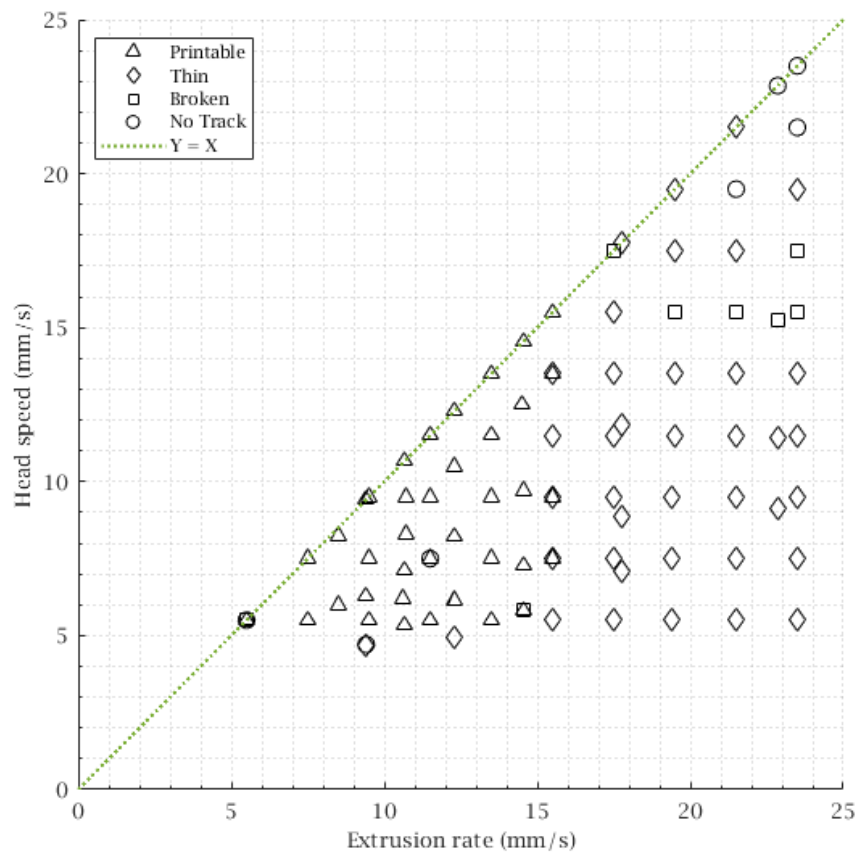
Figure 4.2: Classification of tracks printed to identify the 800W Process Window.
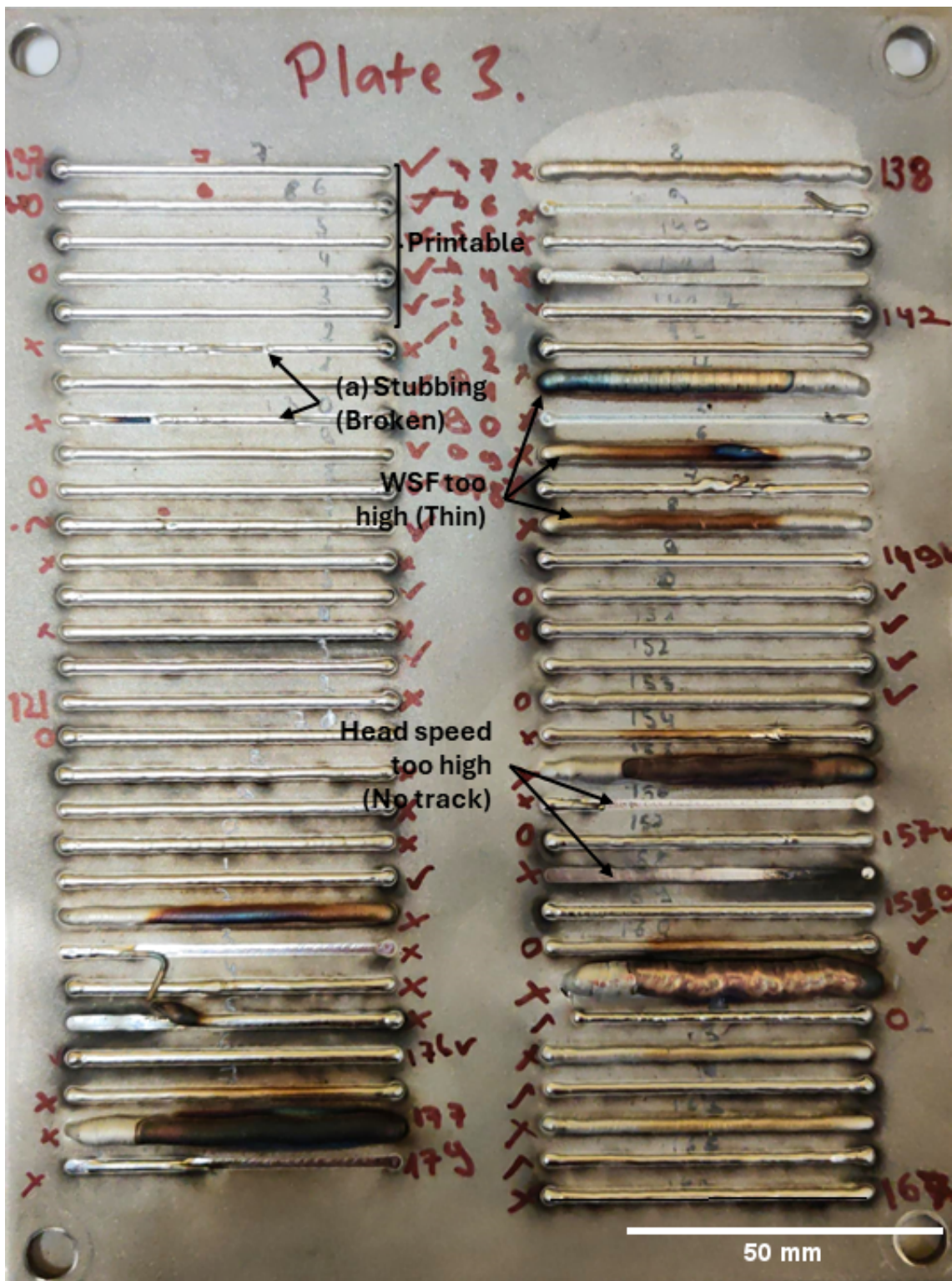
Figure 4.3: Example plate of tracks created to explore the 800W Process Window.
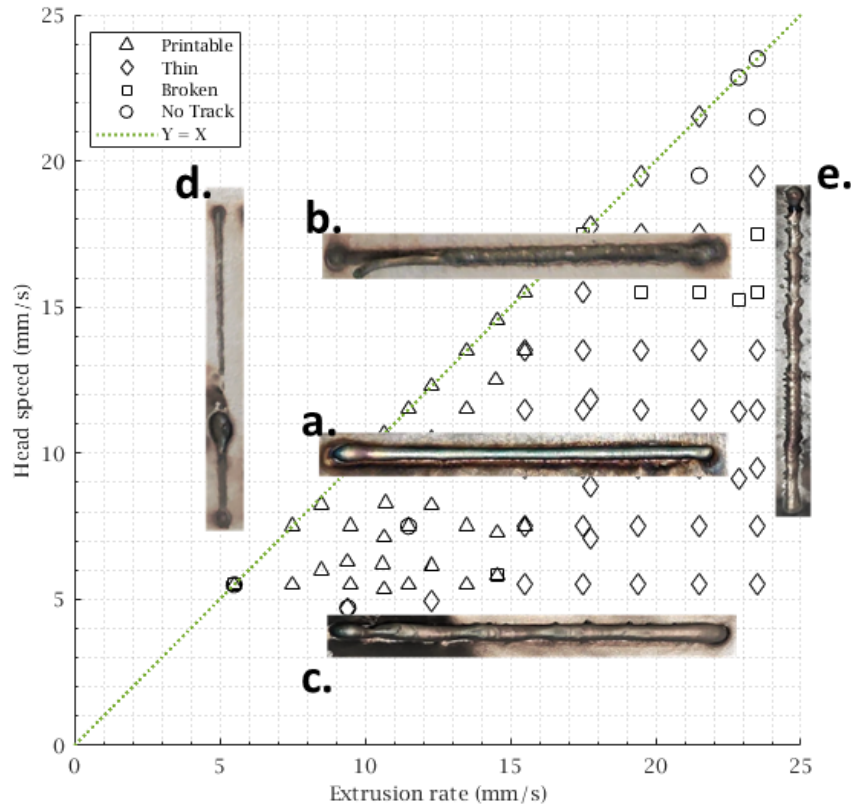
Figure 4.4: Examples of 800W track morphology in associated with different approximate locations in the process window. Showing (a) a successful track, (b) stubbing, (c) dripping and (d and e) balling.

The classification of the tracks shows that consistent tracks, which are bonded to the substrate can be produced at all extrusion rates used within the range. Tracks stop being classified as Printable at 15.5mm/s, as the volume of material becomes too high, resulting in unacceptable contact angles and increased variability in track height. Repeat tracks at 15.5mm/s extrusion rate vary between being classified as Printable or Thin across the range of head speeds used, which is similarly the case for tracks at 5.5mm/s head speed. This aligns with the 'transition zone' (Motta, Demir, and Previtali, 2018) between high-quality tracks and those that are considered poor.

These results underline the assertions regarding the energy efficiency of coaxial LWAM systems versus the more conventional radial laser LWAM systems. The process windows shown in Figure 2.8 of the Literature Review show process windows

for tracks in the power range of 1200W - 2200W, which is significantly higher power than that required for this system.

The process window for Printable tracks is generated from these data using MATLAB R2022a. The dataset is algorithmically analysed to identify the boundary that distinguishes between Printable and non-Printable parameter combinations. A boundary function is used to create an outline around these high-quality repeatable points, defining the process window for Printable tracks, shown in Figure 4.5, the boundaries for this are summarised in Table 4.1. To ensure that the process window covers only parameter combinations which reliably produce tracks that are Printable, the boundary is drawn inside the transition zone where duplicate tracks can receive different classifications.
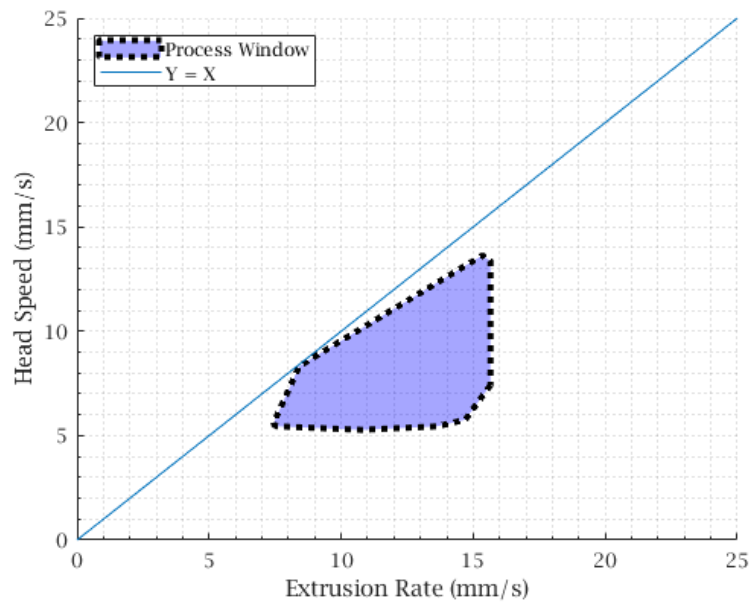
Figure 4.5: Algorithmically derived 800W process window.

Maximum Extrusion Rate	15.25mm/s
Minimum Extrusion Rate	7.5mm/s
Maximum Head Speed	13.6 mm/s
Minimum Head Speed	5.5mm/s
Maximum Wire Speed Factor	2.5
Minimum Wire Speed Factor	1

Table 4.1: 800W Process Window Boundaries.

4.1.3 Meltio M450 Default parameters

Meltio supply the M450 with a default combination of process parameters which they have empirically identified to produce repeatable high-quality tracks in 316LSi stainless steel. These are a laser power of 800W, head speed of 7.5mm/s and an extrusion rate of 11.5mm/s, creating a WSF of 1.53. These parameters can provide a useful baseline for the overall variability of the deposition process.

A set of six sample tracks were deposited using these parameters, to serve as the baseline for the process. These tracks are used for the definition of a 'Printable' track during visual assessment and, since these parameters can successfully produce multi-layer parts, define the level of acceptable variability of a track's height and width.

The six baseline tracks were deposited and measured for height and width; Figure 4.6 shows an example of a 50mm single track and Figure 4.7 its etched cross-section. Figure 4.8 shows example cross-sections of each of the tracks, taken using the OLS5000 confocal laser microscope, their mean height and width summarised in Table 4.2.
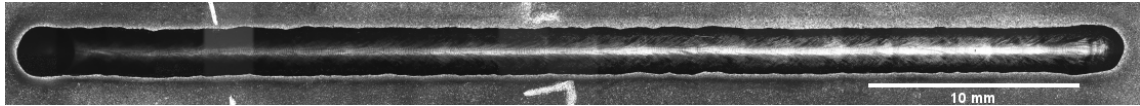
Figure 4.6: Image of example track printed using Meltio's default parameters (V_h 7.5mm/s and V_f 11.5mm/s).
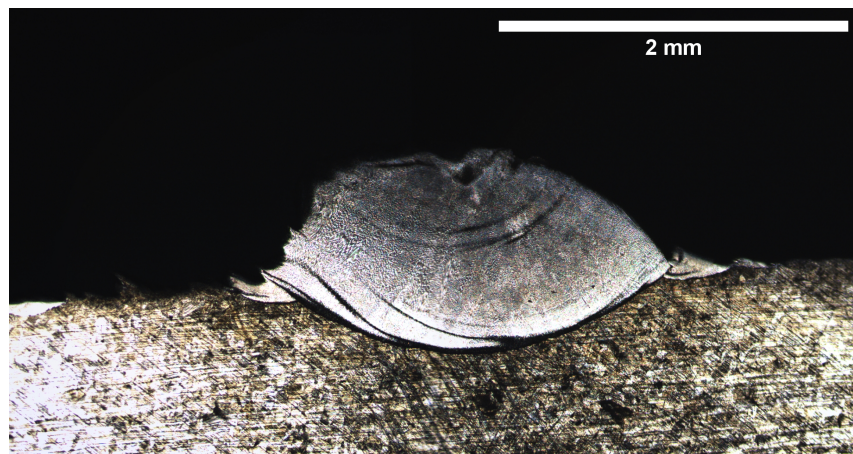
Figure 4.7: Etched cross-section of track printed using Meltio's default parameters, flaws seen in the track are due to cutting.
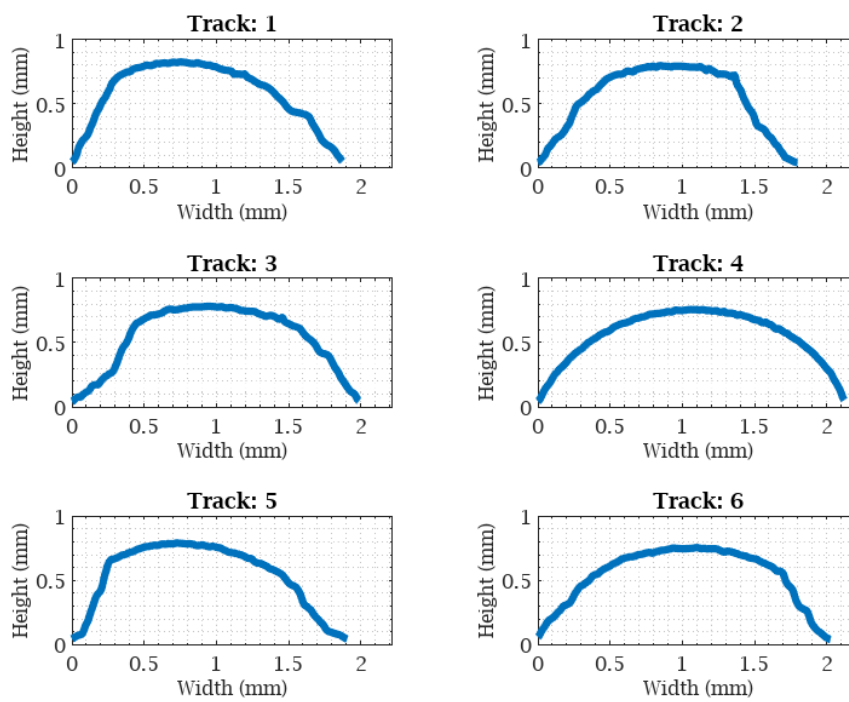
Figure 4.8: Example cross-section measurements of six tracks created with Metlio Default Parameters.

	Height (mm)	Width (mm)	Height/Width
Track 1	0.823	1.950	0.42
Track 2	0.794	1.873	0.42
Track 3	0.783	2.070	0.38
Track 4	0.757	2.210	0.34
Track 5	0.789	1.985	0.40
Track 6	0.754	2.110	0.36
Mean	0.783	2.033	
Standard Deviation	0.026	0.121	
Coefficient of Variation (%)	3.27	5.96	
Range	0.069	0.337	
Range as % of Mean	8.81	16.58	

Table 4.2: Height and width measurements of six tracks printed with Meltio's default parameters.

These data show that the height and width measurements for the tracks are consistent as a set, with slightly less variability in height than in width measurements. The top-down nature of the microscope measurements prevent detection of undercutting at the track edges; however, all contact angles are well below 90°and visual assessment of the track did not identify any undercutting. The contact angle of the etched cross-section is estimated to be 56°, with a dilution (Equation 2.9) of 38%. This level of dilution exceeds the suggested optimum of between 10% and 30% (Dass and Moridi, 2019). The track geometry is comparable to the tracks shown in F. Liu et al. (2022), who used a coaxial system, suggesting that this geometry is acceptable for a coaxial laser energy source; the track is well bonded to the substrate and the track height is sufficiently high to create a layer.

The track dimensions are consistent across the set, but the cross-sections and track images show variation in shape, deviating from a regular cross-section, which is typical of the process and forms the baseline for acceptable track variability.

4.1.3.1 Isolating Individual Variables to Determine Track Geometry

To investigate the effects of varying the individual parameters, the extrusion rate was fixed at 11.5mm/s and head speeds from the machine's minimum of 5.5mm/s up to 11.5mm/s were used, increasing in 1mm/s increments. Head speeds above this were excluded to prevent broken tracks, as the WSF would fall below unity, where the head is moving faster than the material extruded. Subsequently, the head speed was fixed at 7.5mm/s and the extrusion rates varied from 7.5mm/s, to the maximum extruder speed of 25mm/s

Dimensions for tracks classified as 'Printable' with fixed extrusion rate are plotted in Figure 4.9 and summarised in Table 4.3; Printable tracks with fixed head speed are plotted in Figure 4.10 and summarised in Table 4.4. Tracks printed with a fixed head speed were classified as 'Printable' up to an extrusion rate of 15mm/s, and beyond this speed, tracks were classified as 'Thin'. As the WSF increased above 2, the additional material produced large variable tracks with high contact angles, shown in image b of Figure 4.1.
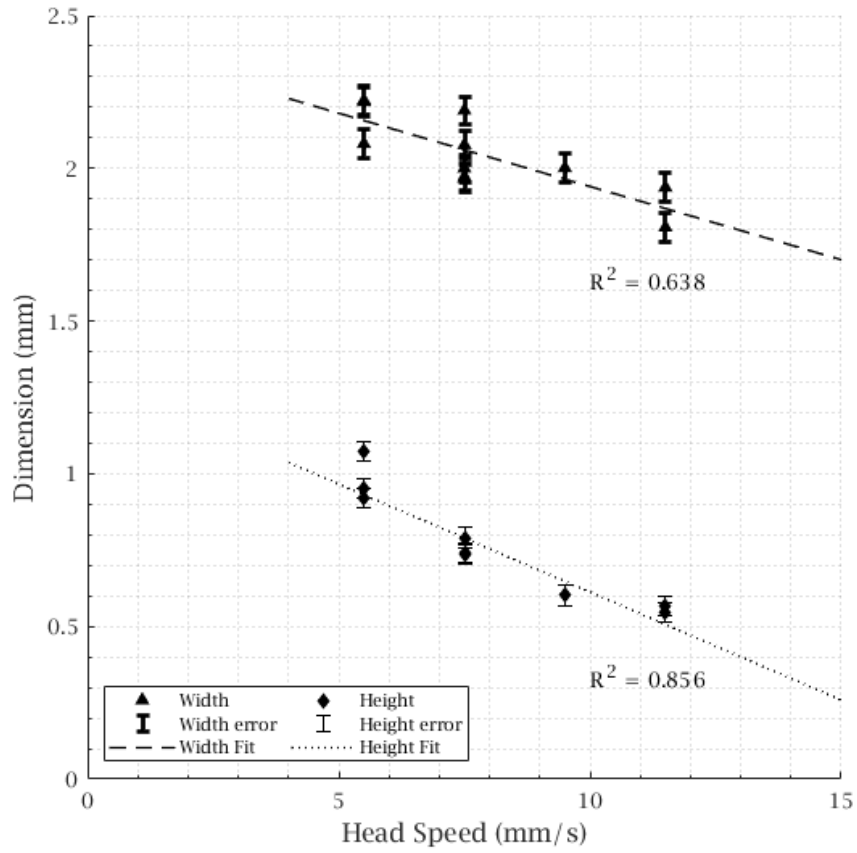
Figure 4.9: Track height and width measurements versus head speed, for a fixed extrusion rate of 11.5mm/s.

Head Speed (mm/s)	WSF	Width (mm)	Height (mm)	Contact Angle (degrees)
5.5	2.09	2.22	0.95	39
7.5	1.53	2.19	0.74	54
9.5	1.21	2.00	0.60	50
11.5	1	1.81	0.55	50

Table 4.3: Track measurements for a fixed extrusion rate of 11.5mm/s.
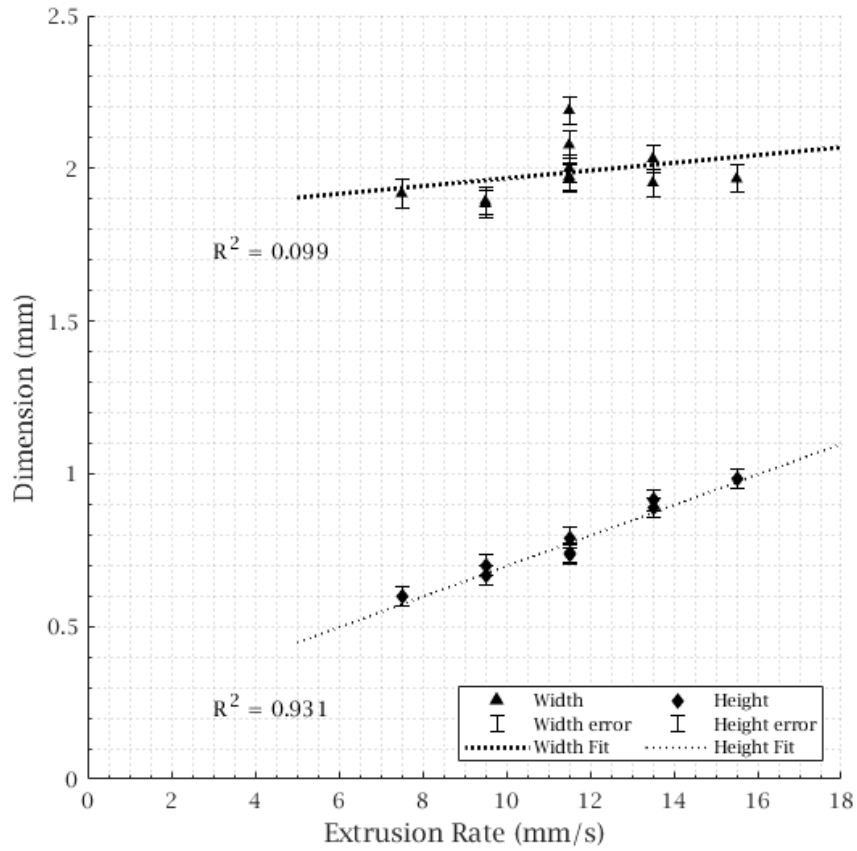
Figure 4.10: Track height and width measurements versus extrusion rate, for a fixed head speed of 7.5mm/s.

Extrusion Rate (mm/s)	WSF	Width (mm)	Height (mm)	Contact Angle (degrees)
7.5	1	1.918	0.6	51
9.5	1.27	1.884	0.701	55
11.5	1.53	2.03	0.783	56
13.5	1.8	1.992	0.901	61
15.5	2.07	1.966	0.983	43

Table 4.4: Track measurements for a fixed head speed of 7.5mm/s.

These data show that when other parameters remain constant, increasing the head speed reduces the track height, whereas increasing the extrusion rate raises it, resulting in high values of R^2 shown in the linear fit lines. This is consistent with the volume conservation described in Equation 2.2, a decreasing WSF results in a decreased cross-sectional area. The relationship between the process parameters and the track width is weaker. The maximum track width is limited by the laser spot size, additional material from an increased extrusion rate cannot go wider than the laser spot width making the track height grow. Decreasing the extrusion rate reduces the volume of material deposited, which consequently reduces the amount of material to melt, increases the heat in the melt pool and increasing wetting, as shown by Oliari, D'Oliveira, and Schulz (2017), creating a wider and flatter track. Therefore, changes in head speed have more of an effect on width, increasing head speed narrows the size of the melt pool and as the energy density is reduced, a narrower track is created.

This effect is also shown in the aspect ratio of the track ($height/width$) versus head speed and extrusion rate, Figures 4.11 and 4.12 respectively. As the head speed increases, the aspect ratio decreases. In contrast, as the extrusion rate increases, the aspect ratio increases. The aspect ratio reflects the relative height of the track compared to its width; a higher ratio implies a taller and narrower track. Therefore, modifying the head speed changes the shape of the track, becoming wider relative to its height as the speed increases and taller relative to its width as the extrusion rate increases.
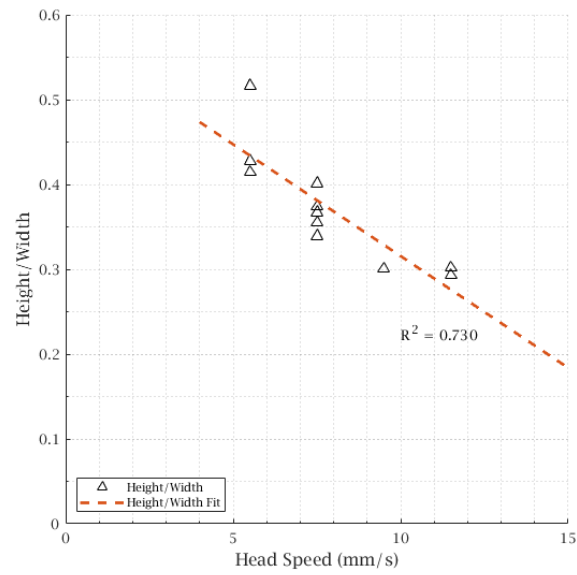
Figure 4.11: Aspect ratio of track versus head speed, for a fixed extrusion rate 11.5mm/s.
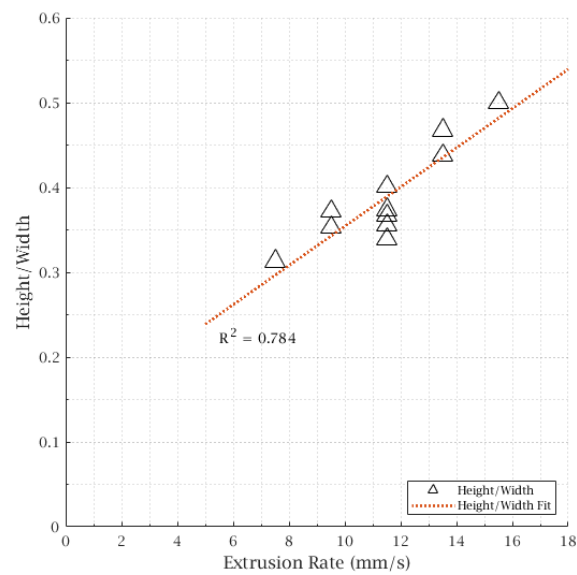
Figure 4.12: Aspect ratio of track versus extrusion rate, for a fixed head speed of 7.5mm/s.

To confirm these findings an experiment was conducted using a fixed WSF of 1.53 and first varying the extrusion rate and head speed combinations and, secondly using the same head speed and extrusion rate, varying the laser power. The parameter combinations and track measurements are summarised in Tables 4.5 and 4.6; these data are plotted in Figures 4.13 and 4.14 for the varied head speed and extrusion rate with a fixed WSF and Figures 4.15 and 4.16 for the Fixed WSF with varied power.

Head Speed (mm/s)	Extrusion Rate (mm/s)	Height (mm)	Width (mm)	Area (mm^2)	Height / Width
5.50	8.40	0.75	2.29	1.35	0.33
7.50	11.46	0.78	2.10	1.29	0.37
7.50	11.46	0.78	2.11	1.29	0.37
7.50	11.46	0.78	2.04	1.25	0.38
8.83	13.50	0.81	2.02	1.29	0.40
9.50	14.51	0.81	2.01	1.28	0.41
10.00	15.28	0.82	1.96	1.27	0.42
12.50	19.06	0.82	1.88	1.22	0.44

Table 4.5: Process parameters and measured track dimensions for a fixed WSF of 1.53 and fixed Power of 800W.

Power	Height (mm)	Width (mm)	Area (mm^2)	Height/ Width
800	0.78	2.10	1.29	0.37
650	0.85	1.86	1.24	0.46
950	0.73	2.36	1.36	0.31
800	0.78	2.11	1.29	0.37
800	0.78	2.04	1.25	0.38
700	0.83	1.94	1.26	0.43
600	0.89	1.75	1.22	0.51

Table 4.6: Process parameters and measured track dimensions for a fixed extrusion rate of 7.5mmm/s and extrusion rate of 11.5mm/s (WSF of 1.53) and varied powers.
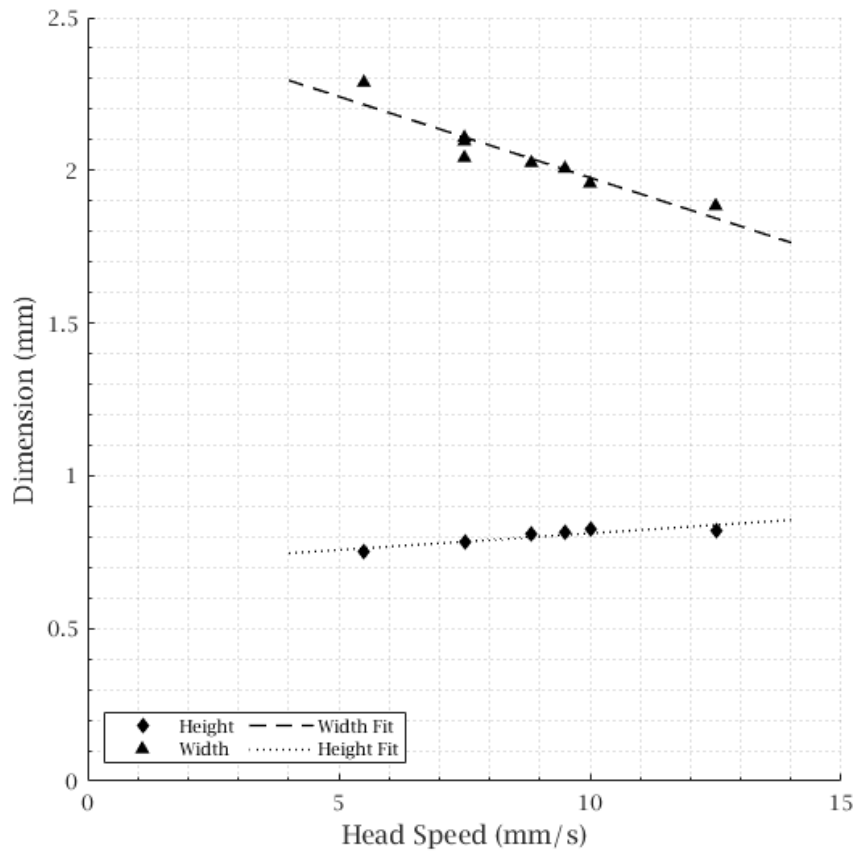
Figure 4.13: Track height and width versus head speed for fixed WSF 800W tracks.
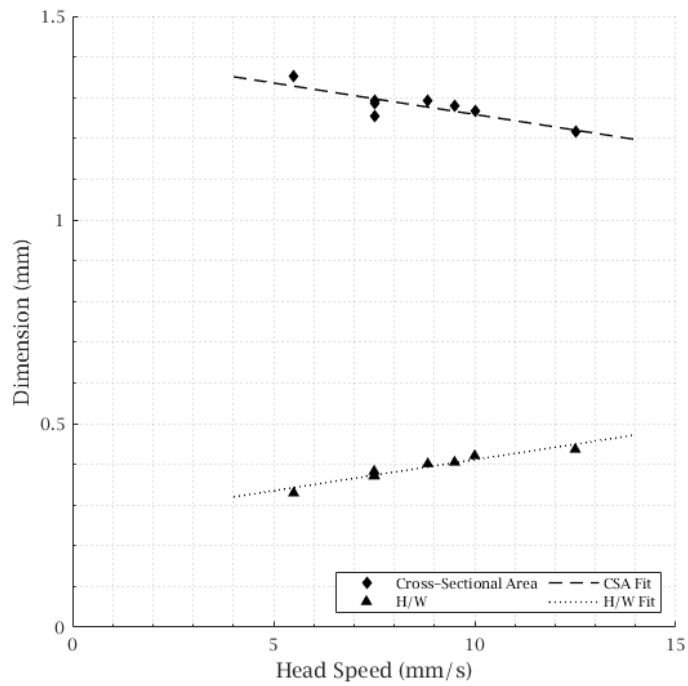
Figure 4.14: Track cross-section area and height:width versus head speed for fixed WSF 800W tracks.
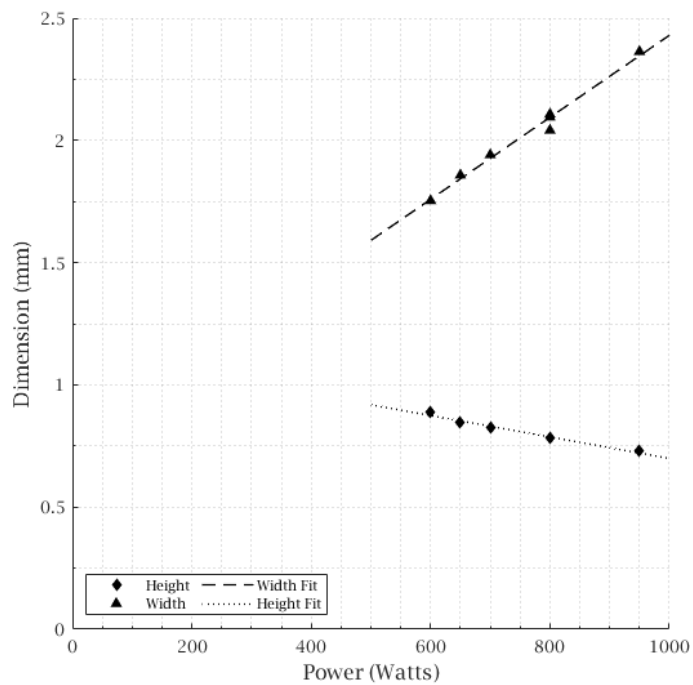
Figure 4.15: Track height and width versus laser power for fixed WSF tracks.
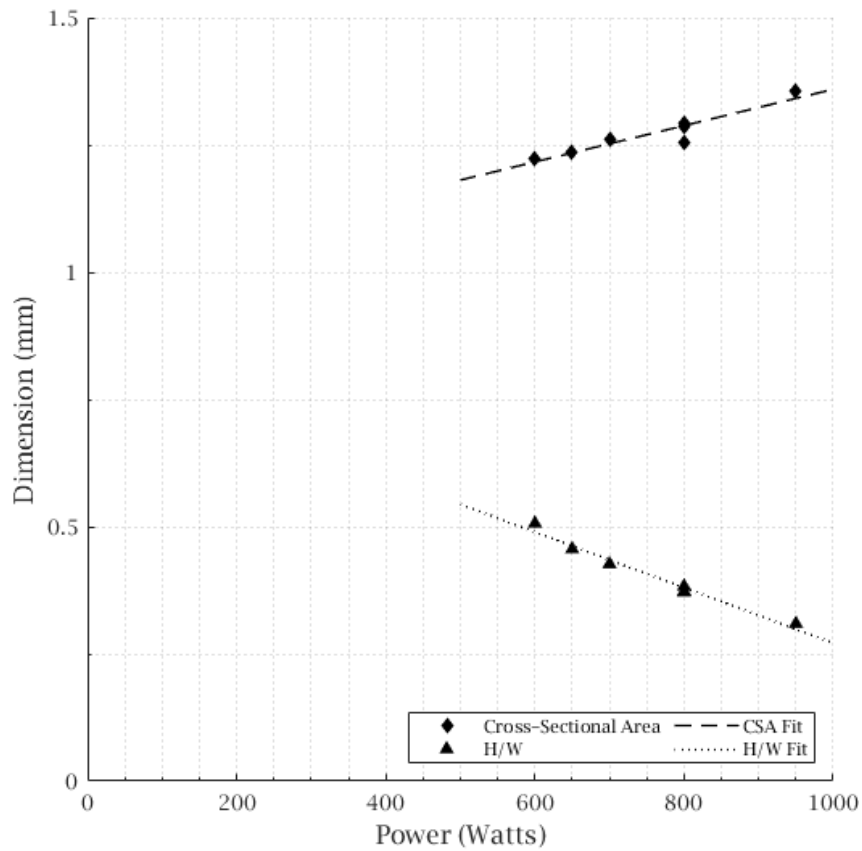
Figure 4.16: Track cross-section area and height:width versus laser power for fixed WSF tracks.

By isolating the WSF and hence the mass flow into the tracks, these data support the observations that increases in head speed reduce the track width and the overall cross-sectional area of the track. As the laser power is increased, it can be seen to have a significant effect on the track width as track wetting increases, consequently reducing the height, supporting the observations made by Oliari, D'Oliveira, and Schulz (2017).

4.2 Numerical Model of Track Geometry

Track height and width for all Printable 800W tracks are plotted against WSF in Figure 4.17. It supports the observations seen previously for fixed head speed and extrusion rates, showing a strong relationship between increasing WSF and track height and a much weaker relationship with track width. Figure 4.18 shows these height data with the coefficients for the best-fit line, allowing the height, h_t, to be estimated from the WSF, described in Equation 4.1.
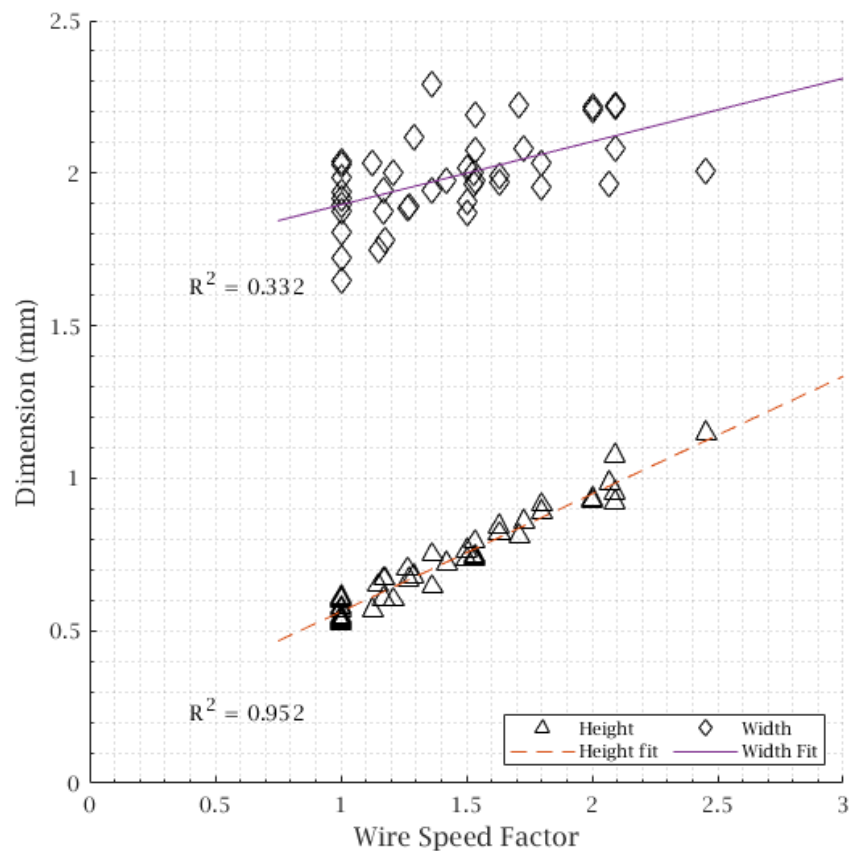
Figure 4.17: Track height and width versus WSF for all the Printable 800W tracks.
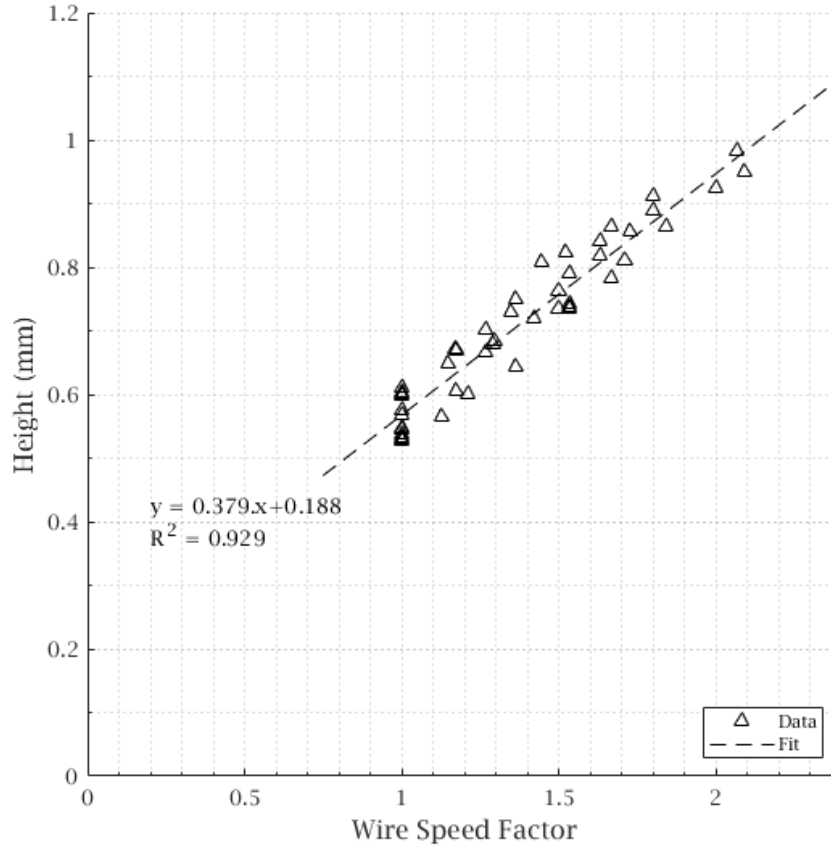
Figure 4.18: Track height versus WSF with beset fit line for all the Printable 800W tracks.

$$h_t \approx 0.38 \times WSF + 0.19 \tag{4.1}$$

The relationship between WSF and the cross-sectional area of the track is shown in Figure 4.19, which plots the *height* $\times$ *width* versus the WSF. This shows a linear relationship between the two, the results aligning closely to a $y = x$ line of equality, represented in Equation 4.2. The calculation of the cross-sectional area of the track is described in Equation 4.3, where x is the shape factor of the cross-section and d the diameter of the wire, if it were a semi-ellipse $x = \pi/4$ or a parabola $x = 2/3$.

$$h_t \times w_t = \frac{v_f}{v_h} \tag{4.2}$$
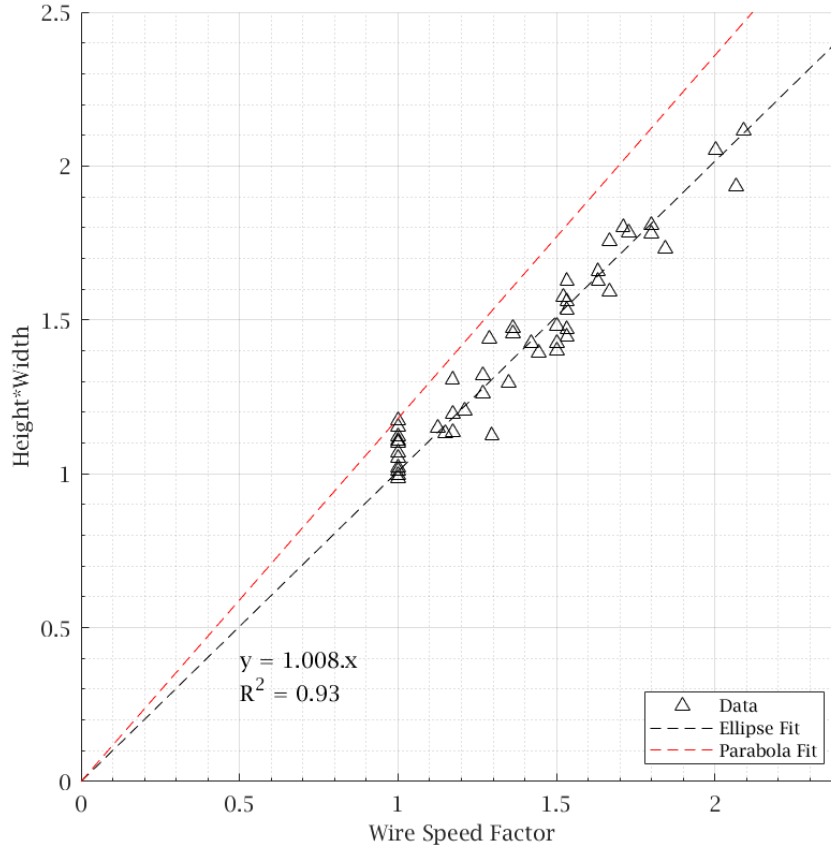
Figure 4.19: $Height \times Width$ versus WSF with fits for semi-ellipse and parabola track shapes.

$$h_t \times w_t \times \frac{\pi}{4} = \frac{v_f}{v_h} \times x \times d^2 \tag{4.3}$$

As the diameter of the wire is 1mm, d can be removed from the equation. Therefore, this would imply that if the experimental data showed a semi-elliptical shape for the track, a plot of $height \times width$ versus the WSF would align to a line of equality for a semi-ellipse or to a line with a gradient of 1.18 for a parabolic shape. Both fit lines are plotted in Figure 4.19 and show a fit to a semi-elliptical shape.

The two Equations 4.1 and 4.3 allow an approximation of the track height to be made for the 800W process parameters, within the process window defined in Figure 4.5. Figures 4.17, 4.18 and 4.19 show a number of tracks printed at a WSF of 1 and 1.53 (Meltio baseline tracks), which should all have the same height and

width results from these equations; however, the plots show various track geometries. Tracks with a WSF of one have varied head speeds and extrusion rates and have a spread of height measurements of 0.08mm and a spread of width measurements of 0.39mm. When considering the R^2 of 0.952 for the fit of the track height, most of the variability shown therefore comes from the measurement of the track width. Therefore, both sets of fixed WSF are within the range of the variability of the baseline process (16. 6% of the measured value for width and 8.8% for height).

The causes of variability in the process remain unexplained and are particularly associated with the width of the track, which reduces the overall accuracy of the prediction of the geometry of the track. There are likely to be many sources causing this variability and to characterise these further requires further research, as there is little in the literature relevant to this process. Sources of this variability may include measurement accuracy, varying energy density due to changes in head speed, plate surface quality and temperature, machine tolerances, cooling rates, atmospheric conditions, consistency of shielding gas flow, laser stability and health of the laser system (Suryakumar et al., 2011; Zapata et al., 2022).

4.2.1 Determination of Cross-Section Shape

A description of the cross-sectional shape of the track is required to calculate its cross-sectional area, allowing the optimal overlap of the tracks to be determined for a single layer and the likely height of the layer to be predicted.

To determine which shape fits the experimental data more closely, the equivalents of a semi-ellipse and parabola were calculated for all 800W tracks measured using the height and width of the track. To compare the fit of each shape the Residual Sum of Squares (RSS) was calculated. The equation for calculating RSS is shown in Equation 4.4, where y_{CSA} is the curve that describes the actual cross-sectional area of the track and $f(x)$ the parabola or semi-ellipse curve.

Tracks were characterised as either a semi-ellipse or parabola based on which had the lower RSS value. The cross sections were also visually checked to confirm this.

This resulted in 71% of the tracks being classified as a semi-ellipse. This supports the results shown in Figure 4.19, where *height* $\times$ *width* align to a line of equality.

A sample of six of the track cross-sections compared to their equivalent semi-ellipse and parabola is shown in Figure 4.20, the calculated RSS and subsequent classifications are summarised in Table 4.7. The single-layer model developed in the following chapter therefore assumes a semi-ellipse track cross-section.

$$RSS = \sum_{i=1}^{n}(y_{CSA,i} - f(x_i))^2 \qquad (4.4)$$
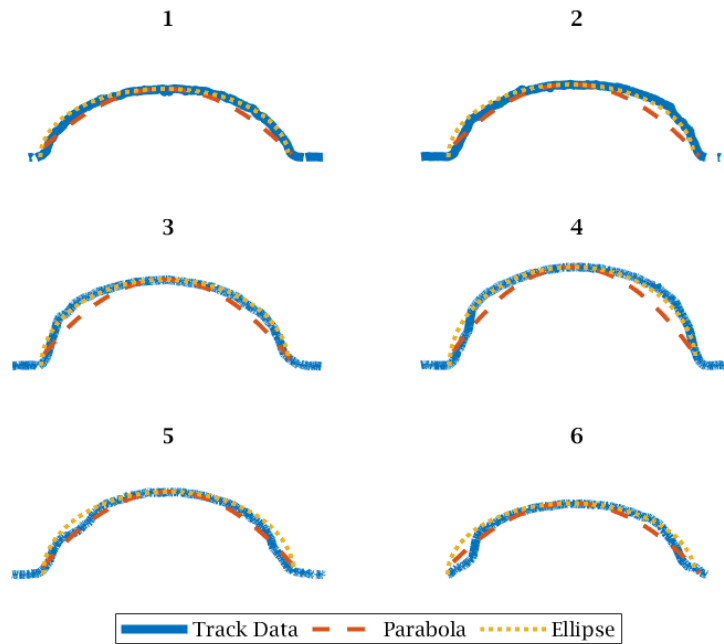
Figure 4.20: Example track cross-sections compared to their equivalent parabola and semi-ellipse.

ID	Head Speed (mm/s)	Extrusion Rate (mm/s)	Track Height (mm)	Track Width (mm)	Contact angle (degrees)	RSS (Parabola)	RSS (Ellipse)	Classification
1	9.5	9.5	0.59	2.08	47	1.24E+06	4.28E+05	Ellipse
2	7.5	7.5	0.60	1.99	51	1.19E+06	4.96E+06	Parabola
3	13.5	15.5	0.65	1.75	39	7.58E+05	6.47E+05	Ellipse
4	19.5	23.5	0.75	1.54	38	2.02E+06	5.72E+06	Parabola
5	7.5	9.5	0.71	1.92	53	4.24E+06	1.43E+06	Ellipse
6	8.3	10.7	0.68	2.12	49	2.45E+06	1.79E+06	Ellipse

Table 4.7: Track cross-section measurements, evaluated for their fit to an equivalent parabola or semi-ellipse.

4.3 Machine Learning Derived Process Window

Given the variability in the data, particularly with respect to track width measurements and the experimental overhead in determining the process parameters for a single laser power, Machine Learning (ML) tools were investigated. The objective of this investigation was to determine whether these tools could be used to predict process windows for a wider range of powers than those examined experimentally.

To support this objective, a limited number of additional tracks were also created for 550W, 750W and 950W, their process windows shown in Figures 4.21, 4.22 and 4.23 and their boundaries summarised in Tables 4.8 and 4.9. These plots show that as the laser power is reduced, the viable range of parameters decreases as a result of the reduced energy density of the process. Counterintuitively, this window appears to sit at higher extrusion rates but with decreasing head speeds, around a WSF of two, rather than closer to a WSF of one where less material is being extruded to melt. The data available for 950W was limited; however, at this power it is possible to produce thin tracks, but very few that meet the definition of Printable; consequently, no process window is drawn for this power.
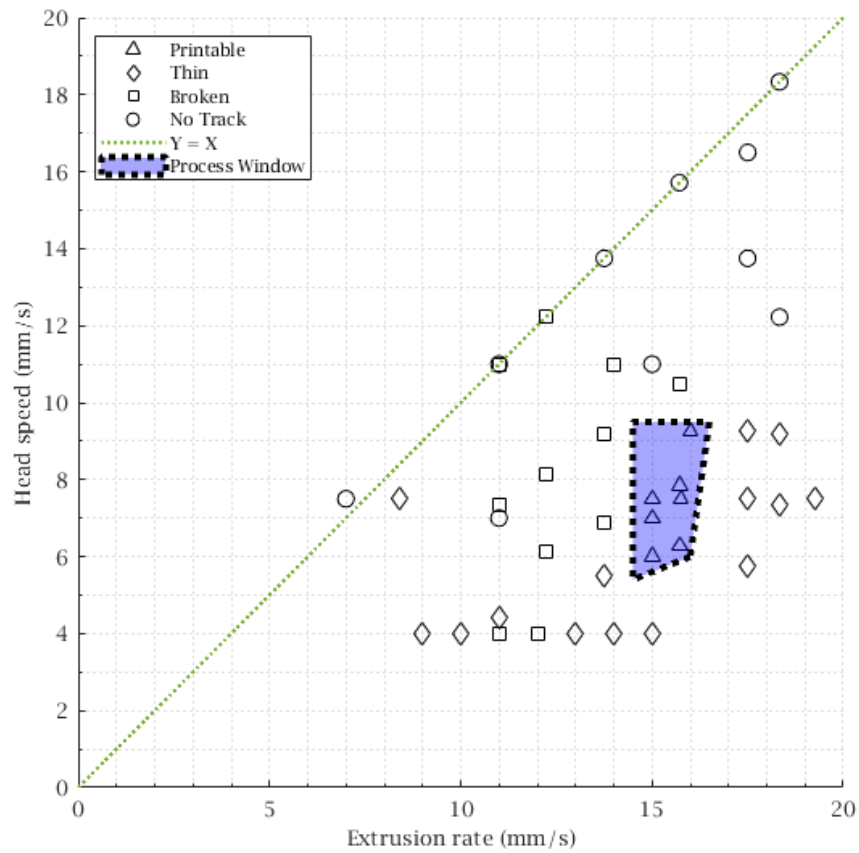
Figure 4.21: 550W track classification and process window.

Maximum Extrusion Rate	16.5mm/s
Minimum Extrusion Rate	14.5mm/s
Maximum Head Speed	9.5mm/s
Minimum Head Speed	5.4 mm/s
Maximum Wire Speed factor	2.75
Minimum Wire Speed factor	1.5

Table 4.8: 550W Process Window Boundaries.
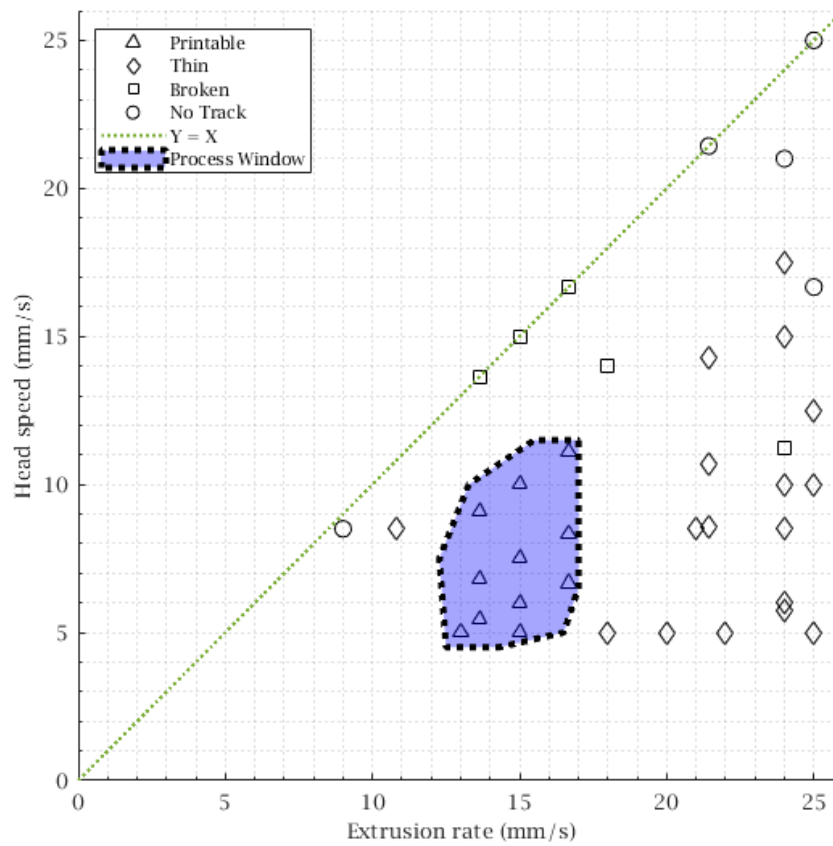
Figure 4.22: 750W track classification and process window.

Maximum Extrusion Rate	16.7mm/s
Minimum Extrusion Rate	12.2mm/s
Maximum Head Speed	11.1mm/s
Minimum Head Speed	5 mm/s
Maximum Wire Speed factor	3
Minimum Wire Speed factor	1.5

Table 4.9: 750W Process Window Boundaries.

Figure 4.23: 950W track classification.

4.3.1 Machine Learning Prediction of Visual Track Assessment

To predict the outcome of the visual assessment of the quality of the track, a predictive classification ensemble was found to be the most accurate, showing approximately 90% accuracy of its prediction of the validation data prior to optimisation of hyperparameters. The performance of the architectures evaluated at this initial stage is shown in Table 4.10. It is not possible to compare the fit or appropriateness of this network architecture type with the literature, as this stage of network architecture selection is typically omitted from published work. This is likely because network architectures can have a wide variety of performance based on the specifics of the data used in each case.

A Predictive Classification Ensemble is a supervised learning algorithm used primarily for classification problems, making it particularly suitable for this kind of classification. A classification ensemble is made up of a weighted combination of multiple classification models, which increases predictive performance and flexibility. Predictive Classification Ensemble work by identifying a hyperplane with the

maximum possible margin that best separates data into classes (*Machine Learning with MATLAB* 2022). The optimal configuration of hyperparameters is summarised in Table 4.11, input data was normalised by the MatLab function but not scaled (i.e. not scaled to have a mean of zero and a standard deviation of one).

Model Architecture	Accuracy (Validation)
Optimisable Tree	90%
Bagged Trees	88%
Support Vector Machine	87%
Neural Network	86%
Fine Tree	85%
Medium Tree	85%
Fine KNN	85%
Cubic KNN	83%
Weighted KNN	83%
Optimisable Discriminant	82%
Naïve Bayes	82%
Medium KNN	81%
Logistic Regression	80%
Coarse KNN	78%
Cosine KNN	78%
Logistic Regression Kernel	78%
Coarse Tree	76%

Table 4.10: Comparison of the performance of ML network architectures for prediction of visual track assessment.

Model Property	Value
MinParent	2
MinLeaf	1
MaxSplits	23
NVarToSample	10
MergeLeaves	off
Prune	off
Version	3
Method	Tree
Type	Classification
Nlearn	12
LearnRate	1
Default Score	0
Method	Bag
Type	Classification
NumObservations	121
Prior	[0.5867,0.4132]
Cost	[0,1;1,0]
ScoreTransform	None
FitInfoDescription	None
NumTrained	12
CombineWeights	WeightedAverage
Fresample	1
Replace	1

Table 4.11: Optimised hyperparameters for Predictive Classification Ensemble network.

To further improve the accuracy of the training data, augmentation was used to duplicate and add the original data set back onto itself. A training algorithm was created to iteratively train networks with the above hyperparameter configuration, while successively switching in and out different training parameters to identify whether the full set of training data was optimum for accuracy. For all iterations, head speed, extrusion rate and WSF were included as training parameters, combinations of other key process information were changed in and out and their accuracy compared, summarised in Table 4.12. It was found that there was little difference for many of the combinations of training data in terms of accuracy or fit; however, using no additional parameters or all of them was found to reduce the accuracy of the network. The ID 6 combination was selected for the final network as it contained the most parameters that characterise the material properties, which is anticipated to make the network more portable should it be used to predict the performance of other alloys, and it was also the best performing combination of parameters for the track geometry network, reducing the complexity of managing the dataset.

The network was trained using all the experimental data available, including observations made with powers other than 800W, provided in Appendix B. However, experimental data for the 750W tracks were excluded, to examine how accurately the network could predict the outcome of tracks for which it had not been trained. Figure 4.24 compares the process windows determined by the network with those determined algorithmically from the experimental data, the window properties are compared in Table 4.13.

ID	$\frac{P}{V_f}$	$\frac{P}{V_h}$	Energy Per Unit Length	Fourier No	Heat to Melt	Energy Density	% Correct	R^2
1	FALSE	FALSE	FALSE	TRUE	FALSE	FALSE	0.981	0.920
2	TRUE	FALSE	TRUE	FALSE	TRUE	FALSE	0.981	0.916
3	TRUE	TRUE	FALSE	FALSE	FALSE	TRUE	0.981	0.916
4	TRUE	TRUE	TRUE	FALSE	FALSE	FALSE	0.981	0.913
5	FALSE	TRUE	TRUE	FALSE	FALSE	FALSE	0.981	0.910
6	FALSE	TRUE	TRUE	TRUE	TRUE	TRUE	0.981	0.910
7	TRUE	TRUE	TRUE	TRUE	TRUE	TRUE	0.962	0.836
8	FALSE	FALSE	FALSE	FALSE	FALSE	FALSE	0.868	0.394

Table 4.12: Results from assessment of successively switching in and out different training parameters on network accuracy.
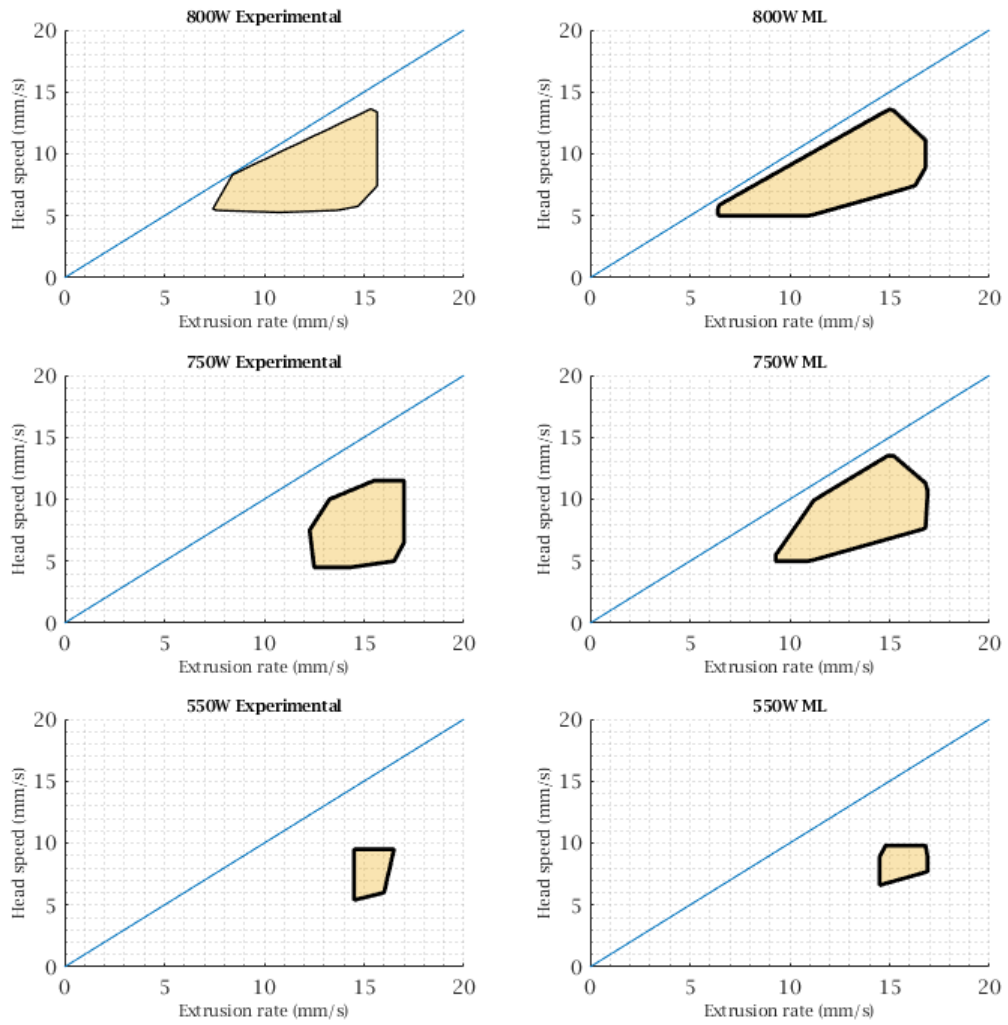
Figure 4.24: ML predicted process windows compared to those seen experimentally.

	800W		750W		550W	
	Experiment	ML	Experiment	ML	Experiment	ML
Maximum Extrusion Rate (mm/s)	15.6	16.8	16.8	16.9	16.5	16.8
Minimum Extrusion Rate (mm/s)	7.5	6.4	12.9	9.3	14.5	14.5
Maximum Head Speed (mm/s)	13.6	13.6	16.5	13.5	9.5	9.8
Minimum Head Speed (mm/s)	5.5	5	5	5	5.4	6.6
Maximum Wire Speed factor	<2.5	2.2	3.1	2.2	<2.75	2.2
Minimum Wire Speed factor	>1	1.1	1.5	1.1	>1.5	1.5

Table 4.13: Comparison of ML and experimental process window boundaries.

These data show that the model has predicted process windows for the 550W and 800W data, showing that it is capable of interpreting the training data well. The window predicted for 750W is more conservative in terms of the maximum WSF, which comes from the maximum predicted extrusion rate with the lowest anticipated head speed, the bottom right-hand corner of the process window. At the other extreme, the ML process window predicts a lower minimum WSF than seen experimentally in the bottom left corner of the window. Although the windows do not completely align with the experimentally derived window, they overlap well and are transitioning to a smaller window from 800W to the 550W and would serve as a starting point to steer a reduced experimental investigation.

4.3.2   Machine Learning Prediction of Track Geometry

For predicting track geometry, a Cascade Forward Network architecture was identified as having the best performance during the initial comparison of architecture types, with a Root Mean Square Error (RMSE) of 0.036 for the predictions of the test data using an unoptimised network. The performance of the network compared to the others assessed is summarised in Table 4.14.

A Cascade Forward Network is a form of feed forward artificial neural network where each neuron has connections to every subsequent layer, creating a "cascade"

of information flow that includes not just the outputs from the previous layer but also from all preceding layers. This structure extends the layer interaction within the network, which can be particularly beneficial for capturing complex patterns in data.

Custom code was written to iteratively explore both the number of layers and the number of nodes in each layer. The networks were trained with one to four layers and between one and twenty nodes in each layer. Three architectures had similar performance: a three-layer network with 3, 10 and 7 nodes in its layers or a two-layer network with layers containing 4 and 16 nodes or 9 and 11 nodes. Although they had similar accuracies, the two-layer network of 9 and 11 nodes was used, as simpler networks are less prone to overfitting and hence better at generalisation.

A range of transfer functions can be used for each of the layers, the default hyperbolic tangent sigmoid functions in the first hidden layer and a linear transfer function for the second proved to be most effective. Training was limited to 200 epochs, which defines how many times the learning algorithm will work through the entire training dataset, allowing sufficient training for the network to converge to an optimal set of weights for each node. The network performed more accurately without scaling or normalisation, but the training data were augmented in the same manner as the track quality prediction network, providing a training data set of 148 measurements. As with the visual assessment network, a training algorithm was created to iteratively train networks, switching in and out different training parameters to identify whether the entire set of training data was optimum; the five highest performing combinations are summarised in Table 4.15, the highest performing combination was used.

Model Architecture	RMSE
Cascade Forward Network	0.035
Quadratic SVM	0.036
Exponential GPR	0.038
Matern 5/2 GPR	0.038
Narrow Neural Network	0.038
Rational Quadratic Gaussian Process Regression (GPR)	0.039
Coarse Gaussian SVM	0.042
Cubic SVM	0.047
Fine Tree	0.054
Medium Tree	0.054
Boosted Trees	0.055
Bagged Trees	0.056
Medium Gaussian SVM	0.079
Narrow Neural Network	0.084
Coarse Tree	0.088
Medium Neural Network	0.107
Fine Gaussian SVM	0.109
Linear SVM	0.127
SVM Kernel	0.159
Wide Neural Network	0.237
Fine Tree	0.605
Linear Regression	11.61

Table 4.14: Comparison of the performance of ML network architectures for geometry prediction.

ID	$\frac{P}{V_f}$	$\frac{P}{V_h}$	Energy Per Unit Length	Fourier No	Heat to Melt	Energy Density	R^2
1	FALSE	TRUE	FALSE	FALSE	TRUE	TRUE	0.845
2	TRUE	TRUE	TRUE	TRUE	TRUE	TRUE	0.831
3	TRUE	TRUE	FALSE	FALSE	FALSE	TRUE	0.824
4	TRUE	FALSE	TRUE	FALSE	TRUE	FALSE	0.785
5	FALSE	FALSE	FALSE	TRUE	FALSE	FALSE	0.752

Table 4.15: Results from assessment of successively switching in and out different training parameters on network accuracy.

Track geometry measurements taken for 800W Printable tracks were used to train the, the data is provided in Appendix C. To test the network, 15% of the experimental data was randomly selected and removed from the training and validation data. These test data were used to assess the accuracy of the ML trained network. The predicted height and widths for the same test data were calculated using Equations 4.1 and 4.3, which were calculated from the line fit polynomials taken from the experimental results. The results of the predictions, ordered by WSF are shown in Table 4.16 and Figure 4.25.

The polynomial-based prediction of height shows a good fit, with a slightly better performance than the ML model. The accuracy of the width prediction is much weaker, discussed in the previous section, the variability of the data is not well accounted for in the polynomial; the ML model is able to overcome this limitation and predict the width of the tracks with much higher accuracy. This is likely because of the model's ability to make additional inferences between the process parameters and the track dimensions through the additional dimensionality created by the network's data processing. Therefore, it can infer connections between training data and responses that have not been detected in the analysis to create the polynomial.

The literature review found little published on the strength of ML tools to reduce the effects of process variation in this discipline, or to support the process characterisation of coaxial systems. This result shows a useful application of ML tools to provide insight and additional accuracy when characterising the process window, mitigating the effects of process variation and the experimental burden of characterising it.
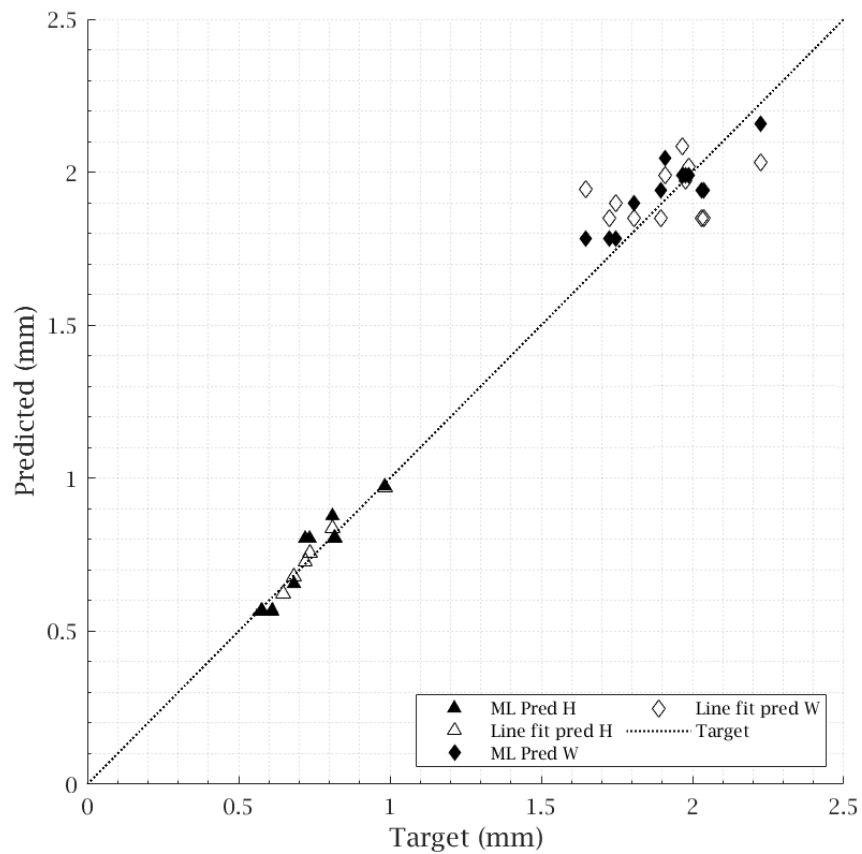
Figure 4.25: Comparison of ML predicted track height and width accuracy versus experimentally derived polynomial.

Head Speed (mm/s)	Extrusion Rate (mm/s)	WSF	Measured Width (mm)	Measured Height (mm)	Polynomial Width (mm)	Polynomial Height (mm)	ML Width (mm)	ML Height (mm)
9.4	9.4	1	1.897	0.533	1.849	0.568	1.939	0.566
13.5	13.5	1	1.724	0.610	1.849	0.568	1.785	0.566
13.5	15.5	1.15	1.746	0.648	1.900	0.624	1.785	0.566
13.5	17.5	1.30	1.646	0.683	1.943	0.679	1.785	0.655
9.5	13.5	1.42	1.976	0.720	1.974	0.726	1.990	0.804
8.2	12.3	1.50	1.908	0.734	1.991	0.756	2.045	0.804
9.5	15.5	1.63	1.989	0.818	2.017	0.805	1.990	0.804
6.2	10.6	1.71	2.224	0.810	2.032	0.835	2.159	0.877
7.5	15.5	2.07	1.966	0.983	2.085	0.969	1.990	0.974
				R^2	0.391	0.964	0.901	0.859

Table 4.16: Comparison of ML predicted track height and width versus experimentally derived polynomial.

4.4   Conclusions

The study has evaluated the process parameters at 800W and how they can create high-quality tracks. It has established a process window to determine successful combinations of parameters and an equation to estimate track height and width. The experimental data supports a semi-elliptical cross-sectional shape, which can be used when creating a single-layer model for this process. These conclusions add to the limited research published on track geometry models for coaxial systems.

A strong correlation is observed between the process parameters and the height of the track compared to the width, with a greater variability in the measured track width. The factors that determine this variability are not fully understood and could be further characterised. To counteract this, the development of an ML network for the prediction of track width improved the accuracy of the prediction. Although substantial research has been published regarding ML applications within this field, this work adds new insight into its benefits for mitigating the causes of process variability when predicting track geometries.

It was shown that the ML model could be used to interpolate the experimental results, supporting the need to reduce the experimental time and cost, by streamlining the characterisation process. A continuation of the application of the tool with the methods seen above could reduce the volume of experiments and measurements by providing information about the likely process windows, reducing the range of parameter combinations to explore.

Chapter 5

Optimisation of Single and Multi-Layer Deposition

The optimal 800W process parameters and the macro-level dynamics identified for track deposition allow the development of a single-layer model. A single-layer model supports parameter planning when slicing CAD models into multi-layer builds by allowing layer heights to be accurately predicted, optimising geometric accuracy and limiting the likelihood of pores. This single-layer model can form the basis for identifying the optimum multi-layer process parameters, particularly the Z-axis increment, to ensure that layers are predictable and consistent.

5.1   Optimisation of Single Layer Deposition

5.1.1   Effect of Track Separation on Layer Height

Layers were printed for a range of combinations of track parameters from within the 800W process window. The tracks were selected to represent a range of track geometries by choosing a variety of height-to-width ratios (HWR). The combinations used are summarised in Table 5.1. The literature suggests an optimal track separation x (the overlap ratio of the track width, see Equation 5.1) of between

$x = 2/3$ and $x = 0.7$ of the track width (Ding et al., 2015). However track shape is affected by many variables and the available literature uses different deposition methods (WAAM, single laser etc.), which will therefore result different shaped cross sections to the Meltio M450. These values for x can therefore only be used as a guide. Layers were created with values for x of 0.5, 2/3, $\pi/4$ and 0.9 of the measured track widths for each track type.

Figure 5.1 shows an example of a plate with some of these layers. It is clear from this image that as the separation of the tracks increases, the ridges on the surface become more pronounced as the individual tracks become more apparent.

ID	Head Speed (mm/s)	Extrusion Rate (mm/s)	WSF	Track Width (mm)	Track Height (mm)	Height/Width
1	5.50	15.50	2.82	2.20	1.07	0.49
2	7.50	11.50	1.53	2.18	0.74	0.34
3	7.50	13.50	1.80	1.95	0.91	0.47
4	7.50	15.50	2.07	1.99	1.04	0.52
5	8.21	12.31	1.50	1.91	0.73	0.38
6	9.50	17.50	1.84	2.01	0.86	0.43
7	11.50	15.50	1.35	1.81	0.73	0.41
8	12.31	12.31	1.00	1.94	0.53	0.27
9	13.50	17.50	1.30	1.04	0.15	0.15
10	13.50	22.50	1.67	1.64	0.77	0.47

Table 5.1: Combinations of track parameters and their dimensions used for single-layer experiment.
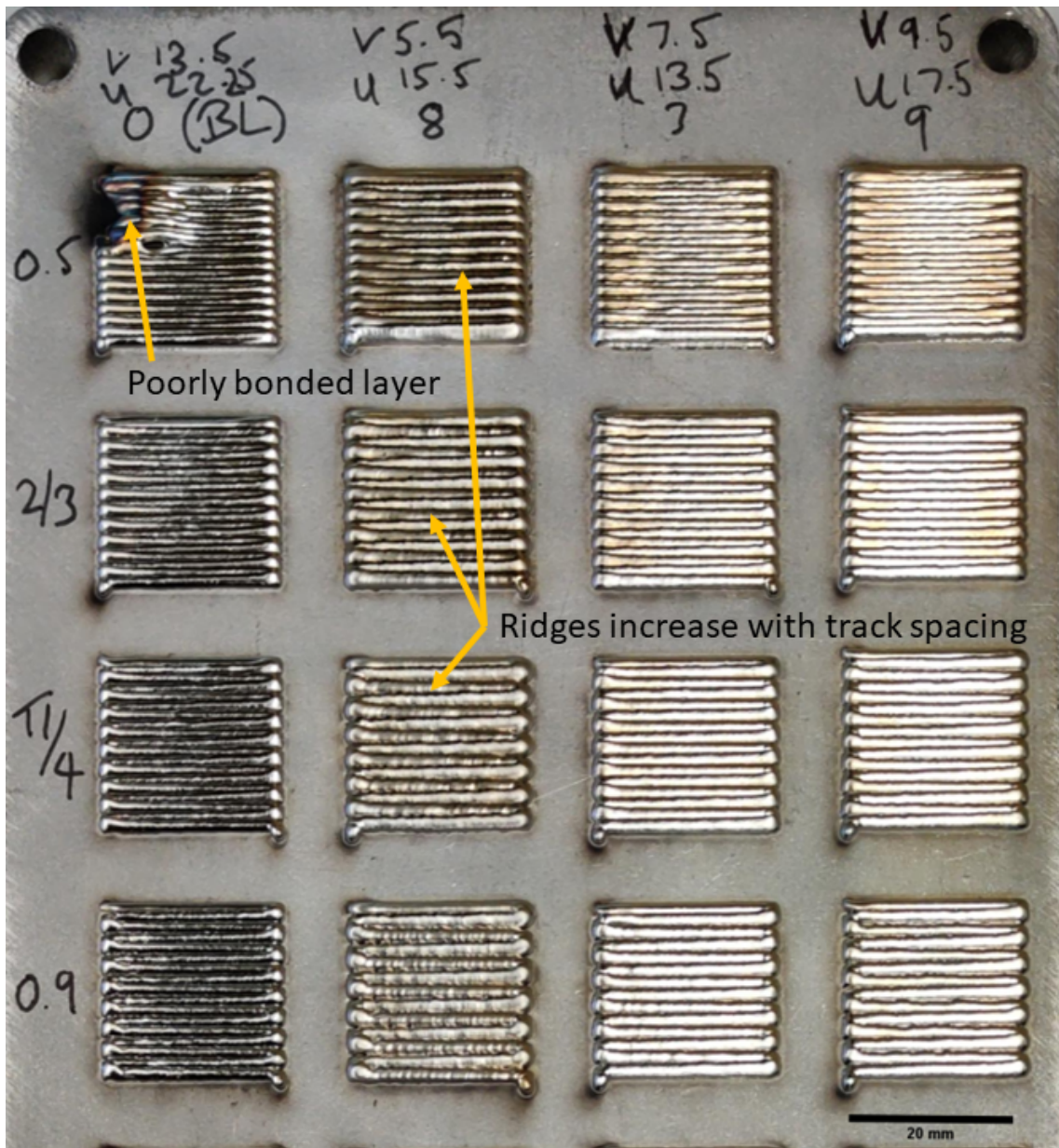
Figure 5.1: Example of plate with single-layer samples, with a range of track settings and track spacings.

Measurements of the height of the layer, h_l, its standard deviation and the width of the layer, w_l, are shown in Table 5.2 for setting IDs 2, 6 and 10; Figures 5.2, 5.4 and 5.5 show their measured cross sections and Figure 5.3 the etched cross sections for setting ID 2.

133

x	No. Tracks	Mean h_l (mm)	Max h_l (mm)	Min h_l (mm)	Std. Dev. (Height)	w_l (mm)
ID 2- V_f 11.5mm/s, V_h 7.5mm/s, h_t 0.74mm, w_t 2.18						
0.5	24	1.17	1.33	0.96	0.074	25.03
2/3	19	0.84	1.04	0.55	0.138	25.13
$\pi/4$	16	0.66	0.91	0.38	0.183	25.46
0.9	14	0.51	0.71	0.19	0.288	26.31
ID 6- V_f 17.5mm/s, V_h 9.5mm/s, h_t 0.86mm, w_t 2.01						
0.5	25	1.43	1.68	1.23	0.064	26.35
2/3	19	1.09	1.26	0.83	0.074	25.67
$\pi/4$	16	0.88	1.06	0.61	0.119	26.66
0.9	14	0.7	0.98	0.27	0.201	26.22
ID 10- V_f 22.5mm/s, V_h 13.5mm/s, h_t 0.77mm, w_t 1.64						
0.5	30	1.57	1.88	1.31	0.069	26.55
2/3	23	1.11	1.31	0.85	0.094	25.56
$\pi/4$	20	0.93	1.14	0.66	0.113	26.01
0.9	17	0.81	1.16	0.32	0.228	27.09

Table 5.2: Measurements of the layer height, its standard deviation and layer width, for track setting IDs 2, 6 and 10.
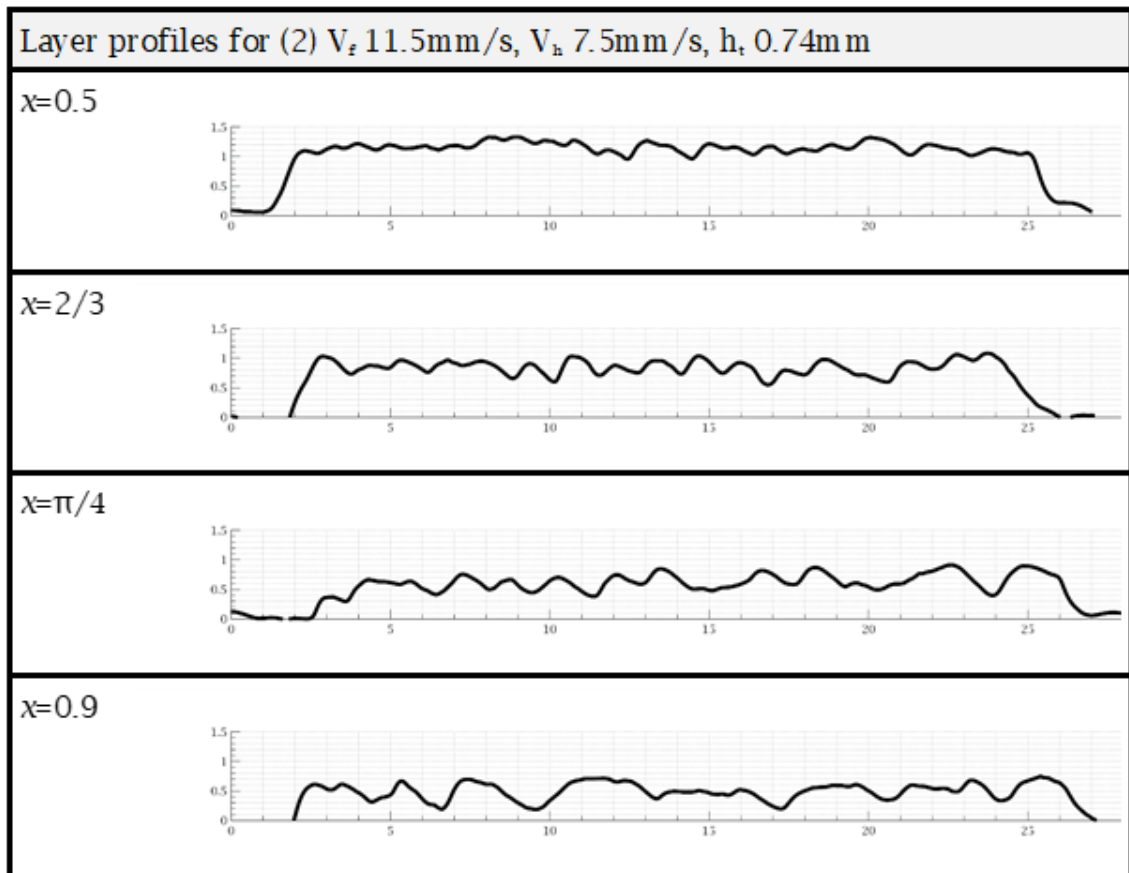
Figure 5.2: Measured layer height cross sections for track parameter setting ID 2.
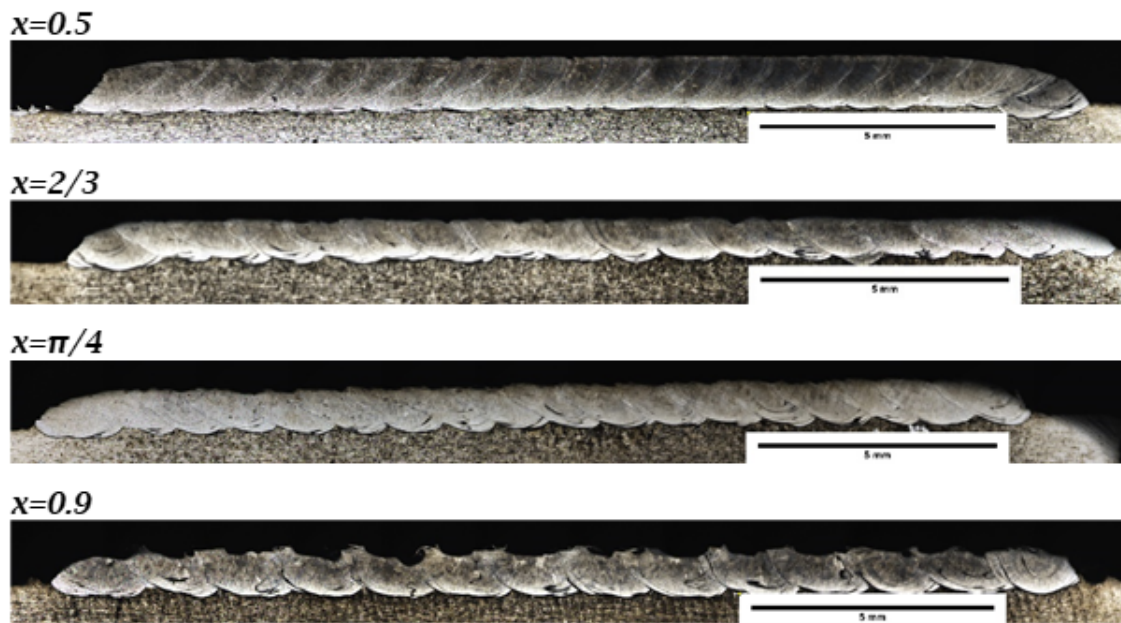
Figure 5.3: Etched layer cross sections for track parameter ID 2, with a scale bar of 5mm.
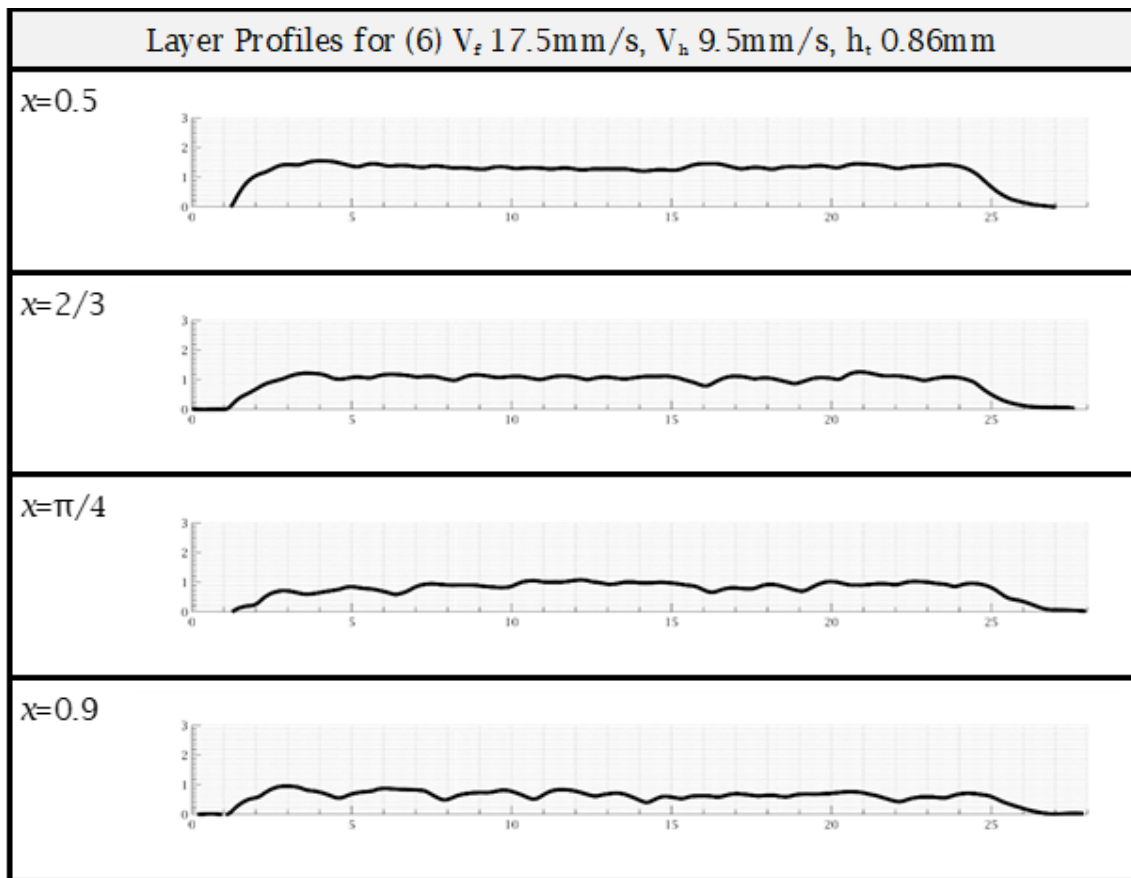
Figure 5.4: Measured layer height cross sections for track parameter setting ID 6.
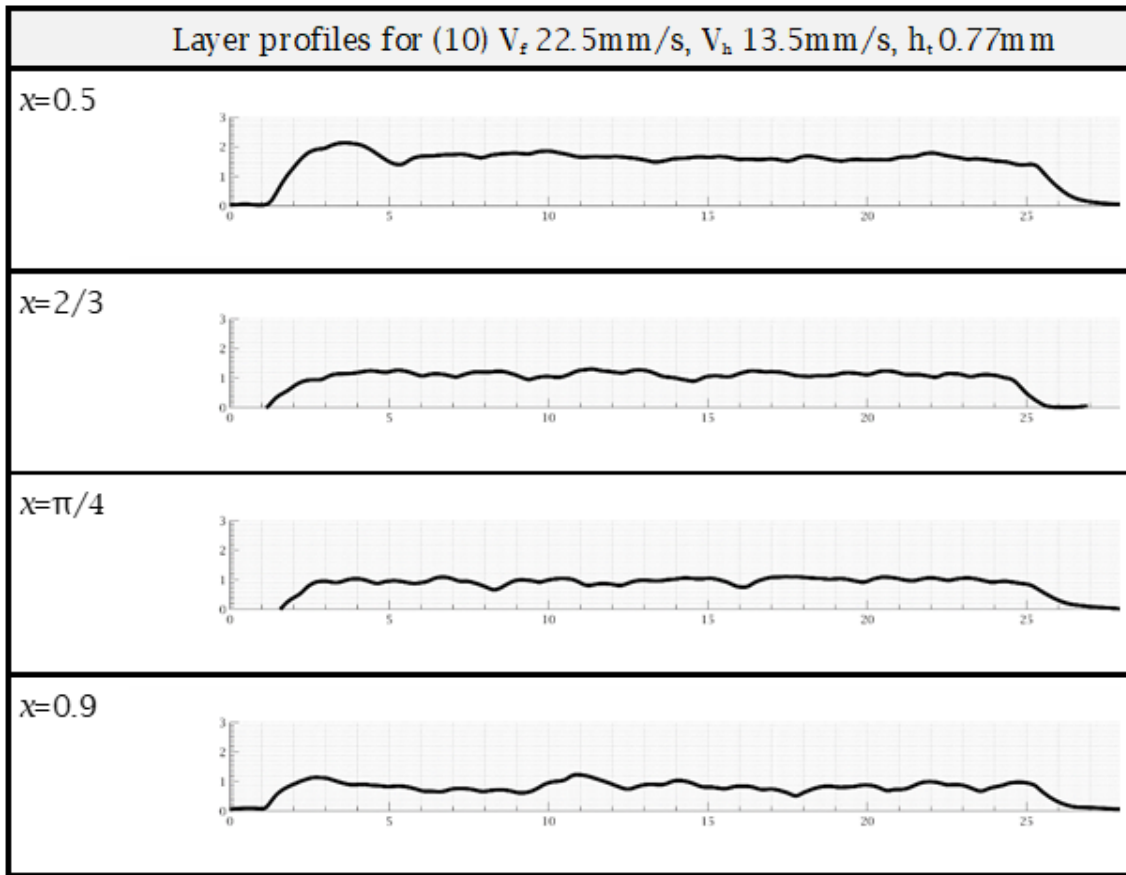
Figure 5.5: Measured layer height cross sections for track parameter setting ID 10.

These data show that the stepover with the lowest layer height variability, seen by visual inspection and in the calculated standard deviation, is $x = 0.5$. This seems sensible, as the tracks become spaced further apart, the individual tracks become more pronounced, increasing the variability of the surface. The etched cross sections of the layers show a clean flat layer for $x = 0.5$, with tracks that are consistent and regular in their overlap and remelting. The etches show the layer surface and the layer overlaps becoming increasingly irregular as the track separation increases.

The etches would also suggest that the penetration depth is deeper for the higher stepover values, approximately 8% for $x = 0.5$, 13% for $x = 2/3$, 22% for $x = \pi/4$ and 31% for $x = 0.9$. This effect is caused by less remelting of each of the previously deposited tracks. As the track separation distance increases, more of the substrate is melted, resulting in more dilution into the substrate. This reduced level of dilution into the substrate would suggest that a greater proportion of the laser energy remains in the deposited layer, which could reduce bulk heating in a multi-layer build. However, the reduction in dilution in the previous layer increases the need for the layers to be flat, and the reduced remelting may not remove the waviness of the surface, resulting in interlayer porosity.

Tracks that remelt less of the previous layer may result in better outcomes due to fewer reheating cycles of deposited material and slower bulk heating of the component, as more of the laser energy is likely to remain in the deposited layer. However, wider spaced tracks may result in greater tolerance of surface variability due to additional remelting of the previous layer and potentially better bonding between the layers. The convention in the literature is to optimise the process to achieve the flattest possible surface and no link was identified in the literature between stepover and dilution with the previous layer. This effect may only become evident with the relatively low powers and dilution levels achieved with a coaxial LWAM system.

The ratio of layer height to track height versus track stepover is shown in Figure 5.6; it shows that as the track separation increases, the mean layer height decreases

and the ratio to track height eventually goes below 1 as the individual tracks become more distinct. The error bars show that the standard deviation increases with increasing stepover distances.
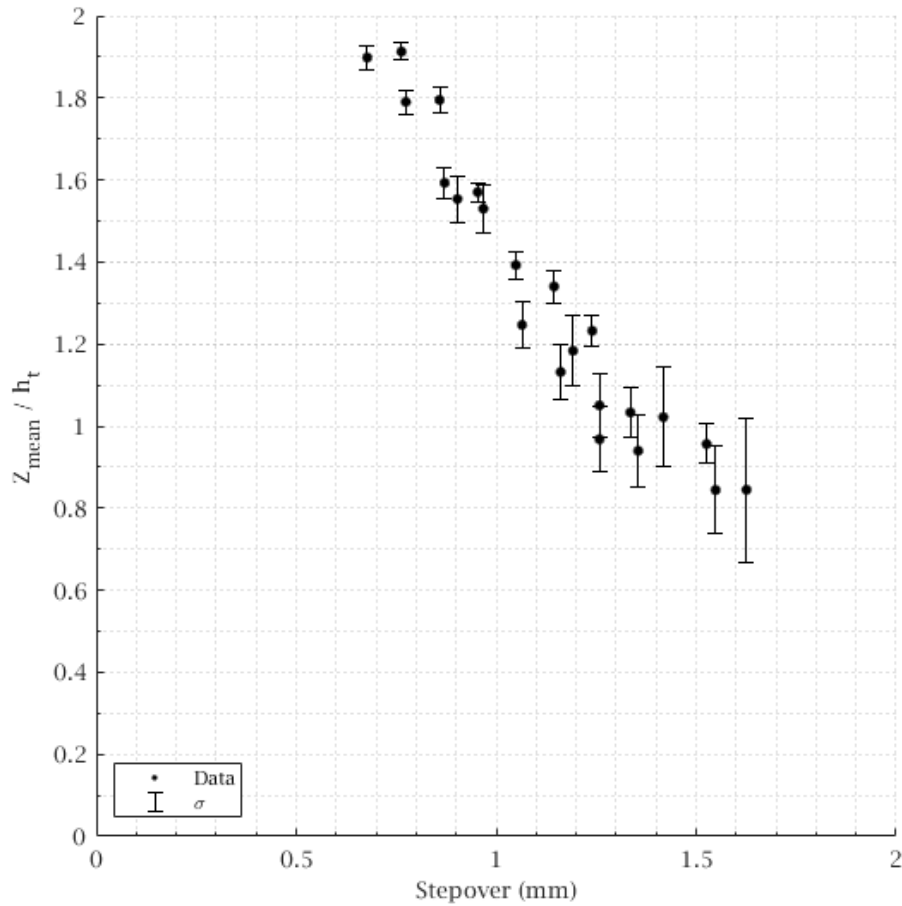
Figure 5.6: The ratio of layer height to track height versus track stepover distance for all layers in Table 5.1.

The increase in standard deviation with the stepover can be seen in Figure 5.7, the standard deviations have been normalised by dividing the standard deviation by its mean layer height. As the tracks are spaced further apart, the additional material created by the overlapped tracks is reduced and the created valley cannot be bridged, revealing more of the surface of the individual tracks. This increases the variability in the height of the layer's surface and reduces the mean layer height. These results support the literature that, whilst it is not possible to achieve a perfectly flat surface (Ding et al., 2015), there is an optimal separation of tracks where material from the overlapping tracks is equivalent to the valley space created between them (Cao et al., 2011). The optimal track separation for this process is lower than the values identified in the literature; however, the published work in this area is for WAAM-based technologies, which result in tracks with a different height to width profile.
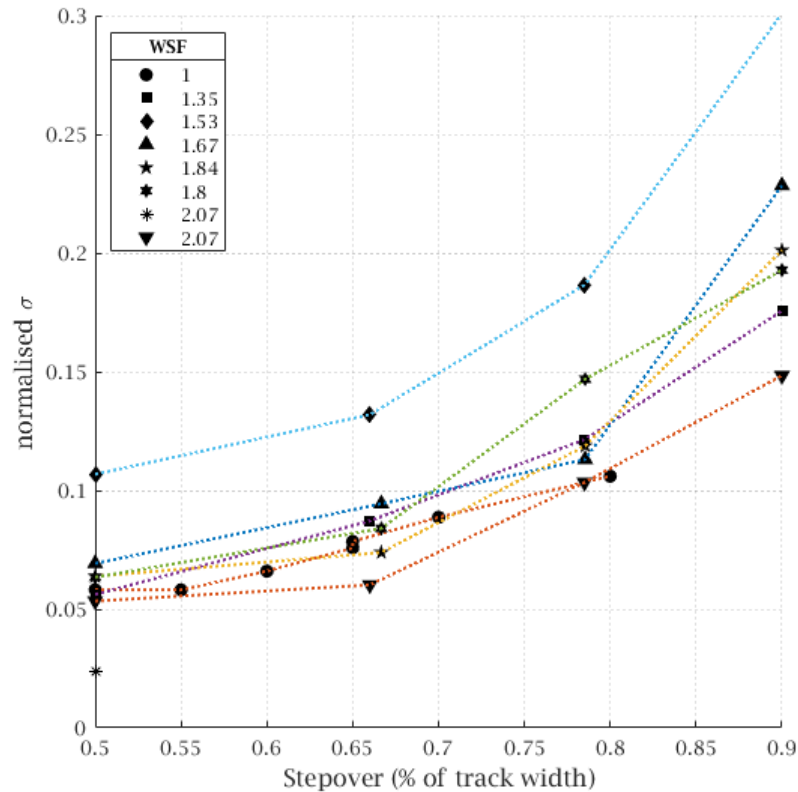
Figure 5.7: Normalised standard deviation versus stepover as a percentage of track width for all layers in Table 5.1.

5.1.2   Impact of Track Count on Layer Thickness

The review of the literature identified that some single-layer models show a relationship between the height of the layer and the number of tracks used within the layer (Ding et al., 2015; Cao et al., 2011). To evaluate this effect, layers were created with a range of track numbers; all tracks used a fixed stepover of $x = 0.5$, the lowest surface variability identified above. Layers were created using 2, 4, 8 and 20 tracks for three different extrusion rate and head speed combinations. The track settings and the resulting layer measurements are shown in Table 5.3, and an image of the plate produced is shown in Figure 5.8.

These data show that there is a clear relationship between the mean height of the layer and the number of tracks used to create the layer, the height increasing with the number of tracks in the layer. These results support the models developed by Ding et al. (2015) and Cao et al. (2011); however, their models did not quantify this effect or evaluate it experimentally.

V_h	V_h	WSF	Track Height h_t (mm)	Track Width w_t (mm)	No. Tracks	Mean h_l (mm)	Max h_l (mm)	Min h_l (mm)	Std. Dev. (h_l)
7.5	7.5	1	0.60	1.92	1	0.60	0.60	-	0.02
					2	0.78	0.78	-	0.16
					4	0.78	0.81	-	0.22
					8	0.85	0.91	0.79	0.06
					20	0.90	0.95	0.64	0.05
7.5	11.5	1.53	0.74	2.18	1	0.79	0.79	-	0.01
					2	0.96	0.96	-	0.09
					4	1.09	1.19	-	0.04
					8	1.12	1.21	1.07	0.04
					20	1.17	1.23	0.96	0.05
7.5	15.5	2.07	0.98	1.97	1	0.98	0.98	-	0.01
					2	1.25	1.25	-	0.08
					4	1.41	1.41	-	0.09
					8	1.51	1.56	1.27	0.04
					20	1.51	1.58	1.13	0.04

Table 5.3: Track settings and the resulting layer measurements to determine the effect of the number of tracks on the resulting layer height.
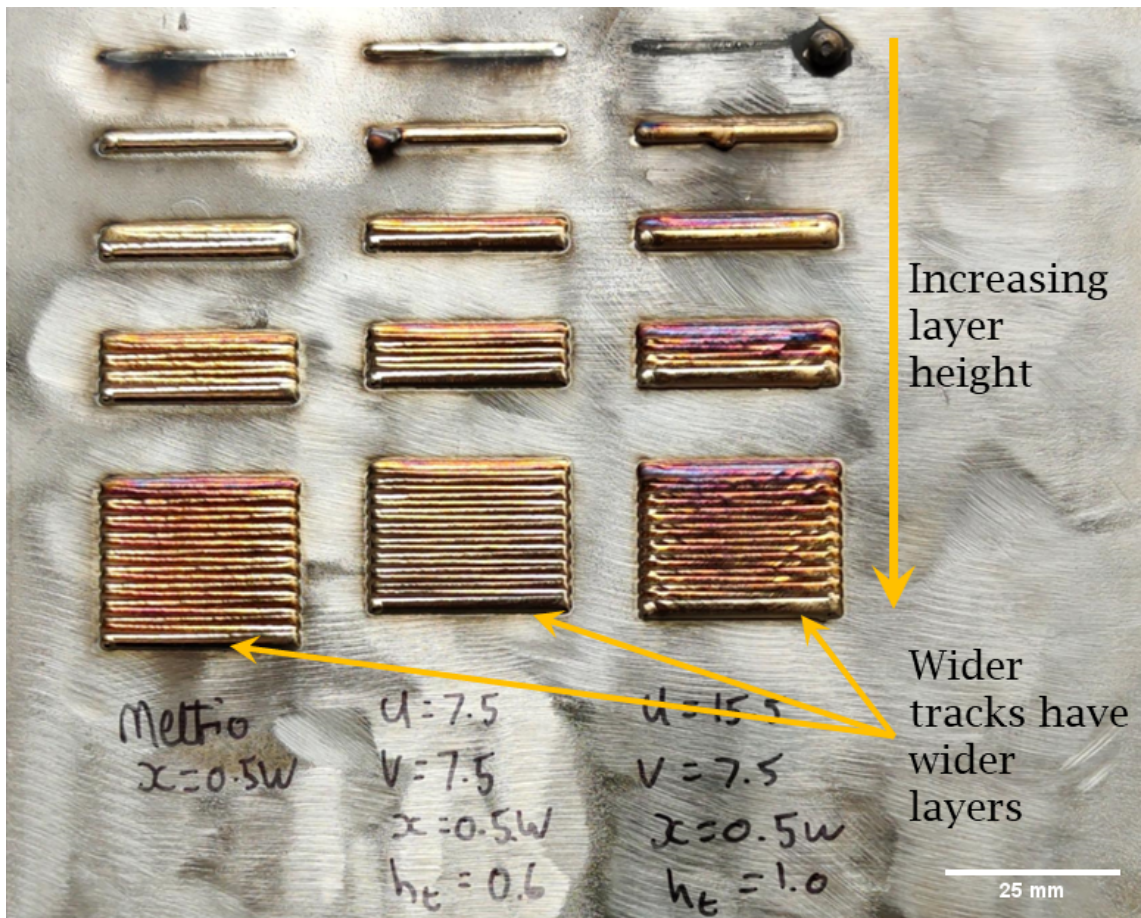
Figure 5.8: Example of plate with single-layer samples to investigate effect of the number of tracks on layer height.

5.1.3   Development of a Single-Layer Model

To create a mathematical description of the layer, a simple model can be used to predict the height of the layer based on the overlap between tracks, their dimensions and cross-section shape. A single-layer model estimates the layer height based on the track height, track width and separation distance of the tracks. These parameters are illustrated in Figure 5.9 and show the additional material in the overlaps that fill the valleys between the tracks.

The separation distance between the tracks is described in Equation 5.1. Sometimes referred to as stepover, x is the proportion of the width of the track, w_t, used to determine the distance between the tracks, d.

$$d = x \times w_t \tag{5.1}$$

The width of the layer, w_l, is a function of the width of the overlapping tracks. This is described in Equation 5.2, where n is the number of tracks in the layer, assuming that the tracks are consistent along their length and separation and meet the criteria defined as 'printable'.

$$w_l = (n - 1)xw_t + w_t \tag{5.2}$$

The cross-sectional area of the layer can be determined by first considering the cross-sectional area of a track, assuming that this shape is a semi-ellipse, the cross-sectional area of the track, A_t, can be described as shown in Equation 5.3.

$$A_t = \frac{\pi}{4}h_t w_t \tag{5.3}$$

The cross-sectional area of the layer, Equation 5.4, is expressed in terms of Equations 5.3 and 5.2.

$$n\frac{\pi}{4}h_t w_t = (n - 1)xh_l w_t + (\frac{\pi}{4}h_l w_t) \tag{5.4}$$
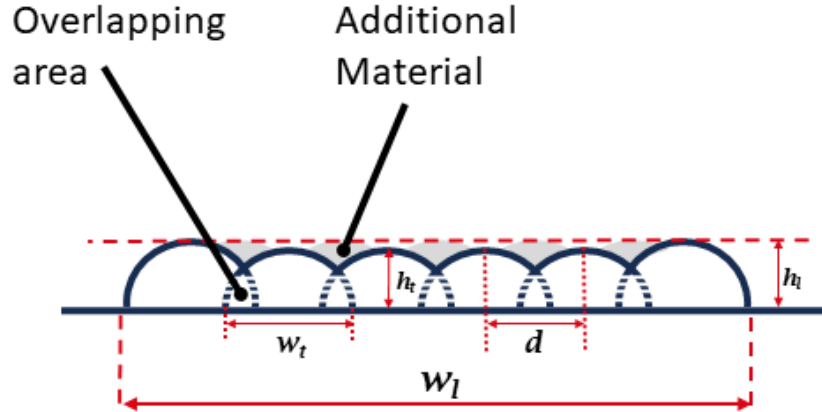
Figure 5.9: Illustration of key parameters to describe the single-layer model.

Equation 5.4 can be simplified and rearranged to describe the ratio of layer height to track height as shown in Equation 5.5.

$$\frac{h_l}{h_t} = \frac{n\pi}{4((n-1)x + \frac{\pi}{4})} \tag{5.5}$$

There are three different conditions where the ratio of layer height to track height differs in result according to Equation 5.5, where $x > \pi/4$, $x < \pi/4$ and $x = \pi/4$, these are illustrated in Figures 5.10 and 5.11. These conditions underscore the sensitivity of layer height to three key things: stepover distance, the number of tracks deposited and the height of the track:

$x > \pi/4$: The mean layer height remains below the track height, regardless of the number of tracks in the layer, as the track separation is too great for the overlapped material to fill the valleys between the tracks.

$x = \pi/4$: The layer is equal to the height of the track regardless of the number of tracks in the layer.

$x < \pi/4$: The height of the layer exceeds the height of the track, due to the additional material in the overlapped tracks. The difference in layer height increases significantly for layers with fewer than eight tracks.

145
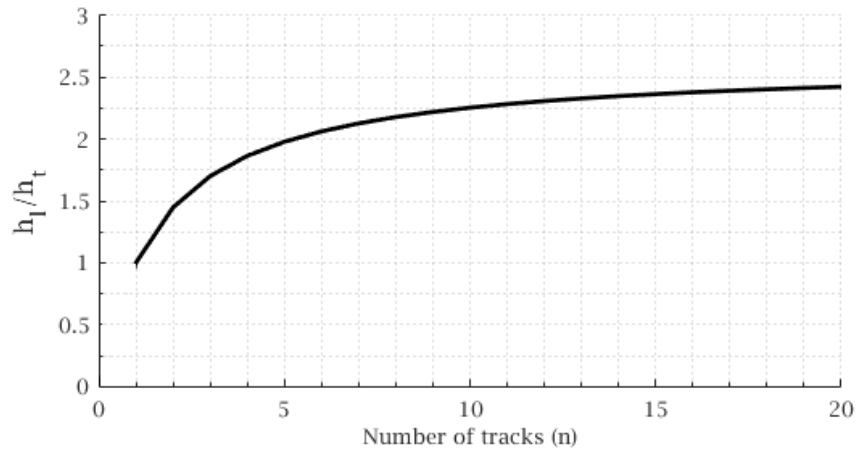
Figure 5.10: h_l/h_t for $x < \pi/4$, where track height is unity.
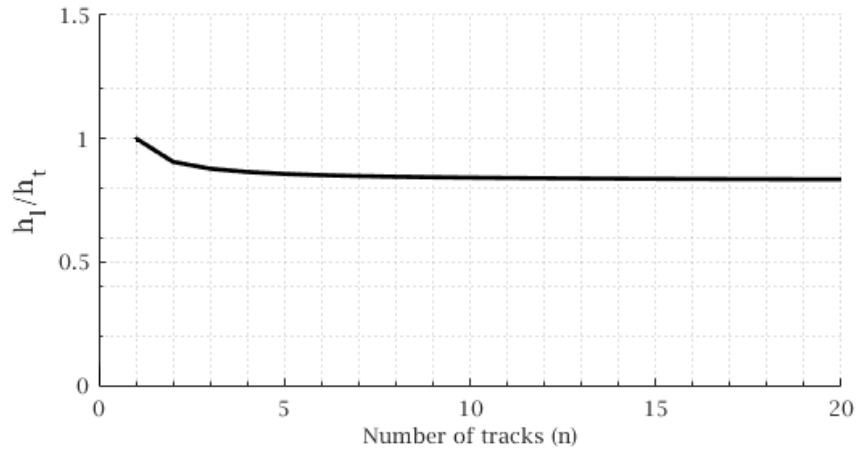
Figure 5.11: h_l/h_t for $x > \pi/4$, where track height is unity.

Equation 5.5 suggests that as the track overlap increases, the additional material in the overlapped region is greater than the volume of the valley between the tracks, which creates a layer height greater than the individual track height, consistent with Ding et al. (2015) and Cao et al. (2011). This means that the closer the tracks are to each other, the greater the difference between the track height and the layer height. The optimal stepover, $x = 0.5$, is the condition in which the overlapping area between adjacent tracks just counterbalances the valley area, resulting in a surface that is as flat as possible.

Figure 5.12 shows the comparison of the predicted h_l/h_t values versus the
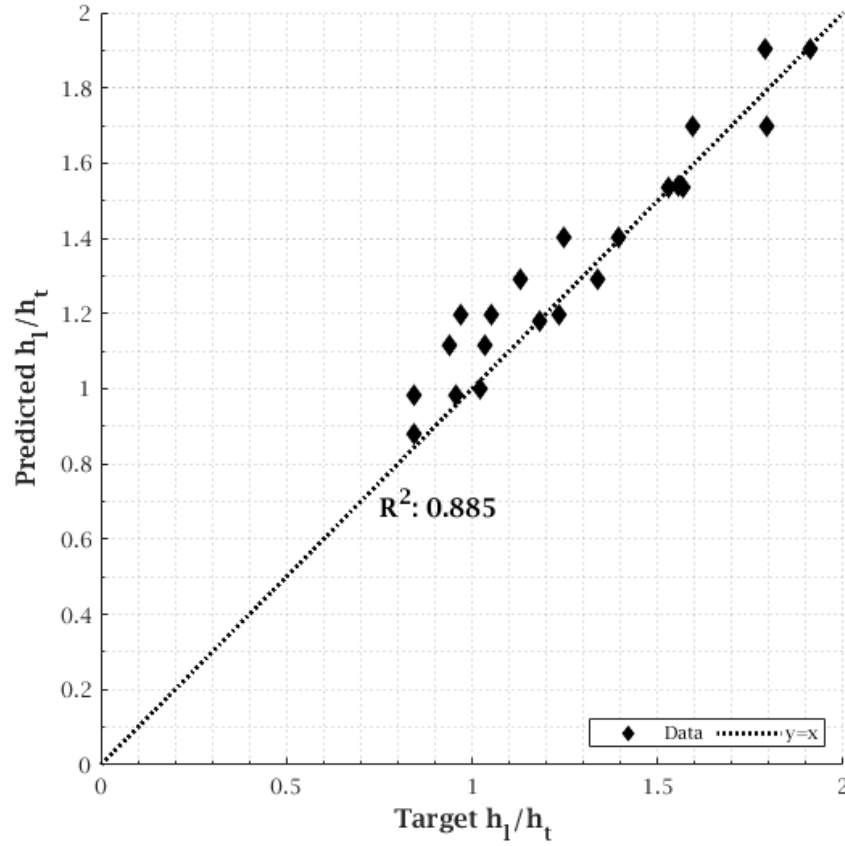
Figure 5.12: Comparison of the predicted h_l/h_t values versus the experimental measurements made for the single-layers.

experimental measurements made for single layers. Noting that there is a high degree of variability in the surface, particularly for layers with higher track separation, the plot and the fit of the data (R^2 of 0.885) suggest that the model is effective in predicting layer heights across the range and the data support an assumption of a semi-elliptical shape for the track.

Although the accuracy of layer height prediction is varied, it is an expected outcome due to measuring the height of a surface with variable height. In addition to this, as with the measurement of single-track widths, there are other dynamics which may affect the layer height that have not been identified such as surface plate quality, drift in calibration and thermal distortions. The Z-score of statistical significance, Equation 5.6, was calculated for the height measurements taken, determining how

147

many standard deviations the predicted layer height is from the mean height. The Z scores for the 'effect of stepover experiments' are summarised in Table 5.4 and for the second experiment, the 'track count effect on layer height' in Table 5.5. The Z value suggests that the predictions are well within the range of two standard deviations of the observed heights, which implies that the model is close to the observed data.

$$Z = \frac{h_{l(predicted)} - h_{l(measured)}}{\sigma_{measured}} \qquad (5.6)$$

x	No. Tracks	Mean h_l (mm)	Max h_l (mm)	Std. Dev. (h_l)	Predicted h_l (mm)	Z Score
ID 2 - V_f 11.5mm/s, V_h 7.5mm/s, h_t 0.74mm, w_t 2.18mm						
0.5	24	1.17	1.33	0.074	1.14	-0.41
2/3	19	0.84	1.04	0.138	0.86	0.14
$\pi/4$	16	0.66	0.91	0.183	0.74	0.44
0.9	14	0.51	0.71	0.288	0.65	0.49
ID 6 - V_f 17.5mm/s, V_h 9.5mm/s, h_t 0.86mm, w_t 2.01mm						
0.5	25	1.43	1.68	0.064	1.32	-1.72
2/3	19	1.09	1.26	0.074	1	-1.22
$\pi/4$	16	0.88	1.06	0.119	0.86	-0.17
0.9	14	0.7	0.98	0.201	0.76	0.3
ID 10 - V_f 22.5mm/s, V_h 13.5mm/s, h_t 0.77mm, w_t 1.64mm						
0.5	30	1.57	1.88	0.069	1.19	-5.5
2/3	23	1.11	1.31	0.094	0.9	-2.23
$\pi/4$	20	0.93	1.14	0.113	0.77	-1.42
0.9	17	0.81	1.16	0.228	0.68	-0.57

Table 5.4: Summary of the Z scores for the 'effect of stepover experiments'.

Vh (mm/s)	Vf (mm/s)	WSF	Track Height h_t (mm)	Track Width w_t (mm)	No Tracks	Predicted h_l (mm)	Mean h_l (mm)	Max h_l (mm)	Min h_l (mm)	Predicted wl (mm)	Layer Width (mm)	Std. Dev. (Height)	Z Score (Height)
7.5	7.5	1	0.60	1.92	1	0.60	0.60	0.60	-	1.92	1.92	0.02	0.00
					2	0.73	0.78	0.78	-	2.88	4.45	0.16	-0.29
					4	0.82	0.78	0.81	-	4.80	5.56	0.22	0.21
					8	0.88	0.85	0.91	0.79	8.63	9.60	0.06	0.43
					20	0.92	0.90	0.95	0.64	20.14	23.43	0.05	0.36
7.5	11.5	1.53	0.74	2.18	1	0.79	0.79	0.79	-	1.99	1.99	0.01	0.00
					2	0.96	0.96	0.96	-	2.99	4.23	0.09	0.04
					4	1.08	1.09	1.19	-	4.98	6.83	0.04	-0.23
					8	1.15	1.12	1.21	1.07	8.96	10.58	0.04	0.97
					20	1.20	1.17	1.23	0.96	20.90	24.80	0.05	0.44
7.5	15.5	2.07	0.98	1.97	1	0.98	0.98	0.98	-	1.97	1.97	0.01	0.00
					2	1.20	1.25	1.25	-	2.95	3.84	0.08	-0.69
					4	1.35	1.41	1.41	-	4.92	6.13	0.09	-0.60
					8	1.44	1.51	1.56	1.27	8.85	9.05	0.04	-1.56
					20	1.50	1.51	1.58	1.13	20.64	21.91	0.04	-0.33

Table 5.5: Summary of the Z scores for the 'track count effect on layer height'

The layers created for the stepover distance experiment are plotted in Figure 5.13, showing the h_l/h_t ratio versus the number of tracks in the layer, as well as the prediction from Equation 5.5. This experiment investigated layers with a relatively large number of tracks in the layer, where the model suggests that there is little variability in the layer height for the number of tracks deposited, the plot suggests that the prediction of the height of the layer works well, showing the experimental data following the behaviour described in the three separate conditions for $x > \pi/4$, $x < \pi/4$ and $x = \pi/4$.

The layers created for the experiment investigating the effect of the number of tracks on the height of the layer are plotted in Figure 5.14. This shows that the experimental results fit closely to Equation 5.5, the data having a low Z-score of statistical significance, typically well below 0.7.
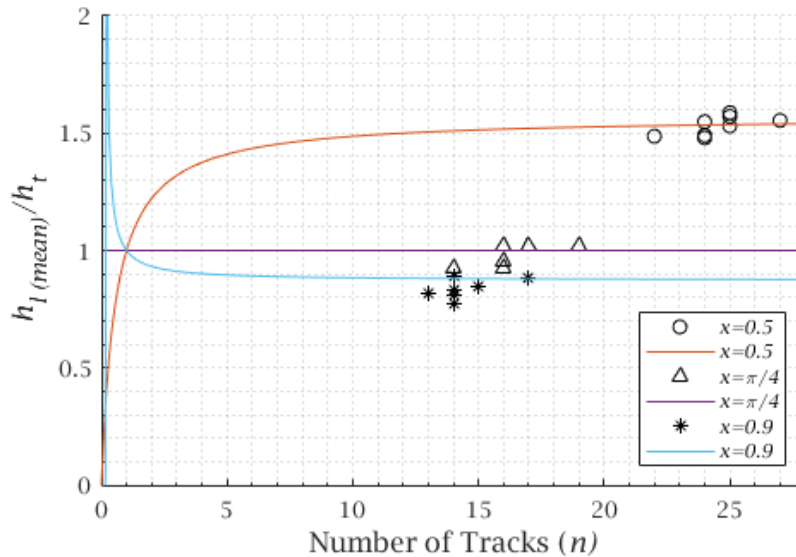
Figure 5.13: h_l/h_t versus the number of tracks compared to single layer model for stepover distance experiment.
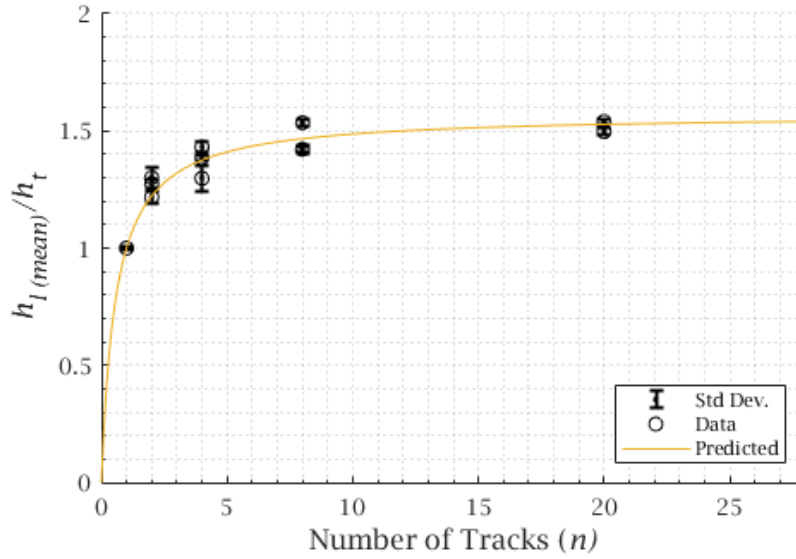
Figure 5.14: h_l/h_t versus the number of tracks layer compared to single layer model for number of tracks in layer experiment.

Equation 5.6 describes the height of the layer well and is supported by the experimental data. This information is key for planning multi-layer builds, allowing layer heights to be estimated for different parameter combinations and track numbers. This knowledge alone would be sufficient to calculate the thickness of a single layer for the purposes of cladding and can support the development of a multi-layer model.

Understanding this behaviour is particularly important for this process, as most real parts have a range of track numbers throughout the layer due to features such as curves, thin walls and holes. It is also common to use perimeters in LWAM parts to improve surface finish, effectively creating a separate layer of up to three tracks wide. Without understanding the dynamics of how layer height is affected by the number of tracks, it is likely that the overall layer will become uneven. On a multi-layer build, this could result in an underbuilt part in some areas.

5.1.4 Proving the Single-Layer Model

A 'model proving' layer was created to evaluate the model and demonstrate the potential variability in the height of the layer throughout a build. A four-pronged 'E' shape was deposited with a varied number of tracks in each prong of the 'E'. This shape was chosen as a simple model that is representative of the range of track numbers that could be deposited across a typical layer of a part.

Using the parameters of Track ID 2 from Table 5.1, the layer consisted of 2, 4, 6, 8 and 50 tracks, its toolpath is shown in Figure 5.15. The expectation should be that as the number of tracks in each part of the 'E' increases, so does the height of the layer. The measurements of layer height are summarised in Table 5.6, and the plots of the measured cross sections are shown in Figure 5.16 for the 50-track section and Figure 5.17 for the 2-8-track section.
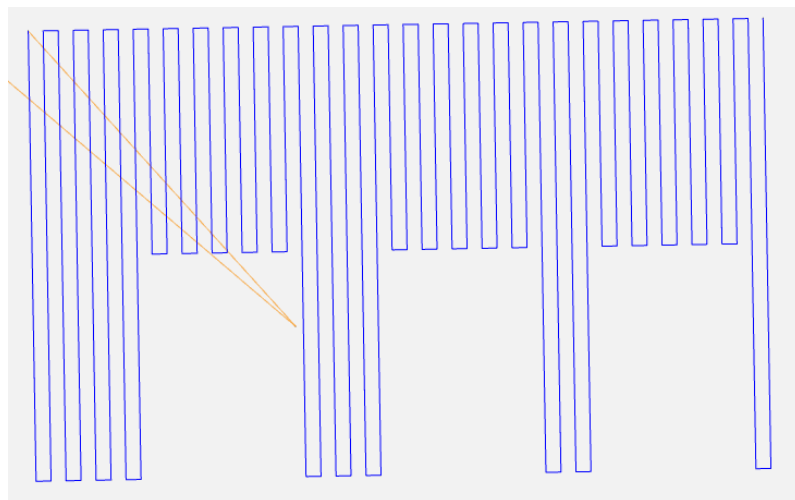
Figure 5.15: Toolpath for the four pronged 'E' used to prove the single layer model.

No. Tracks	Predicted h_l (mm)	Measured h_l (mm)
2	0.90	0.73
4	1.02	1.02
6	1.06	1.05
8	1.08	1.12
50	1.15	1.11

Table 5.6: Summary of layer height measurements from the model proving 'E'.
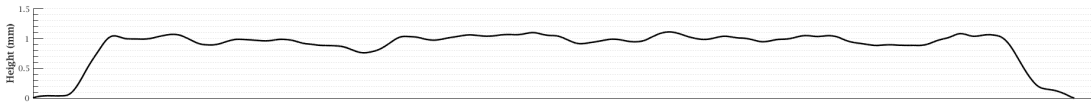
Figure 5.16: Cross section height measurements of the 50-track body of the model proving 'E'.
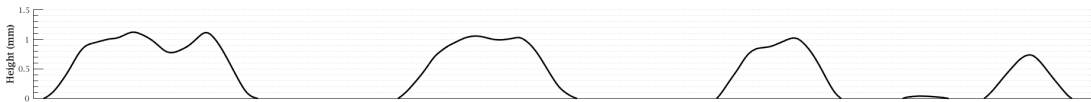
Figure 5.17: Cross section height measurements of the 8, 6, 4 and 2-track sections of the model proving 'E'.

The experimental results agree with the model; predicted height calculations suggested that the measured range in layer heights would be approximately 0.24mm, the results suggest that the range of heights was larger than this at 0.39mm, which is between a half and a third of the expected layer height.

Current slicing tools assume that for a fixed extrusion rate, head speed and stepover, the layer height remains constant and does not take the number of tracks as a factor affecting this. Similarly, beyond showing this behaviour to occur, it is not well described in the literature. Propagated over several layers, there is a risk of inconsistencies in height, which will cause changes to the calibrated laser spot size as the deposition head passes, further increasing inconsistencies in the deposition process.

5.2 Multi-Layer Deposition and Optimum Z-Axis Increments

The development of a repeatable and predictable multi-layer deposition method is based on the single-layer model, consistent with P. Kumar, Jain, and Mayur Sudhakar Sawant (2022), Caiazzo and Alfieri (2019), and F. Liu et al. (2022). These papers predict layer height solely as a function of track stepover distance and track shape. For coaxial systems, there is an additional, more significant variable affecting multi-layer deposition, the Z-axis increment of the deposition head. Incorrect increments of this distance can result in the laser spot becoming defocussed, which could potentially cause the wire to melt before it reaches the previously deposited layer, if the head is too high, or create a ring of laser spots too wide to form a melt pool, if too low.

5.2.1 Optimisation of Z Axis Step Increments

Cubes were created using the layer parameters in Table 5.7. The assumption for depositing this set of cubes was to increment the Z-axis for each layer a distance equal to the expected layer height of 1.2mm. This layer was identified as the flattest (lowest standard deviation of height measurements) and likely to be the most stable in a multi-layer build.

Head Speed (V_h)	7.5mm/s
Extrusion Rate (V_f)	11.5mm/s
Track Height (h_t)	0.78mm
Track Width(w_t)	2.03mm
Track stepover (d)	$0.5.w_t$ (1mm)
Mean Layer Height $(h_{l(mean)})$	1.2mm
Maximum Layer Height	1.33mm
Layer Height Standard Deviation	0.074mm
Z increment	1.2mm

Table 5.7: Single-layer parameters used to create multi-layer cubes.

Figure 5.18 shows the height profiles taken with the laser displacement sensor and Table 5.8 summarises the height measurements. The predicted heights were calculated assuming a layer height of 1.2 mm, based on the initial layer. The overbuild is expressed as a percentage of one layer, allowing an assessment of the total height of the part in relation to each deposited layer. This approach is useful for evaluating the feasibility of using part height prediction in build planning. The overbuild calculation is described in Equation 5.7.

$$Overbuild = \frac{Z_{mean} - Z_{predicted}}{h_{l(mean)}} \tag{5.7}$$
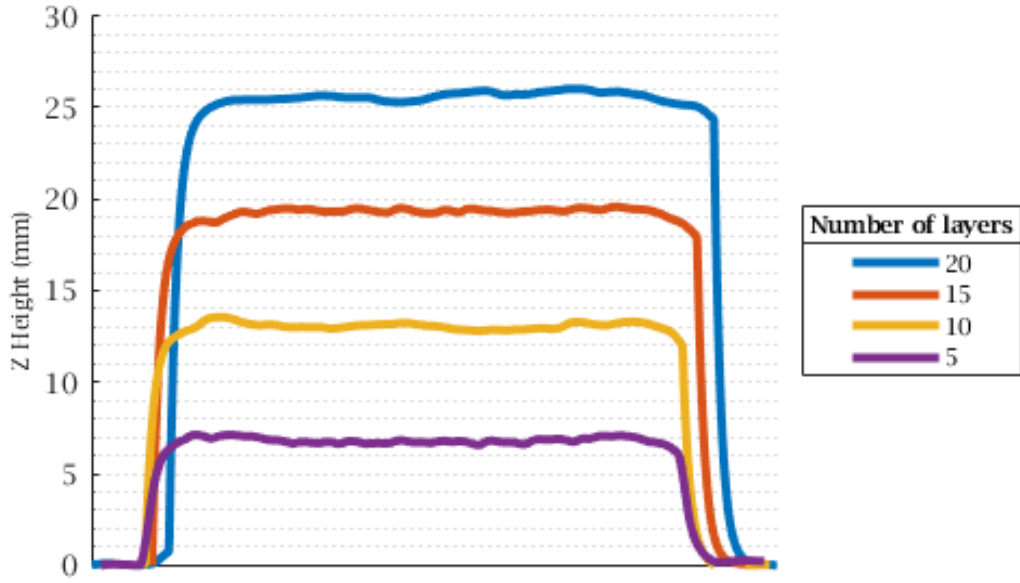
Figure 5.18: Displacement sensor scan of 1.2mm Z height increment cubes.

No. Layers	Z_{max} (mm)	Z_{min} (mm)	Z_{mean} (mm)	Std. Dev.	Predicted Height Z (mm)	Overbuild (% layer)	Offset Distance (mm)
5	6.88	6.25	6.59	0.012	6.0	49%	5.41
10	13.50	12.80	13.06	0.010	12.0	88%	4.94
12	15.86	15.26	15.55	0.009	14.4	96%	4.85
15	19.58	19.07	19.38	0.004	18.0	115%	4.62
20	26.43	24.30	25.73	0.008	24.0	144%	4.27

Table 5.8: Summary of the height measurements for displacement sensor scan of 1.2mm Z increment cubes.

The results indicate an increase in the average layer height as the number of layers increases, as shown in the increasing overbuild values. This trend is likely due to the increase in Z that exceeds the thickness of the previously deposited layer. Consequently, the laser focal point, which should be below the surface of the previous layer, will move closer to the top surface. This is indicated by the increasing offset distance, the lasers are calibrated to a distance of 6mm. This reduces dilution due to

the increased depth of the melt pool, consistent with Figure 2.9 showing the effects of increasing offset distance and reduced energy density. This effect of the offset distance on the laser spot calibration is shown in Figures 5.19 and 5.20.

Focal Point, underbuilt
7.13mm offset distance

Underbuilt
6.5mm offset distance

Calibrated height
6mm offset
distance

Overbuilt
5.5mm offset distance

Overbuilt
5mm offset distance
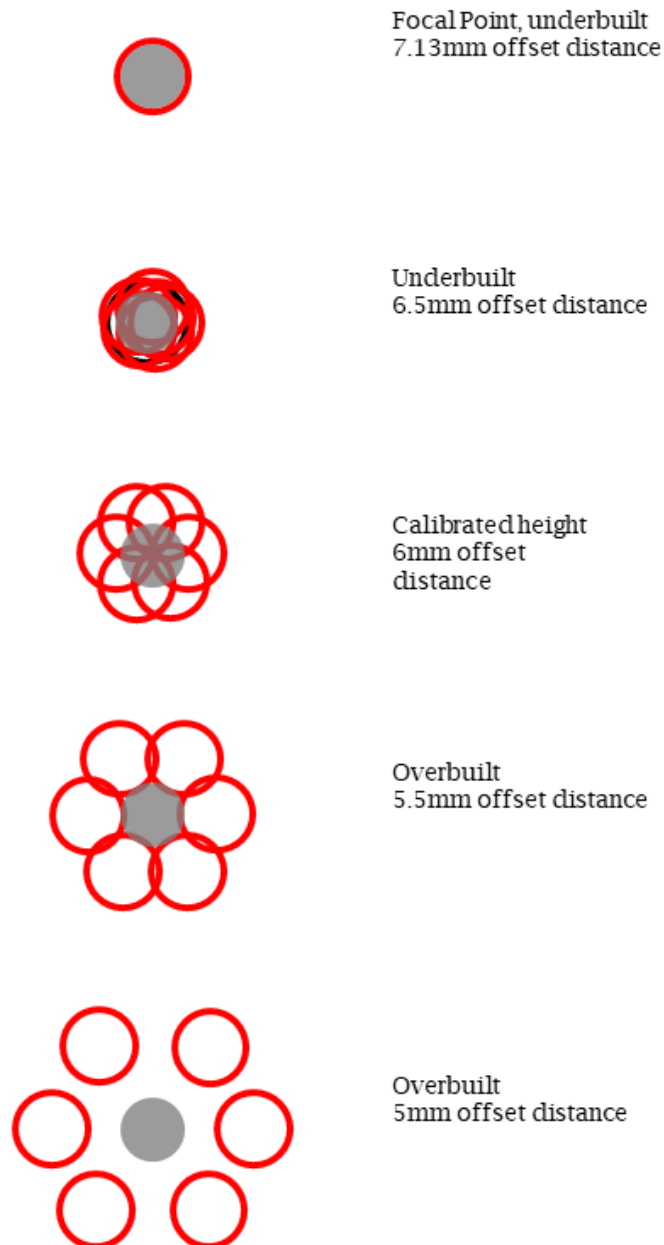
Figure 5.19: Effect of changes to the offset distance on the laser spot focus due to overbuild and underbuild.

6mm calibrated
offset distance

Overbuilt
Offset Distance < 6mm

Underbuilt
Offset Distance > 6mm
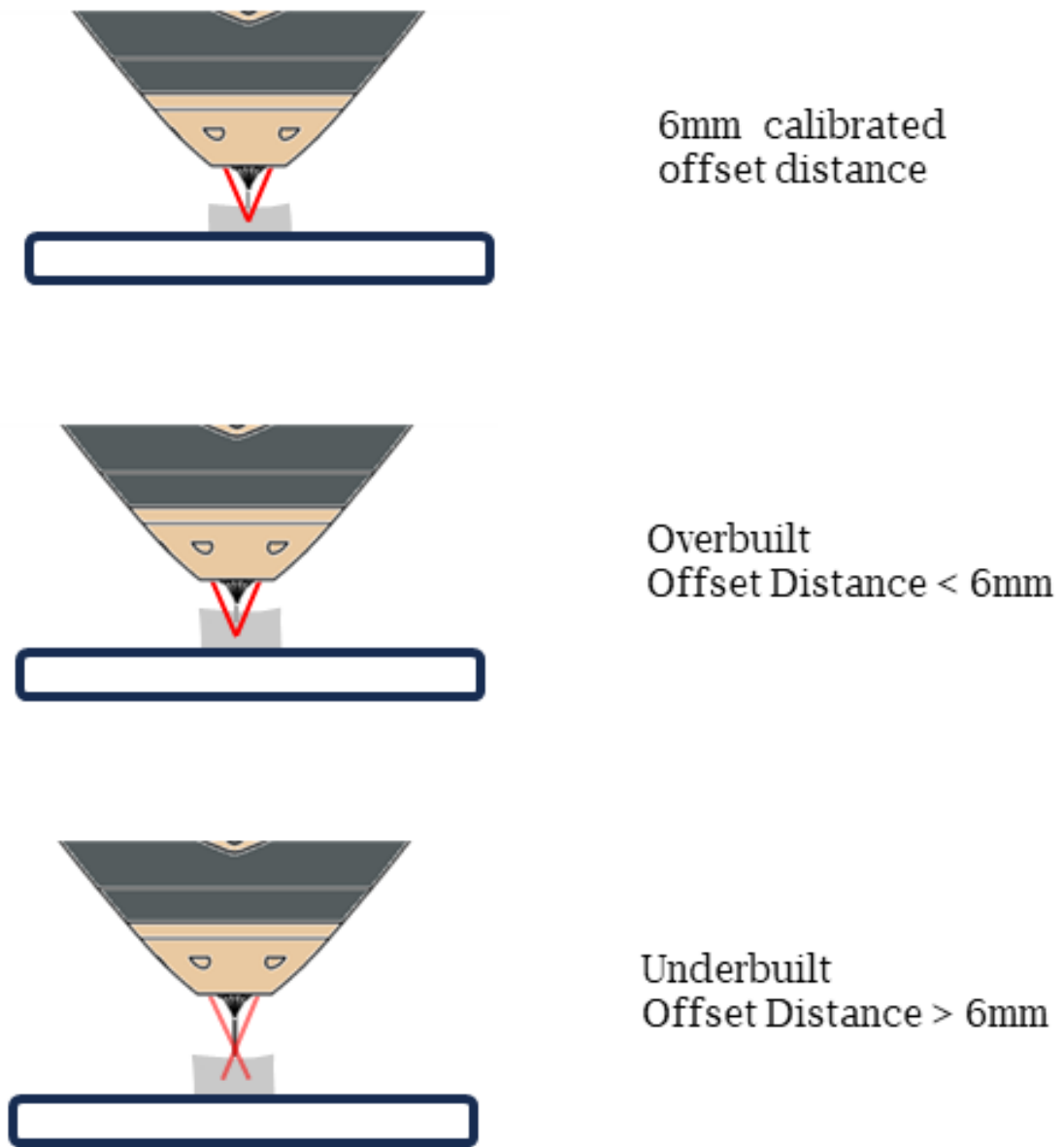
Figure 5.20: Effect of changes to the offset distance on the focal point due to overbuild and underbuild.

The variability of the peak-to-peak height of the surface decreases as the number of layers increases, seen in the reducing standard deviations and visible in the first column of cubes shown in Figure 5.21. The causes for this have not been identified, the flatness of the surface can be improved by the increase in wetting caused by the

increase in the temperature of the part as the number of layers increases (Mukherjee et al., 2017).

To further investigate the effect of the increase in Z on the average layer height, cubes were created for increments of Z steps of 1mm, 1.1mm, 1.3mm and 1.4mm. During the experimental work, it was identified that 1.4mm increments were too large to produce successful cubes. During layers $1-3$, the Z-step increments were too large, defocusing the lasers to the extent that they caused burning on the substrate, illustrated in Figure 5.22. By layer 12, the offset distance was very low, risking a collision with the nozzle. This caused the experiment to be terminated early and the 1.4mm increments were removed from the experimental data. This experiment also resulted in the 15 layer cube for 1.3mm increments not being completed for the same reason; the available data for 11 layers is used. Cross-section measurements for 1mm, 1.1mm and 1.3mm cubes are shown in Figure 5.23 and summarised in Table 5.9.
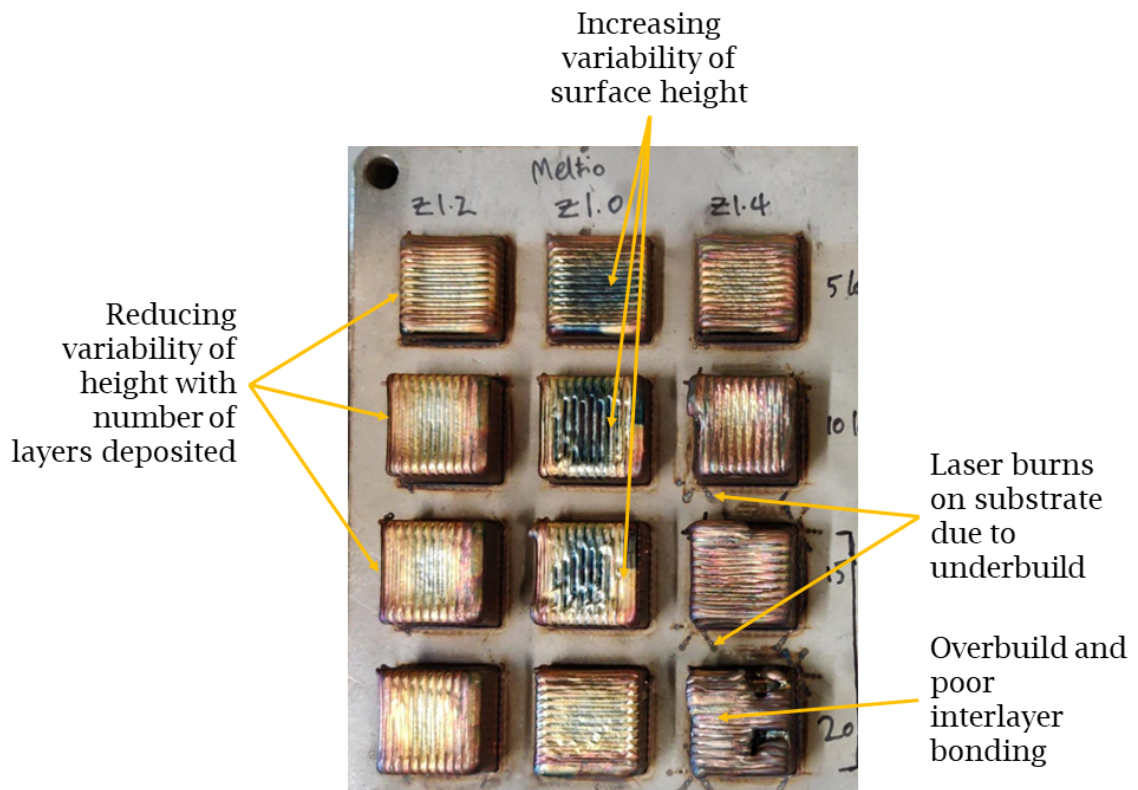
Figure 5.21: Annotated example of experimental plate containing multi-layer Z-increment test samples.
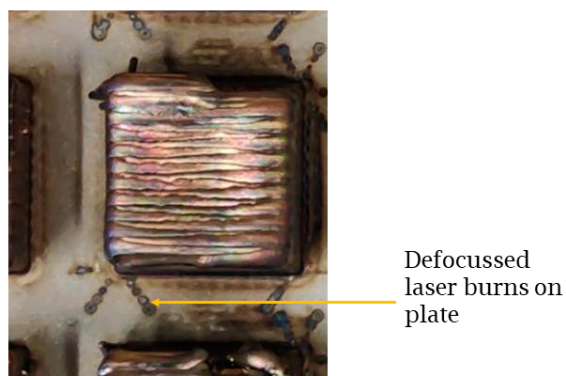
Figure 5.22: Example of laser burns on the substrate due to severely defocused laser.

(a) 1.0mm
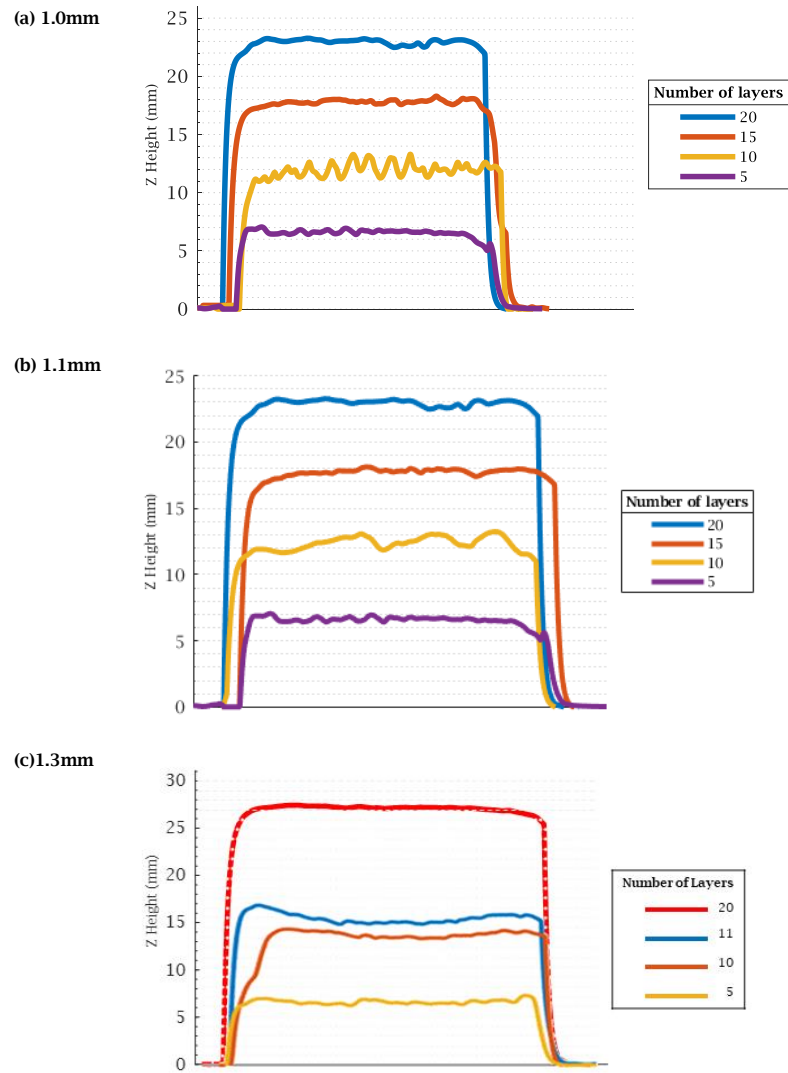
(b) 1.1mm

(c)1.3mm

Figure 5.23: Cross-section height measurements for (a) 1mm, (b) 1.1mm and (c) 1.3mm cubes.

Z-step (mm)	No. Layers	Z_{max} (mm)	Z_{min} (mm)	Z_{mean} (mm)	Std. Dev.	Predicted Part Height (mm)	Overbuild (% of layer)	Offset Distance (mm)
1.0	5	6.85	5.91	6.31	0.033	6	26%	5.69
1.0	10	12.05	11.56	11.85	0.009	12	-12%	6.15
1.0	11	13.25	12.68	12.93	0.011	13.2	-23%	6.27
1.0	12	14.76	13.37	13.99	0.016	14.4	-34%	6.41
1.0	20	23.32	21.70	22.41	0.016	24	-132%	7.59
1.1	5	6.86	5.94	6.48	0.037	6	40%	5.52
1.1	10	13.23	11.65	12.49	0.026	12	41%	5.51
1.1	15	18.29	17.16	17.81	0.008	18	-16%	6.19
1.1	20	23.59	22.68	23.10	0.009	24	-75%	6.9
1.3	5	6.72	6.09	6.42	0.023	6	35%	5.58
1.3	10	13.71	12.91	13.23	0.018	12	103%	4.77
1.3	11	15.84	14.37	14.82	0.024	13.2	135%	4.38
1.3	20	27.43	26.83	27.18	0.002	24	265%	2.82

Table 5.9: Summary of cross-section height measurements for 1mm, 1.1mm and 1.3mm cubes.

These data support the observations made with the 1.2mm increment, showing that increases in Z-step greater than 1.2mm result in overbuilding. The cubes for the 1.4mm Z increment were not measured, but the reason for abandoning the build of these was due to excessive overbuild of the part and poor layer adhesion, which can be seen in the right column of Figure 5.21, which supports the overbuild theory. The increments of 1.0mm and 1.1mm exhibit the opposite effect, which is likely because the focal point is moving deeper into the previously deposited layer, increasing the size of the laser spot and, therefore, the width of the track, reducing the layer height, as shown in Figure 5.19. It was confirmed that the expected total material volumes were conserved, meaning that the resulting over or underbuilds will cause a slight decrease or increase in the width of the cuboid. In all cases, the variability of the surface peak-to-peak height can be seen to be reducing with increasing layer height.

The increase in layer height follows a linear trend as the number of deposited layers increases at a consistent rate, the growth in layer thickness being proportional to the Z offset, shown in Figure 5.24.
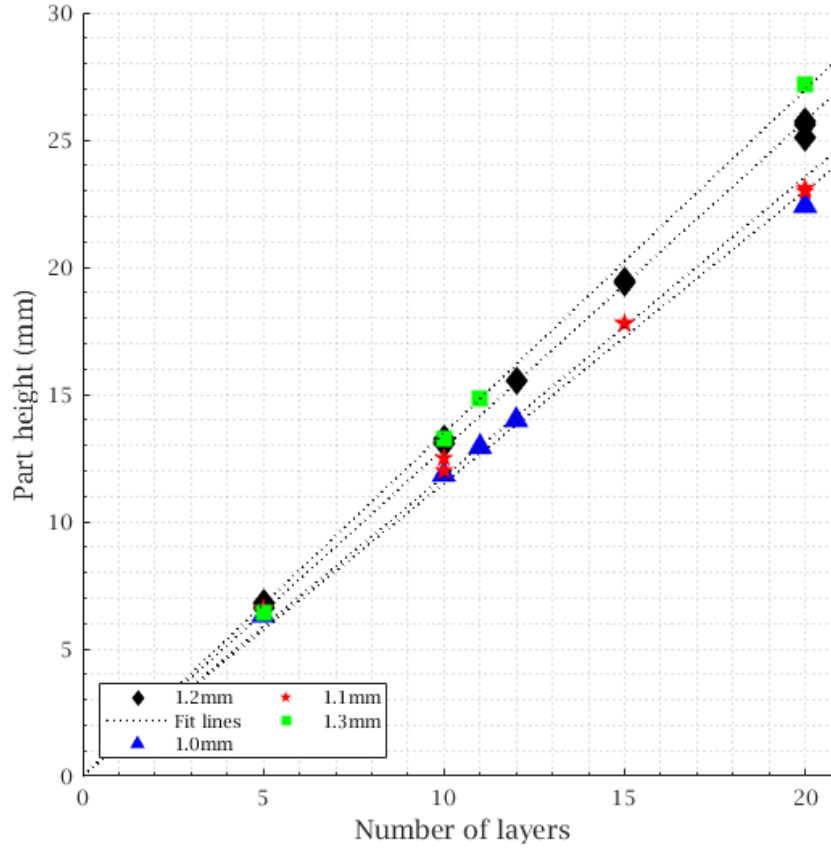
Figure 5.24: Relationship of part height to the number of layers deposited, showing a linear trend.

This allows a best-fit line to be derived to estimate the increase in height of the part, based on the Z for the conditions described in Table 5.1. This is shown in Equation 5.8, where h_{part} is the height of the cube measured at n_l number of layers high and Z_s is the Z-step increment used.

$$h_{part} = n_l \times 1.08 \times Z_s \tag{5.8}$$

This best-fit line has an R^2 of 0.993, showing a strong fit to the data, shown in Figure 5.25. Using this polynomial results in an accuracy of prediction for the height of the part within approximately 10 % of a layer, or 0.12mm. Such a result is more accurate than what is seen in the literature, but is not a general rule for any part or set of process parameters. However, it establishes an important relationship between

the focus of a coaxial laser system and the resulting multi-track layer thickness, which is not described in the literature.

If the Z-step is greater than or equal to the thickness of the first layer, there will be a growth in the layer thickness as the laser spot becomes smaller, remelting less of the layer below resulting in thicker layers; if the Z-step is less than the deposited layer thickness, the layer thickness reduces as the laser defocuses and grows, creating wider lower tracks which overlap more. A value for the Z-step can be selected that minimises the level of overbuilding or underbuilding as the height of the layer increases, summarised in Table 5.10. Understanding this mechanism in the change of the mean layer height also allows it to be factored into the build planning and corrected for during slicing of the part.
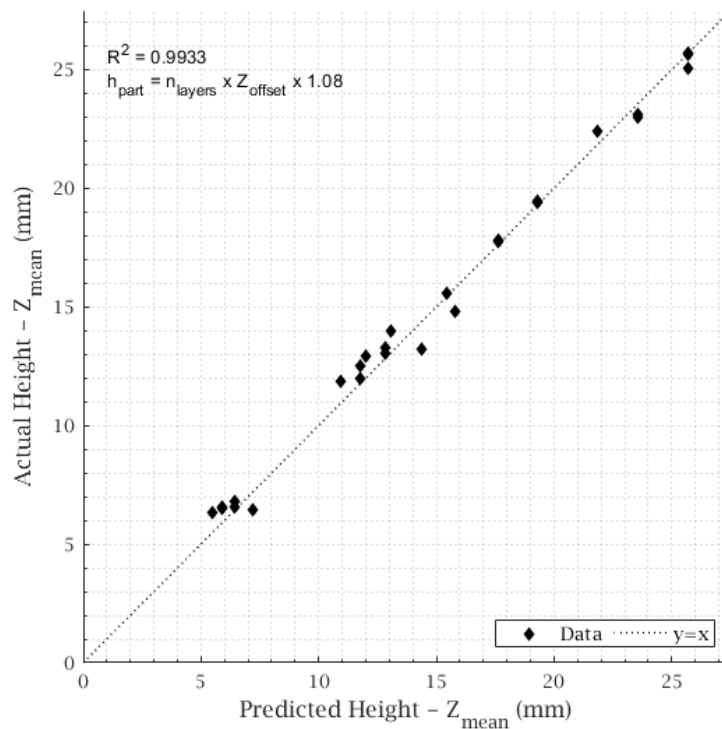
Figure 5.25: Predicted versus measured cube height using best fit line derived from experimental data.

Z Step	Layer Height	Part Width	Laser Spot Size
Equal to layer one height	Equal to layer one height	As planned	Calibrated spot
Greater than layer one height	Increasing	Decreasing	Decreasing
Less than layer one height	Decreasing	Increasing	Increasing

Table 5.10: Summary of Z offset effects on layer height, part width and laser spot size.

5.3 Conclusion

This study establishes the influence of track height, stepover distance, and track number on layer height. A predictive model for single-layer height was developed, supporting the need for process planning and optimisation, which is currently oversimplistic in slicing software and has limited coverage in the literature for this deposition method. The effect of the size of the Z-step was investigated, highlighting the impact of incorrect estimation of layer thickness on the offset of the head and consequently the size of the laser spot, increasing the height of the final part.

Chapter 6

Measuring and Modelling the Thermal History

Managing the thermal conditions throughout the deposition process of a multi-layer build is particularly important for the successful fabrication of LWAM components. Heating and cooling cycles and the resulting thermal gradients and melt pool behaviour are key determinants of the consistency of the resulting mechanical properties and residual stresses within the component.

Consistent interlayer temperatures during the deposition process are key to supporting uniform temperature gradients and consistent track geometries (Dass and Moridi, 2019; B. Wu et al., 2018). Interlayer pauses serve as a common approach to controlling the thermal field, particularly for managing the temperature of the layer immediately prior to the deposition of the subsequent layer. Modelling can support the achievement of optimal interlayer temperatures by reducing the range of experiments required, helping to predict layer temperatures, which are inherently challenging to measure.

There is no definitive consensus on a single objective value for interlayer temperatures for 316L stainless steel; the ideal temperature range appears to fall between 180°C and 300°C. However, there is a consensus that controlling the temperature within these limits is beneficial to the final quality of the printed part

in terms of improving the uniformity of shape and microstructure (Yadollahi et al., 2015). Datasheets for 316L stainless steel recommend using an objective maximum interlayer temperature of 200°C (ArcelorMittal Industeel, 2016), which is used as a target for this work.

6.1 Impact of Emissivity on Measurement of the Layer Temperature

The emissivity of 316L stainless steel varies significantly with temperature, surface morphology and particularly oxidation of the surface (Valiorgue et al., 2011). When very shiny, it can be approximately 0.25 (Al Zubaidi et al., 2019) and when heavily oxidised, it can reach 0.8 (D. Shi et al., 2015). Consequently, this can have a significant effect on the accuracy of temperature measurements and their fit to modelling data.

Figure 6.1 shows four examples of surface oxidation on the samples produced. It shows the first layer deposited in an inert environment, with a low emissivity of 0.25, image b shows a range of colours from light straw to regions of blue, indicating that the surface temperature was in the range of 290°C to 540°C (Łabanowski and Głowacka, 2011). Image C shows a range of red and brown colouring at 20 layers with short pauses between layers, suggesting a more consistent surface temperature, which reached 390 - 450°C. These estimated temperatures are indicative of the consistency of surface temperature, as the heat tint colours are highly dependent on the atmospheric oxygen content, the time at that temperature, and the surface finish (Łabanowski and Głowacka, 2011). These images show the range of oxidation that can be seen during and after the deposition process, which can significantly affect the emissivity (D. Shi et al., 2015).

Knowing the emissivity for each layer as the build progresses is challenging, and corrections are required to the data throughout the experimental process as the emissivity changes. To minimise changes in emissivity, seven-layer sample cuboids
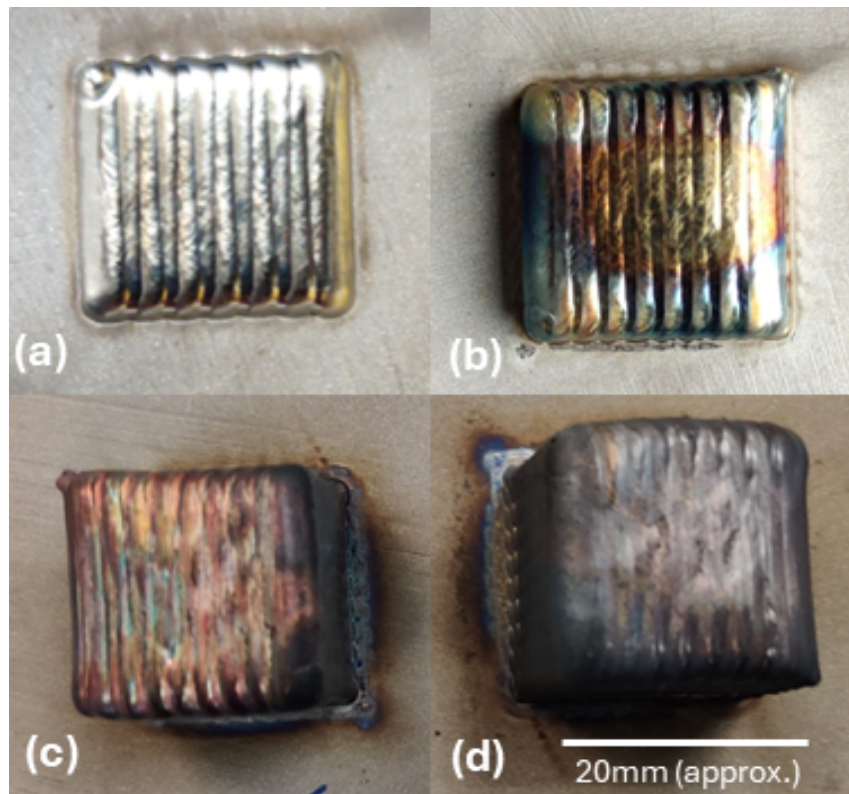
Figure 6.1: Surface oxidation for different numbers of layer depositions, (a) 1 layer (inert chamber), (b) 5 layers (inert chamber), (c) 20 layers – 30 second interlayer pause (local inert gas supply), (d) 20 layers – 150 second pause (local inert gas supply).

were printed in a fully inert chamber to minimise oxidation, the reading of the chamber oxygen sensor was maintained at 0.0% (sensor accuracy ±0.2%) using constant argon flow into the chamber. The small layer size ensured that the surface could be quickly deposited and moved to the infrared temperature sensor prior to oxidation. The sensor emissivity was calibrated to 0.25 and subsequently corrected in MatLab to align the infrared temperature measurements with the pyrometer sensor data measured on the substrate's base.

End-to-end alignment of sensor data is not possible because of the constant flux in the emissivity values, and the sensors only measure the same temperatures when thermal equilibrium is reached in the Z axis of the part. A point in time must

be selected on the cooling curves of the top and bottom sensors to calibrate the readings of the deposited layer. The data are aligned by assuming that the top of the deposited layer and the bottom of the plate measurement reach equilibrium and the plots align for a period.

Figure 6.2 shows an example of a single heating and cooling cycle taken from a sixteen-layer experiment with a 150 second interlayer pause. The pyrometer and thermocouple measure the increasing heat in the substrate as the layer is deposited, the pyrometer measures a lower temperature because of the increased distance from the layer and the effects of convective cooling on the surface of the substrate. The infrared sensor shows a vertical increase in temperature as the layer moves under the sensor approximately 8 seconds after the layer deposition is complete. Therefore, the data recorded are not the peak layer temperature.
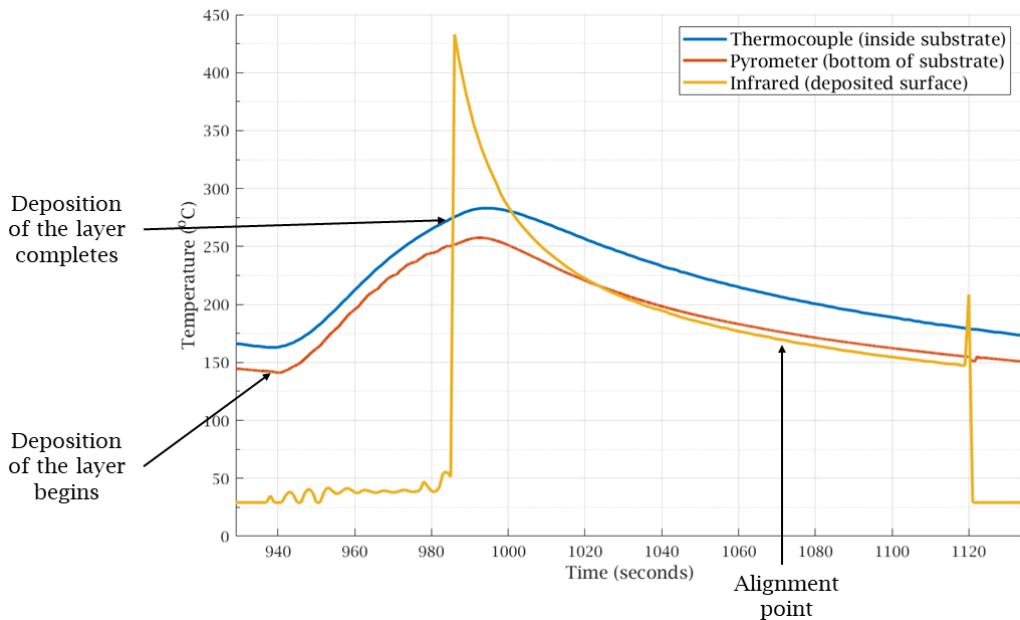
Figure 6.2: Plot of a single heating and cooling cycle, showing internal substrate (thermocouple), substrate base (pyrometer) and deposited layer (infrared) temperature.

Heating of the substrate continues after the deposition of the layer finishes. The alignment in terms of the time that the pyrometer peak is reached and the infrared sensor measurement begins varies throughout the experiments as a result of the rate of heating of the substrate, which is influenced by both the number of layers deposited and the duration of the pause used.

The layer cools during the pause period, and the cooling rate of the infrared sensor eventually matches that of the pyrometer as the part reaches thermal equilibrium on the Z axis. At this point, both sensors must be measuring the same temperatures as well as the same rate of cooling, and this point in the curves is chosen as the point to align their temperatures. The temperature of the infrared sensor appears to spike as the part is moved away for the next layer deposition and the substrate continues to cool until the next layer begins.

As the alignment point between the curves can only be for one point in time, a cooling curve must be selected from the measured layers to align the whole plot. Figure 6.3 shows the infrared data measurements aligned with each of the first four cooling curves of the pyrometer sensor of a seven-layer build. Table 6.1 details how close each aligned curve is to the other cooling curves, indicating the accuracy of alignment to each of the cooling curves. This indicates that the cooling curves for the second and third layers are aligned more closely across the whole experiment. Aligning at any point in the plot will mean that the other cooling curves do not fit quite as well, and the selection of the curve to align should minimise this difference. Consequently, the alignment for layer three was chosen for the seven-layer experimental data and layer five for the sixteen-layer data. To perform the data, the measured values were multiplied by a constant value to align the plots, which was consistently between 1.18 and 1.25.

(a) Layer 1

(b) Layer 2

(c) Layer 3

(d) Layer 4
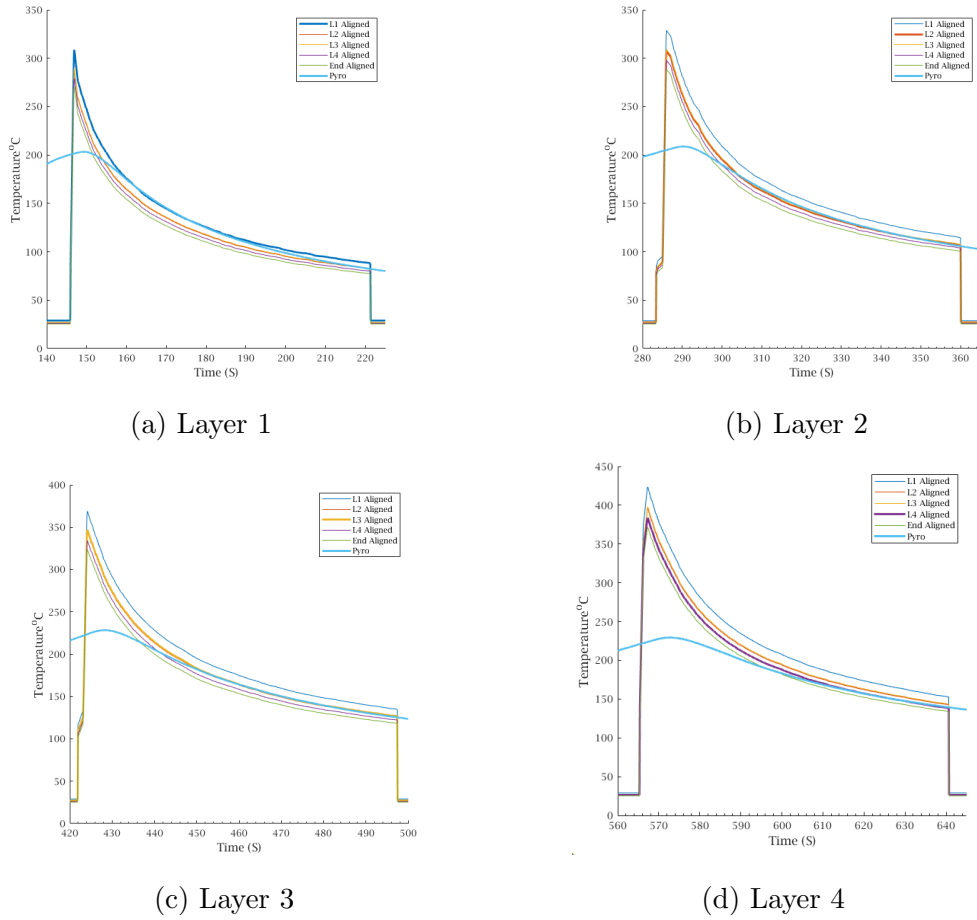
Figure 6.3: Closer examination of infrared data alignment for the first four cooling curves.

Layer No.	L1 Aligned (°C)	L2 Aligned (°C)	L3 Aligned (°C)	L4 Aligned (°C)	End of Cooling Aligned (°C)
1	0	-10.8	-10.7	-12.1	20.6
2	12.6	0	1.1	-5.5	-11.
3	10.5	1.	0	-5.9	-10.9
4	16.1	4.8	5.8	0	-4.9

Table 6.1: Alignment of cooling curves to neighbouring curve, to infer fit of the plot.

6.1.1   Interlayer Temperature Development During the Deposition Process

To measure the overall heating and cooling of the deposition process, two sets of 16-layer cuboids were deposited, one with 150-second pauses between layers and the other with 30-second pauses. Figures 6.4, 6.5 and 6.6 show the sensor data recorded for these experiments. The sixteen-layer experiments were completed with local inert gas only, due to temperature limits on the laser glass in the Meltio M450's door. This requires the use of the door fan, which operates inside the door cavity, but causes some extra airflow through the chamber, resulting in an average oxygen content in the chamber of approximately 17%.

Consequently, this causes increased oxidation of the part, particularly on the higher layers. Therefore, infrared sensor measurements of the deposited surface are treated as indicative. The correction of these data to layer five shows that the data align closely at the very beginning and at the end of the final cooling curve, suggesting good general alignment. Layers 3, 7, 11 and 13 were not measured with the infrared sensor, as their height was measured after these layers were deposited.
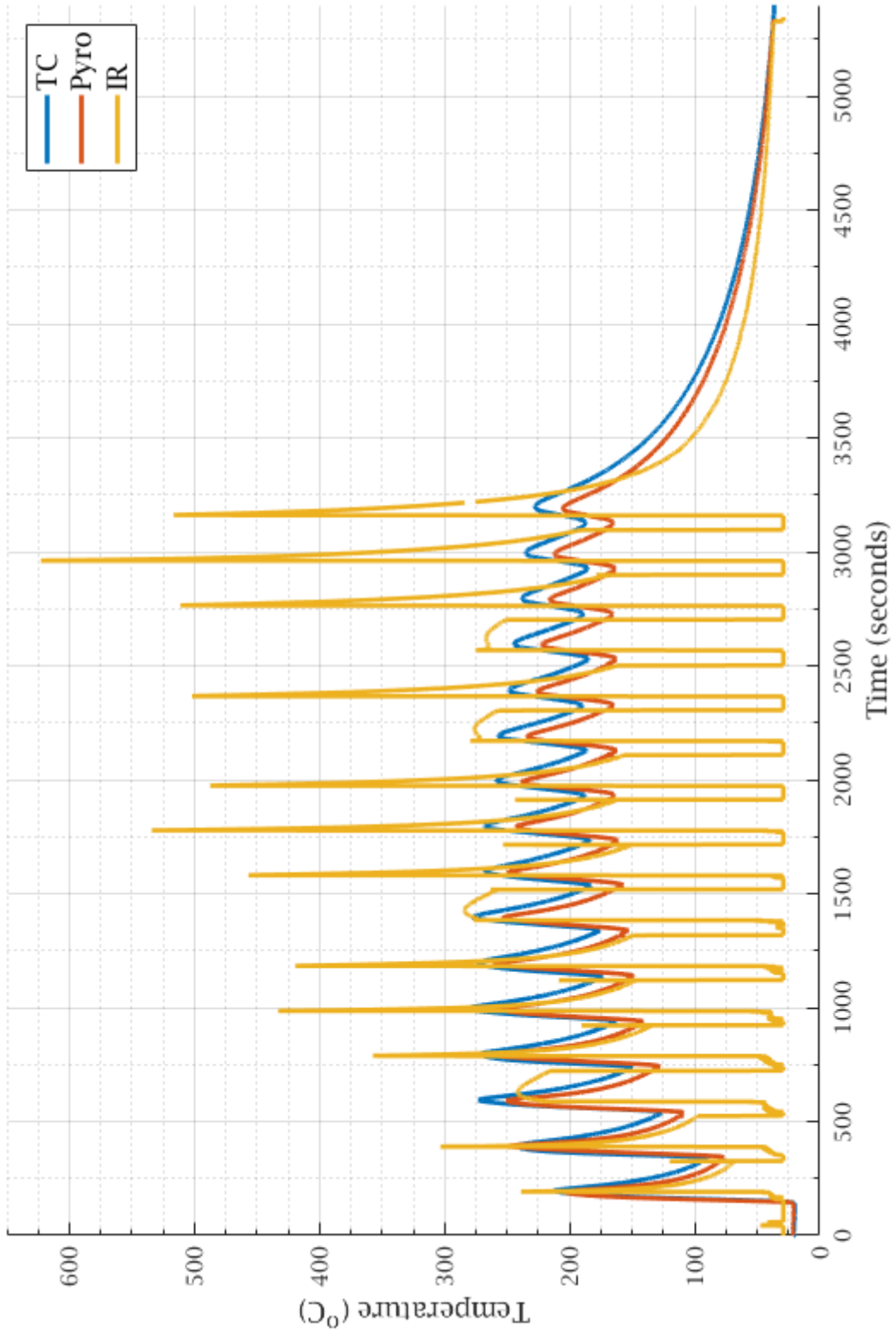
Figure 6.4: The sensor data recorded for 16-layer cuboid with 150-second pauses between layers.
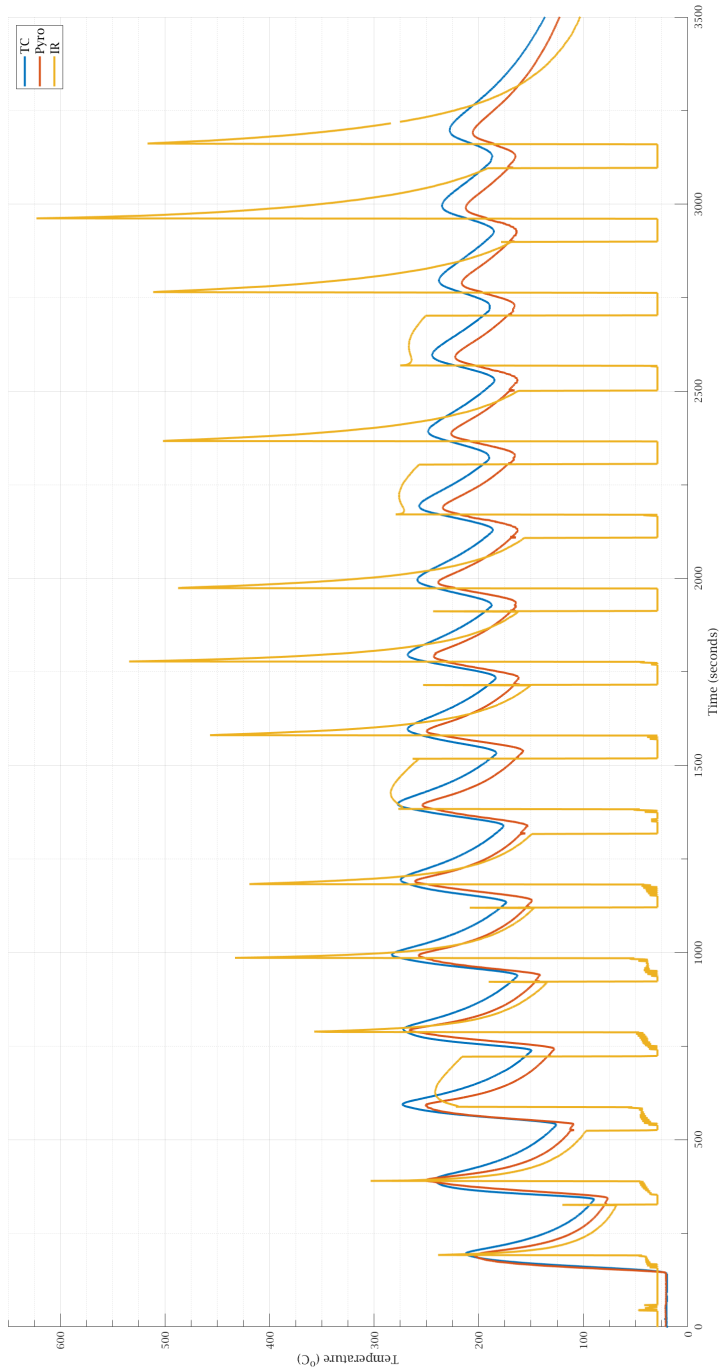
Figure 6.5: Closer view of the sensor data recorded for 16-layer cuboid with 150-second pauses between layers without the final cooling curve.

Figure 6.6: The sensor data recorded for 16-layer cuboid with 30-second pauses between layers without the final cooling curve.

The experiment with a 150-second pause shows rapid substrate heating post-deposition, observed via thermocouple and pyrometer data. The cooling time allows the newly deposited layer to reach a temperature close to the bottom surface as equilibrium is reached on the Z-axis.

The heating and cooling cycles can be seen for each individual layer, but an equilibrium is reached around layer six, where the mean temperature of the substrate remains around approximately 200°C. This is likely to be the point where the conduction of heat to the substrate becomes less effective and the heat is mostly radiated into the chamber. Above layer eight, the rate of cooling observed by the two sensors begins to differ, which would support this observation.

From layer three, the temperatures of the upper layer and the base of the substrate are within five degrees of each other within 30 to 40 seconds of the layer finishing. This is within the measurement error between the sensors of approximately 7°C. This would indicate that a pause shorter than 30 seconds would not result in an equilibrium between the base and the deposited layer, suggesting more severe temperature gradients across the deposited layer and in the Z-axis between the layer and the base of the substrate. Pauses longer than 30 seconds result in temperature and cooling rates aligning, suggesting that the base can be used to imply the layer temperature.

The deposited layer reaching the same temperature as the base before adding the next layer is an indicator of thermal equilibrium on the Z-axis of the part and the substrate. The consistency of the thermal gradient throughout the build reduces residual stresses and a uniform temperature distribution helps achieve consistent microstructural properties across layers (Yu et al., 2022).

The data for the 30 second pause between layers show that the bulk heating of the substrate is much greater, with significantly reduced time for cooling between layers, the substrate temperature reaching approximately 300°C, the layer did not have time to cool to an equilibrium with the plate surface in the time between layers.

This analysis shows that the surface temperature of the deposited layer and

the substrate base temperature are sufficient to estimate the interlayer temperature during the deposition process. Therefore, measurements were not taken with the thermocouple for subsequent experiments. This adjustment also simplifies the experimental configuration without sacrificing the quality or relevance of the thermal data collected.

6.1.2 Measurement of the Interlayer Temperature

Cuboids of 20mm x 20mm dimensions, consisting of seven layers were deposited in an inert chamber with pauses of 30, 60 and 90 seconds. This shape was chosen, as it was considered to be representative of a smaller section within a build, where temperatures build more rapidly and Singh et al. (2021) suggest interlayer pauses are particularly effective.

The results are plotted in Figures 6.7, 6.8 and 6.9, the pyrometer data measuring the substrate base temperature for each cuboid are overlaid in Figure 6.10. The inert chamber environment and the reduced number of layers allow for a confident interpretation of the temperature measurements from the infrared sensor. These data support the observation that 30 second pauses do not provide sufficient time for the substrate and the deposited layer temperatures to reach equilibrium before the deposition of the subsequent layer.

The estimated interlayer temperature increases between each deposited layer for all pause lengths, for short pauses it cannot be determined because the plots do not reach an equilibrium state, it must however be higher than the base temperature, making it unacceptably high compared to the objective interlayer temperature of 200°C. Short pauses of this order could have utility in increasing the part and substrate up to this limit in the first few deposited layers.

Interlayer temperatures can be estimated for longer pauses, for the 60 second pause experiment an estimated interlayer temperature of 90°C at the start of layer 2 and 170°C at the start of layer 7. The 90 second pause data show a narrower range of interlayer temperatures, with 80°C predicted for layer 2 starting and 150°C

for layer 7. Longer pauses also appear to reduce bulk heating, resulting in a lower mean substrate temperature, compared to shorter pauses.
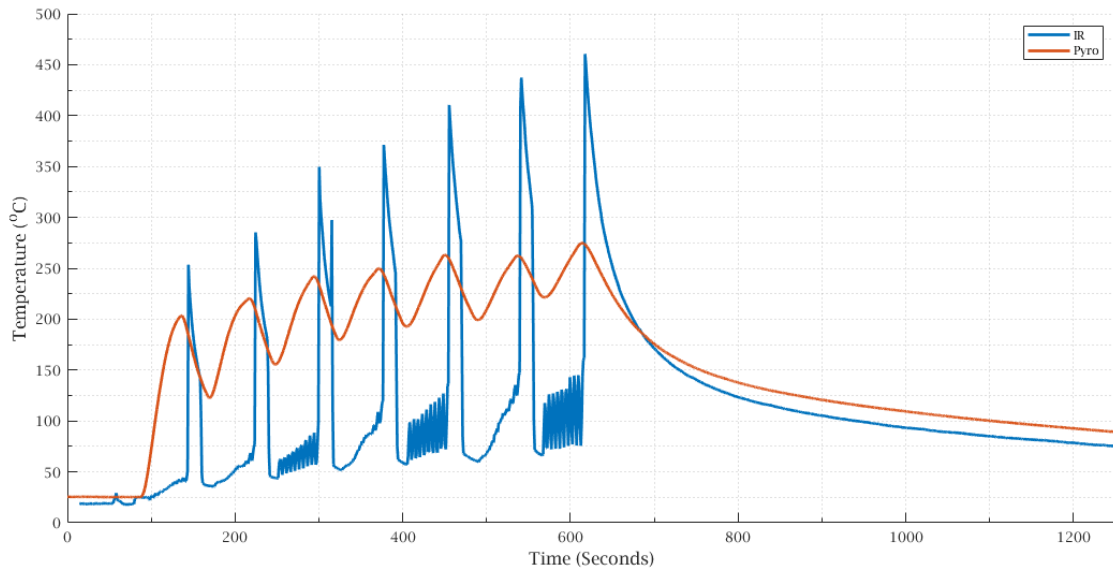
Figure 6.7: The sensor data recorded for 7-layer cuboid with 30-second pauses between layers.
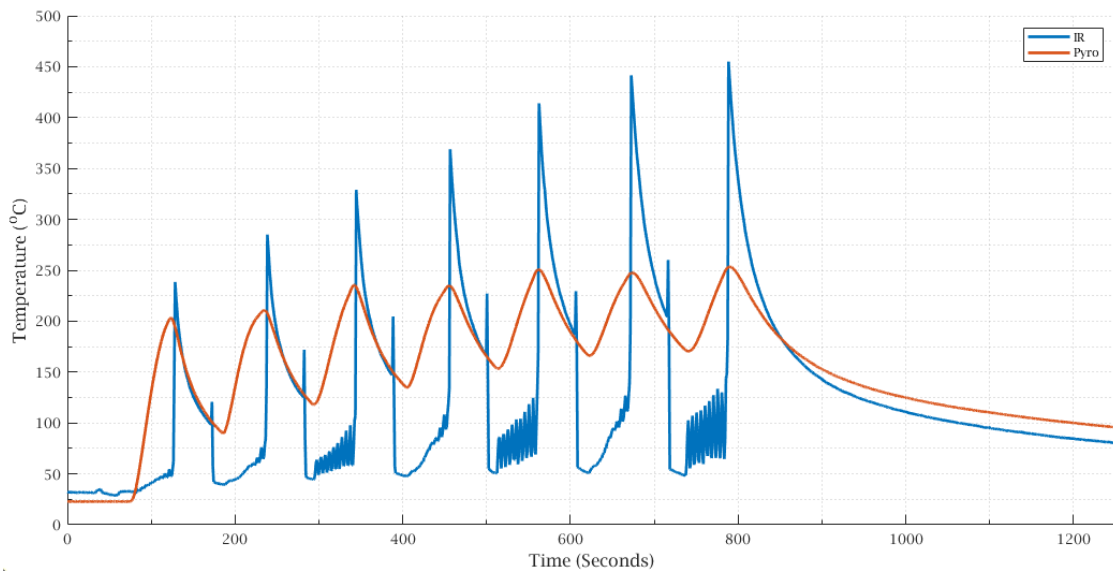
Figure 6.8: The sensor data recorded for 7-layer cuboid with 60-second pauses between layers.

180
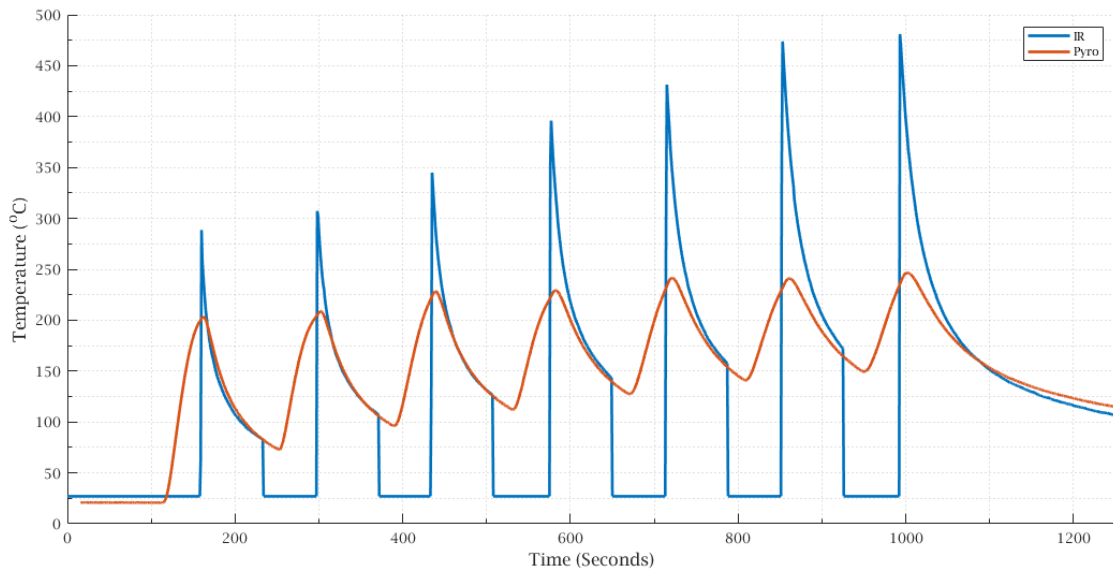
Figure 6.9: The sensor data recorded for 7-layer cuboid with 90-second pauses between layers.
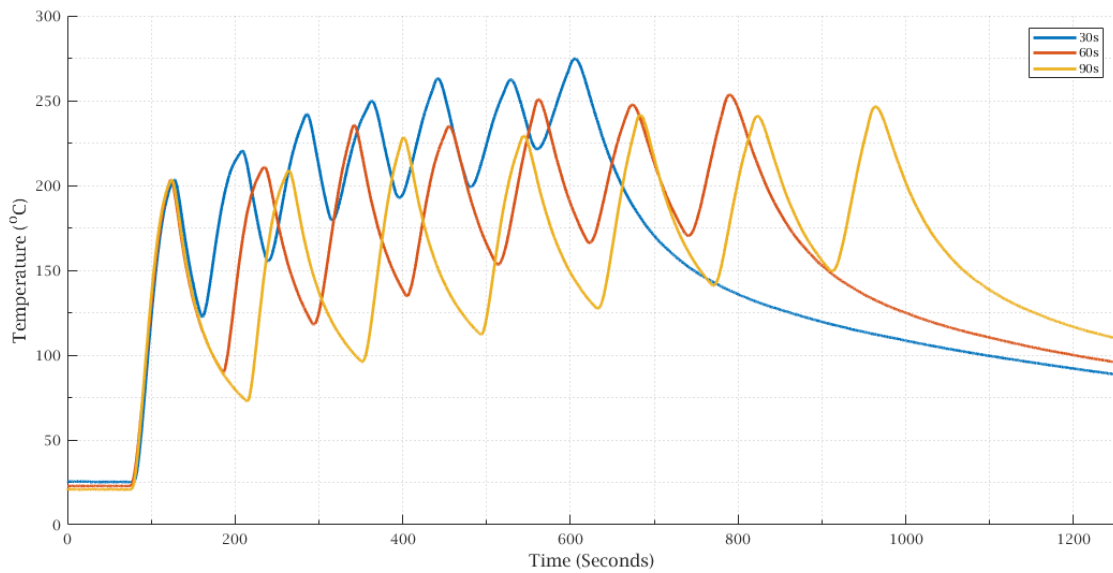
Figure 6.10: The pyrometer base temperature data recorded for 7-layer cuboids with 30, 60 and 90-second pauses between layers overlaid together.

6.2   Modelling the Interlayer Temperature During Deposition

The interlayer pauses described above were modelled using Netfabb Local Simulation to investigate the effectiveness of an off-the-shelf AM thermal modelling tool for the prediction of the part temperatures developed during the deposition process. Through this, further insight into the deposition process can be gained by modelling the heat flow in the deposited part, supporting the identification of optimum interlayer pause times for this case.

6.2.1   Configuring Netfabb Local Simulation

The adaptive meshing and h values must be set to meet the simulation requirements. To determine the effect of different meshing configurations, a series of simulations were run and compared to identify the optimum configuration.

The mesh is defined with three parameters: the number of elements per heat source radius, the number of fine layers below the heat source radius and the number of adaptivity levels, which specifies how many times the mesh size can be incremented. Autodesk recommends one or two elements per heat source radius, and one element per heat source radius was selected to avoid convergence problems. Five fine layers below the source were selected to ensure sufficient detailed modelling of the deposited layers. The accuracy of one, two and four refinement levels was compared, Figure 6.11 shows the meshing for a five-layer 20mm x 20mm cuboid with these different refinement levels. It was found that with one refinement level, the computational time was several hours, with two levels this was reduced by 25% and with four levels it was reduced by almost 50%.

Figure 6.12 shows a comparison of the temperature probe readings taken from the bottom face of the print substrate for each of the meshes shown in Figure 6.11. It shows that with four levels of refinement, the peak temperature is significantly lower than the other two simulations. However, there is little else to discriminate
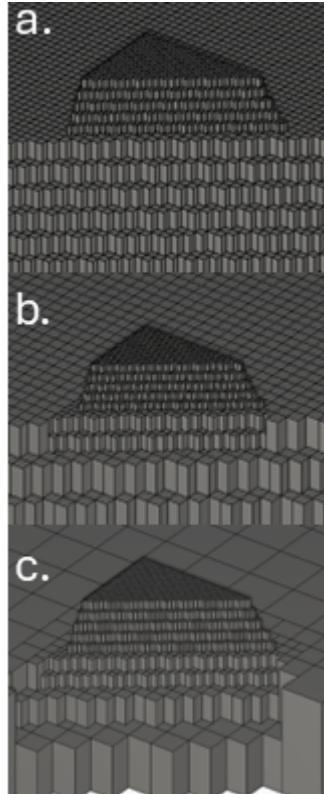
Figure 6.11: The meshing for a five layer, 20mm x 20mm cuboid with (a) one, (b) two and (c) four refinement levels.

between two and one refinement level; therefore, two refinement levels were selected to capitalise on the reduced modelling time. The effects of adaptive time steps can also be seen in the cooling curves: the heating phase, during the deposition process, showing a thick line of data points, with few generated during the cooling phase.

Netfabb has a simplistic representation of the melt pool and the deposition of the track within the model. Despite the capability to define multiple voxels within a single-track width, the laser spot size cannot exceed the track width, and tracks are deposited discretely in parallel with no stepover or remelting. The simulation was therefore configured to deposit the same number of tracks as the experiment and the same total energy was deposited for the layer. However, the tracks and laser spot were 1mm wide, rather than the 2mm wide overlapped tracks seen in the experiment, effectively doubling the energy density in the melt pool.
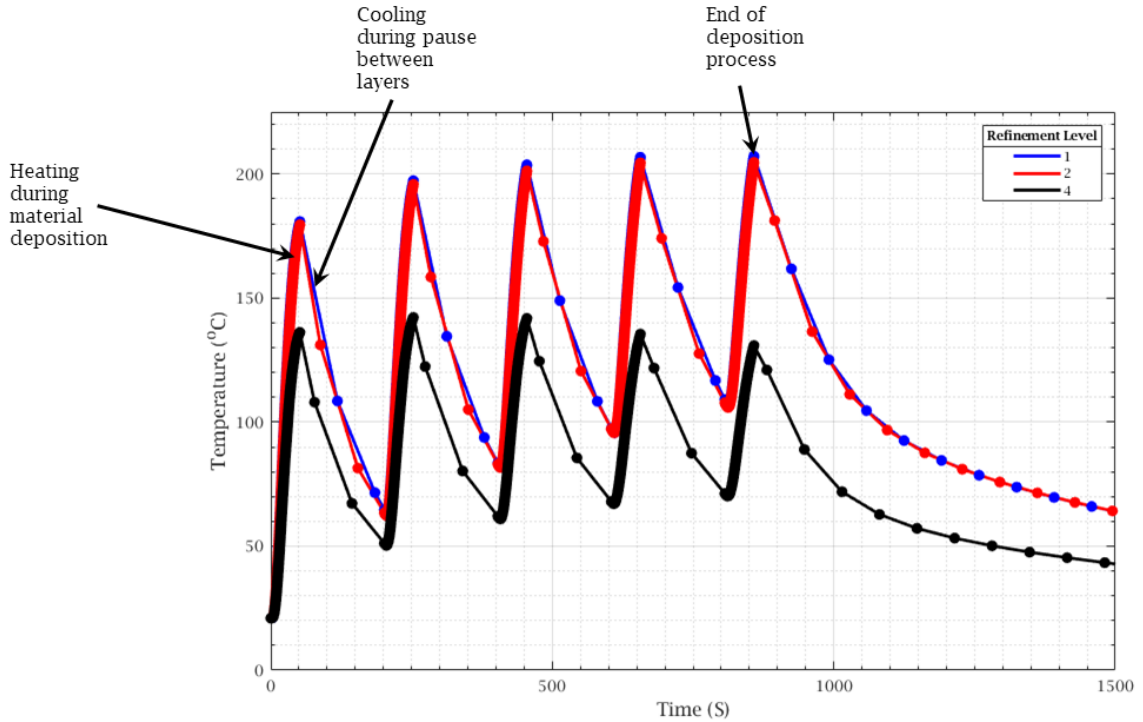
Figure 6.12: Comparison of the cooling curves for one, two and four refinement levels.

Although these constraints are particularly limiting when trying to model the discrete dynamics of track deposition and melt pool formation, processes that are crucial to understanding the microstructural evolution and mechanical properties of the deposited material. For the purposes of evaluating the cooling phase after the deposition of a complete layer, these constraints can be considered acceptable, as the total number of passes of the deposition head and the total energy density for the layer are equivalent to the experiment; meaning that the layer can be treated as a 'slab' model, which makes it possible to approximate the thermal history of the deposited layer and observe the cooling phase immediately after the layer is complete. This results in the temperature probe measurements in the layers during the deposition of the layer not being representative or comparable to the measured data, but the base temperature measurements can be used.

The tool was configured with the predefined material parameters for 316L

stainless steel from the Netfabb material library, described in Table 3.6. The constraints in track size and the improved absorption efficiency of coaxial laser systems result in the simulation absorption efficiency being set to 100%. To determine the most appropriate value of the thermal coefficient, h, which is a fixed global value for the whole simulation, a simulation of a 20mm x 20mm 16-layer cuboid was run with a variety of values for h, 15, 23 and 50 $W/(m^2K)$. Figure 6.13 shows a plot of the temperature measurements taken from a probe on the bottom of the substrate, plotted against experimental data taken using the laser pyrometer aligned to the same point on the physical plate.

Due to the limitation of a global h value throughout the process, any chosen value is a compromise, either fitting well with the rapid cooling phase seen immediately after the layer deposition of the layer is complete for 50 $W/(m^2K)$, seen in the cooling rates of the first few layers shown in Figure 6.13. Alternatively, bulk heating of the component can be well simulated, as seen with the other two curves. The main objective of the modelling was to understand the minimum layer temperature reached before the deposition of the next layer. The value of 23 $W/(m^2K)$ is more closely aligned with the bulk heating and cooling, particularly the minimum temperature reached, which was the value chosen for all simulations; this value fits within the expected thermal conductivity of stainless steel in air, typically $10 - 40$ $W/(m^2K)$ (Lienhard, 2011).
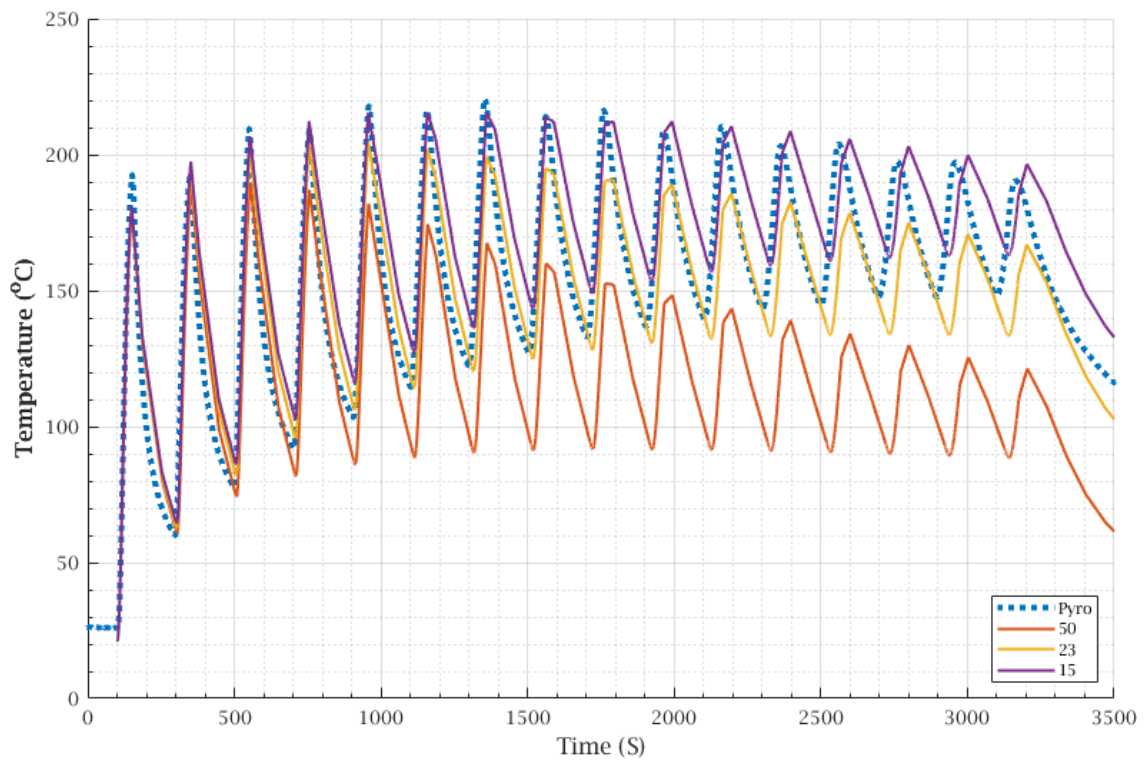
Figure 6.13: Comparison of the effects of different values of the thermal coefficient, h, on simulated heating and cooling cycles.

6.2.2 General Model of Part Cooling

Modelling has concentrated on the seven-layer models produced in an inert chamber, where infrared sensor data are most accurate. To investigate the general cooling mechanisms within the component, some initial modelling of the 16-layer process with 150 second pauses was carried out.

Figure 6.14 shows screenshots of the steps modelled immediately after the final layer is deposited, due to the reduced number of data points generated by adaptive time steps during the cooling cycle, this figure is indicative of the resolution of the data available to describe the cooling. The melt pool can be seen immediately after the deposition of the last layer on the cuboid (image a), revealing a melt pool at approximately 8000°C, which is likely to be much higher than the actual melt pool temperature. This is caused by the limitations of the model, which create a much narrower melt pool than is seen in the system.

Thirty seconds later, the temperature gradient remains, the corner is reduced to 630°C and most of the part is above 500°C (image b), which approximates the infrared sensor (Figure 6.4). The temperature gradient on the Z-axis between the top of the layer and the base is shown to be approximately 250°C, consistent with the experimental data, which shows a range at this point of 236°C. The base temperature is still rising at this point. By 90 seconds, the temperature across the surface becomes uniform at approximately 350°C and the substrate below the part continues to heat up; the temperature gradient between the part and the substrate provides effective cooling. The gradient in the Z-axis between the top surface and the base is approximately 50°C, which was measured experimentally at 46°C.

Six minutes later, the top surface begins to cool faster than the core, as heat is drawn into the substrate and dissipated through radiation into the chamber's atmosphere. At this stage, most of the plate maintains a uniform temperature within a range of 10°C. By nine minutes, the temperature of the plate below the part exceeds that of the part itself, showing the continued, higher rate of cooling enabled by conduction of heat into the larger volume substrate and cooling from the

top of the part to the chamber atmosphere. This behaviour aligns with experimental data, where infrared sensor measurements of the final deposited surface fall below the temperatures recorded by a pyrometer on the substrate's underside. At this point, the relatively uniform temperature across the substrate negates the rapid cooling of the part through the substrate.
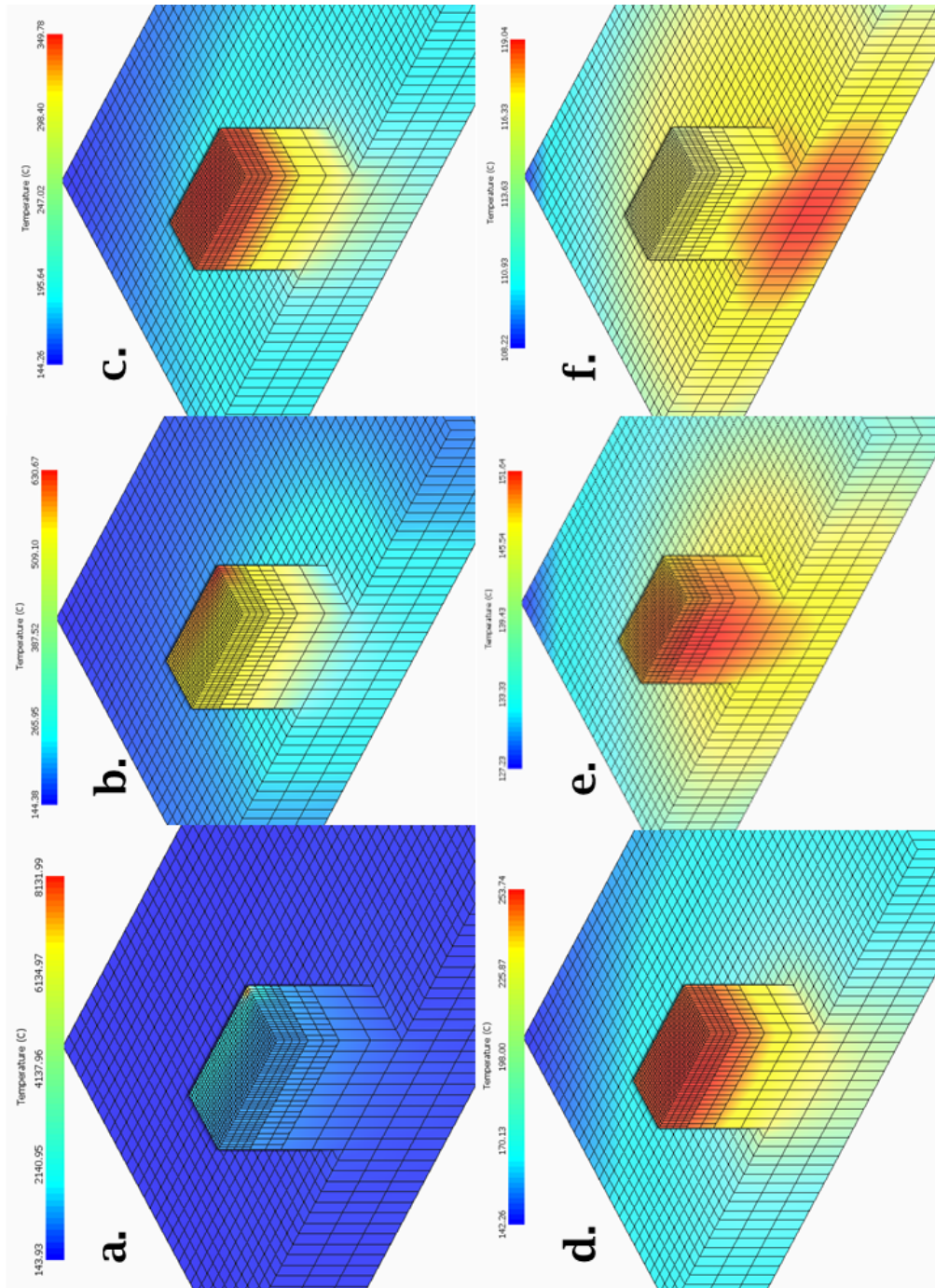
Figure 6.14: Screenshots taken from Netfabb of 16 layer cuboid, 150s pause between layers. The images show simulation immediately after (a) the end of the final layer, (b) after 30 seconds, (c) 90 seconds, (d) 3 minutes, (e) 6 minutes and (f) 9 minutes.

6.2.3   Modelling the Seven Layer Deposition Process

The simulations of seven-layer cuboids with 90, 60 and 30-second pauses are shown in Figures 6.15, 6.16, 6.17, 6.18, 6.19 and 6.20 respectively. The simulations were created to replicate the physical experiments but continued to sixteen layers, which was not possible with the restrictions of the machine. The data shown from these models use the measurement point on the substrate aligned with the pyrometer data, using this as the indicator of interlayer temperature, discussed above.
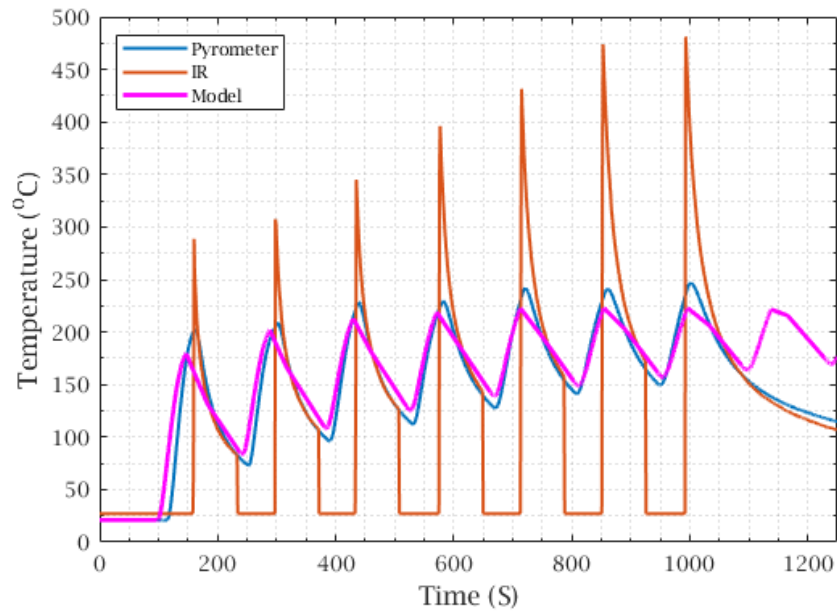
Figure 6.15: 90 second pause, modelled substrate temperature with matching pyrometer and infrared measurements.
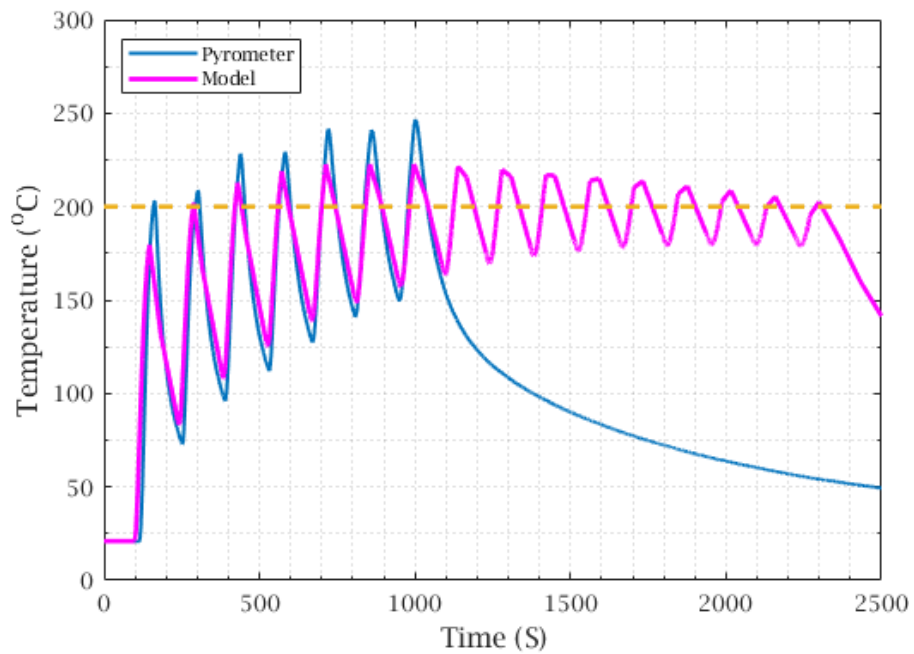
Figure 6.16: 90 Second Pause, modelled substrate temperature to 16 layers and 200°C objective interlayer temperature.
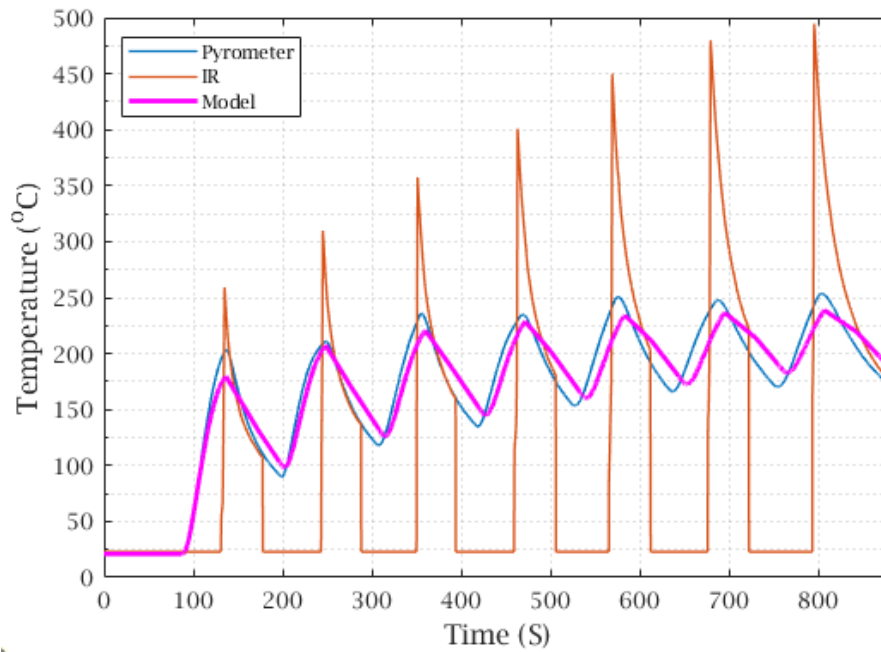
Figure 6.17: 60 second pause, modelled substrate temperature with matching pyrometer and infrared measurements.
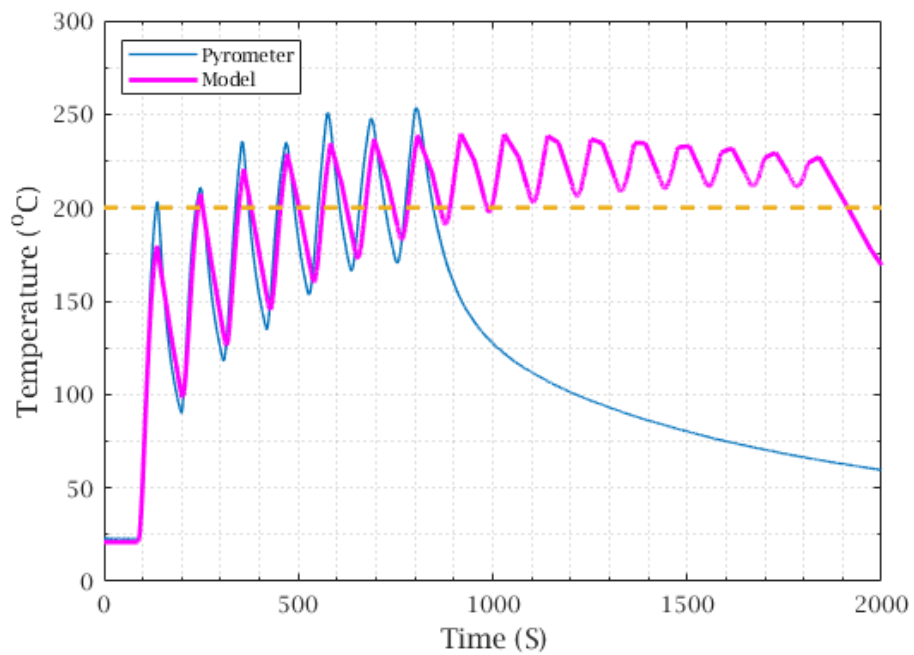
Figure 6.18: 60 Second Pause, modelled substrate temperature to 16 layers and 200°C objective interlayer temperature.
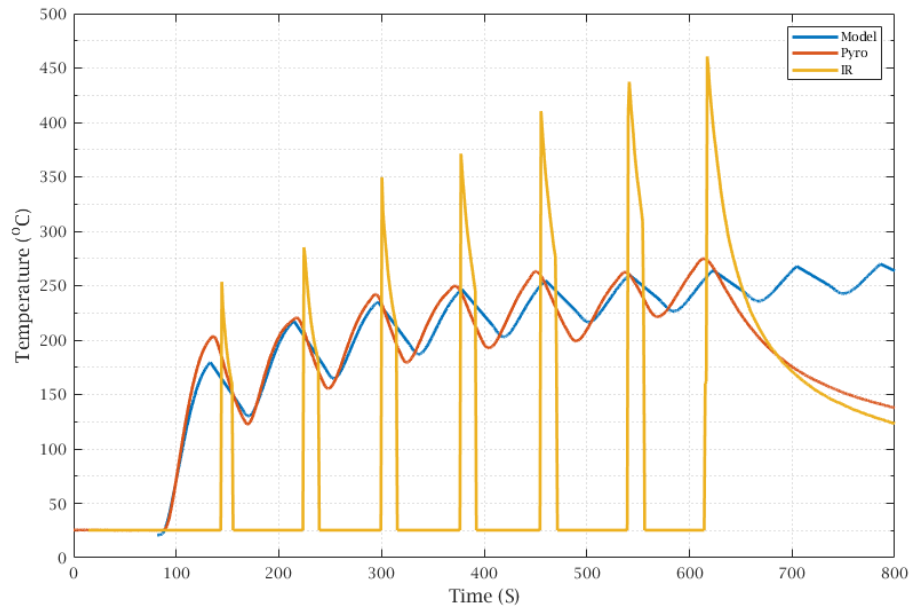
Figure 6.19: 30 second pause, modelled substrate temperature with matching pyrometer and infrared measurements.
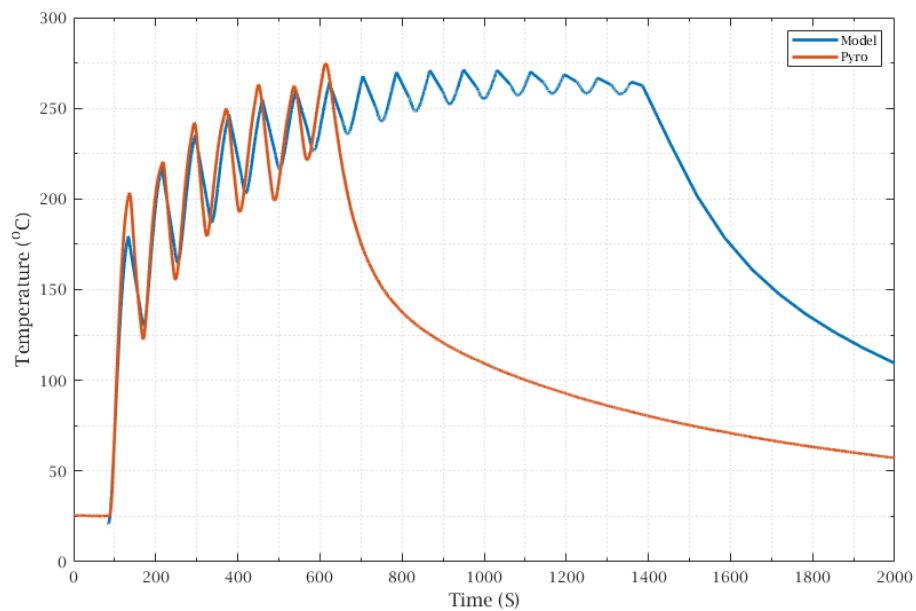
Figure 6.20: 30 Second Pause, modelled substrate temperature to 16 layers and 200°C objective interlayer temperature.

From these data, it can be seen that the model performs well in predicting the heating and cooling of the substrate, closely matching the heating and cooling cycles. The minimum temperatures seen in each cooling cycle have a typical variance of approximately 10°C. In all cases, the model predicted a slightly higher temperature than that seen in the experimental data, which could not be corrected by adjustments to the value for h. The fit of the cooling rates decreases with increasing layer height, which is likely due to the changing value of h due to increased convectional cooling through the greater surface area of the part. This is compounded by the changing emissivity, which increases with increasing temperature.

Figure 6.21 shows a comparison of the sixteen-layer pyrometer data and its equivalent modelled data. The minimum base temperature and therefore the inferred interlayer temperature are still within 13°C of the temperatures seen experimentally, despite the decreasing fit to the cooling rates. This characteristic is acceptable for a study of interlayer temperatures, since the important feature of the model is the estimated minimum interlayer temperatures rather than the time synchronisation.
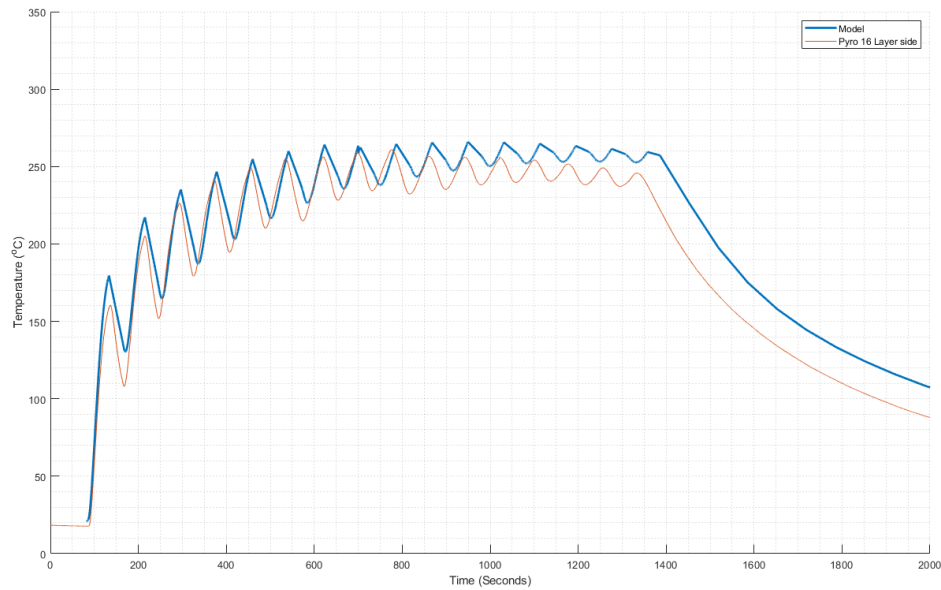
Figure 6.21: Comparison of modelled sixteen-layer build, 30 second pause base temperature data to the equivalent pyrometer data.

The predictions for the interlayer temperatures of the seven-layer process, when continued to sixteen layers, indicate that, with a 90-second pause, temperatures consistently fall around 20°C below the targeted 200°C maximum interlayer temperature threshold, once the bulk heating of the substrate stabilises from the eighth layer onwards. In contrast, the interlayer temperatures with 60-second pauses remain approximately 10°C above this threshold. Although the error margin of the model is about the same range, it suggests that the interlayer temperature could exceed the 200°C limit.

A pause time of 75 seconds between these two is likely to reach the objective temperature without exceeding it. Figure 6.22 shows the predicted substrate temperature for a 75-second pause, and Figure 6.23 shows the predicted substrate base temperatures for each of the pauses modelled or measured experimentally.

195
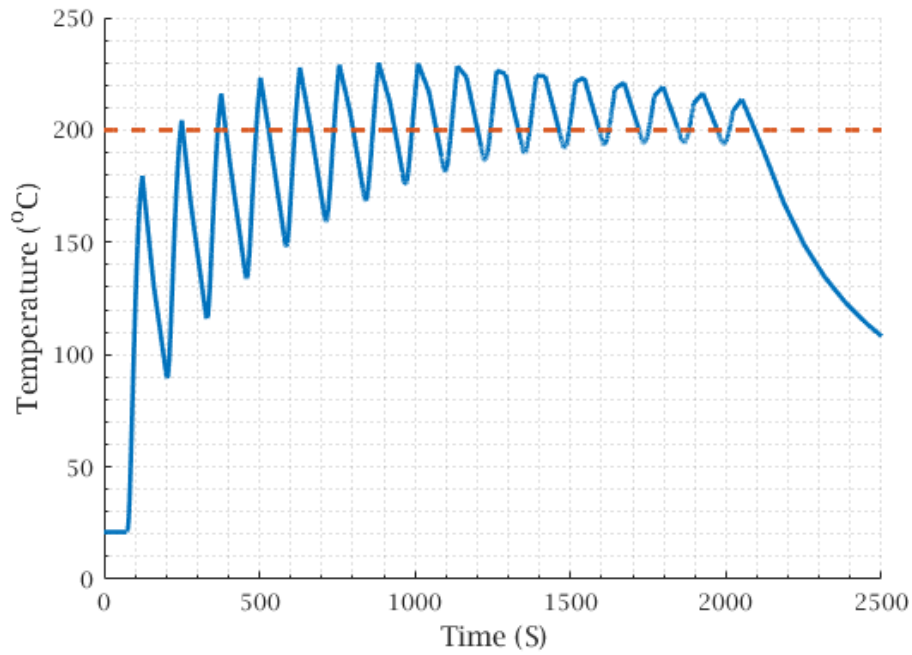
Figure 6.22: Predicted heating and cooling cycles for 75 second interlayer pause with target 200°C line.
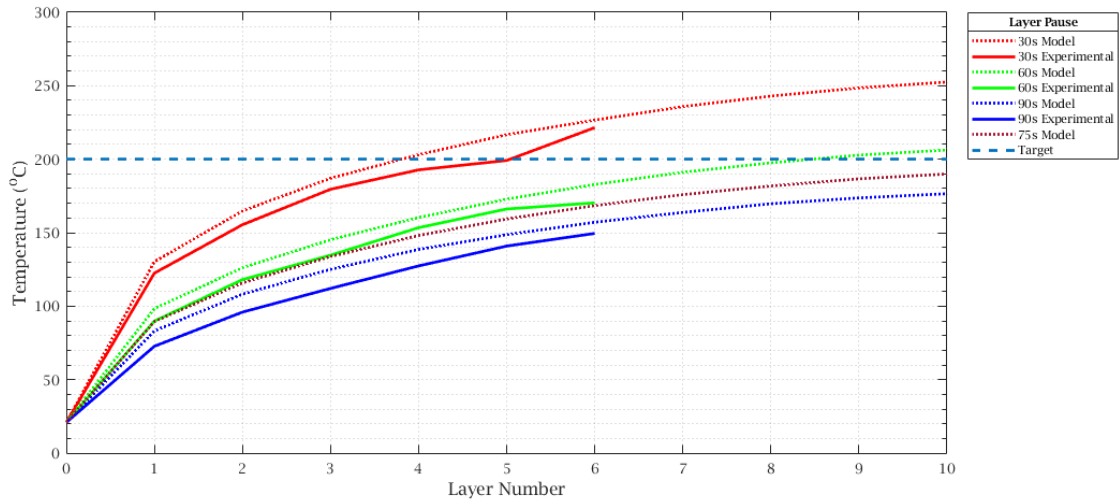
Figure 6.23: The predicted and measured substrate base temperatures for all pauses.

Figure 6.23 shows that base temperatures increase uniformly and that the models slightly overpredict interlayer temperatures across the range of pauses. Given the accumulated error across the experimental and modelled data, this gap in the order of approximately 10°C falls within these errors which, when combined, are in the

range of 13 to 20°C. The curves flatten between layers eight and ten as the substrate and part reach thermal equilibrium.

From these data, it can be concluded that the duration of the pause has a clear effect on the rate at which the interlayer temperature increases. For pauses above thirty seconds, these data can be used to infer the interlayer temperature; it was seen in the experimental data that equilibrium in the Z-axis is reached in this time frame. Should the interlayer temperature target be changed, the duration of the pause can be adjusted to achieve it. This knowledge can be used to print a raft beneath a part to overcome the ramp-up in interlayer temperatures before the relatively steady state is reached for the deposition of the part at around layer five, allowing the component to benefit from the consistency of the part temperature.

These results and conclusions are also consistent with the work of Yu et al. (2022), who investigated the effects of interlayer pauses and power reduction for the deposition of thin walls in DED powder. Their work showed that interlayer pauses to maintain consistent deposition temperatures for each layer resulted in improved uniformity of the cross-sectional shape, finer microstructure, and higher microhardness. To do this, pauses were used in conjunction with incremental reductions in laser power to level off the interlayer temperatures to a 'steady state' in a lower layer, increasing the uniformity of the wall's properties. Combining the effects of pauses with reductions in power would be a useful next step.

This approach of using the base temperature to infer the interlayer temperature, in conjunction with interlayer pauses, was not found in the literature. While only proven in this limited case, it may scale to other more complex parts and offers a more practical method of monitoring in process temperatures of the part. This work could particularly benefit from the research published in this area regarding the enhancement of thermal modelling with machine learning techniques to speed up the adaptation of simulations to different part geometries, such as Mozaffar et al. (2018) and Le et al. (2023) .

Farias, Cruz Payão Filho, and Oliveira (2021) determined the interlayer

temperature for single-track thin walls, with a simple ANN architecture. The developed network had an accuracy similar to that of the equivalent FEA model. Due to the speed of the trained model, it could be used to determine the interlayer temperature for a range of pause times not modelled and to quickly determine the effect of varying other process parameters on the overall temperature of the wall, saving many hours of simulation time.

6.3   Conclusions

These results can improve the understanding of thermal management in the LWAM deposition process and broader conclusions can be drawn for more general applications. For this geometry and process parameters, pauses of less than 30 seconds between layers lead to an increase in interlayer temperatures, which exacerbates thermal gradients and reduces the consistency of the geometry and microstructure of the component. Although the specific threshold of thirty seconds may vary depending on the type of part, this incremental heating scenario is likely to occur in other geometries. Toolpath durations are typically longer than thirty seconds for single layers in most parts; however, specific scenarios, such as infill patterns and perimeters of thin sections, or where the starting point for a layer is at the same point as where the previous layer was completed, pauses may fall within this timeframe. General rules of minimum time limits for layers are sometimes used to mitigate this, a more nuanced approach through calculating the interlayer pause times for different sections of the layer to achieve a more consistent temperature across the layer, an extension of Michel et al. (2019), would improve on this.

This work also confirms the value of a more constrained, simplistic modelling tool such as Netfabb Local Simulation to offer insights into the deposition process, which can be used to improve the quality and consistency of the final part.

Chapter 7

Conclusions and Further Work

7.1 Novelty and Key Conclusions

This thesis has determined how fundamental process parameters of extrusion rate, head speed and laser power can be controlled to create high quality single-tracks for a novel, coaxial LWAM System. It has shown how they can be used effectively to create multi-track layers and how the layer height can be predicted. It has established the relationships between the extrusion rate and head speed and the resulting track heights and widths, which can be described with process windows. It has described for the first time how layer deposition can result in overbuilding due to defocussing of the lasers and how this can be estimated to aid its mitigation during build planning.

The heating and cooling cycles for the deposited layers were investigated experimentally, and the effects of interlayer pauses on the resulting steady-state mean temperature due to bulk heating were described. This was modelled using Netfabb Local Simulation to identify an optimal pause duration to achieve a target maximum interlayer temperature of 200 °C for the cuboids produced in the experimental stage. Key conclusions and novel contributions to the field include:

Chapter 4 - Effect of Process Parameters on Single-Track Geometry

This chapter developed a refined definition for high-quality tracks for LWAM systems

and the process parameter ranges that could be used to create such tracks with this experimental configuration. The relationship between changes in extrusion rate and head speed on the resulting cross section was defined, and the principles were demonstrated to be consistent with the literature for other DED technologies. A Cascade Forward Neural Network was shown to be more accurate in predicting the width of tracks than polynomials derived from experimental results. It was shown that Machine Learning can be used to address the uncertainty in track width measurements in this process, even when the causes of this uncertainty are not fully characterised.

Chapter 5 - Optimisation of Single and Multi-Layer Deposition

This chapter developed a simple mathematical single-layer model to predict layer height as a function of the number of tracks, the stepover between tracks, and the track height. It quantified the effect of the number of tracks in a layer on the resulting layer height, which has not been described mathematically in the literature. It was also identified in this work that the stepover of the track affects the dilution and remelting between layers. It was shown that inaccurate layer height prediction and the resulting Z-axis increments can result in defocused lasers, a characteristic specific to LWAM. This results in melt pools that create track widths and overlaps that differ from the planned layer, leading to layers that are thicker or thinner than planned. This adds to the limited published work on LWAM coaxial systems, which has focused on thin-wall parts. These characteristics are poorly captured in slicing tools, which can result in suboptimal parts if not addressed.

Chapter 6 - Measuring and Modelling the Thermal History

This chapter adds to the limited material published on the thermal behaviour (part heating and cooling) of coaxial LWAM systems. It shows that for interlayer pauses of 60 seconds or more, the base temperature could be used to infer the interlayer temperature for small cuboids because the part and substrate reach a thermal equilibrium in the Z-axis plane. The work characterises the bulk heating and the

mean temperature of the steady-state conditions once cooling from the substrate becomes minimal.

7.2 Contributions to the Knowledge Gaps

7.2.1 Precision, Tolerance Variability and Toolpaths

Knowledge gaps associated with precision, tolerance to geometry variability and toolpaths addressed in a number of chapters. Firstly, through describing how extrusion rates, laser power and head speed settings can be used to predict track cross-sectional shape, height and width. Secondly, through the single-layer model, describing mathematically how the number of tracks and their separation translate into layer thickness, an effect not well characterised in the current literature. Finally, this was addressed through the exploration of overbuilding due to defocussing of the laser. It was shown that this could be a cause of overbuilding, which is not documented in the current literature or captured in slicing tools, which assume a fixed Z-step. In the discussion, it was highlighted that this effect can be planned for and corrected with varied Z increments and corrective layers. However, within limits, the deposition process is tolerant of this effect, because of the advantages of the melt pool being created with multiple lasers.

7.2.2 Temperature Management Strategies

Methods for managing the bulk heating and maximum interlyer temperatures were investigated and modelled and it was shown that pauses could be used to change the level of bulk heating in the test components and substrate and could be used to stay below an objective maximum interlayer temperature. For consistent interlayer temperatures, rafts should be used prior to the deposition of the part; the discussion linked the outcomes of this work to Yu et al. (2022), which could be implemented in this context to use shorter pauses and incremental power reductions to achieve

steady-state interlayer temperatures at a lower level in the build.

7.2.3 Machine Learning for LWAM

ML techniques were investigated, showing a similar accuracy to polynomials and process windows to predict whether printable tracks would be produced for combinations of head speed and extrusion rate using a Predictive Classification Ensemble architecture. It was also shown that Cascade Forward Neural Networks could be used to address the uncertainty in width measurements to create accurate track width predictions, even when the causes of the uncertainty are not fully characterised.

7.3 Recommended Further Work

The following were identified through the course of the research as opportunities for further investigation.

Variability of track width - It was identified that it is challenging to fully isolate and characterise the causes of variability in the consistency of track width. However, as technology develops with tighter tolerances, finer feature sizes and smaller wire diameters, determining and controlling these causes will be increasingly important.

Fully characterise other powers - The research focused primarily on process windows for 800W, the knowledge and machine learning tools developed can be used to efficiently identify optimum process parameter combinations over a wider range of powers. Using the Machine Learning tools to improve the efficiency of this characterisation would add valuable insights into the current body of published work. The training parameters used for the ML models were selected to ensure that they could support characterising other alloys without a full experimental investigation, which can now be explored.

Machine Learning for thermal modelling - A body of work was identified regarding how thermal modelling data can produce highly accurate and flexible tools for modelling the thermal field, reducing the time taken once trained to a few seconds. It is suggested that ANN models are flexible enough to adapt to new conditions and part geometries due to their ability to infer outcomes beyond those for which they have been trained. This could augment the limits of a tool such as Netfabb Local Simulation by using training data from experimental results and more complex thermal models, as well as to help to overcome the time and computing resource burden of modelling new parts and processes.

Track stepover and dilution - Building on the identified link between track separation within a layer and the resulting dilution between layers. The process may be tolerant to higher surface variability due to increased dilution. Creating parts with a wider range of track separations and investigating the relative tolerance to increased surface height variability and the resulting porosity could result in layers that require fewer tracks.

Adaptive and corrective layers - Use a range of Z-step sizes for different layers in the same deposition process to investigate whether the overbuilding of the part can be planned and corrected by intermittently using a different layer thickness or Z-step. The insights from the single-layer model could be used to investigate whether a complex layer shape could be produced with a consistent thickness by varying process parameters, number of tracks and track separation.

Adaptive interlayer pauses and power control - Research was identified by Yu et al. (2022) which showed that a combination of interlayer pauses and incremental reductions in laser power, as the layer height increases, achieved a steady state temperature at a lower layer number than the work here. This research could develop the Yu et al. (2022) powder DED thin wall research to

203

solid multilayer parts to achieve the desired consistent interlayer temperatures earlier in the build.

Substrate temperature of more complex builds - The results here using the substrate base temperature to infer the interlayer temperature could be evaluated for its effectiveness with more complex layer shapes where different thermal dynamics are likely and therefore, more complex thermal gradients across the layer. It is also an important next step to further develop the insights into heating and cooling cycles developed here through in-process measurement techniques into measurement systems that can be used in routine part production.

Appendix A

G-code Generation Flow Charts
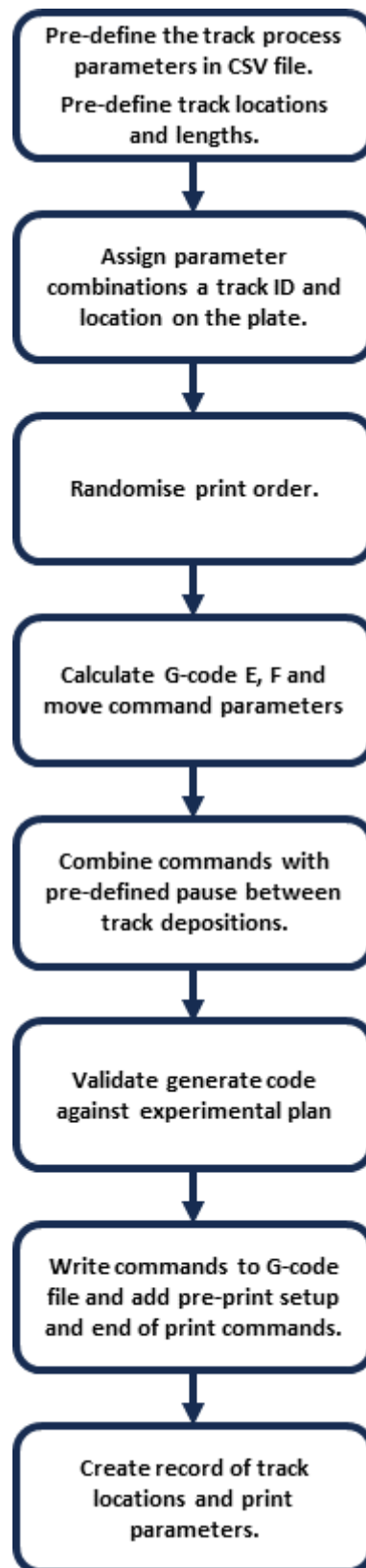
Figure A.1: Flow chart for the generation of the G-code for single-track experiments.
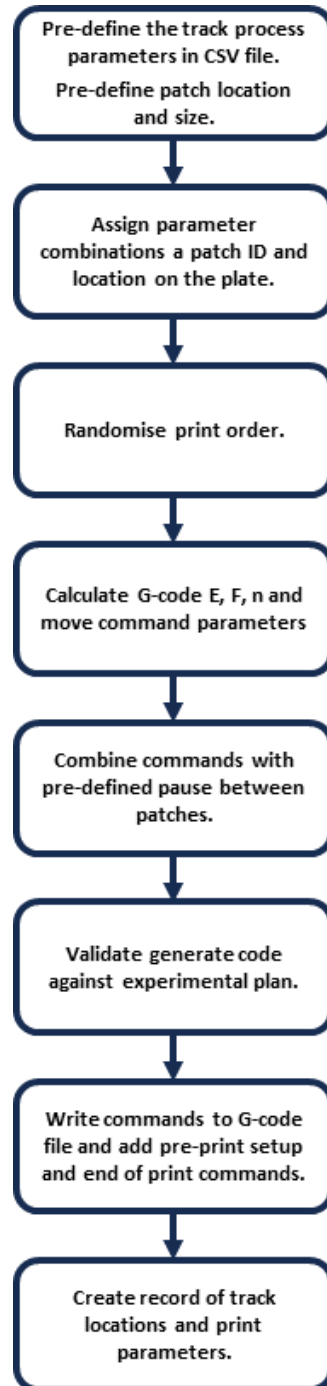
Figure A.2: Flow chart for the generation of the G-code for single-layer experiments.
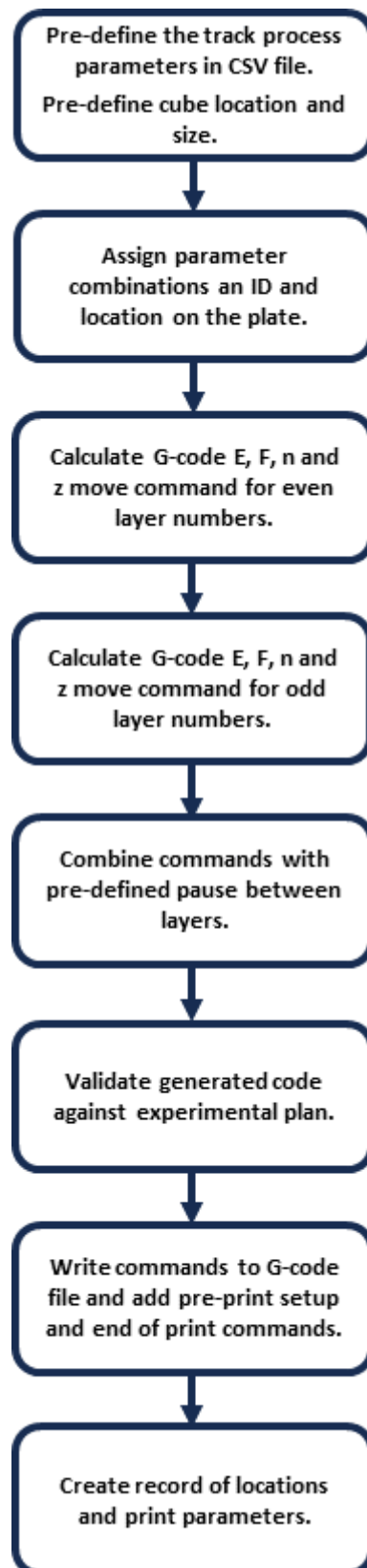
Figure A.3: Flow chart for the generation of the G-code for multi-layer experiments.
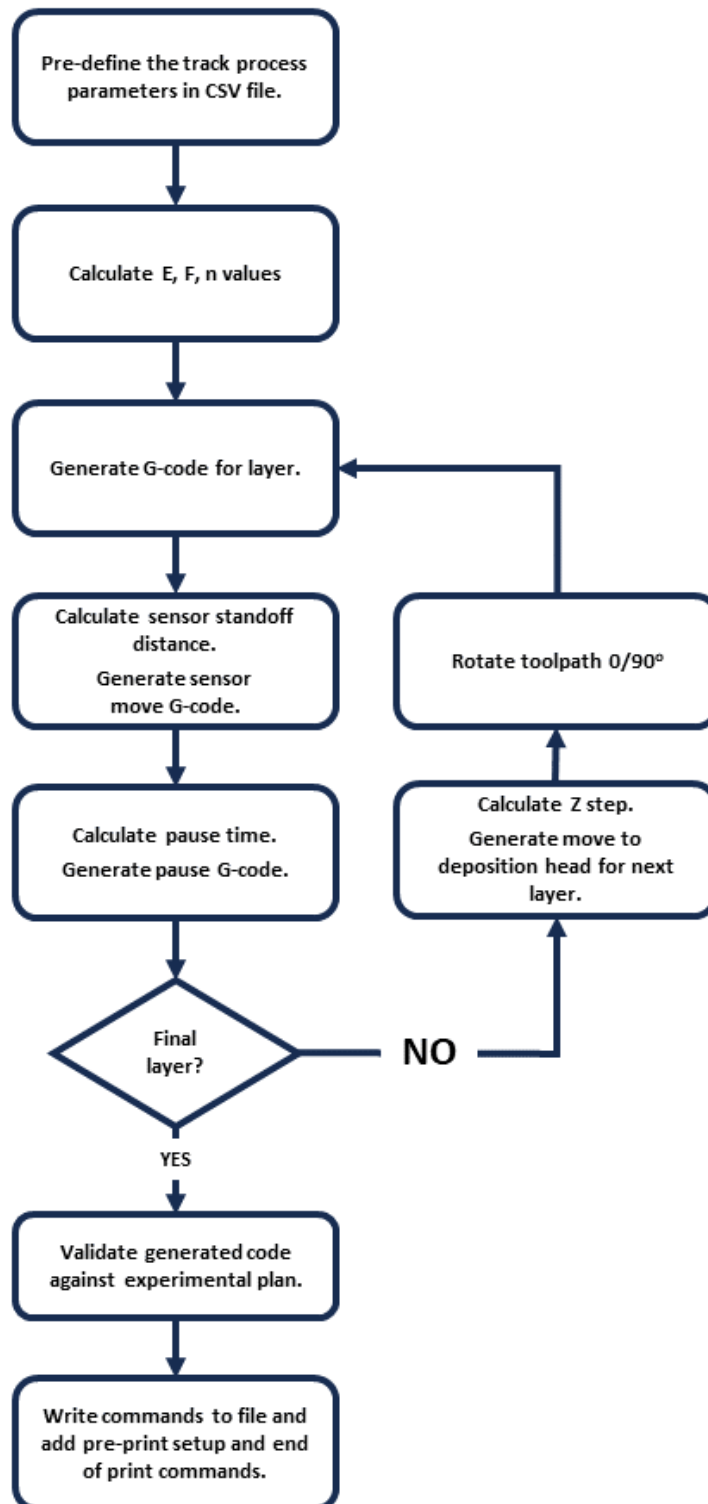
Figure A.4: Flow chart for the generation of the G-code for multi-layer thermal experiments.

Appendix B

Machine Learning Training Data for Prediction of Visual Track Assessment

Power	Vh	Vf	WSF	P_U	P_V	Printable	EPL	Fourier	HTM	EnergyDensity
800	5.0	25.0	5.00	32.00	160.00	N	160.000	0.144	2.806	30135847213
800	5.0	24.0	4.80	33.33	160.00	N	160.000	0.144	2.923	30135847213
800	9.4	9.4	1.00	85.00	85.00	Y	85.000	0.077	7.454	16009668832
800	10.7	10.7	1.00	75.00	75.00	Y	75.000	0.068	6.577	14126178377
800	12.3	12.3	1.00	65.00	65.00	Y	65.000	0.059	5.700	12242687928
800	14.5	14.5	1.00	55.00	55.00	Y	55.000	0.050	4.823	10359197476
800	6.3	9.4	1.50	85.00	127.50	Y	127.500	0.115	7.454	24014503247
800	8.2	12.3	1.50	65.00	97.50	Y	97.500	0.088	5.700	18364031896
800	7.5	11.5	1.53	69.57	106.67	Y	106.667	0.096	6.101	20090564808
800	7.5	9.5	1.27	84.21	106.67	Y	106.667	0.096	7.385	20090564808
800	7.5	11.5	1.53	69.57	106.67	Y	106.667	0.096	6.101	20090564808
800	7.5	13.5	1.80	59.26	106.67	Y	106.667	0.096	5.197	20090564808
800	7.5	15.5	2.07	51.61	106.67	Y	106.667	0.096	4.526	20090564808
800	5.5	9.5	1.73	84.21	145.45	Y	145.455	0.131	7.385	27396224739
800	5.5	11.5	2.09	69.57	145.45	Y	145.455	0.131	6.101	27396224739
800	9.5	17.5	1.84	45.71	84.21	Y	84.211	0.076	4.009	15860972217
800	9.5	11.5	1.21	69.57	84.21	Y	84.211	0.076	6.101	15860972217

Power	Vh	Vf	WSF	P_U	P_V	Printable	EPL	Fourier	HTM	EnergyDensity
800	9.5	15.5	1.63	51.61	84.21	Y	84.211	0.076	4.526	15860972217
800	11.5	15.5	1.35	51.61	69.57	Y	69.565	0.063	4.526	13102542266
800	13.5	17.5	1.30	45.71	59.26	Y	59.259	0.053	4.009	11161424894
800	13.5	19.5	1.44	41.03	59.26	Y	59.259	0.053	3.598	11161424894
800	13.5	21.5	1.59	37.21	59.26	N	59.259	0.053	3.263	11161424894
800	13.5	23.5	1.74	34.04	59.26	N	59.259	0.053	2.985	11161424894
800	9.5	9.5	1.00	84.21	84.21	Y	84.211	0.076	7.385	15860972217
800	11.5	9.5	0.83	84.21	69.57	N	69.565	0.063	7.385	13102542266
800	11.5	11.5	1.00	69.57	69.57	Y	69.565	0.063	6.101	13102542266
800	11.5	13.5	1.17	59.26	69.57	Y	69.565	0.063	5.197	13102542266
800	13.5	11.5	0.85	69.57	59.26	N	59.259	0.053	6.101	11161424894
800	13.5	13.5	1.00	59.26	59.26	Y	59.259	0.053	5.197	11161424894
800	7.5	11.5	1.53	69.57	106.67	Y	106.667	0.096	6.101	20090564808
800	4.9	12.3	2.50	64.99	162.60	Y	162.602	0.147	5.699	30625860988
800	5.3	10.7	2.00	74.98	150.09	Y	150.094	0.135	6.575	28270025528
800	5.5	7.5	1.36	106.67	145.45	Y	145.455	0.131	9.354	27396224739
800	5.5	11.5	2.09	69.57	145.45	Y	145.455	0.131	6.101	27396224739

Power	Vh	Vf	WSF	P_U	P_V	Printable	EPL	Fourier	HTM	EnergyDensity
800	6.2	12.3	2.00	64.99	130.08	Y	130.081	0.117	5.699	24500688791
800	7.5	13.5	1.80	59.26	106.67	Y	106.667	0.096	5.197	20090564808
800	9.5	10.7	1.13	74.77	84.21	Y	84.211	0.076	6.557	15860972217
800	9.5	13.5	1.42	59.26	84.21	Y	84.211	0.076	5.197	15860972217
800	9.5	15.5	1.63	51.61	84.21	Y	84.211	0.076	4.526	15860972217
800	9.7	14.6	1.50	54.98	82.47	Y	82.474	0.074	4.822	15533941862
800	10.5	12.3	1.17	65.04	76.19	Y	76.190	0.069	5.704	14350403435
800	13.5	15.5	1.15	51.61	59.26	Y	59.259	0.053	4.526	11161424894
800	11.5	17.5	1.52	45.71	69.57	Y	69.565	0.063	4.009	13102542266
800	13.5	13.5	1.00	59.26	59.26	Y	59.259	0.053	5.197	11161424894
800	8.3	10.7	1.29	74.77	96.39	Y	96.386	0.087	6.557	18154124827
800	5.5	7.5	1.36	106.67	145.45	Y	145.455	0.131	9.354	27396224739
800	6.2	10.6	1.71	75.47	129.03	Y	129.032	0.116	6.619	24303102591
800	5.5	11.5	2.09	69.57	145.45	Y	145.455	0.131	6.101	27396224739
800	5.5	13.5	2.45	59.26	145.45	Y	145.455	0.131	5.197	27396224739
800	7.5	7.5	1.00	106.67	106.67	Y	106.667	0.096	9.354	20090564808
800	7.5	9.5	1.27	84.21	106.67	Y	106.667	0.096	7.385	20090564808

Power	Vh	Vf	WSF	P_U	P_V	Printable	EPL	Fourier	HTM	EnergyDensity
800	7.5	11.5	1.53	69.57	106.67	Y	106.667	0.096	6.101	20090564808
800	7.5	11.5	1.53	69.57	106.67	Y	106.667	0.096	6.101	20090564808
800	9.5	9.5	1.00	84.21	84.21	Y	84.211	0.076	7.385	15860972217
800	11.5	11.5	1.00	69.57	69.57	Y	69.565	0.063	6.101	13102542266
800	11.5	13.5	1.17	59.26	69.57	Y	69.565	0.063	5.197	13102542266
800	19.5	23.5	1.21	34.04	41.03	N	41.026	0.037	2.985	7727140311
800	7.5	15.5	2.07	51.61	106.67	Y	106.667	0.096	4.526	20090564808
800	9.5	9.5	1.00	84.21	84.21	Y	84.211	0.076	7.385	15860972217
800	9.5	13.5	1.42	59.26	84.21	Y	84.211	0.076	5.197	15860972217
800	9.5	15.5	1.63	51.61	84.21	Y	84.211	0.076	4.526	15860972217
800	15.5	17.5	1.13	45.71	51.61	N	51.613	0.047	4.009	9721241036
800	5.5	15.5	2.82	51.61	145.45	Y	145.455	0.131	4.526	27396224739
800	9.5	17.5	1.84	45.71	84.21	Y	84.211	0.076	4.009	15860972217
800	9.5	11.5	1.21	69.57	84.21	Y	84.211	0.076	6.101	15860972217
800	11.5	19.5	1.70	41.03	69.57	Y	69.565	0.063	3.598	13102542266
800	5.0	7.5	1.50	106.67	160.00	Y	160.000	0.144	9.354	30135847213
800	6.3	8.8	1.40	91.43	128.00	Y	128.000	0.116	8.018	24108677770

214

Power	Vh	Vf	WSF	P_U	P_V	Printable	EPL	Fourier	HTM	EnergyDensity
800	5.0	10.0	2.00	80.00	160.00	Y	160.000	0.144	7.016	30135847213
800	7.5	10.0	1.33	80.00	106.67	Y	106.667	0.096	7.016	20090564808
800	10.0	10.0	1.00	80.00	80.00	Y	80.000	0.072	7.016	15067923606
800	7.5	11.0	1.47	72.73	106.67	Y	106.667	0.096	6.378	20090564808
800	7.5	12.5	1.67	64.00	106.67	Y	106.667	0.096	5.613	20090564808
800	10.0	12.5	1.25	64.00	80.00	Y	80.000	0.072	5.613	15067923606
800	5.0	12.5	2.50	64.00	160.00	Y	160.000	0.144	5.613	30135847213
800	5.0	15.0	3.00	53.33	160.00	Y	160.000	0.144	4.677	30135847213
800	7.5	15.0	2.00	53.33	106.67	Y	106.667	0.096	4.677	20090564808
800	10.0	15.0	1.50	53.33	80.00	Y	80.000	0.072	4.677	15067923606
800	12.5	15.0	1.20	53.33	64.00	Y	64.000	0.058	4.677	12054338885
800	15.0	15.0	1.00	53.33	53.33	N	53.333	0.048	4.677	10045282404
800	12.5	17.5	1.40	45.71	64.00	Y	64.000	0.058	4.009	12054338885
800	15.0	17.5	1.17	45.71	53.33	Y	53.333	0.048	4.009	10045282404
800	7.5	17.5	2.33	45.71	106.67	Y	106.667	0.096	4.009	20090564808
800	10.0	20.0	2.00	40.00	80.00	Y	80.000	0.072	3.508	15067923606
800	15.0	20.0	1.33	40.00	53.33	Y	53.333	0.048	3.508	10045282404

Power	Vh	Vf	WSF	P_U	P_V	Printable	EPL	Fourier	HTM	EnergyDensity
800	17.5	20.0	1.14	40.00	45.71	N	45.714	0.041	3.508	8610242061
750	5.0	7.5	1.50	100.00	150.00	N	150.000	0.144	8.770	28252356762
750	6.3	8.8	1.40	85.71	120.00	N	120.000	0.116	7.517	22601885409
750	5.0	10.0	2.00	75.00	150.00	Y	150.000	0.144	6.577	28252356762
750	7.5	10.0	1.33	75.00	100.00	Y	100.000	0.096	6.577	18834904508
750	10.0	10.0	1.00	75.00	75.00	Y	75.000	0.072	6.577	14126178381
750	7.5	11.0	1.47	68.18	100.00	Y	100.000	0.096	5.979	18834904508
750	7.5	12.5	1.67	60.00	100.00	Y	100.000	0.096	5.262	18834904508
750	10.0	12.5	1.25	60.00	75.00	Y	75.000	0.072	5.262	14126178381
750	5.0	12.5	2.50	60.00	150.00	N	150.000	0.144	5.262	28252356762
750	5.0	15.0	3.00	50.00	150.00	N	150.000	0.144	4.385	28252356762
750	7.5	15.0	2.00	50.00	100.00	Y	100.000	0.096	4.385	18834904508
750	10.0	15.0	1.50	50.00	75.00	Y	75.000	0.072	4.385	14126178381
750	12.5	15.0	1.20	50.00	60.00	Y	60.000	0.058	4.385	11300942705
750	15.0	15.0	1.00	50.00	50.00	Y	50.000	0.048	4.385	9417452254
750	12.5	17.5	1.40	42.86	60.00	Y	60.000	0.058	3.758	11300942705
750	15.0	17.5	1.17	42.86	50.00	Y	50.000	0.048	3.758	9417452254

Power	Vh	Vf	WSF	P_U	P_V	Printable	EPL	Fourier	HTM	EnergyDensity
750	7.5	17.5	2.33	42.86	100.00	N	100.000	0.096	3.758	18834904508
750	10.0	20.0	2.00	37.50	75.00	Y	75.000	0.072	3.289	14126178381
750	15.0	20.0	1.33	37.50	50.00	Y	50.000	0.048	3.289	9417452254
750	17.5	20.0	1.14	37.50	42.86	Y	42.857	0.041	3.289	8072101932
850	5.0	7.5	1.50	113.33	170.00	Y	170.000	0.144	9.939	32019337663
850	6.3	8.8	1.40	97.14	136.00	Y	136.000	0.116	8.519	25615470131
850	5.0	10.0	2.00	85.00	170.00	N	170.000	0.144	7.454	32019337663
850	7.5	10.0	1.33	85.00	113.33	Y	113.333	0.096	7.454	21346225109
850	10.0	10.0	1.00	85.00	85.00	Y	85.000	0.072	7.454	16009668832
850	7.5	11.0	1.47	77.27	113.33	Y	113.333	0.096	6.777	21346225109
850	7.5	12.5	1.67	68.00	113.33	Y	113.333	0.096	5.963	21346225109
850	10.0	12.5	1.25	68.00	85.00	Y	85.000	0.072	5.963	16009668832
850	5.0	12.5	2.50	68.00	170.00	N	170.000	0.144	5.963	32019337663
850	5.0	15.0	3.00	56.67	170.00	N	170.000	0.144	4.970	32019337663
850	7.5	15.0	2.00	56.67	113.33	Y	113.333	0.096	4.970	21346225109
850	10.0	15.0	1.50	56.67	85.00	Y	85.000	0.072	4.970	16009668832
850	12.5	15.0	1.20	56.67	68.00	Y	68.000	0.058	4.970	12807735065

Power	Vh	Vf	WSF	P_U	P_V	Printable	EPL	Fourier	HTM	EnergyDensity
850	15.0	15.0	1.00	56.67	56.67	N	56.667	0.048	4.970	10673112554
850	12.5	17.5	1.40	48.57	68.00	Y	68.000	0.058	4.260	12807735065
850	15.0	17.5	1.17	48.57	56.67	Y	56.667	0.048	4.260	10673112554
850	7.5	17.5	2.33	48.57	113.33	Y	113.333	0.096	4.260	21346225109
850	10.0	20.0	2.00	42.50	85.00	N	85.000	0.072	3.727	16009668832
850	15.0	20.0	1.33	42.50	56.67	N	56.667	0.048	3.727	10673112554
850	17.5	20.0	1.14	42.50	48.57	N	48.571	0.041	3.727	9148382190
800	5.0	7.5	1.50	106.67	160.00	Y	160.000	0.144	9.354	30135847213
800	6.3	8.8	1.40	91.43	128.00	Y	128.000	0.116	8.018	24108677770
800	5.0	10.0	2.00	80.00	160.00	Y	160.000	0.144	7.016	30135847213
800	7.5	10.0	1.33	80.00	106.67	Y	106.667	0.096	7.016	20090564808
800	10.0	10.0	1.00	80.00	80.00	N	80.000	0.072	7.016	15067923606
800	7.5	11.0	1.47	72.73	106.67	Y	106.667	0.096	6.378	20090564808
800	7.5	12.5	1.67	64.00	106.67	Y	106.667	0.096	5.613	20090564808
800	10.0	12.5	1.25	64.00	80.00	Y	80.000	0.072	5.613	15067923606
800	5.0	12.5	2.50	64.00	160.00	Y	160.000	0.144	5.613	30135847213
800	5.0	15.0	3.00	53.33	160.00	Y	160.000	0.144	4.677	30135847213

Power	Vh	Vf	WSF	P_U	P_V	Printable	EPL	Fourier	HTM	EnergyDensity
800	7.5	15.0	2.00	53.33	106.67	Y	106.667	0.096	4.677	20090564808
800	10.0	15.0	1.50	53.33	80.00	Y	80.000	0.072	4.677	15067923606
800	12.5	15.0	1.20	53.33	64.00	Y	64.000	0.058	4.677	12054338885
800	15.0	15.0	1.00	53.33	53.33	N	53.333	0.048	4.677	10045282404
800	12.5	17.5	1.40	45.71	64.00	Y	64.000	0.058	4.009	12054338885
800	15.0	17.5	1.17	45.71	53.33	Y	53.333	0.048	4.009	10045282404
800	7.5	17.5	2.33	45.71	106.67	Y	106.667	0.096	4.009	20090564808
800	10.0	20.0	2.00	40.00	80.00	Y	80.000	0.072	3.508	15067923606
800	15.0	20.0	1.33	40.00	53.33	Y	53.333	0.048	3.508	10045282404
800	17.5	20.0	1.14	40.00	45.71	N	45.714	0.041	3.508	8610242061
650	5.0	7.5	1.50	86.67	130.00	N	130.000	0.144	7.600	24485375860
650	6.3	8.8	1.40	74.29	104.00	N	104.000	0.116	6.515	19588300688
650	5.0	10.0	2.00	65.00	130.00	Y	130.000	0.144	5.700	24485375860
650	7.5	10.0	1.33	65.00	86.67	N	86.667	0.096	5.700	16323583907
650	10.0	10.0	1.00	65.00	65.00	N	65.000	0.072	5.700	12242687930
650	7.5	11.0	1.47	59.09	86.67	N	86.667	0.096	5.182	16323583907
650	7.5	12.5	1.67	52.00	86.67	Y	86.667	0.096	4.560	16323583907

Power	Vh	Vf	WSF	P_U	P_V	Printable	EPL	Fourier	HTM	EnergyDensity
650	10.0	12.5	1.25	52.00	65.00	Y	65.000	0.072	4.560	12242687930
650	5.0	12.5	2.50	52.00	130.00	N	130.000	0.144	4.560	24485375860
650	5.0	15.0	3.00	43.33	130.00	N	130.000	0.144	3.800	24485375860
650	7.5	15.0	2.00	43.33	86.67	N	86.667	0.096	3.800	16323583907
650	10.0	15.0	1.50	43.33	65.00	Y	65.000	0.072	3.800	12242687930
650	12.5	15.0	1.20	43.33	52.00	Y	52.000	0.058	3.800	9794150344
650	15.0	15.0	1.00	43.33	43.33	N	43.333	0.048	3.800	8161791953
650	12.5	17.5	1.40	37.14	52.00	Y	52.000	0.058	3.257	9794150344
650	15.0	17.5	1.17	37.14	43.33	Y	43.333	0.048	3.257	8161791953
650	7.5	17.5	2.33	37.14	86.67	N	86.667	0.096	3.257	16323583907
650	10.0	20.0	2.00	32.50	65.00	N	65.000	0.072	2.850	12242687930
650	15.0	20.0	1.33	32.50	43.33	Y	43.333	0.048	2.850	8161791953
650	17.5	20.0	1.14	32.50	37.14	Y	37.143	0.041	2.850	6995821674
950	5.0	7.5	1.50	126.67	190.00	Y	190.000	0.144	11.108	35786318565
950	6.3	8.8	1.40	108.57	152.00	Y	152.000	0.116	9.521	28629054852
950	5.0	10.0	2.00	95.00	190.00	Y	190.000	0.144	8.331	35786318565
950	7.5	10.0	1.33	95.00	126.67	Y	126.667	0.096	8.331	23857545710

Power	Vh	Vf	WSF	P_U	P_V	Printable	EPL	Fourier	HTM	EnergyDensity
950	10.0	10.0	1.00	95.00	95.00	Y	95.000	0.072	8.331	17893159283
950	7.5	11.0	1.47	86.36	126.67	Y	126.667	0.096	7.574	23857545710
950	7.5	12.5	1.67	76.00	126.67	Y	126.667	0.096	6.665	23857545710
950	10.0	12.5	1.25	76.00	95.00	Y	95.000	0.072	6.665	17893159283
950	5.0	12.5	2.50	76.00	190.00	N	190.000	0.144	6.665	35786318565
950	5.0	15.0	3.00	63.33	190.00	N	190.000	0.144	5.554	35786318565
950	7.5	15.0	2.00	63.33	126.67	N	126.667	0.096	5.554	23857545710
950	10.0	15.0	1.50	63.33	95.00	Y	95.000	0.072	5.554	17893159283
950	12.5	15.0	1.20	63.33	76.00	Y	76.000	0.058	5.554	14314527426
950	15.0	15.0	1.00	63.33	63.33	N	63.333	0.048	5.554	11928772855
950	12.5	17.5	1.40	54.29	76.00	N	76.000	0.058	4.761	14314527426
950	15.0	17.5	1.17	54.29	63.33	Y	63.333	0.048	4.761	11928772855
950	7.5	17.5	2.33	54.29	126.67	N	126.667	0.096	4.761	23857545710
950	10.0	20.0	2.00	47.50	95.00	N	95.000	0.072	4.166	17893159283
950	15.0	20.0	1.33	47.50	63.33	N	63.333	0.048	4.166	11928772855
950	17.5	20.0	1.14	47.50	54.29	N	54.286	0.041	4.166	10224662447
800	7.5	11.5	1.53	69.57	106.67	Y	106.667	0.096	6.101	20090564808

Power	Vh	Vf	WSF	P_U	P_V	Printable	EPL	Fourier	HTM	EnergyDensity
800	10.0	12.5	1.25	64.00	80.00	Y	80.000	0.072	5.613	15067923606
800	12.5	15.0	1.20	53.33	64.00	Y	64.000	0.058	4.677	12054338885
800	15.0	17.5	1.17	45.71	53.33	Y	53.333	0.048	4.009	10045282404
750	7.5	11.5	1.53	65.22	100.00	Y	100.000	0.096	5.719	18834904508
750	10.0	12.5	1.25	60.00	75.00	Y	75.000	0.072	5.262	14126178381
750	12.5	15.0	1.20	50.00	60.00	Y	60.000	0.058	4.385	11300942705
750	15.0	17.5	1.17	42.86	50.00	Y	50.000	0.048	3.758	9417452254
850	7.5	11.5	1.53	73.91	113.33	Y	113.333	0.096	6.482	21346225109
850	10.0	12.5	1.25	68.00	85.00	Y	85.000	0.072	5.963	16009668832
850	12.5	15.0	1.20	56.67	68.00	Y	68.000	0.058	4.970	12807735065
850	15.0	17.5	1.17	48.57	56.67	Y	56.667	0.048	4.260	10673112554
650	7.5	11.5	1.53	56.52	86.67	Y	86.667	0.096	4.957	16323583907
650	10.0	12.5	1.25	52.00	65.00	Y	65.000	0.072	4.560	12242687930
650	12.5	15.0	1.20	43.33	52.00	Y	52.000	0.058	3.800	9794150344
650	15.0	17.5	1.17	37.14	43.33	Y	43.333	0.048	3.257	8161791953
950	7.5	11.5	1.53	82.61	126.67	Y	126.667	0.096	7.245	23857545710
950	10.0	12.5	1.25	76.00	95.00	Y	95.000	0.072	6.665	17893159283

Power	Vh	Vf	WSF	P_U	P_V	Printable	EPL	Fourier	HTM	EnergyDensity
950	12.5	15.0	1.20	63.33	76.00	Y	76.000	0.058	5.554	14314527426
950	15.0	17.5	1.17	54.29	63.33	Y	63.333	0.048	4.761	11928772855

Table B.1: Training data used for Machine Learning model training for prediction of visual assessment outcomes and process windows.

Appendix C

Machine Learning Training Data for Prediction of Track Height and Width

Power (W)	Head Speed (mm/s)	Extrusion Rate (mm\s)	WSF	$\frac{P}{V_f}$	$\frac{P}{V_h}$	Energy Density	Fourier No.	Heat to Melt	Width (mm)	Height (mm)
800	9.41	9.41	1.00	85.00	85.00	16009668831.53	0.08	7.45	1.897	0.533
800	10.67	10.67	1.00	75.00	75.00	14126178376.52	0.07	6.58	1.878	0.530
800	12.31	12.31	1.00	65.00	65.00	12242687927.85	0.06	5.70	1.936	0.526
800	14.55	14.55	1.00	55.00	55.00	10359197476.12	0.05	4.82	1.646	0.604
800	9.50	9.50	1.00	84.21	84.21	15860972217.19	0.08	7.39	1.986	0.538
800	11.50	11.50	1.00	69.57	69.57	13102542266.38	0.06	6.10	1.938	0.567
800	13.50	13.50	1.00	59.26	59.26	11161424893.58	0.05	5.20	1.873	0.598
800	13.50	13.50	1.00	59.26	59.26	11161424893.58	0.05	5.20	1.724	0.610
800	7.50	7.50	1.00	106.67	106.67	20090564808.44	0.10	9.35	1.918	0.600
800	9.50	9.50	1.00	84.21	84.21	15860972217.19	0.08	7.39	2.029	0.546
800	11.50	11.50	1.00	69.57	69.57	13102542266.38	0.06	6.10	1.807	0.545
800	9.50	9.50	1.00	84.21	84.21	15860972217.19	0.08	7.39	2.036	0.576
800	9.50	10.70	1.13	74.77	84.21	15860972217.19	0.08	6.56	2.031	0.566
800	13.50	15.50	1.15	51.61	59.26	11161424893.58	0.05	4.53	1.746	0.648
800	11.50	13.50	1.17	59.26	69.57	13102542266.38	0.06	5.20	1.874	0.606

Power (W)	Head Speed (mm/s)	Extrusion Rate (mm\s)	WSF	$\frac{P}{V_f}$	$\frac{P}{V_h}$	Energy Density	Fourier No.	Heat to Melt	Width (mm)	Height (mm)
800	10.50	12.30	1.17	65.04	76.19	14350403434.60	0.07	5.70	1.944	0.671
800	11.50	13.50	1.17	59.26	69.57	13102542266.38	0.06	5.20	1.781	0.670
800	9.50	11.50	1.21	69.57	84.21	15860972217.19	0.08	6.10	2.002	0.601
800	7.50	9.50	1.27	84.21	106.67	20090564808.44	0.10	7.39	1.884	0.701
800	7.50	9.50	1.27	84.21	106.67	20090564808.44	0.10	7.39	1.892	0.667
800	8.30	10.70	1.29	74.77	96.39	18154124826.91	0.09	6.56	2.116	0.679
800	13.50	17.50	1.30	45.71	59.26	11161424893.58	0.05	4.01	1.646	0.683
800	11.50	15.50	1.35	51.61	69.57	13102542266.38	0.06	4.53	1.776	0.729
800	5.50	7.50	1.36	106.67	145.45	27396224738.79	0.13	9.35	2.290	0.644
800	5.50	7.50	1.36	106.67	145.45	27396224738.79	0.13	9.35	1.944	0.749
800	9.50	13.50	1.42	59.26	84.21	15860972217.19	0.08	5.20	1.976	0.720
800	13.50	19.50	1.44	41.03	59.26	11161424893.58	0.05	3.60	1.724	0.807
800	6.27	9.41	1.50	85.00	127.50	24014503247.29	0.12	7.45	2.015	0.734
800	8.21	12.31	1.50	65.00	97.50	18364031895.51	0.09	5.70	1.908	0.734
800	9.70	14.55	1.50	54.98	82.47	15533941862.20	0.07	4.82	1.868	0.762

Power (W)	Head Speed (mm/s)	Extrusion Rate (mm\s)	WSF	$\frac{P}{V_f}$	$\frac{P}{V_h}$	Energy Density	Fourier No.	Heat to Melt	Width (mm)	Height (mm)
800	11.50	17.50	1.52	45.71	69.57	13102542266.38	0.06	4.01	1.912	0.823
800	7.50	11.50	1.53	69.57	106.67	20090564808.44	0.10	6.10	1.967	0.735
800	7.50	11.50	1.53	69.57	106.67	20090564808.44	0.10	6.10	2.000	0.734
800	7.50	11.50	1.53	69.57	106.67	20090564808.44	0.10	6.10	2.190	0.743
800	7.50	11.50	1.53	69.57	106.67	20090564808.44	0.10	6.10	1.973	0.791
800	7.50	11.50	1.53	69.57	106.67	20090564808.44	0.10	6.10	2.077	0.738
800	9.50	15.50	1.63	51.61	84.21	15860972217.19	0.08	4.53	1.968	0.842
800	9.50	15.50	1.63	51.61	84.21	15860972217.19	0.08	4.53	1.989	0.818
800	5.00	8.33	1.67	480.00	96.00	30135847212.67	0.14	8.42	2.240	0.783
800	10.00	16.67	1.67	480.00	48.00	15067923606.33	0.07	4.21	1.845	0.863
800	6.20	10.60	1.71	75.47	129.03	24303102590.86	0.12	6.62	2.224	0.810
800	5.50	9.50	1.73	84.21	145.45	27396224738.79	0.13	7.39	2.080	0.857
800	7.50	13.50	1.80	59.26	106.67	20090564808.44	0.10	5.20	1.952	0.913
800	7.50	13.50	1.80	59.26	106.67	20090564808.44	0.10	5.20	2.032	0.890
800	9.50	17.50	1.84	45.71	84.21	15860972217.19	0.08	4.01	2.006	0.863

Power (W)	Head Speed (mm/s)	Extrusion Rate (mm\s)	WSF	$\frac{P}{V_f}$	$\frac{P}{V_h}$	Energy Density	Fourier No.	Heat to Melt	Width (mm)	Height (mm)
800	6.15	12.31	2.00	64.99	130.08	24500688790.79	0.12	5.70	2.220	0.924
800	7.50	15.50	2.07	51.61	106.67	20090564808.44	0.10	4.53	1.966	0.983
800	5.50	11.50	2.09	69.57	145.45	27396224738.79	0.13	6.10	2.223	0.951

References

Abadi, SMA Noori Rahim et al. (2023). "Influence of laser-wire interaction on heat and metal transfer in directed energy deposition". In: *International Journal of Heat and Mass Transfer* 205, p. 123894.

Abioye, TE et al. (2017). "Laser metal deposition of multi-track walls of 308LSi stainless steel". In: *Materials and Manufacturing Processes* 32.14, pp. 1660–1666.

Abuabiah, Mohammad et al. (2023). "Advancements in Laser Wire-Feed Metal Additive Manufacturing: A Brief Review". In: *Materials* 16.5, p. 2030.

Al Zubaidi, Faten N et al. (2019). "The effect of long-term oxidation on the total hemispherical emissivity of type 316L stainless steel". In: *Nuclear Technology* 205.6, pp. 790–800.

Aliyev, Alissultan, Kwang-Kyu Lee, and Dong-Gyu Ahn (2022). "Effects of deposition strategies on thermo-mechanical characteristics of inconel 718 deposited region on AISI 1045 substrate with a cantilever structure by LENS process". In: *Journal of Mechanical Science and Technology* 36.9, pp. 4695–4705.

Amine, Tarak, Joseph W. Newkirk, and Frank Liou (2014). "Investigation of effect of process parameters on multilayer builds by direct metal deposition". In: *Applied Thermal Engineering* 73.1, pp. 500–511. ISSN: 1359-4311. DOI: `https://doi.org/10.1016/j.applthermaleng.2014.08.005`.

ArcelorMittal Industeel (2016). *UR 316L Stainless Steel Data Sheet*. `https://industeel.arcelormittal.com/fichier/ur-316l/`. Accessed: 2023-06-07.

Autodesk (2023). *Netfabb 2024 User Manual: GUID-6BAF550D-C179-4785-99AA-2355A3FCFC90*. Accessed: 17-May-2023. URL: `https://help.autodesk.`

`com / view / NETF / 2024 / ENU / ?guid = GUID – 6BAF550D – C179 – 4785 – 99AA – 2355A3FCFC90`.

Bandyopadhyay, Amit et al. (2022). "Alloy design via additive manufacturing: Advantages, challenges, applications and perspectives". In: *Materials Today* 52, pp. 207–224.

Bastola, Nabin et al. (2023). "A review of the residual stress generation in metal additive manufacturing: Analysis of cause, measurement, effects, and prevention". In: *Micromachines* 14.7, p. 1480.

Bayat, Mohamad et al. (2021). "A review of multi-scale and multi-physics simulations of metal additive manufacturing processes with focus on modeling strategies". In: *Additive Manufacturing* 47, p. 102278.

Brennan, MC, JS Keist, and TA Palmer (2021). *Defects in metal additive manufacturing processes*.

Caiazzo, Fabrizia (2018). "Additive manufacturing by means of laser-aided directed metal deposition of titanium wire". In: *The International Journal of Advanced Manufacturing Technology* 96, pp. 2699–2707.

Caiazzo, Fabrizia and Vittorio Alfieri (2019). "Simulation of laser-assisted directed energy deposition of aluminum powder: prediction of geometry and temperature evolution". In: *Materials* 12.13, p. 2100.

Cao, Yong et al. (2011). "Overlapping model of beads and curve fitting of bead section for rapid manufacturing by robotic MAG welding process". In: *Robotics and computer-integrated manufacturing* 27.3, pp. 641–645.

Chen, Shu-Guang et al. (2022). "Review on residual stresses in metal additive manufacturing: formation mechanisms, parameter dependencies, prediction and control approaches". In: *Journal of Materials Research and Technology* 17, pp. 2950–2974. ISSN: 2238-854. DOI: `https://doi.org/10.1016/j.jmrt.2022.02.054`.

Chen, Xi et al. (2021). "A review on wire-arc additive manufacturing: typical defects, detection approaches, and multisensor data fusion-based model". In: *The International Journal of Advanced Manufacturing Technology* 117, pp. 707–727.

Cheng, Manping et al. (2023). "Residual Stress Control Using Process Optimization in Directed Energy Deposition". In: *Materials* 16.19, p. 6610.

Cui, W. et al. (2020). "Metal Additive Manufacturing Parts Inspection Using Convolutional Neural Network". In: *Applied Sciences* 10.2, p. 545.

Cunningham, C.R. et al. (2018). "Invited review article: Strategies and processes for high quality wire arc additive manufacturing". In: *Additive Manufacturing* 22, pp. 672–686.

Dass, Adrita and Atieh Moridi (2019). "State of the art in directed energy deposition: From additive manufacturing to materials design". In: *Coatings* 9.7, p. 418.

DebRoy, T. et al. (2019). "Scientific, technological and economic issues in metal printing and their solutions". In: *Nat Mater* 18.10, pp. 1026–1032.

DebRoy, T. and H.K.D.H. Bhadeshia (2021). "Picture to parts, one thin metal layer at a time". In: *Innovations in Everyday Engineering Materials*, pp. 35–49.

Denlinger, E.R. et al. (2015). "Effect of inter-layer dwell time on distortion and residual stress in additive manufacturing of titanium and nickel alloys". In: *Journal of Materials Processing Technology* 215, pp. 123–131.

Ding, D et al. (2015). "A multi-bead overlapping model for robotic wire and arc additive manufacturing (WAAM)". In: *Robotics and Computer-Integrated Manufacturing* 31, pp. 101–110.

Ding, Donghong et al. (2014). "A tool-path generation strategy for wire and arc additive manufacturing". In: *The international journal of advanced manufacturing technology* 73, pp. 173–183.

Farias, Francisco Werley Cipriano, João da Cruz Payão Filho, and Victor Hugo Pereira Moraes e Oliveira (2021). "Prediction of the interpass temperature of a wire arc additive manufactured wall: FEM simulations and artificial neural network". In: *Additive Manufacturing* 48, p. 102387.

Feenstra, D.R., A. Molotnikov, and N. Birbilis (2021). "Utilisation of artificial neural networks to rationalise processing windows in directed energy deposition applications". In: *Materials & Design* 198.

Ferro, Paolo et al. (2020). "A modified volumetric energy density–based approach for porosity assessment in additive manufacturing process design". In: *The International Journal of Advanced Manufacturing Technology* 110, pp. 1911–1921.

Fetni, S. et al. (2021). "Thermal field prediction in DED manufacturing process using Artificial Neural Network". In: "1–10".

Froend, M et al. (2018). "Process development for wire-based laser metal deposition of 5087 aluminium alloy by using fibre laser". In: *Journal of Manufacturing Processes* 34, pp. 721–732.

Ghasempour, M, D Afonso, and R Torcato (2021). "Numerical investigation of deposition strategies on the residual stress and geometrical deviation in Laser Metal Deposition". In: *IOP Conference Series: Materials Science and Engineering.* Vol. 1193. 1. IOP Publishing, p. 012095.

Graf, B. et al. (2018). "3D laser metal deposition: process steps for additive manufacturing". In: *Welding in the World* 62.4, pp. 877–883.

Greer, Clayton et al. (2019). "Introduction to the design rules for metal big area additive manufacturing". In: *Additive manufacturing* 27, pp. 159–166.

Grierson, D., A.E.W. Rennie, and S.D. Quayle (2021). "Machine Learning for Additive Manufacturing". In: *Encyclopedia* 1.3, pp. 576–588.

Gurmesa, Fakada Dabalo and Hirpa Gelgele Lemu (2023). "Literature Review on Thermomechanical Modelling and Analysis of Residual Stress Effects in Wire Arc Additive Manufacturing". In: *Metals* 13.3, p. 526.

Hatala, Glenn W. et al. (2021). "A Thermo-Mechanical Analysis of Laser Hot Wire Additive Manufacturing of NAB". In: *Metals* 11.7. ISSN: 2075-4701. DOI: 10.3390/met11071023.

Huang, W. et al. (2021). "Laser wire-feed metal additive manufacturing of the Al alloy". In: *Optics & Laser Technology* 134, "106627".

Kim, Ho et al. (2021). "Effects of deposition strategy and preheating temperature on thermo-mechanical characteristics of Inconel 718 super-alloy deposited on AISI 1045 substrate using a DED process". In: *Materials* 14.7, p. 1794.

Kshirsagar, R. et al. (2019). "Prediction of Bead Geometry Using a Two-Stage SVM–ANN Algorithm for Automated Tungsten Inert Gas (TIG) Welds". In: *Journal of Manufacturing and Materials Processing* 3.2, p. 39.

Kumar, Manish, S Surya Kumar, and Abhay Sharma (2021). "Bi-polynomial fourth-order weld bead model for improved material utilization and accuracy in wire-arc additive manufacturing: A case of transverse twin-wire welding". In: *Advances in Industrial and Manufacturing Engineering* 2, p. 100049.

Kumar, Pravin, Neelesh Kumar Jain, and Mayur S Sawant (2020). "Modeling of dimensions and investigations on geometrical deviations of metallic components manufactured by μ-plasma transferred arc additive manufacturing process". In: *The International Journal of Advanced Manufacturing Technology* 107, pp. 3155–3168.

Kumar, Pravin, Neelesh Kumar Jain, and Mayur Sudhakar Sawant (2022). "Development of theoretical models for dimensions of single-layer multi-track and multi-layer multi-track depositions by μ-PTA additive manufacturing process". In: *Journal of Materials Research and Technology* 17, pp. 95–110.

Łabanowski, Jerzy and Maria Głowacka (2011). "Heat tint colours on stainless steel and welded joints". In: *Welding International* 25.7, pp. 509–512.

Laghi, Vittoria et al. (2021). "Experimentally-validated orthotropic elastic model for wire-and-arc additively manufactured stainless steel". In: *Additive Manufacturing* 42, p. 101999.

Le, Van Thao et al. (2023). "Efficient prediction of thermal history in wire and arc additive manufacturing combining machine learning and numerical simulation". In: *The International Journal of Advanced Manufacturing Technology*, pp. 1–13.

Leach, RK et al. (2019). "Geometrical metrology for metal additive manufacturing". In: *CIRP annals* 68.2, pp. 677–700.

Li, X. et al. (2018). "A Transfer Learning Approach for Microstructure Reconstruction and Structure-property Predictions". In: *Sci Rep* 8.1, p. 13461.

Li, Zhiqiang et al. (2023). "Optimization of the Overlap Rate of Multi-track Laser Cladding Based on the Flat-Top Overlapping Model". In: *Transactions of the Indian Institute of Metals*, pp. 1–10.

Lienhard, John H. (2011). *A heat transfer textbook*. eng. 4th ed. Dover Civil and Mechanical Engineering. Mineola, N.Y.: Dover Publications. ISBN: 9780486318370.

Liu, Fan et al. (2022). "Parametric study of the three-beam laser inside coaxial wire feeding additive manufacturing". In: *The International Journal of Advanced Manufacturing Technology* 123.1-2, pp. 313–330.

Liu, Sen, Craig Brice, and Xiaoli Zhang (2021). "Comprehensive Quality Investigations of Wire-feed Additive Manufacturing by Learning of Experimental Data". In: *arXiv preprint arXiv:2103.12662*.

Liu, Yang, Jing Shi, and Yachao Wang (2023). "Evolution, Control, and Mitigation of Residual Stresses in Additively Manufactured Metallic Materials: A Review". In: *Advanced Engineering Materials*.

Lu, X.F. et al. (2019). "Residual stress and distortion of rectangular and S-shaped Ti-6Al-4V parts by Directed Energy Deposition: Modelling and experimental calibration". In: *Additive Manufacturing* 26, pp. 166–179.

Machine Learning with MATLAB (2022). Accessed: July 2022. URL: `https://matlabacademy.mathworks.com/details/machine-learning-with-matlab/mlml`.

Meltio (Mar. 2021). `https://meltio3d.com/metal-3d-printers/meltio-m450/`. Accessed: 2021-03-04.

Meltio M450 Manual (Feb. 2022). 2nd ed. Accessed: 2022-02-01. Meltio. Online. URL: `https://www.meltio3d.com`.

Michel, Florent et al. (2019). "A modular path planning solution for Wire+ Arc Additive Manufacturing". In: *Robotics and Computer-Integrated Manufacturing* 60, pp. 1–11.

Motta, Maurizio, Ali Gökhan Demir, and Barbara Previtali (2018). "High-speed imaging and process characterization of coaxial laser metal wire deposition". In: *Additive Manufacturing* 22, pp. 497–507.

Mozaffar, M. et al. (2018). "Data-driven prediction of the high-dimensional thermal history in directed energy deposition processes via recurrent neural networks". In: *Manufacturing Letters* 18, pp. 35–39.

Mukherjee, T. et al. (2017). "Dimensionless numbers in additive manufacturing". In: *Journal of Applied Physics* 121.6.

Nalajam, P.K. and R. Varadarajan (2021). "A Hybrid Deep Learning Model for Layer-Wise Melt Pool Temperature Forecasting in Wire-Arc Additive Manufacturing Process". In: *IEEE Access* 9, pp. 100652–100664.

O'Regan, P. et al. (2016). "Metal Based Additive Layer Manufacturing: Variations, Correlations and Process Control". In: *Procedia Computer Science* 96, pp. 216–224.

Oliari, S.H., A.S.C.M. D'Oliveira, and M. Schulz (2017). "Additive Manufacturing of H11 with Wire-Based Laser Metal Deposition". In: *Soldagem & Inspecao* 22.4, pp. 466–479.

Petrat, Torsten et al. (2018). "Build-up strategies for temperature control using laser metal deposition for additive manufacturing". In: *Welding in the World* 62, pp. 1073–1081.

Roberts, Matthew, Min Xia, and Andrew Kennedy (2022). "Data-driven Process Parameter Optimisation for Laser Wire Metal Additive Manufacturing". In: *2022 27th International Conference on Automation and Computing (ICAC)*. IEEE, pp. 1–6.

Roch, Clément, Christophe Tournier, and Sylvain Lavernhe (2023). "Process based modelling of power density for wire laser additive manufacturing using a coaxial head". In: *Additive Manufacturing*, p. 103648.

Sefene, Eyob Messele, Yeabsra Mekdim Hailu, and Assefa Asmare Tsegaw (2022). "Metal hybrid additive manufacturing: state-of-the-art". In: *Progress in Additive Manufacturing* 7.4, pp. 737–749.

Shamsaei, Nima et al. (2015). "An overview of Direct Laser Deposition for additive manufacturing; Part II: Mechanical behavior, process parameter optimization and control". In: *Additive manufacturing* 8, pp. 12–35.

Sharma, Ruchi et al. (2023). "Forecasting of process parameters using machine learning techniques for wire arc additive manufacturing process". In: *Materials Today: Proceedings* 80. 3rd International Congress on Mechanical and Systems Engineering (CAMSE 2022), pp. 248–253. ISSN: 2214-7853. DOI: `https://doi.org/10.1016/j.matpr.2022.12.081`.

Shi, Deheng et al. (2015). "Modeling the effect of surface oxidation on the normal spectral emissivity of steel 316L at 1.5 μm over the temperatures ranging from 800 to 1100 K in air". In: *Infrared Physics & Technology* 71, pp. 370–377.

Singh, S. et al. (2021). "Effect of Interlayer Delay on the Microstructure and Mechanical Properties of Wire Arc Additive Manufactured Wall Structures". In: *Materials* 14.15.

Spranger, Felix et al. (2018). "Build-up strategies for additive manufacturing of three dimensional Ti-6Al-4V-parts produced by laser metal deposition". In: *Journal of Laser Applications* 30.2.

Srivastava, S. et al. (2021). "Measurement and Mitigation of Residual Stress in Wire-Arc Additive Manufacturing: A Review of Macro-Scale Continuum Modelling Approach". In: *Archives of Computational Methods in Engineering* 28.5, pp. 3491–3515.

Suryakumar, S et al. (2011). "Weld bead modeling and process optimization in hybrid layered manufacturing". In: *Computer-Aided Design* 43.4, pp. 331–344.

Svetlizky, D. et al. (2021). "Directed energy deposition (DED) additive manufacturing: Physical characteristics, defects, challenges and applications". In: *Materials Today*.

Syed, Waheed Ul Haq, Andrew J Pinkerton, and Lin Li (2005). "A comparative study of wire feeding and powder feeding in direct diode laser deposition for rapid prototyping". In: *Applied surface science* 247.1-4, pp. 268–276.

Tapia, G. and A. Elwany (2014). "A Review on Process Monitoring and Control in Metal-Based Additive Manufacturing". In: *Journal of Manufacturing Science and Engineering-Transactions of the Asme* 136.6.

Thomas-Seale, L.E.J. et al. (2018). "The barriers to the progression of additive manufacture: Perspectives from UK industry". In: *International Journal of Production Economics* 198, pp. 104–118.

Tomar, Bunty, S Shiva, and Tameshwer Nath (2022). "A review on wire arc additive manufacturing: Processing parameters, defects, quality improvement and recent advances". In: *Materials Today Communications* 31, p. 103739.

Vafadar, A. et al. (2021). "Advances in Metal Additive Manufacturing: A Review of Common Processes, Industrial Applications, and Current Challenges". In: *Applied Sciences-Basel* 11.3.

Valiorgue, Frédéric et al. (2011). "Emissivity calibration for temperature measurement using infrared thermography in orthogonal cutting of 316L and 100Cr6 grinding". In: *AIP Conference Proceedings*. Vol. 1315. 1. American Institute of Physics, pp. 1053–1058.

Wacker, C. et al. (2021). "Geometry and Distortion Prediction of Multiple Layers for Wire Arc Additive Manufacturing with Artificial Neural Networks". In: *Applied Sciences-Basel* 11.10.

Wang, C. et al. (2020). "Machine learning in additive manufacturing: State-of-the-art and perspectives". In: *Additive Manufacturing* 36.

Wu, Bintao et al. (2018). "A review of the wire arc additive manufacturing of metals: properties, defects and quality improvement". In: *Journal of manufacturing processes* 35, pp. 127–139.

Xia, C.Y. et al. (2020). "A review on wire arc additive manufacturing: Monitoring, control and a framework of automated system". In: *Journal of Manufacturing Systems* 57, pp. 31–45.

Xiong, Jun et al. (2014). "Bead geometry prediction for robotic GMAW-based rapid manufacturing through a neural network and a second-order regression analysis". In: *Journal of Intelligent Manufacturing* 25, pp. 157–163.

Xu, Peng et al. (2022). "In-process adaptive dimension correction strategy for laser aided additive manufacturing using laser line scanning". In: *Journal of Materials Processing Technology* 303, p. 117544.

Yadollahi, Aref et al. (2015). "Effects of process time interval and heat treatment on the mechanical and microstructural properties of direct laser deposited 316L stainless steel". In: *Materials Science and Engineering: A* 644, pp. 171–183. ISSN: 0921-5093. DOI: `https://doi.org/10.1016/j.msea.2015.07.056`.

Yan, Z. et al. (2018). "Review on thermal analysis in laser-based additive manufacturing". In: *Optics & Laser Technology* 106, "427–441".

Ye, Zhi-peng et al. (2017). "Study of hybrid additive manufacturing based on pulse laser wire depositing and milling". In: *The International Journal of Advanced Manufacturing Technology* 88, pp. 2237–2248.

Yu, Tianbiao et al. (2022). "Research on the temperature control strategy of thin-wall parts fabricated by laser direct metal deposition". In: *The International Journal of Advanced Manufacturing Technology* 122.2, pp. 669–684.

Zapata, Avelino et al. (2022). "Investigation on the cause-effect relationships between the process parameters and the resulting geometric properties for wire-based coaxial laser metal deposition". In: *Metals* 12.3, p. 455.

Zhang, Li et al. (2022). "Improvement of mechanical properties through inhibition of oxidation by adding TiC particles in laser aided additive manufacturing of stainless steel 316L". In: *Materials Science and Engineering: A* 853, p. 143767.

Zhang, YuMing et al. (2003). "Weld deposition-based rapid prototyping: a preliminary study". In: *Journal of Materials Processing Technology* 135.2-3, pp. 347–357.

Zhang, Z.Y., Z.C. Liu, and D.Z. Wu (2021). "Prediction of melt pool temperature in directed energy deposition using machine learning". In: *Additive Manufacturing* 37.

Zhu, K., J.Y.H. Fuh, and X. Lin (2021). "Metal-based Additive Manufacturing Condition Monitoring: A Review on Machine Learning Based Approaches". In.

Zhu, Q., Z. Liub, and J. Yana (2020). "Machine learning for metal additive manufacturing: Predicting temperature and melt pool fluid dynamics using physics-informed neural networks". In.